



HAL
open science

Development of a laser heterodyne radiometer for atmospheric remote sensing

Fengjiao Shen

► **To cite this version:**

Fengjiao Shen. Development of a laser heterodyne radiometer for atmospheric remote sensing. Instrumentation and Detectors [physics.ins-det]. Université du Littoral Côte d'Opale, 2019. English. NNT : 2019DUNK0542 . tel-02483498

HAL Id: tel-02483498

<https://theses.hal.science/tel-02483498>

Submitted on 18 Feb 2020

HAL is a multi-disciplinary open access archive for the deposit and dissemination of scientific research documents, whether they are published or not. The documents may come from teaching and research institutions in France or abroad, or from public or private research centers.

L'archive ouverte pluridisciplinaire **HAL**, est destinée au dépôt et à la diffusion de documents scientifiques de niveau recherche, publiés ou non, émanant des établissements d'enseignement et de recherche français ou étrangers, des laboratoires publics ou privés.

Development of a Laser Heterodyne Radiometer for Atmospheric Remote Sensing

**D éveloppement d'un radiom ètre h é érodyne laser pour la
t é é d éction atmosph érique**

THESIS

Presented to

Université du Littoral Côte d'Opale

To obtain

Doctoral degree at the Université du Littoral Côte d'Opale

Discipline : Physics

By

Fengjiao SHEN

Doctoral School : Sciences de la Matière, du Rayonnement et de l'Environnement

Laboratoire de Physico-Chimie de l'Atmosph ère

Defended on **December 2019**

Members of the jury :

Aurore VICET , MCF (HDR), Université de Montpellier	President of jury, Examiner
Bertrand PARVITTE , Professor, Université de Reims	Reporter
Martina WIEDNER , Chercheur, Observatoire de Paris	Reporter
Gunther ROELKENS , Professor, Ghent University	Examiner
Weidong CHEN , Professor, Université du Littoral Côte d'Opale	Director of thesis
Yao TE , MCF (HDR), Sorbonne Université	Invited member

Acknowledgements

Here in is the last phase of writing this thesis. In fact, it is not the easiest part, but certainly the closest to my heart. Indeed, all of this work would not have been possible without the support of some very special people.

This work was realized at the Laboratoire de Physico-Chimie de l' Atmosphère (LPAC) at the Université Littoral Côte d'Opale (ULCO).

First, I would like to express my heartfelt appreciation to Mr. Weidong CHEN, my thesis director, for giving me the opportunity to do my PhD in LPCA. My progress on my PhD work would not have been possible without his insight and guidance, including the attention to all of the little details which sometimes passed me by. He has taught me how to think like a scientist.

I would like to give my sincere acknowledgement to the members of the jury who have accepted to evaluate my thesis work. Thanks to Mr. Bertrand PARVITTE and Mrs. Martina WIEDNER for being my reporters and giving me some valuable comments and advices. Thanks to Mrs. Aurore VICET for chairing my defense as well as being my examiner. Thank to Mr. Gunther ROELKENS for being my examiner and providing me some valuable comments.

I would like to thank Mr. Eric FERTAIN, who worked closely with me at the beginning of my experimental stage and always help me when I have problems in life.

I would like to express my sincere gratitude to Mr. Yao TE for his help in the field measurement at the Université Pierre-et-Marie-Curie (UPMC) as well as providing corrections and comments related to retrieval algorithm in my thesis.

I would like to sincerely appreciate to Dong CHEN for his care, his patient guidance and his distance mentorship during my PhD study and tough life. He is not only my mentor, my friend, but also my father.

Additional acknowledgments go out to Gaoxuan WANG, a post-doctor who always worked together with me when I was in troubles. In daily life, he treats me as his little sister, always tolerates me and has been really good to me for my tough five years in France.

I do really appreciate Tu TAN for his help in the last year of my thesis, and always tried to enlighten me when I was in a bad mood.

I feel very grateful to my Chinese master supervisor Mr. Fengzhong DONG. Thank you for your patience and careful guidance during my master's study and life in China. The biggest regret in my life is not seeing you for the last time and not attending your funeral. I hope you will feel happy and proud of me in heaven when you see me graduate successfully.

I acknowledge all of my best friends in France including Khaoula KARROUM, Layal FAYAD, and Ghidda BADRAN for their sincere love and support which let me never give up. They are really very warm and lovely, and their enthusiasm has infected me, which makes my tough and boring life in France full of happiness, surprise and expectation. When I return to China, I will remember this foreign friendship forever and hope that one day we will meet again somewhere in the world. I don't want the last goodbye in France to be the last goodbye in our lives.

Thanks to my team members including Tong and Lingshuo. Thanks to my friends in LPCA and UCEIV including Rayan, Hadi, Tinehinane, Bouthayna, Jonas, Lamia, St éphanie, Alla, and Allen.

Thanks to my Chinese friends Jie ZHANG, Luo HAN, Huili ZHANG, Pengshuai SUN, Jingjing WANG, Huadong WANG, Wei WANG, Yan XIANG, and Jiajin CHEN,

My parents, my elder brother, my sister-in-law, my niece (Zhongchenxi SHEN) and my nephew (Hongyi SHEN) deserve special thanks for their love and support throughout this process. It's safe to say that I wouldn't be here if they hadn't guided me through my life, including the tough times.

And finally, I could probably go on and list countless more people, but I'm afraid I only have so much space to work with. Please contact me if I have left you out.

Table of Contents

List of Figures	viii
List of Tables	xvi
List of Acronyms	xviii
Abstract	xxiii
Introduction	1
I Remote sensing of vertical concentration profiles of atmospheric trace gases.....	1
II Techniques of passive remote sensing of vertical concentration profile.....	4
III Laser heterodyne radiometer.....	15
III.1 History of the LHR technique.....	16
III.2 Local oscillator involved in LHR.....	18
III.3 State of the art.....	20
IV Aim of this work.....	23
References.....	24
1 Principle of laser heterodyne radiometer	39
1.1 Sunlight collection.....	40
1.2 Heterodyne receiver.....	42
1.2.1 Photomixer.....	42
1.2.2 RF amplifier and band-pass filter.....	43
1.2.3 Square law detector.....	44
1.2.4 Lock-in amplifier.....	45
1.3 Heterodyne efficiency.....	46
1.3.1 Spatial distribution of the beams being mixed.....	47
1.3.1.1 Beam spot size.....	47
1.3.1.2 Phase front alignment.....	50
1.3.2 Polarization-sensitive photomixing.....	53
1.3.3 Coupling of the mixed beams to the mixer.....	53
1.4 Noise sources.....	53
1.4.1 Detection chain noise.....	54
1.4.1.1 Johnson noise.....	54

1.4.1.2	Background noise.....	54
1.4.1.3	Dark current noise.....	55
1.4.2	Laser-induced noise.....	55
1.4.2.1	Laser-induced shot noise.....	55
1.4.2.2	Coherently detected thermal noise.....	56
1.4.2.3	Laser excess noise.....	57
1.4.3	Signal-induced noise.....	57
1.4.3.1	Signal-induced shot noise.....	58
1.4.3.2	Signal excess noise.....	58
1.5	Instrument SNR and sensitivity (Limit of detection, LoD).....	59
1.6	Extraction of heterodyne signal using a lock-in amplifier.....	62
1.7	Comparing the LHR with a Fourier Transform Spectrometer.....	63
1.8	From atmospheric column absorption spectrum to vertical profile concentration.....	64
1.8.1	Retrieval principle.....	65
1.8.1.1	Atmospheric radiative transfer forward model.....	65
1.8.1.2	Inversion method in atmospheric vertical profile.....	65
1.8.2	Baseline treatment.....	67
1.8.3	Vertical resolution.....	68
	Conclusion.....	68
	References.....	70
2	Mid-IR LHR instrumental consideration and configuration.....	75
2.1	Key devices involved in a mid-IR LHR.....	75
2.1.1	Sun-tracker.....	75
2.1.2	IR blackbody source.....	79
2.1.3	Local oscillator (LO).....	81
2.1.4	Photomixer.....	84
2.1.5	RF receiver.....	86
2.1.5.1	Band-pass filter.....	86
2.1.5.2	RF amplifier.....	87
2.1.5.3	Square law detector.....	87
2.1.6	Lock-in amplifier and optical chopper system.....	89
2.2	LHR configurations.....	94
2.2.1	Sunlight collection using a free-space telescope cage system.....	95

2.2.1.1	Sunlight beam contraction and laser beam expander.....	96
2.2.1.2	Coupling of sunlight and LO beams to the mixer.....	99
2.2.2	Sunlight collection using a fiber coupling system.....	102
2.2.2.1	Description of a fiber coupling system for sunlight collection.....	102
2.2.2.2	Test of the fiber coupling and sun-tracking performance.....	104
	Conclusion.....	106
	References.....	107
3	Performance evaluation of the local oscillator being used.....	109
3.1	Introduction.....	109
3.2	Experimental details.....	110
3.2.1	N ₂ O monitoring by long optical path absorption spectroscopy.....	110
3.2.2	Selection of a N ₂ O absorption line for sensitive and selective concentration measurement.....	112
3.2.3	Frequency metrology and N ₂ O absorption spectrum retrieval.....	112
3.2.4	N ₂ O concentration retrieval.....	113
3.2.5	Laser line width evaluation.....	115
3.2.6	Measurement precision and limit of detection.....	116
3.3	Experimental results and discussions.....	118
3.3.1	N ₂ O evolution in catalytic reaction of NO with CO.....	119
	Conclusion.....	120
	References.....	121
4	Development of a proof of concept mid-IR LHR.....	123
4.1	A PoC LHR operating at 8 μm.....	123
4.2	LHR performance characterization.....	125
4.2.1	Beat signal generation.....	125
4.2.1.1	SNR of the beating signal.....	125
4.2.1.2	Beating level vs. the LO power.....	126
4.2.2	Laser heterodyne spectrum of CH ₄	127
4.2.2.1	CH ₄ absorption line selection for sensitive and selective heterodyne measurement.....	127
4.2.2.2	Laser heterodyne spectrum of CH ₄ absorption at 8 μm.....	129
4.2.2.3	Frequency scanning speed vs. time constant of the LIA.....	130

4.3	Field measurement in Paris.....	136
4.3.1	LHR involving a telescope system for free-space coupling of sunlight.....	136
4.3.2	Preliminary field test results of the developed PoC LHR.....	139
4.3.2.1	LHR baseline treatment.....	139
4.3.2.2	Heterodyne measurement of atm. CH ₄ absorption spectrum.....	140
	Conclusion.....	142
	References.....	144
5	Development of a portable mid-IR LHR prototype.....	145
5.1	LHR prototype involving a mid-IR fiber to couple blackbody radiation.....	145
5.1.1	Instrumental description.....	145
5.1.2	Performance characterization of the LHR prototype.....	147
5.1.2.1	SNR of the beating signal.....	147
	I. SNR of the LHR using fiber coupling system.....	147
	I.1 Noise sources in LHR system.....	148
	I.2 Theoretical SNR vs. measured SNR.....	154
	I.3 Heterodyne signal and SNR of the LHR vs. LO photocurrent.....	155
	II. SNR comparison between LHRs using free-space coupling and fiber coupling for sunlight collection.....	157
5.1.2.2	Spectroscopic performance.....	158
	I. BB-laser heterodyne spectrum of CH ₄ absorption at 8 μm.....	158
	II. Impact of RF pass-band on LHR spectrum.....	160
	III. LHR spectral line-shape vs. scanning speed of LO frequency.....	162
5.2	LHR prototype involving a mid-IR fiber to couple sunlight radiation.....	164
5.2.1	Instrumental description.....	164
5.2.2	Heterodyne measurement of atmospheric CH ₄ and N ₂ O.....	166
	Conclusion.....	168
	References.....	170
	Summary and prospects.....	171
	Résumé.....	174
	Appendix.....	196
	Appendix 1 All fiber-coupled LHR.....	196

Appendix 2 Optimization using Zemax.....	205
Appendix 3 Conversion from the measured intensity (in [V]) to the radiation (in [W/m ²]).....	207
Appendix 4 Solar emission spectru.....	208
Appendix 5 Article : Real-time monitoring of N ₂ O production in a catalytic reaction process using mid-infrared quantum cascade laser.....	210
Appendix 6 Invited talk, 41st PIERS, 17-20 June 2019, Rome, Italy.....	222
Publications and conferences.....	223

List of Figures

Figure 1	<i>left</i> : characteristic time scales for vertical transport; <i>right</i> : typical time scales for global horizontal transport in the troposphere.....	2
Figure 2	Schematic diagram of the nadir viewing geometry in BUV mode.....	4
Figure 3	Solar occultation viewing geometry.....	6
Figure 4	Limb scattering viewing geometry with single scattering, surface reflection, and second order of scattering, respectively (the atmosphere’s curvature is exaggerated)	6
Figure 5	Limb emission viewing geometry.....	7
Figure 6	Principle of MAX-DOAS.....	9
Figure 7	Optical scheme of SAOZ instrument.....	11
Figure 8	Schematic of a FTS for retrieving vertical concentration profile of atmospheric trace gas.....	12
Figure 9	<i>upper</i> : map of the TCCON sites; <i>lower</i> : map of the NDACC sites.....	13
Figure 10	Schematic of a LHR for retrieving vertical concentration profile of atmospheric trace gas.....	15
Figure 11	Optical layout of the EC-QC-LHR developed by D. Weidmann et al.....	20
Figure 12	Schematic of the mini-LHR developed by E. L. Wilson et al.....	21
Figure 13	Schematic diagram of the experimental setup of R. Alexander et al.....	22
Figure 14	Schematic diagram of the experimental setup of a mid-IR LHR developed by J. Wang et al.....	22
Figure 1.1	Basic concept of a typical LHR.....	40
Figure 1.2	<i>left</i> : geometric restriction of the antenna theory; <i>right</i> : solid angle Ω_s vs. radiation wavelength λ	41
Figure 1.3	Geometry restriction of the solid angle Ω_s and FoV in the antenna theory.....	41
Figure 1.4	Schematic diagram of a heterodyne receiver.....	42
Figure 1.5	Schematic diagram of a LHR for photomixing of the sunlight beam and the LO beam.....	43
Figure 1.6	Receiving bandwidth of double sidebands of a LHR receiver.....	44

Figure 1.7	Schematic diagram of a LHR for amplifying and filtering the RF signal.....	44
Figure 1.8	Schematic diagram of a LHR for power detection of the RF signal.....	45
Figure 1.9	Gaussian beam width $w(z)$ as a function of the distance z along the beam.....	48
Figure 1.10	Coupling wavefronts of two Gaussian beams.....	49
Figure 1.11	Coupling wavefronts of a Gaussian beam and a plane beam.....	49
Figure 1.12	Coupling efficiency of a Gaussian beam with a plane beam.....	50
Figure 1.13	Photomixing illuminated by the solar radiation and the LO light. Phase fronts of the both beams are normal to the propagation direction.....	51
Figure 1.14	<i>left</i> : as a function of the mismatch angle for several values d (at $\lambda=8 \mu\text{m}$); <i>right</i> : as a function of mismatch angle for several values of λ (with $d=0.5 \text{ mm}$).....	52
Figure 1.15	Spatial distribution of the incident beams on the photomixer.....	53
Figure 1.16	Plot of SNR for an ideal LHR vs. wavelength.....	60
Figure 1.17	Heterodyne radiometer sensitivity to thermal radiation.....	61
Figure 1.18	Schematic diagram of a LHR using LIA.....	62
Figure 1.19	Quantitative comparison between SNR_{LHR} and SNR_{FTS}	64
Figure 1.20	(a) Calculated CH_4 absorption spectra at different altitudes in the infrared range of $1254.5\text{-}1255.5 \text{ cm}^{-1}$; (b) Atmospheric transmission spectrum of CH_4 obtained by integrating spectra in (a); (c) Vertical concentration profile of atmospheric CH_4 at the location of TCCON-Paris station (WACCM model (Whole Atmosphere Community Climate Model)).....	64
Figure 1.21	Flow chart of the data retrieval.....	67
Figure 2.1	Schematic diagram of a typical LHR system.....	75
Figure 2.2	Schematic of sun tracker.....	76
Figure 2.3	<i>left</i> : CSPHOT sun-photometer; <i>right</i> : sunlight collection optics (circled by <i>green dotted line</i>) installed on the CSPHOT sun-photometer, involved in NASA's near-IR-LHR setup.....	77
Figure 2.4	Bruker A547N Sun tracker.....	77
Figure 2.5	EKO sun-tracker (model STR-21G).....	78
Figure 2.6	<i>left</i> : blackbody source (Oriel® Model 67030, Newport Inc.); <i>right</i> : major components of the 67030 Blackbody source.....	80

Figure 2.7	(a) Typical irradiance spectra of the used blackbody at different temperatures; (b) Emissivity of the blackbody at 1000 °C from a 0.5 inch (12.7 mm) aperture.....	80
Figure 2.8	<i>left</i> : emitter source IR-Si217; <i>right</i> : packaged emitter source with a CaF2 window.....	81
Figure 2.9	Spectral radiances of an Oriel blackbody source (Model 67030, Newport Inc.) operating at 1000 °C with an emissivity of 1 (red curve) and an IR-Si217 infrared emitter operating at 1385 °C with an emissivity of 0.8 (black curve).....	81
Figure 2.10	<i>left</i> : CW Mode Hop-Free EC-QCL (Model CW-MHF 41000, Daylight Solution, Inc.); <i>right</i> : wide tuning of 1223 to 1263 cm ⁻¹ with output power of ~60 mW at 1223 cm ⁻¹ and more than 80 mW at ≥1247 cm ⁻¹	82
Figure 2.11	<i>upper</i> : Detectable molecules in the spectral coverage region of the EC-QCL used in the present work, based on the HITRAN database; <i>lower</i> : absorption spectra of HONO and N ₂ O ₅	83
Figure 2.12	<i>left</i> : PVMI-4TE-8 VIGO detector; <i>right</i> : detector current responsivity and detectivity vs. wavelength.....	84
Figure 2.13	<i>left</i> : PVI-4TE-10.6 VIGO detector; <i>right</i> : detector current responsivity and detectivity vs. wavelength.....	85
Figure 2.14	<i>left</i> : RF amplifier (ZFL-500LN+); <i>right</i> : Noise Figure vs. frequency.....	87
Figure 2.15	<i>upper</i> : Keysight 8472B schottky diode; <i>lower</i> : typical detector's square-law response (<i>left</i>) and diode V/I characteristics (<i>right</i>).....	88
Figure 2.16	Effective transfer function of a LIA. R is the resistor, C is the capacitor.....	90
Figure 2.17	Simulation output spectra from the LP filter using different parameters (see Table 2.6). Condition of the Hitran simulation spectrum (input : <i>black</i>) : absorption line center: 1233.45 cm ⁻¹ , pressure: 250 mbar, concentration: 0.1, absorption cell: 13 cm.....	92
Figure 2.18	Plot of the time constant vs. ΔT _{scan} , associated with a linear fit.....	93
Figure 2.19	Plot of V _{out} (t) vs. V _{in} (t) in point-by-point frequency tuning mode.....	94
Figure 2.20	Scheme of the LHR configurations involved in the present work.....	95
Figure 2.21	<i>upper</i> : schematic of a free-space telescope cage system for coupling sunlight; <i>lower</i> : photo of the developed telescope cage system.....	95
Figure 2.22	Beam contraction layout (surf: surface of lens, f: focal length, D: lens diameter,	

	STO: Stop surface, IMA: Image surface).....	98
Figure 2.23	Beam expander layout (surf: surface of lens, f: focal length, D: lens diameter, STO: Stop surface, IMA: Image surface).....	98
Figure 2.24	Optical layout of a free-space coupling mid-IR LHR.....	100
Figure 2.25	Emerging beam size after lens 5 as a function of the sunlight size.....	101
Figure 2.26	Focusing angle of the emerging beam by lens 5 as a function of the sunlight size.....	101
Figure 2.27	Distance needed between two lenses ($f_1=150$ mm and $f_2=75$ mm) for the beam contraction as a function of the sunlight size.....	101
Figure 2.28	Schematic of the fiber system for sunlight coupling.....	102
Figure 2.29	Schematic of a fully transportable LHR involving a mid-IR fiber coupling sunlight system.....	103
Figure 2.30	<i>left</i> : polycrystalline IR-fiber coupling system; <i>right</i> : transmission spectra of the PIR fiber.....	104
Figure 2.31	“STRConfig” Setting screen : GPS mode (<i>upper</i>) and manual mode (<i>lower</i>).....	105
Figure 2.32	Measured sunlight intensities (blue curve) in comparison with a reference from a "Davis Vantage Pro2" weather station (black curve).....	106
Figure 3.1	Experimental setup used for N ₂ O monitoring of a chemical catalysis reaction of NO with CO.....	111
Figure 3.2	Simulation spectra of 300 ppbv N ₂ O, 1% H ₂ O, and 450 ppmv CO ₂ absorptions in a multi-pass cell ($L_{\text{eff}}=50$ m) at 120 mbar.....	112
Figure 3.3	Absorption signal of 5 ppmv N ₂ O at 120 mbar (a) and its absorption spectrum (d), obtained using the relative wavenumber calibration curve (c) which allows one to convert “data point number” into “wavenumber” through the FSR of the used etalon (b).....	113
Figure 3.4	(a) N ₂ O absorption spectra at different concentrations at 120 mbar; (b) Plot of the integrated absorbance vs. concentration, associated with a linear fit. Error bars are one standard deviation of the integrated absorbance from Voigt profile fit.....	115

Figure 3.5	Absorption spectrum of 6.13 ppmv N ₂ O (black curve) at 120 mbar, accompanied with a Voigt profile fit (red curve).....	116
Figure 3.6	Allan deviation plot.....	117
Figure 3.7	<i>upper panel</i> : absorption spectrum of N ₂ O in air (black curve) at 120 mbar, accompanied with a Voigt profile fit (red curve); <i>lower panel</i> : fit residual.....	118
Figure 3.8	<i>left</i> : experiment of catalytic reaction of NO with CO to purify CO ₂ in exhaust gas flow from oxyfuel-combustion; <i>right</i> : EC-QCL-based sensor of N ₂ O.....	118
Figure 3.9	Absorption spectrum of 6.13 ppmv N ₂ O during a catalytic reaction of NO with CO over a Pt/SiO ₂ catalyst at 190 °C at 120 mbar.....	119
Figure 3.10	Time series measurement of N ₂ O concentration during a NO-CO reaction over a Pt/SiO ₂ catalyst vs. temperature.....	119
Figure 4.1	<i>upper</i> : schematic of the developed LHR receiver; <i>lower</i> : picture of the developed 8 μm mid-IR LHR in the present work.....	124
Figure 4.2	Beat note signal measured at the output of the LIA.....	125
Figure 4.3	Beat note amplitude vs. LO power.....	126
Figure 4.4	(a) Atmospheric absorption spectrum recorded with a Bruker IFS 125; (b) Simulation spectrum of multi-GHG using 0.5% H ₂ O, 2 ppm CH ₄ , 450 ppm CO ₂ and 320 ppb N ₂ O in the range of 1223-1263 cm ⁻¹	127
Figure 4.5	(a) Atmospheric absorption spectrum; (b) Simulation spectrum of multi-GHG using 0.5% H ₂ O, 2 ppm CH ₄ , 450 ppm CO ₂ and 320 ppb N ₂ O (<i>black</i>); Individually simulated absorption spectra of 0.5% H ₂ O (<i>blue</i>), 2 ppm CH ₄ (<i>orange</i>), 450 ppm CO ₂ (<i>in pink</i>) and 320 ppb N ₂ O (<i>green</i>) in the range of 1241.3-1242.5 cm ⁻¹	128
Figure 4.6	(a) Atmospheric absorption spectrum; (b) Simulation spectrum of multi-GHG using 0.5% H ₂ O, 2 ppm CH ₄ , 450 ppm CO ₂ and 320 ppb N ₂ O (<i>black</i>); Individual Simulation spectra of 0.5% H ₂ O (<i>blue</i>), 2 ppm CH ₄ (<i>orange</i>), 450 ppm CO ₂ (<i>pink</i>) and 320 ppb N ₂ O (<i>green</i>) in the range of 1261.2-1262.8 cm ⁻¹	128
Figure 4.7	<i>upper</i> : direct absorption used as spectrum reference (<i>black</i>) fitted with a Lorentz profile (<i>red</i>); <i>lower</i> : heterodyne spectrum of CH ₄ absorption near 8 μm (<i>black</i>) fitted with a Lorentz profile (<i>red</i>).....	130

Figure 4.8	BB-based heterodyne spectra of CH ₄ absorption at a scanning speed v_{sc} of 0.03148 cm ⁻¹ /s (a scanning time ΔT_{scan} of 1709 ms) combined with different time constants, respectively.....	131
Figure 4.9	BB-based heterodyne spectra of CH ₄ absorption at a scanning speed v_{sc} of 0.0787 cm ⁻¹ /s (a scanning time ΔT_{scan} of 684 ms) combined with different time constants, respectively.....	132
Figure 4.10	BB-based heterodyne spectra of CH ₄ absorption at a scanning speed v_{sc} of 0.1574 cm ⁻¹ /s (a scanning time ΔT_{scan} of 342 ms) combined with different time constants, respectively.....	133
Figure 4.11	BB-based heterodyne spectra of CH ₄ absorption at a scanning speed v_{sc} of 0.3935 cm ⁻¹ /s (a scanning time ΔT_{scan} of 137 ms) combined with different time constants, respectively.....	134
Figure 4.12	<i>left</i> : external heliostat (sun-tracker) installed on the roof terrace; <i>right</i> : Bruker IFS 125HR located in the lower-level experimental room (TCCON-Paris station).....	136
Figure 4.13	<i>upper</i> : schematic of a telescope system for free-space coupling of sunlight; <i>lower</i> : photo of the telescope system.....	137
Figure 4.14	Schematic of the LHR deployed for the field test on the QualAir platform at the UPMC.....	138
Figure 4.15	<i>upper</i> : sun-tracker installed on the roof terrace on the QualAir platform; <i>lower</i> : a free-space telescope coupling system used for sunlight coupling to the LHR in a field test at the UPMC.....	138
Figure 4.16	(a) Local oscillator signal; (b) Sunlight-coupled heterodyne signal; (c) Blackbody-coupled heterodyne signal.....	140
Figure 4.17	(a) LHR CH ₄ absorption signal (<i>red</i>) associated with a baseline of sunlight (<i>blue</i>) and BB-based LHR baseline (<i>black</i>) associated with a baseline of blackbody (<i>pink</i>); (b) Normalized LHR atmospheric CH ₄ absorption signal (<i>red</i>) and LHR baseline (<i>black</i>); (c) Post-processed LHR atmospheric CH ₄ transmission signal (<i>blue</i>) after normalization of the normalized LHR spectrum to the normalized BB baseline, both shown in (b).....	141
Figure 4.18	(a) Recorded LHR signal (<i>red</i>) and baseline (<i>black</i>); (b) Normalized LHR signal (<i>red</i>) and baseline (<i>black</i>); (c) Normalized signal (<i>blue</i>) by dividing the	

	red curve by the black one, both shown in (b).....	141
Figure 4.19	Atmospheric absorption spectrum of CH ₄ recorded with a Bruker IFS 125HR FTS in Paris (a), with our LHR (b), and from an atmospheric transmission model (c).....	142
Figure 5.1	Schematic of a mid-IR LHR prototype using a fiber to couple blackbody radiation.....	146
Figure 5.2	LHR prototype involving a mid-IR fiber to couple blackbody radiation (<i>upper</i> : front view; <i>lower</i> : top view).....	146
Figure 5.3	SNR measurement of the beat note at the output of the LIA. The mixed LO and BB power measured at the output of the photomixer were 3.66 V and 0.70 V, respectively. A filter with a pass-band of 27.5-270 MHz was used. A time constant of 1 s combined with LP filters (12 dB/oct) was used for the LIA.....	147
Figure 5.4	<i>upper</i> : noise amplitude spectra of the heterodyne system in the bandwidth of 1kHz-500 MHz; <i>lower</i> : zoom of the upper figure in the bandwidth of 1kHz-160 MHz.....	150
Figure 5.5	<i>left</i> : noise amplitude spectra of the RF output of the photomixer in the bandwidth of 1kHz-500 MHz with different LO photocurrents; <i>right</i> : enlarged scale in the bandwidth of 1kHz-150 MHz.....	151
Figure 5.6	<i>upper</i> : noise density spectra from the RF output of the photomixer at different LO power-induced photocurrents measured with a signal analyzer; <i>lower</i> : zoom of the upper figure in the pass-band of 27.5-270 MHz.....	152
Figure 5.7	Plots of : (1) detection chain noise density N_{Det} (<i>red line</i>), (2) measured system total noise density N_{total} (<i>black square</i>), deduced from dividing the total noise amplitude measured at 150 MHz (Fig. 5.6 <i>lower</i>) by the square root of the RBW (100 kHz), and (3) the laser-induced noise N_{LIN} (<i>blue triangle</i>) deduced by subtracting the detection chain noise N_{Det} ((1) <i>red line</i>) from the total noise N_{total} ((2) <i>black square</i>), vs. LO photocurrents.....	153
Figure 5.8	Densities of laser-induced noise N_{LIN} ((3) <i>blue triangle</i>), laser-induced shot noise N_{LSN} ((4) <i>black circle</i>), laser excess noise N_{LEN} ((5) <i>green star</i>), and detection chain noise N_{Det} ((1) <i>red line</i>) vs. photocurrent of the LO laser, respectively...	154
Figure 5.9	Evolution of heterodyne signal (<i>black square</i>) and SNR (<i>red square</i>) as a function of LO photocurrent.....	156

Figure 5.10	<i>left</i> : background (<i>red</i>) and direct absorption signal of CH ₄ at 260 mbar (<i>black</i>); direct absorption used as spectrum reference (<i>blue</i>) fitted with a Voigt profile (<i>green</i>); <i>right</i> : background (<i>red</i>) and heterodyne absorption signal of CH ₄ at 260 mbar (<i>black</i>); heterodyne spectrum of CH ₄ absorption (<i>blue</i>) fitted with a Voigt profile (<i>green</i>).....	159
Figure 5.11	Noise amplitude spectrum of the RF output from the photomixer in the bandwidth of 1kHz-500 MHz.....	161
Figure 5.12	Heterodyne spectra of CH ₄ extracted with different RF filter pass-bands.....	162
Figure 5.13	Heterodyne absorption spectra of CH ₄ (<i>red</i>), fitted with Voigt profiles (<i>blue</i>).....	163
Figure 5.14	Schematic of the MIR-LHR prototype involving a fiber to couple sunlight to the LHR receiver.....	165
Figure 5.15	LHR prototype in use for a field measurement test.....	165
Figure 5.16	Noise amplitude spectra of the RF output from the photomixer within the bandwidth of 1kHz-500 MHz.....	166
Figure 5.17	<i>left</i> : laser heterodyne spectrum of CH ₄ and N ₂ O absorptions in the atmospheric column (Sun position: 16.69° Zenith / 156.47° Azimuth, 24 m above sea level, 18 Nov. 2018); <i>right</i> : simulation spectrum of multi-GHG (<i>olive</i>) using 0.5% H ₂ O (<i>green</i>), 2 ppm CH ₄ (<i>orange</i>), 450 ppm CO ₂ (<i>pink</i>) and 320 ppb N ₂ O (<i>cyan</i>) in the range of 1261.2-1262.8 cm ⁻¹ , accompanied with individual simulation spectra of all species mentioned above.....	167
Figure 5.18	(a) Atmospheric absorption spectrum of CH ₄ and N ₂ O from 1261.3 to 1262.3 cm ⁻¹ recorded using a Bruker IFS 125HR FTS on the TCCON observation site in Paris; (b) the corresponding laser heterodyne spectrum of CH ₄ and N ₂ O absorptions in the atmospheric column; (c) the atmospheric transmission modelling spectrum.....	167

List of Tables

Table 1	Comparisons among satellite, ground, and airplane/balloon platforms.....	14
Table 2.1	Specifications of three commercially available sun-trackers.....	79
Table 2.2	Specifications of IR photomixers for LHR application.....	86
Table 2.3	Pass-bands of RF filters available for the present work.....	87
Table 2.4	Specifications of Keysight 8472B and Herotek DHM020BB schottky diodes.....	89
Table 2.5	Specifications of lock-in amplifier (Model 5110, AMETEK, Inc.).....	89
Table 2.6	Simulation of the effect of the LP filter on absorption line-shape with different τ	91
Table 2.7	Lens data editor of the beam contraction.....	98
Table 2.8	Lens data editor of the beam expander.....	99
Table 2.9	The Lens editor.....	100
Table 2.10	Specifications of the PIR fiber.....	104
Table 3.1	Relevant settings and the diluted concentration.....	114
Table 4.1	Selected CH ₄ and N ₂ O absorption lines.....	128
Table 4.2	Used time constants at a given scanning speed of the LO frequency ν_{sc}	130
Table 4.3	Analysis of BB-based heterodyne spectra of CH ₄ absorption at the scanning speed of the LO frequency (ν_{sc}) of 0.03148 cm ⁻¹ /s (the scanning time (ΔT_{scan}) of 1709 ms) with different time constants (τ).....	131
Table 4.4	Analysis of BB-based heterodyne spectra of CH ₄ absorption at the scanning speed of the LO frequency (ν_{sc}) of 0.0787 cm ⁻¹ /s (the scanning time (ΔT_{scan}) of 684 ms) with different time constants (τ).....	132
Table 4.5	Analysis of BB-based heterodyne spectra of CH ₄ absorption at the scanning speed of the LO frequency (ν_{sc}) of 0.1574 cm ⁻¹ /s (the scanning time (ΔT_{scan}) of 342 ms) with different time constants (τ).....	133
Table 4.6	Analysis of BB-based heterodyne spectra of CH ₄ absorption at the scanning speed of the LO frequency (ν_{sc}) of 0.3935 cm ⁻¹ /s (the scanning time (ΔT_{scan}) of 137 ms) with different time constants (τ).....	134
Table 4.7	Analysis of BB-based heterodyne spectra of CH ₄ absorption with optimal τ at given ν_{sc} and ΔT_{scan}	135

Table 5.1	Parameter setting on the Signal Analyzer.....	148
Table 5.2	Comparisons between theoretical Voigt line widths and measured Voigt line widths of LHR spectrum and direct spectrum.....	160
Table 5.3	Noise density with different RF filter pass-bands.....	161
Table 5.4	Analysis of BB-based heterodyne spectra (Fig. 5.13) of CH ₄ absorption with the used time constants (τ) of 1 ms at different scanning speeds of the LO frequency (ν_{sc}).....	163
Table 5.5	Comparisons between LHR and FTS.....	168

List of Acronyms

A

AC	Alternating Current
AD	Amplitude Detector
ADC	Analog Digital Converter
AIOFM	Anhui Institute of Optics and Fine Mechanics
AK	Averaging Kernel
AMF	Air Mass Factor

B

BB	Black Body
BD	Balanced Detector
BG	Back Ground
BP	Band-Pass
BS	Beam Splitter
BUV	Backscatter Ultra Violet

C

CARIBIC	Civil Aircraft for the Regular Investigation of the atmosphere Based on an Instrument Container
CW	Continuous Wave

D

DC	Direct Current
DOAS	Differential Optical Absorption Spectrometer
DFB	Distributed Feedback
DSP	Digital Signal Processing

E

EC-QCL	External-Cavity Quantum Cascade Laser
ECMWF	European Center for Medium Range Weather Forecasts
ESA	European Space Agency

ERS European Remote Sensing
ENVISAT ENVIronmental SATellite

F

FP Fabry-Perot
FASCODE Fast Atmospheric Signature CODE
FC Fiber Coupler
FoV Field of View
FRS Fraunhofer Reference Spectrum
FSR Free Spectral Range
FT-IR Fourier Transform InfraRed
FTS Fourier Transform Spectrometer
FWHM Full Width at Half Maximum

G

GAS Global Analyzer Solutions
GC Gas Chromatograph
GEO Geostationary Equatorial Orbit
GHG Greenhouse Gases
GHSV Gas Hour Space Velocity
GOME Global Ozone Monitoring Experiment
GOSAT Greenhouse Gases Observing Satellite

H

HALOE HALogen Occultation Experiment
HIPPO HIaper Pole-to-Pole Observations
HWHM Half Width at Half Maximum

I

IC Integrated Circuits
ICL Interband Cascade Laser
ILS Instrument Line Shape
IR InfRared

IRENE Innovation Recherche en Environnement
IF Intermediate Frequency

L

LBLRTM Line-By-Line Radiative Transfer Model
LBSD Low Barrier Schottky Diode
LEO Low Earth Orbits
LERMA Laboratoire d'Études du Rayonnement et de la Matière en
Astrophysique et Atmosphères
LM Levenberg Marquardt
LoD Limit of Detection
LPCA Laboratoire de Physico Chimie de l'Atmosphère
LHR Laser Heterodyne Radiometer
LO Local Oscillator
LOS Line Of Sight
LP Low-Pass
LIA Lock-In Amplifier

M

MANTRA Middle Atmosphere Nitrogen Trend Assessment
MAX-DOAS Multi-Axis Differential Optical Absorption Spectrometer
MCT Mercury Cadmium Telluride
MFC Mass Flow Controllers
MHF Mode Hope Free
Mid-IR Mid-InfRared
MIPAS Michelson Interferometer for Passive Atmospheric Sounding
MIPT Moscow Institute of Physics and Technology
MODTRAN MODerate resolution TRANsmittance code

N

NA Numerical Aperture
NI National Instruments
NIST Natinal Institute of Standards and Technology

NDACC Network for the Detection of Atmospheric Composition Change
NEP Noise Equivalent Power

O

OA Optical Attenuator
OAPM Off Axis Parabolic Mirror
OAEM Off Axis Elliptical Mirror
OCO Orbiting Carbon Observatory
OEM Optimal Estimation Method

P

PBL Planet Boundary Layer
PC Personal Computer
PIR Polycrystalline InfRared
PZT PieZoelectric Transducer
PID Proportional, Integral and Derivative
PoC Proof of Concept
PPBV Parts Per Billion by Volume
PPMV Parts Per Million by Volume
PSD Phase Sensitive Detection

Q

QCL Quantum Cascade Laser

R

RAL Rutherford Appleton Laboratory
RBW Resolution BandWidth
RC Reference Cell
RF Radio Frequency
RTE Radiative Transfer Equation
RTM Radiative Transfer Model

S

SAOZ	Système d'Analyse par Observation Zénithale
SCD	Slant Column Density
SCIAMACHY	Scanning Imaging Absorption Spectrometer for Atmospheric CHartographY
SMOF	Single Mode Optical Fiber
SNR	Signal to Noise Ratio
6S	Second Simulation of the Satellite Signal in the Solar Spectrum
SWR	Standing Wave Ratio
SZA	Solar Zenith Angle

T

TANSO	Thermal And Near-infrared Sensor for carbon Observation
TCCON	Total Carbon Column Observing Network
TDLAS	Tunable Diode Laser Absorption Spectroscopy
TELIS	TErahertz and submillimeter LImb Sounder

U

UAV	Unmanned Aerial Vehicle
UARS	Upper Atmospheric Research Satellite
UCEIV	Unit éde Chimie Environnementale et Interactions sur le vivant
UPMC	Universit éPierre et Marie Curie
UV NIR	Ultra Violet Near Infrared

V

VCD	Vertical Column Density
-----	-------------------------

W

WACCM	Whole Atmosphere Community Climate Model
-------	--

Abstract

The measurement of vertical concentration profiles of atmospheric trace gases provides a better insight into air pollution, ozone destruction and climate change as well as a way to validate chemical models and satellite observations. To that end, laser heterodyne radiometer (LHR) offers significant benefits in terms of high spectral resolution, high sensitivity and high vertical resolution in conjunction with a compact instrumental size deployable for field applications.

The aim of this thesis is to develop a fully transportable mid-infrared (mid-IR) LHR instrument for ground-based remote sensing of key trace gases in the atmospheric column.

In order to test our design and characterize its performance, a proof of concept (PoC) mid-IR LHR receiver was first developed. Its field test was carried out on the QualAir platform of the Université Pierre et Marie Curie (UPMC) with the help of a heliostat of the TCCON-Paris station (TCCON : Total Carbon Column Observing Network). LHR absorption spectrum of CH₄ in the atmospheric column was extracted from the solar radiation using the developed ground-based LHR receiver and it is in good agreement with the spectrum measured by the TCCON-Paris station.

After this field test validation, a fully transportable mid-IR LHR instrument was developed and deployed on the roof of the IRENE platform of the Université du Littoral Côte d'Opale (ULCO) in Dunkerque. LHR spectrum of CH₄ and N₂O in the atmospheric column was measured and in good agreement with the TCCON FT-IR spectrum of CH₄ and N₂O, as well as in good agreement with the atmospheric transmission modelling.

The fully transportable mid-IR LHR instrument developed in this PhD work has high potential for use in measurement of vertical concentration profiles of key atmospheric species on spacecraft, on airborne or on ground-based platform.

Keywords : Laser heterodyne radiometer (LHR); Ground-based remote sensing; External-cavity quantum cascade laser (EC-QCL); Mid-infrared (mid-IR); Polycrystalline IR fiber.

Introduction

Objective

This thesis presents studies and development of laser heterodyne radiometer (LHR) for ground-based remote sensing of vertical concentration profiles of atmospheric trace gases. This introductory chapter describes the motivation behind developing LHR as well as other passive remote sensing techniques for the measurements of vertical concentration profile. This chapter will provide a brief history review of LHR techniques and outline the currently state-of-the-art LHRs. At the end of this chapter, the composition of this dissertation is introduced.

I. Remote sensing of vertical concentration profiles of atmospheric trace gases

Vertical concentration profiles of atmospheric trace gases, such as nitrous oxide (N_2O), methane (CH_4), water vapor (H_2O), ozone (O_3), carbon dioxide (CO_2), and dichlorodifluoromethane (CCl_2F_2) [1], are of significant interest, because of their crucial roles in air pollution, ozone depletion, and climate change [2].

As is well known, vertical concentration variation of any trace gas strongly depends on vertical air transport. As a point of reference, the vertical air transport (Fig. 1 *left*) in the troposphere is faster than the horizontal transport (Fig. 1 *right*). Comparing with horizontal variations of trace gas concentrations, their vertical concentration variations are thus larger. The vertical air transport from the surface to the tropopause (~ 10 km) takes about one month on average. Trace gases with lifetimes longer than one month tend to mix well vertically in the troposphere, while trace gases with shorter lifetimes show great vertical concentration variation. Under planet boundary layer (PBL), it takes even 1-2 days for air transport from the PBL down to the surface. Due to the temperature inversion in the stratosphere, the air exchange between the troposphere and the stratosphere is much slower than the mixing of the troposphere. It takes 5-10 years for air transport from the troposphere to the stratosphere, and 1-2 years from the stratosphere down to the troposphere (Fig. 1 *left*) [3]. Therefore, trace gases with atmospheric lifetimes (t) longer than 10 years show little vertical variation within the troposphere [5].

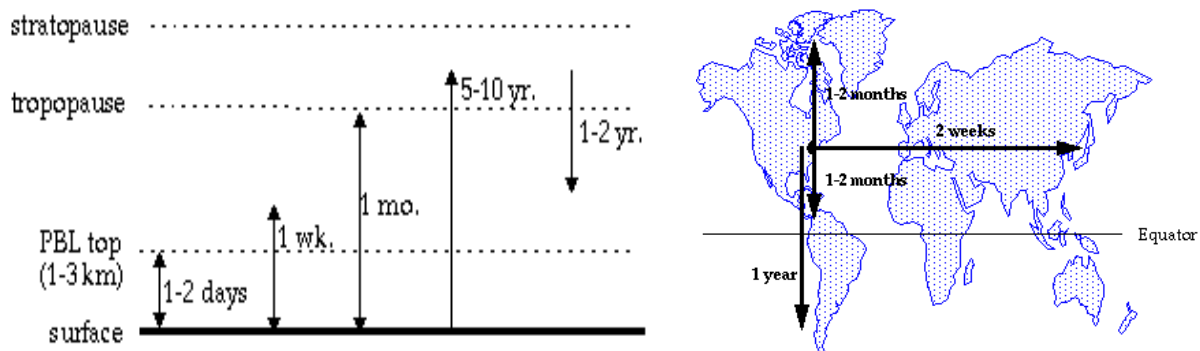


Figure 1 *left*: characteristic time scales for vertical transport; *right*: typical time scales for global horizontal transport in the troposphere [4].

Both nitrous oxide ($t \sim 120$ years) and methane ($t \sim 10$ years) have uniform vertical distributions throughout the troposphere due to their long atmospheric lifetimes and are regulated under the Kyoto Protocol because of their contributions to global warming [5-7]. Compared to other tropospheric greenhouse gases (GHGs), although nitrous oxide has a smaller concentration (~ 320 ppbv for parts per billion by volume), it is an influential global warming molecule due to its particularly long lifetime [5]. Meanwhile nitrous oxide is rather inert in the troposphere, the reduction in its concentration occurs in the stratosphere due to photodissociation [8]. In addition, nitrous oxide is the dominant source of nitrogen oxides active in stratospheric ozone depletion [9].

Similar to nitrous oxide, methane is also well-mixed throughout the troposphere (~ 1.8 ppmv for parts per million by volume) [10]. A combination of slower transport from the troposphere to the stratosphere and reactions with OH generates lower methane concentrations at stratospheric altitudes [11,12].

Water vapor in the troposphere is the most important greenhouse gas [13] and plays a crucial role in climate change as a dominant feedback variable in association with radiative effects and moist dynamics. In the lower troposphere, water vapor acts as the main resource for precipitation in all weather systems, providing latent heating in the process and dominating the structure of diabatic heating in the troposphere [5,14].

Ozone plays an important role in the chemical reaction occurring in the atmosphere, as well as on the climate change [15,16,18]. On average, about 90% of the total ozone vertical column is present in the stratosphere and only 10% exists in the troposphere. However, important variations in the vertical distribution of ozone can be the result of photochemical and dynamic processes. The tropospheric ozone concentration is particularly highly variable in space and time [19]. In the boundary layer, photochemically produced ozone is a polluting

oxidant with major implications for human health starting at mixing ratios below 0.2 ppmv [17].

Dichlorodifluoromethane (CCl_2F_2 , commonly known as Freon-12), which originates from ground-level anthropogenic sources and is photodissociated in the stratosphere, can deplete the protective stratospheric ozone layer via a catalytic photochemical cycle reducing ozone to oxygen [20] and has therefore been banned under the Montreal Protocol [21]. The highest Freon-12 concentration (~ 500 pptv for parts per trillion by volume) is found in the troposphere where it is evenly distributed due to its long lifetime (~ 100 years) [21-23]. In addition, the long lifetime of Freon-12 [24] makes it an ideal tracer for dynamic processes, such as subsidence [25], horizontal transport, and mixing [26].

The accelerating rise of global levels of carbon dioxide in the atmosphere, most likely due to human activity and anthropogenic emissions, is believed to be the main driver of (anthropogenic) climate change [27,28]. Carbon dioxide production and reduction primarily occur on the ground and these variations are quite low in the atmosphere [29], where the variation of CO_2 is likely to be the result of dispersion and transportation controlled by meteorological factors [30]. In the free troposphere, CO_2 has been used as a tracer gas to study the vertical transportation of air pollutants [31,32].

It is, therefore, important to measure the vertical concentration profiles of the key atmospheric trace gases, which helps us to understand pollutant transport, climate change [20,22-26,33-36], globally environmental parameters [37], and anthropogenic effects on atmospheric chemistry [2]. Moreover, vertical concentration profiles provide a powerful means for validating various atmospheric chemical and transport models and satellite observations. Meanwhile, such profiles can also give a scientific and comprehensive basis for environment assessment and the formulation of related policies. For these and other reasons the study of atmospheric trace gas concentrations and their vertical profiles has been of long-standing interest to atmospheric scientists, and over the years these studies have generated plenty of data on vertical concentration profiles of atmospheric trace gases.

Atmospheric trace gas concentrations can be generally measured by local point measurement and vertical profile remote sensing, respectively. In local point measurement of trace gas concentrations, instrumentation is located directly at the point of interest and in contact with the trace gas of interest. While vertical profile remote sensing can provide us not only the concentration but also its vertical distribution.

II. Techniques of passive remote sensing of vertical concentration profile

Global measurements performed from satellite platforms and localized measurements from balloon/aircraft and ground-based platforms can be used for passive remote sensing of vertical concentration profiles of atmospheric trace gases [10,38,39]. These techniques based on three different platforms are complementary to each other to form a complete observation system for atmospheric vertical profile sensing.

(1) Global measurements on satellite platforms

The satellite measurement platforms work in different modes including backscatter ultraviolet (BUV), occultation, limb emission, and limb scattering modes. Each mode involves a different viewing geometry that affects measurements of the atmospheric radiation and vertical resolution.

(1-1) In **BUV** mode (Fig. 2), satellite-platform instruments directly measure the upwelling solar UV light that is either reflected from the Earth's surface or scattered back from the atmosphere based on Nadir viewing geometry [40]. Nadir viewing describes a vertical direction viewing on the Earth's surface directly below the satellite [42].

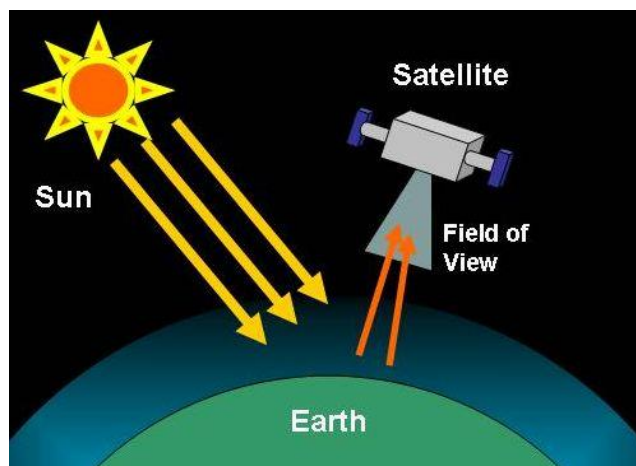


Figure 2 Schematic diagram of the nadir viewing geometry in BUV mode.

BUV mode is widely used for measuring ozone vertical profile. Ozone has a strong absorption at short UV wavelength, which results in UV light at long wavelength being able to penetrate far into the atmosphere. The radiation at short UV wavelengths is significantly absorbed at higher altitudes, so the backscattered radiation at specific UV wavelengths can only be scattered from above a particular height. Below this level, all the radiation is absorbed and there is no backscattered radiation. This allows satellite-platform instruments in

BUV mode to obtain ozone vertical profile by measuring radiation at a series of wavelengths. In addition, this mode can be used to infer information on the concentration of other trace species which absorb in the same wavelength region. Disadvantages of this mode are that it cannot be used at night including the polar night and its vertical resolution is poor (~5-10 km).

GOME (Global Ozone Monitoring Experiment) instrument, launched on-board ERS-2 (European Remote-Sensing Satellite) in April 1995, relies on nadir viewing BUV mode for globally monitoring of atmospheric ozone [41] using a nadir-scanning UV and visible spectrometer to cover the UV- NIR (near-infrared) (240-790 nm) region. Since summer 1996, ESA (European Space Agency) has been delivering to users three-day GOME global observations of total ozone, nitrogen dioxide, water vapor, sulfur dioxide, chlorine and bromine monoxide, and other trace constituents as well as the related cloud information [42].

(1-2) In occultation mode, one measures absorption amount of solar, lunar, and even stellar radiation directly through the limb of the atmosphere at different wavelengths (e.g. UV, visible, infrared (IR)) as the Sun, the Moon, and the stars rise and set (depending on which celestial radiator is being used by the satellite instrument). In solar occultation mode (Fig. 3) transmission of sunlight through the Earth's atmosphere is measured and ratioed to exoatmospheric measurements (solar measurements recorded with no atmospheric attenuation). This is carried out at a series of tangent altitudes (the altitude to which the instrument can see), increasing in altitude during a sunrise or decreasing in altitude during a sunset. From each of the atmospheric measurements a slant column is calculated which can contain contributions from multiple atmospheric layers. The slant columns contain sufficient information on vertical profiles of atmospheric constituents, such as O₃, NO₂, and NO₃. The vertical resolution of measurements in this mode is typically about 1 to 2 km. However, the measurements in solar occultation mode are only possible during orbital sunrises/sunsets. This means that the instruments in this mode provide only limited spatial coverage per orbit.

HALOE (HALogen Occultation Experiment) instrument, on-board the UARS (Upper Atmospheric Research Satellite), launched in 1991, is an instrument operational in occultation mode. It measures solar occultation in the IR region at pre-selected specific wavelengths to measure atmospheric constituents such as ozone, water vapor, methane, hydrochloric acid, and reactive nitrogen species.

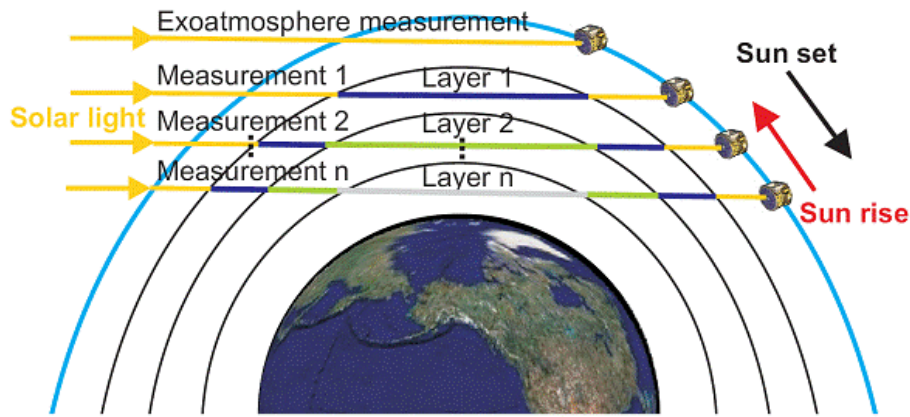


Figure 3 Solar occultation viewing geometry. Note : the distances are not scaled. Solar radiation passes through space and arrives at the upper boundary of the Earth atmosphere. These solar radiations are attenuated by the atmospheric constituents. The blue, green and gray lines indicate the atmospheric absorption lengths at layer 1, 2 and layer n, respectively. These attenuated solar radiations are recorded by the instruments on the satellite in a set of tangent altitudes during an occultation [43].

(1-3) Limb scattering mode (Fig. 4) is a part of limb-sounding mode, whose viewing geometry is similar to that of both limb emission (see (1-4)) and occultation modes. In limb scattering mode, the UV-visible-NIR radiance from the Sun is scattered by the atmosphere into the FoV of the instrument along the line of sight (LOS) [44]. In each scan of the atmosphere, instrument in this mode observes the atmosphere above the Earth's horizon and records spectra at different tangent altitudes to which the instrument can see. The objective of this type of measurements is to determine vertical profiles of trace gases, aerosols and atmospheric parameters (such as temperature and pressure). Satellite measurement in limb scattering mode combines high intrinsic vertical resolution (similar to that of measurements in occultation mode) and rapid global coverage (comparable in BUW mode). But the viewing geometry in limb scattering mode is more complex and the horizontal resolution is poor comparing with other modes.

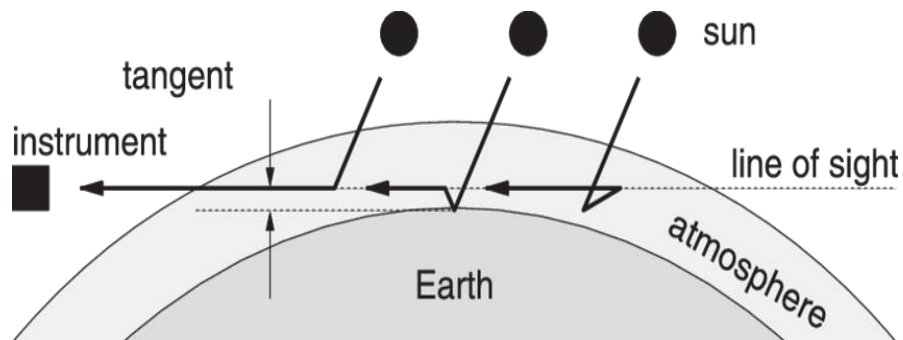


Figure 4 Limb scattering viewing geometry with single scattering, surface reflection, and second order of scattering, respectively (the atmosphere's curvature is exaggerated) [45].

SCIAMACHY (Scanning Imaging Absorption Spectrometer for Atmospheric CHartographY) instrument on-board ENVISAT (ENVIronmental SATellite) [45] is an imaging spectrometer operated in limb scattering mode. The solar radiation transmitted in, back scattered by and reflected from the Earth's atmosphere or surface is recorded with SCIAMACHY at relatively high spectral resolution (0.2-0.5 nm) in the spectral region of 240-1700 nm and 2000-2400 nm [47,48]. The high spectral resolution and the wide wavelength range of SCIAMACHY make it possible to detect different trace gases as well as detecting clouds and aerosols.

(1-4) Limb emission mode (Fig. 5), another limb-sounding mode, is used to retrieve vertical profiles of atmospheric trace gases with an improved vertical resolution and increased sensitivity for higher altitude and minor species [49]. Instruments in limb emission mode measure long-wave (IR or microwave) radiation thermally emitted in the atmosphere along the LOS of the instrument. Vertical profiles of the incoming limb radiances can be measured by changing the elevation angle of the LOS of the instrument such that vertical scans through the atmosphere are performed [50].

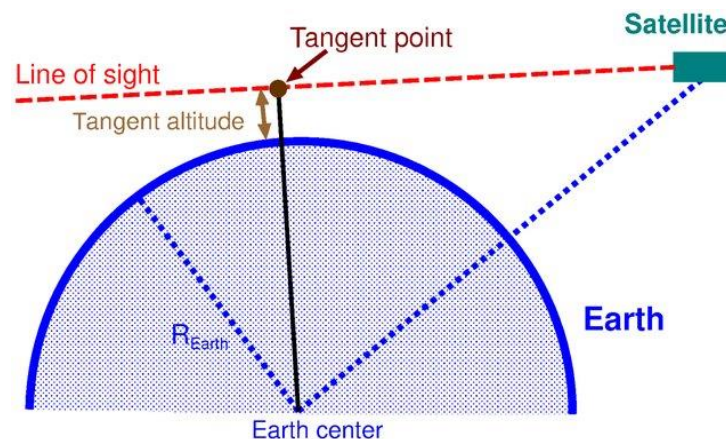


Figure 5 Limb emission viewing geometry. The satellite instrument views toward the Earth's horizon. The point of the instruments' LOS closest to the Earth's surface is called tangent point [50].

The measurements in limb emission mode do not require background radiation source, and the Earth's atmosphere itself is the radiation emitter. Meanwhile, such measurements are independent on the satellite position relative to the radiation source and can provide daytime and nighttime measurements over the full globe (depending on inclination angle). Due to lower temperatures of the atmosphere compared to stars, the Planck function's peak is far lower, and the peak position is shifted to longer wavelengths with lower SNR (signal-to-noise

ratio). The accuracy in this mode is slightly less than BUV mode, and the horizontal path is quite long compared to the tangent altitude.

MIPAS (Michelson Interferometer for Passive Atmospheric Sounding) instrument on-board ENVISAT [45] based on a Fourier transform spectrometer (FTS) is designed for measurement in limb emission mode to detect the middle and upper atmosphere in a wide spectral interval throughout the mid-IR region (4.15-14.6 μm) [51,52]. The detected features can be spectroscopically identified and used as inputs to suitable algorithms for extracting atmospheric vertical profiles of a number of target species.

Since passive remote sensing techniques using satellite platforms can cover the entire Earth or any designated area for a long time, and they can be used to facilitate the remote observation of vertical concentration profiles of the tropospheric trace gases, which would allow us to better understand the source, trends and global distribution of atmospheric species [53]. However, satellite-platform instruments involve complex instrumental characteristics and physical processes [54], and the measured data must be validated to determine its reliability and uncertainty before it can be used to solve practical scientific problems [55-57]. Meanwhile, satellite-platform instruments have a high overhead cost and typically lose sensitivity at lower altitudes [58].

(2) Passive remote sensing based on ground-based platforms

Ground-based platforms incorporate some of the same viewing geometry concepts mentioned in the satellite platforms. Spectrometer on ground-based platforms is an instrument that infers vertical column density of trace gas by measuring the amount of sunlight reaching the Earth's surface, and from this deducing how much trace gas absorption takes place. Three types of spectrometers including MAX-DOAS (Multi-Axis Differential Optical Absorption Spectrometer), SAOZ (Système d'Analyse par Observation Zénithale), and FTS (Fourier Transform Spectrometer) are discussed below.

(2-1) Ground-based passive MAX-DOAS

MAX-DOAS (Multiple Axis, i.e. elevation scanning with DOAS spectral analysis) is a widely used technique for remote sensing of vertical profiles of tropospheric trace gases [59]. It observes scattered sunlight at various slant elevation angles, where solar radiation travels longer absorption paths [60]. Fig. 6 shows the principle of MAX-DOAS measurement. Most often, the scattering event occurs in the lower troposphere due to higher air density and higher particle loadings. For most MAX-DOAS observations, they can be assumed that the

stratospheric absorption is the same in all spectra taken during one elevation sequence measurement.

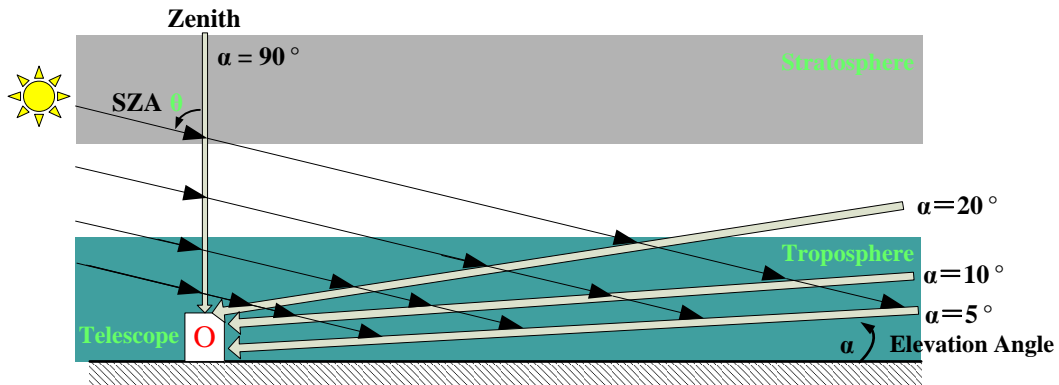


Figure 6 Principle of MAX-DOAS : Scattered sunlight is measured at different elevation angles α of the telescope to obtain vertical profiles of the target trace gases, where solar zenith angle (SZA) θ denotes the angle between the position of the Sun and the zenith direction.

The MAX-DOAS technique analyses the recorded spectra using a DOAS method that separates the spectra as fast and slow varying spectral structures using a Levenberg-Marquardt (LM) fit. In the spectral fit, the rapidly varying part corresponds to the trace gas absorption features, and the slowly varying part is caused by Rayleigh and Mie scatterings. Usually the output of the MAX-DOAS spectral analysis is a slant column density (SCD), i.e. the integrated trace gas concentration along the light path through the atmosphere. To derive the trace gas vertical column density (VCD), a so called air mass factor (AMF) is applied, which is defined as [61] :

$$AMF = \frac{SCD}{VCD} \quad (1)$$

The AMF is usually derived from numerical simulations of the atmospheric radiative transfer. For MAX-DOAS observations, one basic prerequisite is the assumption that the same air parcels are probed by the different viewing directions for accurate analysis of tropospheric species. The MAX-DOAS data analysis can lead to large errors due to rapid change of air masses, in extreme cases even ‘negative concentrations’ might be retrieved, which is a major problem in the MAX-DOAS technique.

In the MAX-DOAS spectral analysis process, several trace gas absorption cross sections (rapidly varying part), a polynomial of 2-5 orders (slowly varying part), a Fraunhofer reference spectrum (FRS) and a Ring spectrum are involved. Here FRS is introduced to correct for the solar Fraunhofer structure that is due to absorption in solar atmosphere (c.f. Appendix 4). In most cases, spectra recorded at zenith direction of 90° have been used as

background FRS. The Ring spectrum is used to correct the Ring effect named by J. F. Grainger and J. Ring (1962) [62]. The Ring effect is mainly caused by rotational Raman scattering and manifests itself by reducing the optical density of the observed Fraunhofer lines observed at large SZA. This reduction is on the order of a few percents. The Ring spectrum can be modeled, as the main constituents of the atmosphere are nitrogen and oxygen with known rotational states [63].

The MAX-DOAS technique has been widely used for measuring atmospheric vertical profiles of halogen oxide (BrO, IO, OIO, ClO), O₃, NO₃, NO₂, SO₂, HCHO and atmospheric aerosols in the past decades. MAX-DOAS observations are not only limited to ground-based applications, but also can be performed on different mobile platforms like cars, ships and airplane. For car measurements, the view at low elevation angles (i.e. at a few degrees) is often blocked by obstacles like buildings or trees. For airborne and ship observations, viewing angles close to the horizon might be used. For ship MAX-DOAS observations, vertical profile retrievals should be in general possible, but for airborne MAX-DOAS observations, vertical profile retrievals might be possible outside from polluted regions or at higher altitudes [64].

(2-2) Ground-based SAOZ

SAOZ spectrometer is a passive remote sensing instrument that was developed in the mid-1980s [65] to measure total vertical column amounts of O₃ and NO₂ at latitudes up to the polar circle [66]. The SAOZ instrument is part of the international Network for the Detection of Atmospheric Composition Change (NDACC). It consists of a conical mirror used for sunlight collection, a commercial JobinYvon flat field spectrometer equipped with a concave holographic grating, and a detector operated at ambient temperature comprising a Hamamatsu 512 or 1024 diode array with a 25 or 50 mm entrance slit, respectively. The optical scheme of the SAOZ instrument is shown in Fig.7. The spectral range is 300-600 nm with a spectral resolution of ~1 nm [67]. The SAOZ observes the zenith sky with a FoV of ~30°, measuring light scattered downwards from a range of altitudes. At twilight (SZA ~90°) the zenith sky is illuminated mainly by molecular scattering from high altitudes, which travels a longer path through the stratosphere compared to a very short vertical path in the troposphere. Therefore, absorption features in the spectra measured at this position are heavily biased towards the stratosphere. This makes zenith-sky spectroscopy ideal for distinguishing stratospheric NO₂ from boundary-layer pollution. SAOZ technique uses the DOAS method to analyse the recorded spectra in order to retrieve vertical concentration profiles.

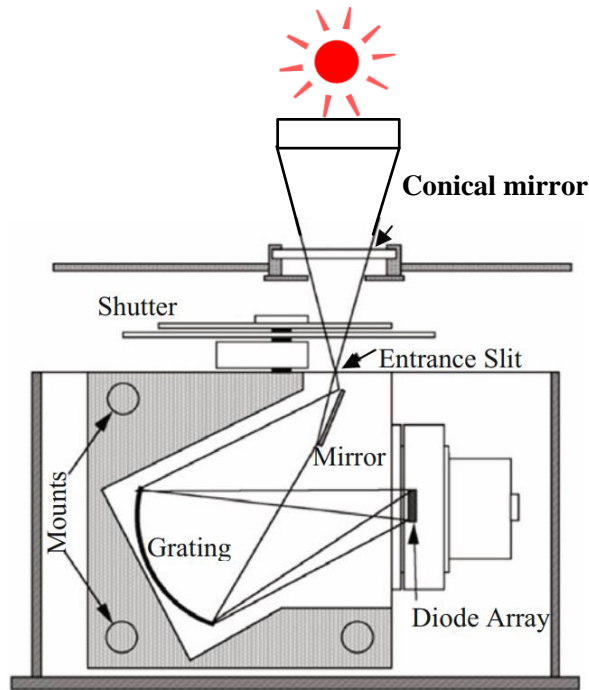


Figure 7 Optical scheme of SAOZ instrument [67].

The SAOZ can be also used for on-board balloon and satellite measurements. However, the SAOZ can only retrieve vertical columns of trace gases in the stratosphere, and is insensitive to the concentration variations of trace gases in the troposphere [68].

Ground-based MAX-DOAS and SAOZ discussed above both only work in the UV-visible range, for IR applications, other ground-based techniques will be presented below.

(2-3) Ground-based FTS

A sun-tracker collects and couples the solar radiation after transmission through the atmosphere to a Michelson interferometer-based FTS (Fig. 8). An interferogram containing sunlight absorption information by atmospheric trace gases is recorded. Infrared absorption spectra of trace gases in the atmospheric column can be retrieved from Fourier transform of the interferogram [69] and then the vertical concentration profiles of these atmospheric constituents can be retrieved from the atmospheric trace gas column absorption spectra with appropriate retrieval algorithms [70-75].

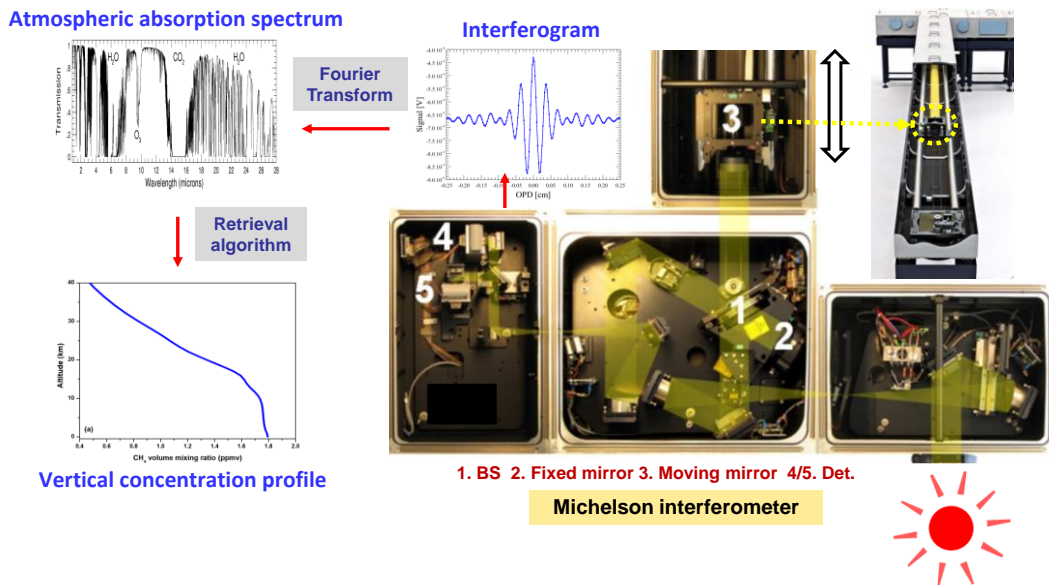


Figure 8 Schematic of a FTS for retrieving vertical concentration profiles of atmospheric trace gases (BS: beam splitter).

Currently, there are two well-known international networks established for measuring vertical concentration profiles of atmospheric trace gases using ground-based solar FT-IR instruments : the Total Carbon Column Observing Network (TCCON) [76-78] established in 2004 [79] and the Network for the Detection of Atmospheric Composition Change (NDACC) established in 1991 [80]. TCCON uses the FTS to record near-IR broadband solar absorption spectra to determine column-averaged abundances of trace gases, such as CO₂, CH₄, N₂O, HF, CO, H₂O, and HDO, with a spectral resolution up to 0.02 cm⁻¹ [79]. Today there are around 26 operational TCCON sites (Fig. 9 upper). Their data can be used for validating data obtained from GOSAT (Greenhouse gases observing satellite) [82], OCO-2 (Orbiting Carbon Observatory-2) [83], etc. The NDACC data is obtained from solar FTS spectra recorded in the mid-IR spectral range for the measurements of various constituents throughout the troposphere and stratosphere up to the lower mesosphere. The NDACC currently consists of 23 sites (Fig. 9 lower) with measurements dating back up to 2 decades. The NDACC data can also be used to validate atmospheric measurements from satellites, such as SCIMACHY aboard ENVISAT and TANSO (Thermal And Near-infrared Sensor for carbon Observation) on GOSAT [84,85].

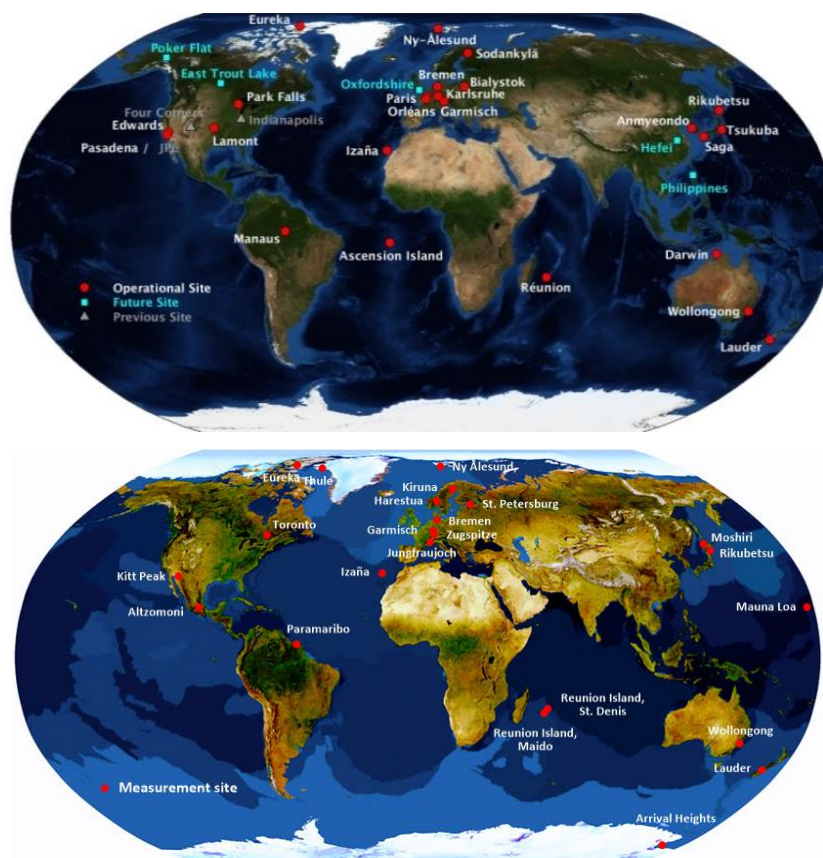


Figure 9 upper: map of the TCCON sites [76]; lower: map of the NDACC sites [81].

Compared to the ground-based MAX-DOAS and SAOZ measurements, the passive ground-based FTS simultaneously measures atmospheric components using their IR absorption spectra, while the measurements of ro-vibrational spectra in the IR request higher spectral resolution. FTS instruments typically sacrifice spectral resolution for more compact instrument size or for faster data collection time. Therefore, the amount of altitudinal information that can be retrieved from emission/absorption data collected with a FTS is limited.

(3) Passive remote sensing technique based on aircraft and balloon platforms

Aircraft and balloon platforms refer to measurement instruments (such as MAX-DOAS, SAOZ and FTS) installed on aircraft [86] and balloon [87] for high-altitude remote sensing.

The CARIBIC (Civil Aircraft for the Regular Investigation of the atmosphere Based on an Instrument Container) aircraft project is an approach to obtain detailed long-term observations over large sections of the globe [88], which uses the MAX-DOAS to measure vertical profiles. NO₂ vertical profiles have been retrieved in nadir slant viewing direction with a 100-200 m height resolution, and in both up and down viewing directions ($\pm 10^\circ$) with a 400-800 m height resolution [88]. HIPPO (HIAPER Pole-to-Pole Observations), another

airplane campaign, includes a suite of sensitive sensors to measure vertical profiles of CH₄ and N₂O on a flight path from the north pole to the south pole over the Pacific Ocean [10]. Balloon-based remote sensing instruments, such as balloon-based TELIS (TERahertz and submillimeter LIMb Sounder) and balloon-based DOAS, can investigate stratospheric trace gas distributions with a vertical resolution of ~2-3 km below the balloon height [89].

Aircraft-based measurements can probe large latitudinal/longitudinal transects in a short time without cloud interference. Vertical profile measurements by aircraft/balloon-based instruments are less affected by transport model errors, making them particularly useful in constraining surface fluxes. Aircraft/balloon-based techniques are valuable links between ground-based and satellite-based measurements [90]. However, lower few hundred meters of the atmosphere, which contains a significant part of tropospheric species, are difficult to reach. Moreover, they could not provide continuous measurements due to limited flight missions.

In order to achieve flight-based measurement data at lower few hundred meters of the atmosphere, unconventional flight platforms can become very useful, like an unmanned aerial vehicle (UAV). UAVs are increasingly used in civilian applications, and a large variety of UAV platforms are now available as remote sensing platforms for scientific research [91]. UAV platforms offer great potential for collecting measurement data with high spatial and temporal resolutions.

Table 1 shows the comparisons among above three kinds of platforms. In this context, ground-based measurement is high desirable.

Table 1 Comparisons among satellite, ground, and airplane/balloon platforms.

Platform	Advantage	Disadvantage
Satellite	<ol style="list-style-type: none"> 1. Covering the entire earth or any designated area for a long time 2. Retrievals of tropospheric vertical profiles 	<ol style="list-style-type: none"> 1. Complex instrumental characteristics and physical processes 2. Data must be validated 3. High overhead cost 4. Low sensitivity at lower altitudes
Ground	<ol style="list-style-type: none"> 1. Accurate and continuous measurements near the ground 2. Validation of satellite observations 	
Airplane/ balloon	<ol style="list-style-type: none"> 1. Large latitudinal/longitudinal transects in a short time without cloud interference 2. Less affect from transport model errors 3. Valuable links between ground-based and satellite-based measurements 	<ol style="list-style-type: none"> 1. Lower few hundred meters of the atmosphere is difficult to measure 2. Discontinuous measurement due to limited flight missions

III. Laser heterodyne radiometer

Laser heterodyne radiometer (LHR) is a ground-based passive instrument, like the FT-IR spectrometer, using sunlight as a spectral source for long-range, long-term and continuous remote measurements of trace gases in the atmospheric column. In comparison to the FTS, LHR is advantageous in terms of spectral resolution, sensitivity and transportability. This technique is particularly attractive in the mid-IR region, which corresponds to the emission or absorption spectra of many key atmospheric molecules. LHR technique exhibits the following merits :

- (1) High spectral purity of laser emission line (~ 10 MHz), resulting in a high resolving power : $\nu/\Delta\nu \approx 10^5$ - 10^7 , which makes that LHR's spectral resolution is not limited by the apparatus function, and only determined by the selected electronic filters. Commonly applicable higher spectral resolution ($\sim 10^3$ cm^{-1}) would allow one to achieve high vertical resolution in vertical profile;
- (2) Higher sensitivity (within a factor of 2-3 of the quantum limit), which allows lower detection limit of gas species with high precision;
- (3) Higher vertical resolution due to very small coherent FoV, which makes LHR have ultrafine geographical coverage with less cloud interferences [92];
- (4) Compact instrumental dimension making LHR easy for field deployment.

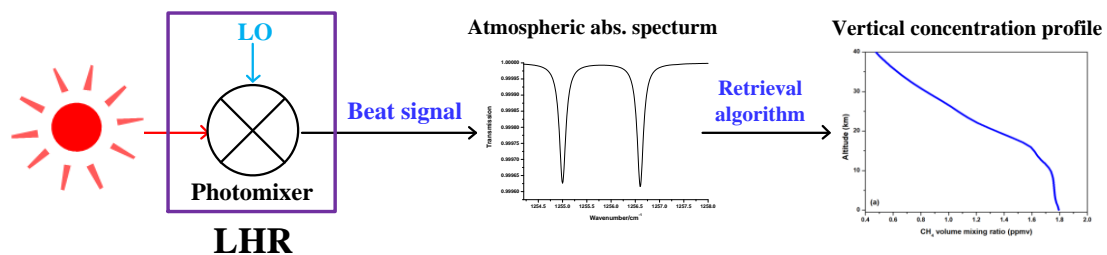


Figure 10 Schematic of a LHR for retrieving vertical concentration profiles of atmospheric trace gases.

LHR (Fig. 10) is a kind of radiometer based on a heterodyne receiver that deals with input sunlight radiation collected from a telescope by mixing it with radiation of a local oscillator (laser) onto a photodetector used as a photomixer [96]. The amplitude of the resulting beat signal from the photomixer varies with the absorption feature of atmospheric trace gases. Scanning the local oscillator (LO) frequency across the absorption feature, atmospheric absorption spectrum can be obtained. The vertical concentration profiles of the target trace

gases can be retrieved based on the measured absorption spectra in the atmospheric column with the help of an appropriate retrieval algorithm.

III.1 History of the LHR technique

Heterodyne history began in 1902 referring to R. Fessenden's patent for "wireless signalling" [93]. The term "heterodyne" was created by J. L. Hogan in 1913 when he published a paper entitled "The heterodyne receiving system and notes on recent Arlington-Salem tests" [94] where it was suggested that only one wave was transmitted from the receiving station and a second frequency was then generated and this produced LO [95]. For more than a century, heterodyning of electromagnetic waves, which produces a low-frequency beat note, has been widely used in radio wave engineering and instrumentation.

Heterodyning expanded in the field of optics even before the advent of lasers. As early as 1940s, A. T. Forrester and co-workers began studying the heterodyning of two waves with very close frequencies and discussed the possibility of observing beat frequency from the heterodyne detection [97,98]. The application of heterodyning in the field of optics took place in 1955, in a classic experiment A. T. Forrester and co-workers observed a beat signal by mixing two Zeeman components of incoherent visible spectral line in a special photomultiplier tube [99]. In the meantime, the idea of the laser was developed and demonstrated by T. H. Maiman in 1960 [100]. As soon as 1961, A. T. Forrester proposed the concept of heterodyne spectrometers in an analogy to radio-receivers, in which coherent light sources, i.e. lasers, acted as optical LOs, which can improve the intensity of the heterodyne signal [101]. Demonstration and studies of heterodyne signals in the visible obtained using two He-Ne lasers at 1.15 μm were subsequently conducted in 1962 by A. Javan and co-workers [102]. Observation of the heterodyning of the axial modes of a ruby laser at 694.3 nm was carried out by B. J. McMurty and A. E. Siegman in 1962 [103].

With the advancement of infrared LO laser technology, the development for application in spectroscopy emerged. The infrared spectral region is attractive due to the availability of trace gas absorption lines and the wavelength dependence of heterodyne sensitivity [104]. In the early arrangement of the heterodyne detection, the LO lasers, in the infrared region, were usually continuous wave (CW) CO₂ lasers or tunable diode lasers (TDLs).

Extension of heterodyne technique to infrared was firstly carried out by M. C. Teich and co-workers [105]. They developed a heterodyne system based on a CO₂ gas laser (LO) working at 10.6 μm by mixing a laser radiation with scattered laser radiation. A minimum

detectable power of 1.3×10^{-19} W in a 1 Hz bandwidth, which is within a factor of 10 of the theoretically perfect photon counter, was obtained. This study demonstrated the high sensitivity of the heterodyne technique for remote sensing of atmospheric trace gases.

The discovery of catalytic destruction of ozone by chlorofluoromethanes (CFCs) and nitrogen (NO_x) in 1970s by H. S. Johnston [108] in general and the report of ozone hole phenomenon over Antarctic region during spring time in 1980s by C. B. Farman in particular [109] generated an unprecedented surge of interest in the monitoring of ozone and other related minor constituents in the atmosphere.

In the field of atmospheric observation, in 1971 R. T. Menzies firstly proposed that LHR could be used for passive remote sensing of the atmospheric trace gases, whose rotation-vibration transitions are nearly coincident to those of CO and CO_2 gas lasers (LOs) [106]. Laboratory demonstration using gas cells simulating the atmosphere was then carried out by his team [104,107]. In 1976, R. T. Menzies et al. made a ground-based LHR measurement of the total burden and the vertical concentration profiles of ozone using a CO_2 laser (LO) in the $9.5 \mu\text{m}$ wavelength region [110-112]. D. Sahoo et al. developed a LHR using a CO laser (LO) in the $9.6 \mu\text{m}$ region which was deployed at Maitri, an Indian Antarctic station, during 1993-1998 Antarctic summer as well as winter to obtain ozone profiles. It was the first application for remote sensing vertical concentration profile of ozone over Antarctic region. Thus the ability of the LHR to monitor ozone vertical profiles in the harsh environment conditions (like Antarctica ozone hole period) [113,114] was successfully demonstrated. In 1993, D. Courtois et al. successfully applied a LHR using a CO_2 laser (LO) around $10 \mu\text{m}$ for measuring atmospheric ozone and CO_2 with a resolution of 5 MHz ($\sim 0.000167 \text{ cm}^{-1}$). The atmospheric ozone and CO_2 concentrations versus altitudes were obtained [115,116].

A limitation of LHR systems using gas laser LOs as mentioned above is their highly restricted tunability. In contrast, TDLs providing much greater frequency coverage [117] than gas lasers were very promising.

In 1971, emerging lead salt semiconductor TDLs were proposed to serve as tunable LOs for LHRs, hence allowing remote measurements of atmospheric species with greater frequency agility [118]. Several early demonstrations were followed using gas cells in the laboratory. In 1977, R. T. Ku and D. L. Spears [119] developed a LHR using a PbSnSe TDL (LO) at $10.6 \mu\text{m}$ and measured blackbody heterodyne absorption spectra of ethylene at high spectral resolution. Eventually, in 1977, M. A. Frerking and D. J. Muehler were the first investigators to succeed in measuring solar absorption spectra of atmospheric ozone around $9.9 \mu\text{m}$ at a resolution of 70 MHz ($\sim 0.0023 \text{ cm}^{-1}$) using a LHR with a PbSnSe TDL (LO)

[120] . At the end of the 1970s and the beginning of 1990s, several LHRs using Pb-salt semiconductor TDL LOs were developed, and atmospheric spectra of ozone and CO₂ around 9.1 μm [121,122], HNO₃, H₂O and CO₂ around 11.2 μm [121], N₂O around 8.4 μm [122] and CH₄ around 8.2 μm were recorded, respectively [123]. Finally at the end of 1990s a LHR using a lead-salt TDL as a LO operating in the 9 μm range for measuring atmospheric spectra of ozone was constructed by B. Parvitte et al. in Reims, France for atmospheric applications [124]. This apparatus was actually an evolution of the CO₂ laser-based LHRs developed by B. Parvitte et al. during the 1980s [125-127].

As discussed above, Pb-salt diode TDLs had long been the only kind of the mid-IR tunable LOs for LHR applications. Although promising results were obtained, some major drawbacks, such as cryogenic cooling, low output optical power, frequency variations, and mode-hop limited wavelength tuning range, have restricted the opportunities for the development and the deployment of LHRs using Pb-salt diode TDLs (LOs).

Since the first experimental demonstration of a quantum cascade laser (QCL) emitting at 4.3 μm in 1994 [128], the laser's performance has greatly improved (wide operation wavelength range, high power level, room temperature operation [129], and narrow spectral line width [130,131]). QCLs seem to have all the properties required for the development and the deployment of LHRs. The first heterodyne experiment with a QCL was carried out with the K öln tuneable heterodyne infrared spectrometer (THIS) [132,133].

These historical elements sketching the development of LHR techniques are by no means exhaustive, and starting from the mid 70's onwards, many works in the development and the deployment of LHRs have been reported. Progress has been continuously made toward the Earth's own atmosphere as well as astronomical atmosphere.

III.2 Local oscillator involved in LHR

(a) Mid-IR LO

Laser LO is the key element in LHR. It's a limiting factor to the performance of the LHR. The 3-5 μm and 8-12 μm atmospheric windows, which correspond to the emission or absorption resulting from strong fundamental ro-vibrational transition of numerous key atmospheric molecules, are very suitable for remote sensing of atmospheric trace gases. Common laser sources being used as LOs in LHRs include color center lasers, CO and CO₂ gas lasers, lead-salt diode lasers, interband-transition diode lasers, and intraband-transition QCLs.

CO₂ gas laser is one of the earliest mid-IR lasers [107] used as LOs for LHRs in the 1970s, with advantages of high laser power and narrower line width. However, CO₂ gas lasers were not continuously tunable in wavelength, which limits the heterodyne measurement at a small fraction (15%) of the CO₂ laser emission wavelength range in 9-12 μm. CO₂ gas lasers were also too bulky and large for field deployment.

Tunable lead-salt diode laser [134,135] was firstly used as a LO (at 10 μm) in a LHR in 2002 to determine vertical stratospheric ozone distribution [136]. In 2003, D. Weidmann and co-workers used a 7.6 μm tunable lead-salt diode laser as a LO for on-line LHR measurement of high-temperature water vapor emission in a combustion process with high spectral resolution, which proves that LHR techniques are also relevant in combustion diagnostics [137]. However, the lead-salt diode laser requires cryogenic cooling to achieve single-mode operation, and the output optical power is relatively low, only about 0.1-0.5 mW. Thermal cycling and aging can easily cause changes in laser frequency. Meanwhile, the mode-hop-free spectral range of the lead-salt diode laser is very limited with a single laser.

The birth of QCL in 1994 [140] was a milestone for the development of modern LHRs [138,139]. QCL can provide good temperature performance and operate at room temperature in CW mode with high single-mode output optical power (tens of mW up to ~W) in the spectral region of 3-15 μm [141]. Distributed feedback (DFB) QCL, external-cavity (EC) QCL, as well as the recently available DFB interband cascade laser (ICL) all reactivate the LHR techniques to confront nowadays atmospheric and environmental challenges.

In the mid-IR, CW DFB QCL can cover more than 1% of the wavenumber around the laser center frequency (corresponding to a tuning range of a few cm⁻¹) with output power up to 100 mW [142]. Recent advances on EC-QCLs have dramatically increased the accessible frequency range. Tuning ranges of ~200 cm⁻¹ have been demonstrated [143], and up to ~400 cm⁻¹ is within reach via the development of broad-gain QCL structures [144]. A LHR with an EC-QCL as a LO has been demonstrated in the laboratory to operate over a range larger than 100 cm⁻¹ [145-147]. This wide frequency tuning range is highly desirable for measurements of atmospheric multi-component. In addition, EC-QCLs can provide high optical output power up to 70 mW through distributed Bragg gratings for single-mode operation [148]. Therefore, EC-QCLs with wide and fast frequency tuning capacity, high optical output power, compactness, long life time and room temperature operation [146,149,150] can be excellent LOs in LHRs.

(b) Near-IR LO

Though in the near-IR range, the overall line-intensities of target molecules are usually lower than those in the mid-IR (and the detectable species are less too). For some key species (such as CH₄, CO₂, H₂O, etc.), the corresponding line-strengths are still strong enough. Meanwhile, in the near-IR owing to the progress in the telecommunications industry [151], high performance DFB lasers and photodetectors, fiber optic components, and fiber collimating optics are very attractive in developing compact and portable miniaturized LHRs for field applications (on ground, on aircraft, on balloon, etc.).

III.3 State of the art

The development of modern LHRs since 2010 is overviewed below :

In 2011, D. Weidmann et al. of Rutherford Appleton Laboratory (RAL, UK) developed an EC-QC-LHR with a spectral tuning range of 118 cm⁻¹ (a spectral region of 1120-1238 cm⁻¹) and a FoV of ~0.087°. High-resolution (60 MHz or 0.002 cm⁻¹) LHR spectra of solar radiation and the corresponding vertical profiles of H₂O, O₃, N₂O, CH₄, and CCl₂F₂ have been measured and retrieved [146,147,151]. As shown in Fig. 11, solar radiation is captured with an external solar tracker and directed into the laboratory, and it is filtered with a narrow-band filter and amplitude modulated with a chopper. It is then directed to a beam splitter and superimposed with the LO beam from an EC-QCL. The combined beams are imaged onto a high-speed (1 GHz) mercury cadmium telluride (MCT) photomixer to produce a heterodyne signal.

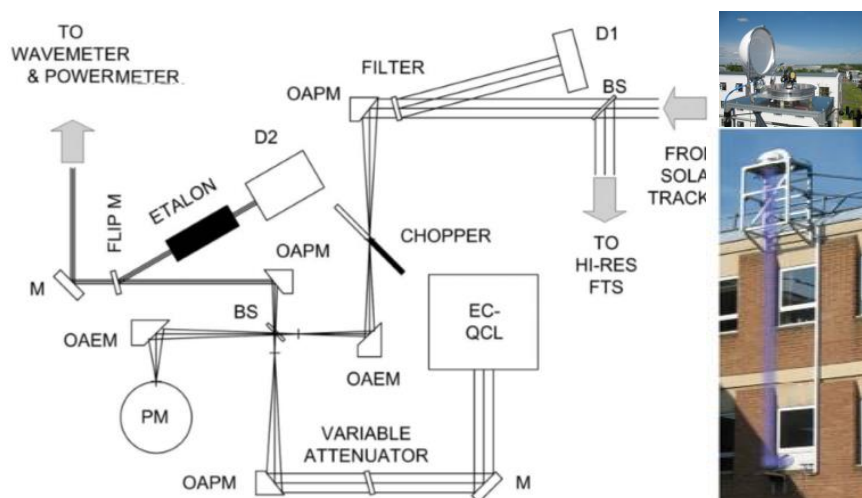


Figure 11 Optical layout of the EC-QC-LHR developed by D. Weidmann et al [151]. M: mirror; BS: beam splitter; D1: solar intensity detector; D2: mid-IR detector; OAEM: off-axis elliptical mirror; OAPM: off-axis parabolic mirror; PM: photomixer.

In 2013, E. L. Wilson et al. (NASA, USA) developed a near-IR LHR using a 1.573 μm DFB laser as a LO, with a spectral resolution of 0.011 nm and a FoV of 0.2° , to measure CO_2 in the atmospheric column with a measurement accuracy of 8 ppm [152] (Fig. 12). The incoming sunlight is modulated with an optical chopper and injected into the LHR receiver through a single-mode optical fiber. The sunlight is then superimposed with the light from the DFB laser (LO) in a 50/50 single-mode fiber coupler. The superimposed lights are photomixed in an InGaAs photodiode with a bandwidth of 5 GHz to generate a heterodyne signal. The use of optical fiber greatly reduces the difficulty of optical coupling alignment in free space and also the LHR system volume.

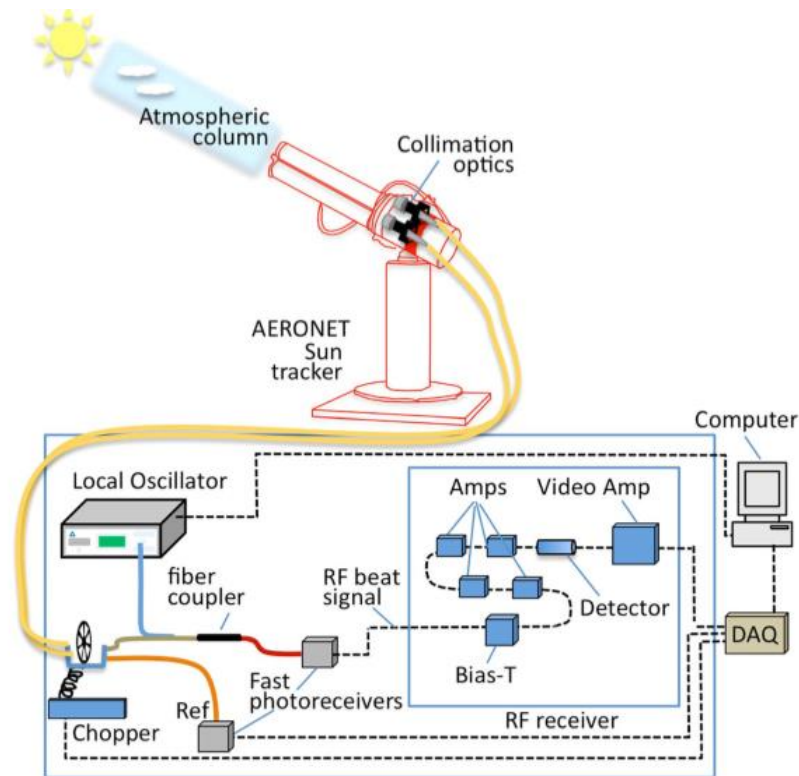


Figure 12 Schematic of the mini-LHR developed by E. L. Wilson et al [152].

In 2014, A. Rodin et al. of Moscow Institute of Physics and Technology (MIPT, Russia) reported a compact and lightweight 1.65 μm DFB laser-based LHR with a FoV of 0.005° [153]. A single-mode silica fiber Y-coupler is served as a diplexer to combine the sunlight and the LO light, the beams mixed in the single-mode fiber are detected by using balanced detection, as shown in Fig. 13. LHR spectra of CO_2 and CH_4 were recorded with a spectral resolution of 2.5 MHz. Inversion algorithm applied to the spectrum of CH_4 resulted in a maximum mixing ratio of 2148 ± 10 ppbv near the surface and a column density of $(4.59 \pm 0.02) \times 10^{22} \text{ cm}^{-2}$.

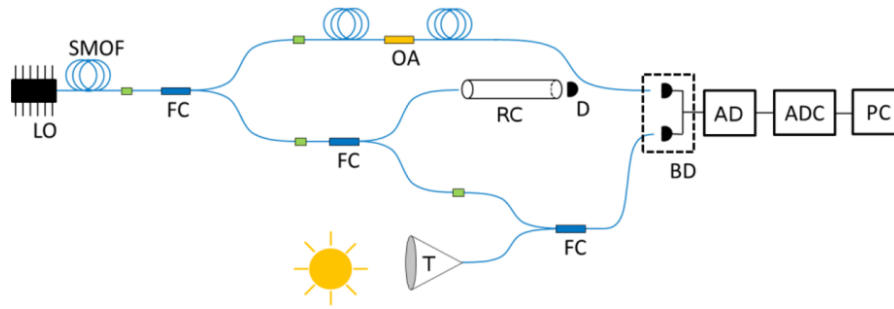


Figure 13 Schematic diagram of the experimental setup of R. Alexander et al. LO: local oscillator, SMOF: single-mode optical fiber; FC: fiber coupler; OA: optical attenuator; T: microtelescope; RC: reference gas cell; BD: balanced detector; AD: amplitude detector; ADC: analog-digital converter; PC: personal computer. fiber connectors are shown as green boxes.

In 2019, J. Wang et al. of Anhui Institute of Optics and Fine Mechanics (AIOFM, China) developed a LHR using an ICL (operating at $3.53 \mu\text{m}$) as a LO with a tuning range of $\sim 10 \text{ cm}^{-1}$ (Fig. 14). LHR spectra of H_2O and CH_4 were recorded with a spectral resolution of 0.0033 cm^{-1} . Inversion algorithm applied to the spectra of H_2O and CH_4 induced a CH_4 volume mixing ratio of $1.88 \pm 0.02 \text{ ppm}$ [154].

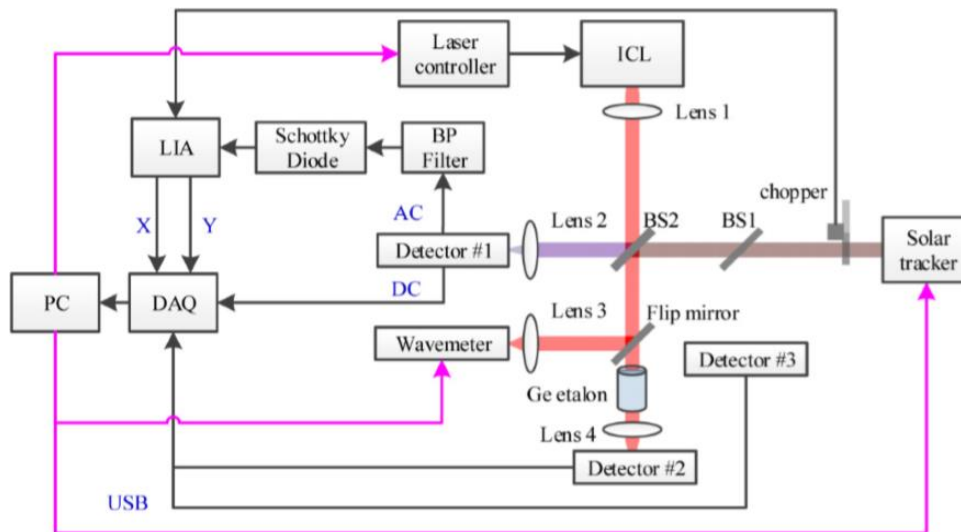


Figure 14 Schematic diagram of the experimental setup of a mid-IR LHR developed by J. Wang et al [154].

Combining the advantages of above mid- and near-IR LHR techniques, a fully transportable LHR based on an EC-QCL operating in the mid-IR of $1223\text{-}1263 \text{ cm}^{-1}$ ($\sim 8 \mu\text{m}$) is developed in the present work. A newly commercially available IR fiber is exploited to couple sunlight to the LHR receiver, equipped with an EKO sun-tracker, which renders the mid-IR LHR highly transportable and stable. The developed LHR is deployed for field remote sensing of CH_4 and N_2O in the atmospheric column.

IV. Aim of this work

The objective of the present PhD work is to develop a fully transportable mid-IR LHR for ground-based in situ measurement of trace gases in the atmospheric column.

Chapter 1 depicts the principle of LHR (Sections 1.1 and 1.2). Section 1.3 deals with the criteria on coupling efficiency of two light beams in a free-space coupling LHR. Instrument noise sources, system SNR and sensitivity are discussed in Section 1.4 to 1.5. The method for extracting heterodyne signal is presented in Section 1.6. The SNR of the LHR is compared with that of the FT-IR instrument in Section 1.7. The principle of vertical profile retrieval from the LHR measured absorption spectrum in the atmospheric column is briefly stated in Section 1.8.

Chapter 2 is devoted to introduction and discussion on practical instrumental considerations and specifications of the devices involved in our mid-IR LHR system. Two systems for sunlight collection are presented, including (1) free-space telescope system, and (2) fiber coupling system.

Chapter 3 evaluates the performance of the EC-QCL being used as the LO in our LHR through N₂O detection in a chemical catalysis process by direct absorption spectroscopy in a multi-pass cell. The laser performance was evaluated in terms of laser emission line width, single-mode wavelength tunability, stabilization of the LO source and wavelength-dependent baseline.

Chapter 4 presents the development of a proof of concept (PoC) mid-IR LHR. The developed LHR was tested on the QualAir platform of the Université Pierre et Marie Curie (UPMC), in collaboration with Dr. Tao TE of the « Laboratoire d'Études du Rayonnement et de la Matière en Astrophysique et Atmosphères (LERMA) ». Ground-based measurements of tropospheric CH₄ in the atmospheric column were performed.

Chapter 5 describes the development of a fully transportable mid-IR LHR prototype. A mid-IR fiber was explored to couple the sunlight to the heterodyne receiver, which makes our LHR, equipped with an EKO sun-tracker, fully transportable. The developed LHR instrument was tested and validated via ground-based field measurements of tropospheric CH₄ and N₂O in the atmospheric column on the roof terrace of the IRENE (Innovation Recherche en Environnement) platform in Dunkerque (51.05°N/2.34°E).

Finally, the major achievements in this PhD work are summarized and some future directions for the ground-based LHR measurements of vertical concentration profiles of atmospheric trace gases are prospected.

References

- [1] M. Pidwirny. Atmospheric Composition, Fundamentals of Physical Geography, 2nd Edition, Date Viewed, 2006.
- [2] T. Tsai. External cavity quantum cascade lasers for spectroscopic applications (Doctoral dissertation), Princeton, NJ : Princeton University, 2012.
- [3] <http://acmg.seas.harvard.edu/publications/jacobbook/bookchap11.pdf>
- [4] <http://acmg.seas.harvard.edu/people/faculty/djj/book/bookchap4.html>
- [5] J. H. Seinfeld and S. N. Pandis. Atmospheric chemistry and physics, John Wiley & Sons, Inc. Hoboken, 2006.
- [6] T. R. Karl and K. E. Trenberth. Modern global climate change, Science 2003, **302**, 1719-1723.
- [7] Kyoto Protocol to the United Nations framework convention on climate change, United Nations, 1998.
- [8] D. R. Bates and P. B. Hays. Atmospheric nitrous oxide, Planet. Space Sci. 1967, **15**, 189-197.
- [9] P. J. Crutzen. The influence of nitrogen oxides on the atmospheric ozone content. Quant. J. Roy. Meteor. Soc. 1970, **96**, 320.
- [10] S. C. Wofsy. HIAPER Pole-to-Pole Observations (HIPPO) : fine-grained, global-scale measurements of climatically important atmospheric gases and aerosols, Philos. Trans. R. Soc. London, Ser. A 2011, **369**, 2073-2086.
- [11] G. P. Brasseur, J. J. Orlando, and G. S. Tyndall. Atmospheric chemistry and global change, Topics in Environmental Chemistry, Oxford University, 1999.
- [12] D. J. Wuebbles and K. Hayhoe. Atmospheric methane and global change, Earth Sci. Rev. 2002, **57**, 177-210.
- [13] J. T. Kiehl and K. E. Trenberth. Earth's annual global mean energy budget, Bull. Amer. Meteorol. Soc. 1997, **78**, 197-208.
- [14] K. Trenberth, J. Fasullo, and L. Smith. Trends and variability in column-integrated atmospheric water vapor, Clim. Dyn. 2005, **24**, 741-758.

- [15] D. Weidmann, W. J. Reburn, and K. M. Smith. Retrieval of atmospheric ozone profiles from an infrared quantum cascade laser heterodyne radiometer : results and analysis, *Appl. Opt.* 2007, **46**, 7162-7171.
- [16] K. W. Bowman, J. Worden, T. Steck, H. M. Worden, S. Clough, and C. Rodgers. Capturing time and vertical variability of tropospheric ozone : A study using TES nadir retrievals, *J. Geophys. Res.* 2002, **107**, 4723.
- [17] P. L. Kinney. The pulmonary effects of outdoor ozone and particle air pollution, *Semin. Respir. Crit. Care Med.* 1999, **20**, 601-607.
- [18] P. F. Coheur, B. Barret, S. Turquety, D. Hurtmans, J. Hadji-Lazaro, and C. Clerbaux. Retrieval and characterization of ozone vertical profiles from a thermal infrared nadir sounder, *J. Geophys. Res.* 2005, **110**, D24303.
- [19] J. Lelieveld and F. J. Dentener. What controls tropospheric ozone? *J. Geophys. Res.* 2000, **105**, 3531-3551.
- [20] Montreal protocol on substances that deplete the ozone layer (United Nations Environment Programme, 2009).
- [21] M. J. Molina and F. S. Rowland. Stratospheric sink for chlorofluoromethanes : chlorine atom-catalysed destruction of ozone, *Nature* 1974, **249**, 810-812.
- [22] E. Mahieu, P. Duchatelet, P. Demoulin, K. A. Walker, E. Dupuy, L. Froidevaux, C. Randall, V. Catoire, K. Strong, C. D. Boone, P. F. Bernath, J. F. Blavier, T. Blumenstock, M. Coffey, M. de Mazière, D. Griffith, J. Hannigan, F. Hase, N. Jones, K. W. Jucks, A. Kagawa, Y. Kasai, Y. Mebarki, S. Mikuteit, R. Nassar, J. Notholt, C. P. Rinsland, C. Robert, O. Schrems, C. Senten, D. Smale, J. Taylor, C. Tédard, G. C. Toon, T. Warneke, S. W. Wood, R. Zander, and C. Servais. Validation of ACE-FTS v2.2 measurements of HCl, HF, CCl₃F and CCl₂F₂ using space-, balloon- and ground-based instrument observations, *Atmos. Chem. Phys.* 2008, **8**, 6199-6221.
- [23] C. P. Rinsland, C. Boone, R. Nassar, K. Walker, P. Bernath, E. Mahieu, R. Zander, J. C. McConnell, and L. Chiou. Trends of HF, HCl, CCl₂F₂, CCl₃F, CHClF₂ (HCFC-22), and SF₆ in the lower stratosphere from atmospheric chemistry experiment (ACE) and atmospheric trace molecule spectroscopy (ATMOS) measurements near 30°N latitude, *Geophys. Res. Lett.* 2005, **32**, L16S03.

- [24] M. K. W. Ko and N. D. Sze. A 2-D model calculation of atmospheric lifetimes for N₂O, CFC-11 and CFC-12, *Nature* 1982, **297**, 317-319.
- [25] G. C. Toon, C. B. Farmer, P. W. Shaper, L. L. Lowes, R. H. Norton, M. R. Schoeberl, L. R. Lait, and P. A. Newman. Evidence for subsidence in the 1989 arctic winter stratosphere from airborne infrared composition measurements, *J. Geophys. Res.* 1992, **97**, 7963-7970.
- [26] D. W. Waugh, R. A. Plumb, J. W. Elkins, D. W. Fahey, K. A. Boering, G. S. Dutton, C. M. Volk, E. Keim, R. S. Gao, B. C. Daube, S. C. Wofsy, M. Loewenstein, J. R. Podolske, K. R. Chan, M. H. Proffitt, K. K. Kelly, P. A. Newman, and L. R. Lait. Mixing of polar vortex air into middle latitudes as revealed by tracer-tracer scatter plots, *J. Geophys. Res.* 1997, **102**, 13119-13134.
- [27] C. Le Qué, R. J. Andres, T. Boden, T. Conway, R. A. Houghton, J. I. House, G. Marland, G. P. Peters, G. R. van der Werf, A. Ahlström, R. M. Andrew, L. Bopp, J. G. Canadell, P. Ciais, S. C. Doney, C. Enright, P. Friedlingstein, C. Huntingford, A. K. Jain, C. Jourdain, E. Kato, R. F. Keeling, K. Klein Goldewijk, S. Levis, P. Levy, M. Lomas, B. Poulter, M. R. Raupach, J. Schwinger, S. Sitch, B. D. Stocker, N. Viovy, S. Zaehle, and N. Zeng. The global carbon budget 1959-2011, *Earth Syst. Sci. Data* 2013, **5**, 165-185.
- [28] G. Myhre, D. Shindell, F. M. Brón, W. Collins, J. Fuglestedt, J. Huang, D. Koch, J. F. Lamarque, D. Lee, B. Mendoza, T. Nakajima, A. Robock, G. Stephens, T. Takemura, and H. Zhang. Anthropogenic and natural radiative forcing, in : *climate change 2013 : The Physical Science Basis. Contribution of Working Group I to the Fifth Assessment Report of the Intergovernmental Panel on Climate Change*, edited by: T. Stocker, D. Qin, G. K. Plattner, M. Tignor, S. K. Allen, J. Boschung, A. Nauels, Y. Xia, V. Bex, and P. M. Midgley, Cambridge University Press, Cambridge, United Kingdom and New York, NY, USA, available at : <http://www.ipcc.ch/report/ar5/wg1/> (last access: 12 October 2015), 2013.
- [29] T. Machida, K. Kita, Y. Kondo, D. Blake, S. Kawakami, G. Inoue, T. Ogawa. Vertical and meridional distributions of the atmospheric CO₂ mixing ratio between northern midlatitudes and southern subtropics, *J. Geophys. Res.* 2003, **108**, BIB (5-1)-(5-9).
- [30] W. Bischof, P. Fabian, and R. Borchers. Decrease in CO₂ mixing ratio observed in the stratosphere, *Nature* 1980, **288**, 347-348.

- [31] K. A. Boering, S. C. Wofsy, B. C. Daube, H. R. Schneider, M. Lowenstein, J. R. Podolske, and T. J. Conway. Stratospheric mean ages and transport rates from observations of carbon dioxide and nitrous oxide, *Science* 1996, **274**, 1340-1343.
- [32] E. J. Hints, K. J. Boering, E. M. Weinstock, J. G. Anderson, B. L. Gary, L. Pfister, B. C. Daube, S. C. Wofsy, M. Loewenstein, J. R. Podolske, J. J. Margitan, and T. P. Bui. Troposphere-to-stratosphere transport in the lowermost stratosphere from measurements of H₂O, CO₂, N₂O and O₃, *J. Geophys. Res.* 1998, **25**, 2655-2658.
- [33] I. M. Held and B. J. Soden. Water vapor feedback and global warming, *Ann. Rev. Energy Environ.* 2000, **25**, 441-475.
- [34] S. Marquart, M. Ponater, F. Mager, and R. Sausen. Future development of contrail cover, optical depth, and radiative forcing : impacts of increasing air traffic and climate change, *J. Climate* 2003, **16**, 2890-2904.
- [35] C. P. Rinsland, E. Mahieu, R. Zander, N. B. Jones, M. P. Chipperfield, A. Goldman, J. Anderson, J. M. Russell III, P. Demoulin, J. Notholt, G. C. Toon, J. F. Blavier, B. Sen, R. Sussmann, S. W. Wood, A. Meier, D. W. T. Griffith, L. S. Chiou, F. J. Murcray, T. M. Stephen, F. Hase, S. Mikuteit, A. Schulz, and T. Blumenstock. Long-term trends of inorganic chlorine from ground-based infrared solar spectra : Past increases and evidence for stabilization, *J. Geophys. Res.* 2003, **108**, 4252.
- [36] M. Ko, P. Newman, S. Reinmann, and S. E. Strahan. Lifetime of halogen source gases, available at : <http://sparcclima.vs89.snowflakehosting.ch/activities/lifetime-halogen-gases/>, last access : 16 July 2012.
- [37] D. H. Ehhalt. Concentrations and distributions of atmospheric trace gases, *Ber. Bunsenges. Phys. Chem.* 1992, **96**, 229-240.
- [38] P. F. Fogal, R. D. Blatherwick, F. J. Murcray, and J. R. Olson. Infrared FTS measurements of CH₄, N₂O, O₃, HNO₃, HCl, CFC-11 and CFC-12 from the MANTRA balloon campaign, *Atmos. Ocean* 2005, **43**, 351-359.
- [39] R. A. Washenfelder, G. C. Toon, J. F. Blavier, Z. Yang, N. T. Allen, P. O. Wennberg, S. A. Vay, D. M. Matross, and B. C. Daube. Carbon dioxide column abundances at the Wisconsin Tall Tower site, *J. Geophys. Res.* 2006, **111**, D22305.

- [40] P. K. Bhartia, R. D. Mcpeters, C. L. Mateer, L. E. Flynn, and C. Wellemeyer, Algorithm for the estimation of vertical ozone profile from the backscattered ultraviolet (BUV) technique. *J. Geophys. Res.*, 1996, **101**, 793-811.
- [41] M. Weber, J. P. Burrows, and R. P. Cebula. GOME solar UV/vis irradiance measurements between 1995 and 1997-First results on proxy solar activity studies, *Sol. Phys.* 1998, **177**, 63-77.
- [42] http://www.ccpo.odu.edu/SEES/ozone/class/Chap_7/7_4.htm
- [43] G. Toon, B. Sen, and J. F. Blavier. Atmospheric composition measured by solar occultation spectrometry, Jet Propulsion Laboratory, California Institute of TEchnology Pasadena, California, USA 2002.
- [44] J. W. Kaiser and J. P. Burrows. Fast weighting functions for retrievals from limb scattering measurements, *J. Quant. Spectrosc. Radiat. Transf.* 2003, **77**, 273-283.
- [45] J. W. Kaiser, C. von Savigny, K. U. Eichmann, S. Nođ, H. Bovensmann, and J. P. Burrows. Satellite-pointing retrieval from atmospheric limb-scattering of solar UV-B radiation, *Can. J. Phys.* 2004, **82**, 1041-1052.
- [46] U. Cortesi, J. C. Lambert, C. De Clercq, G. Bianchini, T. Blumenstock, A. Bracher, E. Castelli, V. Catoire, K. V. Chance, M. De Mazière, P. Demoulin, S. Godin-Beekmann, N. Jones, K. Jucks, C. Keim, T. Kerzenmacher, H. Kuellmann, J. Kuttippurath, M. Iarlori, G. Y. Liu, Y. Liu, I. S. McDermid, Y. J. Meijer, F. Mencaraglia, S. Mikuteit, H. Oelhaf, C. Piccolo, M. Pirre, P. Raspollini, F. Ravegnani, W. J. Reburn, G. Redaelli, J. J. Remedios, H. Sembhi, D. Smale, T. Steck, A. Taddei, C. Varotsos, C. Vigouroux, A. Waterfall, G. Wetzze, and S. Wood. Geophysical validation of MIPAS-ENVISAT operational ozone data, *Atmos. Chem. Phys.* 2007, **7**, 4807-4867.
- [47] <https://earth.esa.int/web/guest/missions/esa-operational-eo-missions/envisat/instruments/sciamachy>
- [48] H. Bovensmann, J. P. Burrows, M. Buchwitz, J. Frerick, S. Nođ, V. V. Rozanov, K. V. Chance, and A. P. H. Goede. SCIAMACHY : Mission objectives and measurement modes, *J. Atmos. Sci.* 1999, **56**, 127-150.
- [49] A. Dudhia. Infrared limb sounding - MIPAS and HIRDLS, Atmospheric, Oceanic and Planetary Physics Oxford University, Oxford, UK, 2002.

- [50] M. Ern, Q. T. Trinh, P. Preusse, J. C. Gille, M. G. Mlynczak, J. M. Russell, and M. Riese. GRACILE : a comprehensive climatology of atmospheric gravity wave parameters based on satellite limb soundings, *Earth Syst. Sci. Data* 2018, **10**, 857-892.
- [51] M. Endemann. MIPAS instrument concept and performance, European Symposium on Atmospheric Measurements from Space, Noordwijk, 1999.
- [52] H. Fischer and H. Oelhaf. Remote sensing of vertical profiles of atmospheric trace constituents with MIPAS limb emission spectrometers, *Appl. Opt.* 1996, **35**, 2787-2796.
- [53] A. Richter, J. P. Burrows, and C. Granier. Increase in tropospheric nitrogen dioxide over China observed from space, *Nature* 2005, **437**, 129-132.
- [54] C. D. Rodgers. Inverse methods for atmospheric sounding : theory and practice, World Scientific, 2000.
- [55] J. P. Burrows, U. Platt, and P. Borrell. Tropospheric remote sensing from space, in: Remote sensing of tropospheric composition from space, Springer Berlin Heidelberg, 2011, 1-65.
- [56] R. A. Scheepmaker, C. Frankenber, N. M. Deutscher, M. Schneider, S. Barthlott, T. Blumenstock, O. E. Garcia, F. Hase, N. C. Jones, E. Mahieu, and J. Notholt. Validation of SCIAMACHY HDO/H₂O measurements using the TCCON and NDACC-MUSICA networks, *Atmos. Meas. Tech.* 2015, **8**, 1799-1818.
- [57] M. Schneider, F. Hase, and T. Blumenstock. Ground-based remote sensing of HDO/H₂O ratio profiles : introduction and validation of an innovative retrieval approach. *Atmos. Chem. Phys.* 2006, **6**, 4705-4722.
- [58] A. J. Geer, W. A. Lahoz, S. Bekki, N. Bormann, Q. Errera, H. J. Eskes, D. Fonteyn, D. R. Jackson, M. N. Juckes, S. Massar, V. H. Peuch, S. Rharmili, and A. Segers. The ASSET intercomparison of ozone analyses : method and first results, *Atmos. Chem. Phys. Discuss.* 2006, **6**, 4495-4577.
- [59] G. Hönninger, C. von Friedeburg, and U. Platt. Multi axis differential optical absorption spectroscopy (MAX-DOAS), 2004, *Atmos. Chem. Phys.* **4**, 231-254.
- [60] Y. Wang, S. Dörner, S. Donner, S. Böhnke, I. De Smedt, R. R. Dickerson, Z. Dong, H. He, Z. Li, Z. Li, D. Li, D. Liu, X. Ren, N. Theys, Y. Wang, Y. Wang, Z. Wang, H. Xu, J. Xu, and T. Wagner. Vertical profiles of NO₂, SO₂, HONO, HCHO, CHOCHO and aerosols derived from MAX-DOAS measurements at a rural site in the central western

- North China Plain and their relation to emission sources and effects of regional transport, *Atmos. Chem. Phys.* 2019, **19**, 5417-5449.
- [61] S. Solomon, A. L. Schmeltekopf, and R. W. Sanders. On the interpretation of zenith sky absorption measurements, *J. Geophys. Res.* 1987, **92**, 8311-8319.
- [62] J. F. Grainger and J. Ring. Anomalous Fraunhofer line profiles, *Nature* 1962, **193**, 762.
- [63] I. Aben, D. M. Stam, and F. Helderman. The ring effect in skylight polarization, *Geophys. Res. Lett.* 2001, **28**, 519-522.
- [64] T. Wagner, O. Ibrahim, R. Shaiganfar, and U. Platt. Interactive comment on “Mobile MAX-DOAS observations of tropospheric trace gases”, *Atmos. Meas. Tech. Discuss.* 2010, **2**, C1120-C1124.
- [65] J. P. Pommereau and F. Goutail. O₃ and NO₂ ground-based measurements by visible spectrometry during Arctic winter and spring 1988, *Geophys. Res. Lett.* 1988, **15**, 891-894.
- [66] F. Goutail, J. P. Pommereau, and A. Sarkissian. Total nitrogen dioxide at the Arctic Polar Circle since 1990, *Geophys. Res. Lett.* 1994, **21**, 1371-740.
- [67] G. Vaughan, P. T. Quinn, A. C. Green, J. Bean, H. K. Roscoe, M. V. Roozendaeld, and F. Goutail. SAOZ measurements of NO₂ at Aberystwyth, *J. Environ. Monit.* 2006, **8**, 353-361.
- [68] J. P. Pommereau and F. Goutail. Stratospheric O₃ and NO₂ observations at the southern polar circle in summer and fall, *Geophys. Res. Lett.* 1998, **15**, 895-899.
- [69] L. Drissen, A. P. Bernier, M. Charlebois, A. Alarie¹, F. Grandmont, and J. Mandar. Imaging Fourier transform spectroscopy for astronomy, In book: *Fourier Transforms - New Analytical Approaches and FTIR Strategies*, 2011, 493-520.
- [70] C. P. Rinsland, A. Goldman, J. W. Elkins, L. S. Chiou, J. W. Hannigan, S. W. Wood, E. Mahieu, and R. Zander. Long-term trend of CH₄ at northern mid-latitudes comparison between ground based infrared solar and surface sampling measurements, *J. Quant. Spectrosc. Radiat. Transfer*, 2006, **97**, 457-466.
- [71] D. Wunch, C. Midwinter, J. R. Drummond, C. T. McElroy, and A. F. Bagès. University of Toronto’s balloon-borne Fourier transform spectrometer, *Rev. Sci. Instrum.* 2006, **77**,093104.

- [72] R. Sussmann, W. Stremme, J. P. Burrows, A. Richter, W. Seiler, and M. Rettinger. Stratospheric and tropospheric NO₂ variability on the diurnal and annual scale : A combined retrieval from ENVISAT/SCIAMACHY and solar FTIR at the Permanent Ground-Truthing Facility Zugspitze/Garmisch, *Atmos. Chem. Phys.* 2005, **5**, 2657-2677.
- [73] F. Hase, T. J. W. Hannigan, M. T. Coey, A. Goldman, M. Höpfner, N. B. Jones, C. P. Rinsland, and S. W. Wood. Intercomparison of retrieval codes used for the analysis of high-resolution: Ground-based FTIR measurements, *J. Quant. Spectrosc. Radiat. Transfer* 2004, **87**, 25-52.
- [74] B. Barret, M. De Mazière, and E. Mahieu. Ground-based FTIR measurements of CO from the Jungfraujoch: Characterisation and comparison with in situ surface and MOPITT data, *Atmos. Chem. Phys.* 2003, **3**, 2217-2223.
- [75] Y. Zhao, Y. Kondo, F. J. Murcray, X. Liu, and M. Koike, K. Kita, H. Nakajima, I. Murata, and K. Suzuki. Carbon monoxide column abundances and tropospheric concentrations retrieved from high resolution ground-based infrared solar spectra at 43.58N over Japan, *J. Geophys. Res.* 1997, **102**, 23403-23411.
- [76] <https://tccodata.org>.
- [77] R. Parker, H. Boesch, and A. Cogan. Methane observations from the greenhouse gases observing satellite : comparison to ground-based TCCON data and model calculations, *Geophys. Res. Lett.* 2001, **38**, L15807.
- [78] C. Frankenberg, D. Wunch, G. Toon, C. Risi, R. Scheepmaker, J. E. Lee, P. Wennberg, and J. Worden. Water vapor isotopologue retrievals from high-resolution GOSAT shortwave infrared spectra, *Atmos. Meas. Tech.* 2013, **6**, 263-274.
- [79] D. Wunch, P. O. Wennberg, G. C. Toon, B. J. Connor, B. Fisher, G. B. Osterman, C. Frankenberg, L. Mandrake, C. O'Dell, P. Ahonen, S. C. Biraud, R. Castano, N. Cressie, D. Crisp, N. M. Deutscher, A. Eldering, M. L. Fisher, D. W. T. Griffith, M. Gunson, P. Heikkinen, G. Keppel-Aleks, E. Kyrö, R. Lindenmaier, R. Macatangay, J. Mendonca, J. Messerschmidt, C. E. Miller, I. Morino, J. Notholt, F. A. Oyang, M. Rettinger, J. Robinson, C. M. Roehl, R. J. Salawitch, V. Sherlock, K. Strong, R. Sussmann, T. Tanaka, D. R. Thompson, O. Uchino, T. Warneke, and S. C. Wofsy. A method for evaluating bias in global measurements of CO₂ total columns from space, *Atmos. Chem. Phys.* 2011, **11**, 12317-12337.

- [80] M. de Mazière, A. M. Thompson, M. J. Kurylo, J. D. Wild, G. Bernhard, T. Blumenstock, G. O. Braathen, J. W. Hannigan, J. Lambert, T. Leblanc, T. J. McGee, G. Nedoluha, I. Petropavlovskikh, G. Seckmeyer, P. C. Simon, W. Steinbrecht, and S. E. Strahan. The Network for the Detection of Atmospheric Composition Change (NDACC): history, status and perspectives, *Atmos. Chem. Phys.* 2018, **18**, 4935-4964.
- [81] <http://www.ndaccdemo.org>.
- [82] GOSAT Project : greenhouse gases observing satellite (National Institute for Environmental Studies (NIES), 2011), retrieved 2011, <http://www.gosat.nies.go.jp/eng/gosat/page6.htm>
- [83] L. Wu, O. Hasekamp, H. Hu, J. Landgraf, A. Butz, J. A. de Brugh, I. Aben, D. F. Pollard, D. W. T. Griffith, D. G. Feist, D. Koshelev, F. Hase, G. C. Toon, H. Ohyama, I. Morino, J. Notholt, K. Shiomi, L. Iraci, M. Schneider, M. de Mazière, R. Sussmann, R. Kivi, T. Warneke, T. Goo, and Y. Té Carbon dioxide retrieval from OCO-2 satellite observations using the RemoTeC algorithm and validation with TCCON measurements, *Atmos. Meas. Tech.* 2018, **11**, 3111-3130.
- [84] A. Ostler, R. Sussmann, M. Rettinger, N. M. Deutscher, S. Dohe, F. Hase, N. Jones, M. Palm, and B. M. Sinnhuber. Multistation intercomparison of column-averaged methane from NDACC and TCCON: impact of dynamical variability, *Atmos. Meas. Tech.* 2014, **7**, 4081-4101.
- [85] E. Sepúlveda, M. Schneider, F. Hase, S. Barthlott, D. Dubravica, O. E. García, A. Gomez-Pelaez, Y. González, J. C. Guerra, M. Gisi, R. Kohlhepp, S. Dohe, T. Blumenstock, K. Strong, D. Weaver, M. Palm, A. Sadeghi, N. M. Deutscher, T. Warneke, J. Notholt, N. Jones, D. W. T. Griffith, D. Smale, G. W. Brailsford, J. Robinson, F. Meinhardt, M. Steinbacher, T. Aalto, and D. Worthy. Tropospheric CH₄ signals as observed by NDACC FTIR at globally distributed sites and comparison to GAW surface in situ measurements, *Atmos. Meas. Tech.* 2014, **7**, 2337-2360.
- [86] D. J. Jacob, E. J. Bucsela, and A. E. Perring. Validation of OMI tropospheric NO₂ observations during INTEX-B and application to constrain NO_x emissions over the eastern United States and Mexico, *Atmos. Environ.* 2008, **42**, 4480-4497.
- [87] G. Durrý and G. Megie. Atmospheric CH₄ and H₂O monitoring with near-infrared InGaAs laser diodes by the SDLA, a balloon-borne spectrometer for tropospheric and stratospheric in situ measurements, *Appl. Opt.* 1999, **38**, 7342-7354.

- [88] B. Dix, C. A. M. Brenninkmeijer, U. Frieß, T. Wagner, and U. Platt. Airborne multi-axis DOAS measurements of atmospheric trace gases on CARIBIC long-distance flights, *Atmos. Meas. Tech.* 2009, **2**, 639-652.
- [89] M. Birk, G. Wagner, G. Lange, A. Lange, B. N. Ellison, M. R. Harman, A. Murk, H. Oelhaf, G. Maucher, and C. Sartorius. TELIS: TERAhertz and subMMW Limb Sounder-Project summary after first successful flight, 21st International Symposium On Space Terahertz Technology, Oxford, 23-25 March, 2010.
- [90] J. Xu, F. Schreier, G. Wetzell, A. de Lange, M. Birk, T. Trautmann, A. Doicu, and G. Wagner. Performance assessment of balloon-borne trace gas sounding with the Terahertz channel of TELIS, *Remote Sens.* 2018, **10**, 315.
- [91] A. C. Watts, V. G. Ambrosia, and E. A. Hinkley. Unmanned aircraft systems in remote sensing and scientific research: classification and considerations of use, *Remote Sens.* 2012, **4**, 1671-1692.
- [92] D. Weidmann, R. Rose, and M. Jenkins. A fully integrated, miniaturized quantum cascade laser heterodyne radiometer for EO, 2009,
- [93] R. A. Fessenden. Wireless telephony, US Pat No. 706, 740, August 1902.
- [94] J. L. Hogan. The heterodyne receiving system and notes in the recent Arlington-Salem tests, *Proc IRE*, 1973, **1**, 75-102.
- [95] S. L. Jain. Laser heterodyne system for measurement of monir constituents in the atmosphere, *Indian J. Radio&Space Phys.* 1996, **25**, 309-317.
- [96] F. Smith, S. Havemann, A. Hoffmann, W. Bell, D. Weidmann, S. Newman. Evaluation of laser heterodyne radiometry for numerical weather prediction applications, *Q. J. R. Meteorol. Soc.* 2018, **144**, 1831-1850.
- [97] A. T. Forrester. On the possibility of observing beat frequencies between lines in the visible spectrum, *Phys. Rev.* 1947, **72**, 728.
- [98] E. Gerjuoy, A. T. Forrester, and W. E. Parkins. Signal-to-noise ratio in photoelectrically observed beats, *Phys. Rev.* 1948, **73**, 922-923.
- [99] A. T. Forrester, R. A. Gudoiindsen, and P. O. Johnson. Photoelectric mixing of incoherent light, *Phys. Rev.* 1955, **99**, 1692-1700.
- [100] T. H. Maiman, Stimulated optical radiation in ruby, *Nature* 1960, **187**, 493-494.

- [101] A. T. Forrester. Photoelectric mixing as a spectroscopic tool, *J. Opt. Soc. Am.* 1961, **51**, 253-259.
- [102] A. Javan, E. A. Ballik, and W. L. Bond. Frequency characteristics of a continuous-wave He-Ne optical maser, *J. Opt. Soc. Am.* 1962, **52**, 96-98.
- [103] B. J. McMurtry and A. E. Siegman. Photomixing experiments with a ruby optical maser and a traveling-wave microwave phototube, *Appl. Opt.* 1962, **1**, 133-135.
- [104] R. T. Menzies. Remote sensing with infrared heterodyne radiometers, *Opto-electron.* 1972, **4**, 179-186.
- [105] M. C. Teich. Optimum heterodyne detection at 10.6 μm in photoconductive Ge : Cu, *Appl. Phys. Lett.* 1966, **9**, 357-360.
- [106] R. T. Menzies. Use of CO and CO₂ lasers to detect pollutants in the atmosphere, *Appl. Opt.* 1971, **10**, 1532-1538.
- [107] R. T. Menzies and M. S. Shumate. Air Pollution : Remote detection of several pollutant gases with a laser heterodyne radiometer, *Science* 1974, **184**, 570.
- [108] H. S. Johnston. Reduction of stratospheric ozone by nitrogen oxide catalysts from supersonic transport exhaust, *Science* 1971, **173**, 517-522.
- [109] J. C. Farman, B. G. Gardiner, and J. D. Shanklin. Large losses of total ozone in Antarctica reveal seasonal ClO_x/NO_x interaction, *Nature* 1985, **315**, 207-210.
- [110] R. T. Menzies. Ozone spectroscopy with a CO₂ waveguide laser, *Appl. Opt.* 1976, **15**, 2597-2599.
- [111] R. T. Menzies and R. K. Seals. Ozone monitoring with an infrared heterodyne radiometer, *Science* 1977, **197**, 1275-1277.
- [112] M. M. Abbas, T. Kostiuk, M. J. Mumma, D. Buhl, V. G. Kunde, and L. W. Brown. Stratospheric ozone measurement with an infrared heterodyne spectrometer, *Geophys. Res. Lett.* 1978, **5**, 317-320.
- [113] D. Sahoo and P. C. Pandey. *Advances in Marine and Antarctic science*, A.P.H. Publishing Corporation, 2002.
- [114] S. L. Jain and O. P. Tripathi. Laser heterodyne system at Maitri, Antarctica, Sixteenth Indian expedition to Antarctica, Scientific Report, Department of Ocean Development, Technical Publication, 2000, **14**, 1-36.

- [115] D. Courtois, D. Delahaigue, and C. Thiebeaux. Detection of thermal emission from atmospheric gases by laser heterodyne radiometry, *Infrared Phys.* 1993, **34**, 407-413.
- [116] J. C. Mouanda, D. Courtois, and C. Thiebeaux. Laboratory and atmospheric ozone measurements by infrared-laser heterodyne detection, *Appl. Phys. B* 1993, **57**, 119-122.
- [117] E. D. Hinkley, R. T. Ku, K. W. Nill, and J. F. Butler, Long-path monitoring: advanced instrumentation with a tunable diode laser, *Appl. Opt.* 1976, **15**, 1653-1658.
- [118] E. D. Hinkley and P. L. Kelley. Detection of air pollutants with tunable diode lasers, *Science* 1971, **171**, 635-639.
- [119] R. T. Ku and D. L. Spears. High-sensitivity infrared heterodyne radiometer using a tunable-diode-laser local oscillator, *Opt. Lett.* 1977, **1**, 84-86.
- [120] M. A. Frerking and D. J. Muehlner. Infrared heterodyne spectroscopy of atmospheric ozone, *Appl. Opt.* 1977, **16**, 526-528.
- [121] C. N. Harward and J. M. Hoell, in: *Heterodyne Systems and Technology*, NASA Conference Publication 1980, **2138**, 1-10.
- [122] H. Fukunishi, S. Okano, M. Taguchi, and T. Ohnuma. Laser heterodyne spectrometer using a liquid nitrogen cooled tunable diode laser for remote measurements of atmospheric O(3) and N(2)O, *Appl. Opt.* 1990, **29**, 2722.
- [123] M. Koide, M. Taguchi, and H. Fukunishi. Ground-based remote sensing of methane height profiles with a tunable diode laser heterodyne spectrometer, *Geophys. Res. Lett.* 1995, **22**, 401-404.
- [124] B. Parvitte, C. Thiebeaux, and D. Courtois, Tunable heterodyne spectrometer in the 9 μm range with selected lead-salt diodes, *Spectrochim. Acta Part A : Mol. Biomol. Spectrosc.* 1999, **55**, 2027-2037.
- [125] D. Courtois, C. Thiebeaux, and A. Delahaigue. Heterodyne spectrometer for the 10 micron region, *Int. J. Infrared Millimeter Waves* 1984, **5**, 185-195.
- [126] D. Courtois, C. Thiebeaux, and A. Delahaigue. Infrared laser heterodyne ozone spectrum, *Int. J. Infrared Millimeter Waves* 1987, **8**, 103-106.
- [127] C. Thiebeaux, D. Courtois, D. Delahaigue, H. L. Corre, J. C. Mouanda, and A. Fayt. Dual-beam laser heterodyne spectrometer : Ethylene Absorption Spectrum in the 10 μm range, *Appl. Phys. B* 1988, **47**, 313-318.

- [128] J. Faist, F. Capasso, D. L. Sivco, C. Sirtori, A. L. Hutchinson, and A. Y. Cho, Quantum cascade laser, *Science* 1994, **264**, 553-556.
- [129] M. Beck, D. Hoffstetter, T. Aellen, J. Faist, U. Oesterle, M. Illegems, E. Gin, and H. Melchior, Continuous wave operation of a mid-infrared semiconductor laser at room temperature, *Science* 2002, **295**, 301-304.
- [130] R. M. Williams, J. F. Kelly, J. S. Hartman, S. W. Sharpe, M. S. Taubman, J. L. Hall, F. Capasso, C. Gmachl, D. L. Sivco, J. N. Baillargeon, and A. Y. Cho. Kiloherz linewidth from frequency-stabilized mid-infrared quantum cascade lasers, *Opt. Lett.* 1999, **24**, 1844-1846.
- [131] H. Ganser, B. Frech, A. Jentsch, M. Mürtz, C. Gmachl, F. Capasso, D.L. Sivco, J. N. Baillargeon, A. L. Hutchinson, A. Y. Cho, and W. Urban. Investigation of the spectral width of quantum cascade laser emission near 5.2 μm by a heterodyne experiment, *Opt. Commun.* 2001, **197**, 127-130.
- [132] D. Wirtz, G. Sonnabend, and R. T. Schieder. THIS : a tuneable heterodyne infrared spectrometer, *Spectrochimica. Acta. Part A* 2002, **58** 2457-2463.
- [133] M. Sornig, T. Livengood, G. Sonnabend, P. Kroetz, D. Stupar, T. Kostiuk, and R. Schieder. Venus upper atmosphere winds from ground-based heterodyne spectroscopy of CO_2 at wavelength, *Planet. Space Sci.* 2008, **56**, 1399-1406
- [134] H. Fukunishi, S. Okano, M. Taguchi, and T. Ohnuma. Laser heterodyne spectrometer using a liquid nitrogen cooled tunable diode laser for remote measurements of atmospheric O_3 and N_2O , *Appl. Opt.* 1990, **29**, 2722-2728.
- [135] D. Weidmann and D. Courtois. Infrared 7.6 μm lead-salt diode laser heterodyne radiometry of water vapor in a CH_4 -air premixed flat flame, *OSA* 2003, **42**, 1115.
- [136] G. Sonnabend, D. Wirtz, F. Schmülling, and R. Schieder. Tunable heterodyne infrared spectrometer for atmospheric and astronomical studies, *Appl. Opt.* 2002, **41**, 2978-2984.
- [137] D. Weidmann and D. Courtois. Passive remote detection in a combustion system with a tunable heterodyne receiver : application to sulfur dioxide, *J. Quant. Spectrosc. Radiat. Transf.* 2004, **83**, 655-666.

- [138] D. Weidmann, W. J. Reburn, and K. M. Smith. Infrared heterodyne radiometry using quantum cascade laser as tunable local oscillator : application to atmospheric studies[C]//Conference on Lasers and Electro-Optics. Opt. Soc. Amer. 2007, CThII6.
- [139] D. Weidmann, W. J. Reburn, and K. M. Smith. Ground-based prototype quantum cascade laser heterodyne radiometer for atmospheric studies, Rev. Sci. Instrum. 2007, **78**, 073107.
- [140] J. Faist, F. Capasso, D. L. Sivco, A. L. Hutchinson, C. Sirtori, S. N. G. Chu, and A. Y. Cho, Quantum cascade laser : Temperature dependence of the performance characteristics and high T_0 operation, Appl. Phys. Lett. 1994, **65**, 2901.
- [141] <https://www.daylightsolutions.com/home/technology/about-mid-ir-quantum-cascade-lasers/>.
- [142] S. R. Darvish, S. Slivken, A. Evans, J. S. Yu, and M. Razeghi. Room-temperature, high-power, and continuous-wave operation of distributed-feedback quantum-cascade lasers at $\lambda \sim 9.6\mu\text{m}$, Appl. Phys. Lett. 2006, **88**, 201114.
- [143] G. Wysocki, R. Lewicki, R. F. Curl, F. K. Tittel, L. Diehl, F. Capasso, M. Troccoli, G. Hofler, D. Bour, S. Corzine, R. Maulini, M. Giovannini, and J. Faist. Widely tunable mode-hop free external cavity quantum cascade lasers for high resolution spectroscopy and chemical sensing, Appl. Phys. B 2008, **92**, 305-311.
- [144] F. Capasso. High-performance midinfrared quantum cascade lasers, Opt. Eng. 2010, **49**, 111102.
- [145] D. Weidmann and G. Wysocki. High-resolution broadband ($>100\text{ cm}^{-1}$) infrared heterodyne spectro-radiometry using an external cavity quantum cascade laser, Opt. Express 2009, **17**, 248-259.
- [146] T. Tsai, R. A. Rose, D. Weidmann, and G. Wysocki. Atmospheric vertical profiles of O_3 , N_2O , CH_4 , CCl_2F_2 , and H_2O retrieved from external-cavity quantum-cascade laser heterodyne radiometer measurements, Appl. Opt. 2012, **51**, 8779-8792.
- [147] D. Weidmann, B. J. Perrett, N. A. Macleod, and R. M. Jenkins. Hollow waveguide photomixing for quantum cascade laser heterodyne spectro-radiometry, Opt. express 2011, **19**, 9074-9085.
- [148] Z. Chao, J. Wu, C. Yin, and Y. Xu. 633-nm tunable external-cavity diode laser with an intra-cavity glass plate as the fine-tuning device, Opt. Eng. **2001**, **40**, 801.

- [149] T. Tsai and G. Wysocki. External-cavity quantum cascade lasers with fast wavelength scanning, *Appl. Phys. B* 2010, **100**, 243.
- [150] D. Stupar, J. Krieg, P. Krötz, G. Sonnabend, M. Sornig, T. F. Giesen, and R. Schieder. Fully reflective external-cavity setup for quantum cascade lasers as a local oscillator in mid-infrared wavelength heterodyne spectroscopy, *Appl. Opt.* 2008, **47**, 2993.
- [151] D. Weidmann, T. Tsai, N. A. Macleod, and G. Wysocki. Atmospheric observations of multiple molecular species using ultra-high-resolution external cavity quantum cascade laser heterodyne radiometry, *Opt. Lett.* 2011, **36**, 1951-1953.
- [152] E. L. Wilson, M. L. McLinden, and J. H. Miller. Miniaturized laser heterodyne radiometer for measurements of CO₂ in the atmospheric column, *Appl. Phys. B* 2014, **114**, 385-393.
- [153] A. Rodin, A. Klimchuk, A. Nadezhdinskiy, D. Churbanov, and M. Spiridonov. High resolution heterodyne spectroscopy of atmospheric methane NIR absorption, *Opt. Express* 2014, **22**, 13825-13834.
- [154] J. Wang, G. Wang, T. Tan, G. Zhu, C. Sun, Z. Cao, X. Gao, and W. Chen. Mid-infrared laser heterodyne radiometer (LHR) based on a 3.53 μm room-temperature interband cascade laser, *Opt. Express* 2019, **27**, 9610-9619.

Chapter 1 Principle of Laser Heterodyne Radiometer

Objective

Laser heterodyne radiometer (LHR) is one of the most important instruments for the measurement of vertical profiles of atmospheric trace gases. The principle of a LHR is described in Section 1.1 to 1.2. Section 1.3 deals with the criteria on coupling efficiency of two light beams in a free-space coupling LHR. Instrument noise sources, system SNR and sensitivity are discussed in Section 1.4 to 1.5. The method for extracting heterodyne signal is presented in Section 1.6. The SNR of the LHR is compared with that of the FT-IR instrument in Section 1.7. The principle of vertical profile retrieval from the measured absorption spectrum in the atmospheric column is briefly presented in Section 1.8.

Principle of Laser Heterodyne Radiometer

In a LHR, the electromagnetic field of the sunlight $E_S(t) = A_{S0}(\omega)\cos(\omega t)$ at frequency ω is mixed in a photomixer with an electromagnetic field $E_L(t) = A_{L0}(\omega_L)\cos(\omega_L t)$ at frequency ω_L from a local oscillator (LO). A beat note at an intermediate frequency (IF, $|\omega - \omega_L|$), produced from the photomixing, is amplified by a low-noise amplifier and filtered by a band-pass filter. This heterodyne signal is then square-law detected and fed into a lock-in amplifier (LIA), the output of the LIA is sampled by a laptop for further data processing.

Heterodyne absorption spectrum of atmospheric species can be recovered by scanning the LO frequency across the absorption feature (leading to change in intensity of the resulting radio frequency (RF) beat signal). The shape of the ground-recovered atmospheric absorption spectrum contains information on vertical distributions of the target absorbers. It is possible to retrieve trace gas abundances at different altitudes through a retrieval algorithm based on an appropriate inversion model [1,2].

The principle of LHR is schematically shown in Fig. 1.1, which mainly includes four parts : sunlight collection, photomixer, RF receiver and LIA.

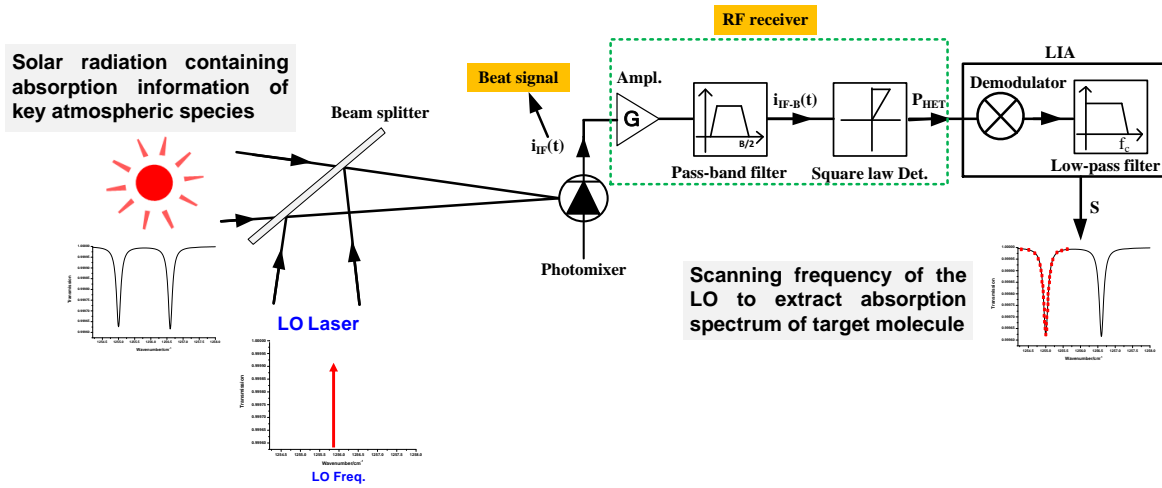


Figure 1.1 Basic concept of a typical LHR. LIA: lock-in amplifier; LO: local oscillator; RF: radio frequency.

1.1 Sunlight collection

An optical heterodyne receiver is, in effect, both a receiver and an antenna, which is constrained by antenna property [3]. In heterodyne detection, only a fraction of sunlight radiation contributes to heterodyning. Indeed, only the part of the same extended sunlight beam that superimposes with the LO will contribute to the heterodyne power. The rest of the illuminating power will contribute to the continuous component and noise [3,4], as shown in Fig. 1.2 (left).

For the simple case of a single flat mixing element, it is obviously necessary to maintain the wavefronts of both sunlight and LO in phase over the photosensitive area if efficient mixing is to be achieved. If an effective aperture of a mixer A_T is illuminated normally by a plane wave LO, effective heterodyning will only occur for sunlight arriving from within a solid angle Ω_S about the normal, given by antenna theory [3] :

$$A_T \cdot \Omega_S = \lambda^2 \quad (1.1)$$

where λ is the radiation wavelength. The throughput is limited by the operating wavelength when the diameter of the collecting optics is fixed. If the effective aperture of the mixing element is known, the solid angle increases with the radiation wavelength, as shown in Fig. 1.2 (right).

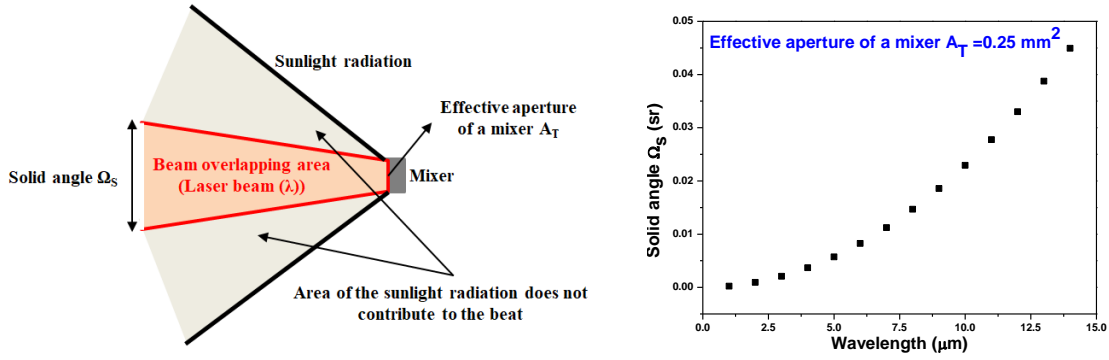


Figure 1.2 *left*: geometric restriction of the antenna theory; *right*: solid angle Ω_s vs. radiation wavelength λ . (effective aperture of the mixer $A_T=0.25 \text{ mm}^2$).

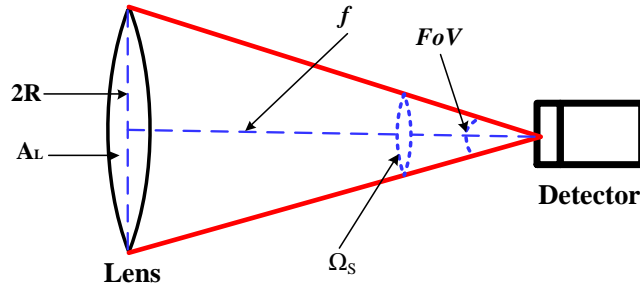


Figure 1.3 Geometry restriction of the solid angle Ω_s and FoV in the antenna theory.

In the case of a LHR instrument which includes an optical system for collecting sunlight, the geometric restriction of the antenna theory can be modified as Fig. 1.3, which always follows the antenna theory [3]. Here, the solid angle through which a detector is sensitive to electromagnetic radiation is usually expressed by FoV. From Fig. 1.3, the geometric expressions of the solid angle Ω_s and FoV in a LHR system can be approximately written as :

$$\Omega_s = \frac{A_L}{f^2} = \frac{\pi \cdot R^2}{f^2} \quad (1.2)$$

$$FoV = \frac{2 \cdot R}{f} \quad (1.3)$$

where f is the focal length of the collecting optics, R and A_L are the radius and the area of the optics used for collecting sunlight radiation, respectively.

From Eqs. (1.1), (1.2), and (1.3), the FoV of a LHR system can thus be expressed by [5] :

$$FoV = \frac{4 \cdot \lambda}{\pi \cdot D} \quad (1.4)$$

where $D = 2R$ is the diameter of the collecting optics.

A smaller FoV would be advantageous for monitoring localized phenomena and increasing the number of useful observations between scattered clouds. Meanwhile, a FoV smaller than the FoV ($\sim 0.5^\circ$) of the Sun ensures that it does not drift off the Sun throughout the day [6].

1.2 Heterodyne receiver

A heterodyne receiver consists of four basic elements, as follows (Fig. 1.4) : (1) Photomixer, (2) RF amplifier and band-pass filter, (3) Square law detector, (4) Lock-in amplifier.

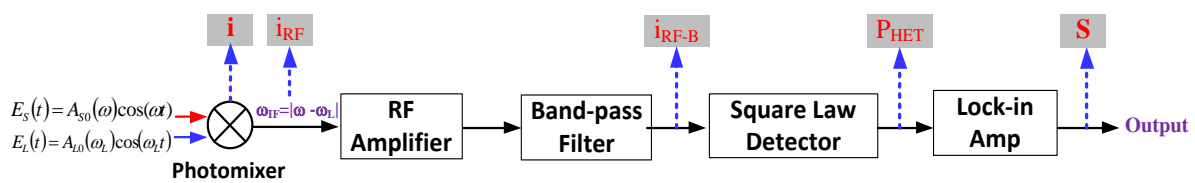


Figure 1.4 Schematic diagram of a heterodyne receiver. i is the resulting photocurrent from the photomixer; i_{IF} is the IF component of the photomixer current i ; i_{IF-B} is the IF signal after amplification and band-pass filtering; P_{HET} is the resulting power from the square law detector; S is the demodulated heterodyne output from the LIA.

1.2.1 Photomixer

Classically, the total electromagnetic field $E(t)$ (in [V/m]) entering the photomixer, as shown in Fig. 1.5, is the sum of sunlight radiation $E_S(t) = A_{S0}(\omega)\cos(\omega t)$ and the LO radiation $E_L(t) = A_{L0}(\omega_L)\cos(\omega_L t)$, i.e. [6] :

$$E(t) = E_S(t) + E_L(t) = A_{S0}(\omega)\cos(\omega t) + A_{L0}(\omega_L)\cos(\omega_L t) \quad (1.5)$$

where $A_{L0}(\omega_L)$ and $A_{S0}(\omega)$ are the amplitudes of electric fields of the LO and the sunlight, respectively, ω_L is the LO frequency, and ω is the optical frequency of the sunlight that beats with the LO light.

The resulting photocurrent $i(t)$ from the photomixer is proportional to the total optical intensity, i.e. to the square of the total electric field amplitude $E(t)$ [7,8] :

$$i(t) = \frac{\eta \cdot e}{h \cdot \nu} \cdot E^2(t) = \frac{\eta \cdot e}{h \cdot \nu} \cdot [A_{S0}(\omega)\cos(\omega t) + A_{L0}(\omega_L)\cos(\omega_L t)]^2$$

$$= \frac{\eta \cdot e}{h \cdot \nu} \cdot \left\{ \frac{A_{S0}^2(\omega) + A_{L0}^2(\omega_L)}{2} + \frac{A_{S0}^2(\omega)}{2} \cos(2\omega t) + \frac{A_{L0}^2(\omega_L)}{2} \cos(2\omega_L t) + A_{S0}(\omega)A_{L0}(\omega_L) \{ \cos[(\omega + \omega_L)t] + \cos[(\omega - \omega_L)t] \} \right\} \quad (1.6)$$

where η is the quantum efficiency of the photomixer, $e = 1.6 \times 10^{-19}$ C is the elementary electric charge, $h = 6.62607 \times 10^{-34}$ J s is the Planck constant, and ν is the frequency of the radiation falling onto the photomixer.

The high frequency components (at 2ω , $2\omega_L$ and $\omega + \omega_L$) and the constant DC components are filtered out, leaving only the signal (beat note) at the intermediate frequency ($\omega_{IF} = |\omega - \omega_L|$) for heterodyne detection. The beat note has an amplitude proportional to the product of the electric field amplitudes ($A_{L0}(\omega_L) \times A_{S0}(\omega)$).

$$i_{IF}(t) = \frac{\eta \cdot e}{h \cdot \nu} \cdot A_{L0}(\omega_L) A_{S0}(\omega) \cos[(\omega - \omega_L)t] \quad (1.7)$$

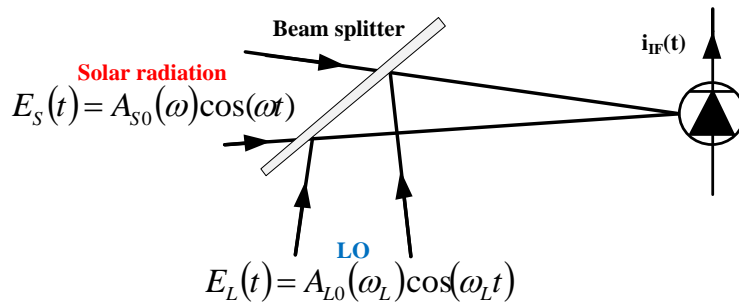


Figure 1.5 Schematic diagram of a LHR for photomixing of the sunlight beam and the LO beam.

1.2.2 RF amplifier and band-pass filter

The heterodyne beat signal at the intermediate frequency ($\omega_{IF} = |\omega - \omega_L|$), contains the spectral information of the sunlight that can be amplified, detected, and analysed with appropriate RF electronics. Typically, the intensity of the beat signal delivered by the photomixer is weak and must be amplified by a RF amplifier. Furthermore, the spectral resolution (B in [Hz]) of the LHR instrument can be defined by the used RF electrical filter bandwidth of $B/2$. B is then the double-sideband bandwidth of the heterodyne receiver, and a LHR system will respond to radiation signals in both IF sidebands of the LO frequency (Fig. 1.6). The detection diagram is shown in Fig. 1.7.

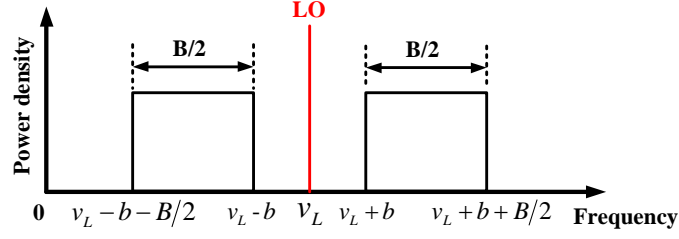


Figure 1.6 Receiving bandwidth of double sidebands of a LHR receiver, assuming the RF filter has a rectangular pass-band stretching from b Hz to $b + B/2$ Hz. (Note : b is the low cut-off frequency of the band-pass filter.)

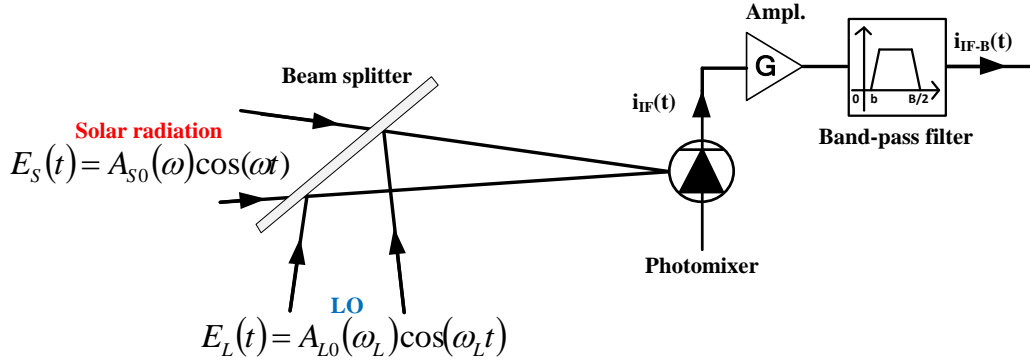


Figure 1.7 Schematic diagram of a LHR for amplifying and filtering the RF signal.

Therefore, the IF signal after the amplifier and the band-pass filter (assuming its cut-off frequency b is zero) can be expressed by [9] :

$$i_{IF-B}(t) = \frac{\eta \cdot e}{h \cdot \nu} \cdot G \cdot A_{L0}(\omega_L) A_{S0}(\omega) \cos[(\omega - \omega_L)t]$$

$$\text{when } 2\pi \cdot \nu_L - \pi \cdot B \leq \omega \leq 2\pi \cdot \nu_L + \pi \cdot B \quad (1.8)$$

where G is the gain of the amplifier. A careful choice of filter's pass-band will be discussed in Chapter 5.1.2.1 related to system noise analysis.

1.2.3 Square law detector

The square law detector is a nonlinear element whose output is proportional to the square of the input, associated with an averaging device, often a low-pass filter [10]. After RF quadratic detection, the resulting signal power P_{HET} is thus given by [9] :

$$P_{HET} \propto i_{IF-B}^2(t) = \left(\frac{\eta \cdot e}{h \cdot \nu} \right)^2 \cdot G^2 \cdot A_{S0}^2(\omega) A_{L0}^2(\omega_L) \cos^2[(\omega - \omega_L)t]$$

$$\begin{aligned}
&= 4 \cdot \left(\frac{\eta \cdot e}{h \cdot \nu} \right)^2 \cdot G^2 \cdot P_S(\omega) P_L(\omega_L) \cos^2[(\omega - \omega_L)t] \\
&= 4 \cdot \left(\frac{\eta \cdot e}{h \cdot \nu} \right)^2 \cdot G^2 \cdot P_S(\omega) P_L(\omega_L) \cdot \frac{1 + \cos[2 \cdot (\omega - \omega_L)t]}{2}
\end{aligned} \tag{1.9}$$

where $P_S(\omega) = \frac{A_{S0}^2(\omega)}{2}$ is the optical power of solar radiation, $P_L(\omega_L) = \frac{A_{L0}^2(\omega_L)}{2}$ is the LO optical power. After the averaging device (low-pass filter), the resulting signal power P_{HET} is given by :

$$P_{HET} \propto 2 \cdot \left(\frac{\eta \cdot e}{h \cdot \nu} \right)^2 \cdot G^2 \cdot P_S(\omega) P_L(\omega_L) \tag{1.10}$$

From Eq. (1.10), the following expression can be obtained :

$$P_{HET} \propto P_S(\omega) P_L(\omega_L) \tag{1.11}$$

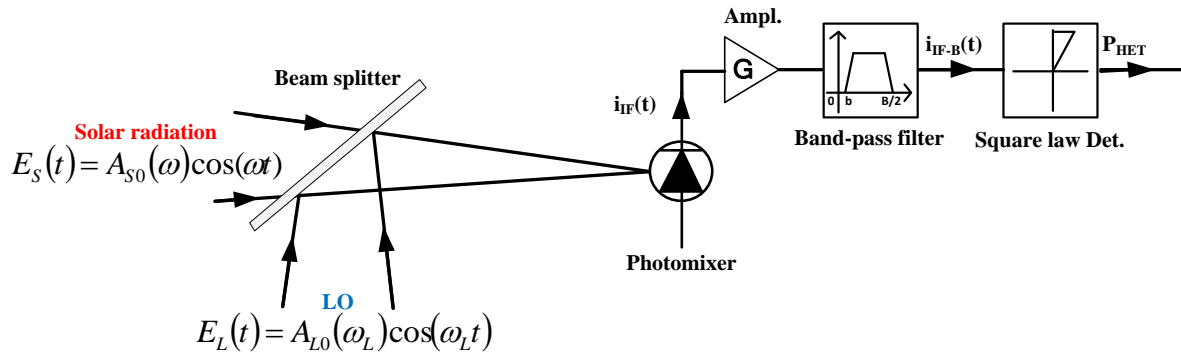


Figure 1.8 Schematic diagram of a LHR for power detection of the RF signal.

Thus, the heterodyne signal power (P_{HET}) is proportional to the product of the sunlight power ($P_S(\omega)$) and the LO power ($P_L(\omega_L)$) within the LHR instrument bandwidth B [4]. In general, the sunlight power is weak, and the LO power is several orders of magnitude greater than the sunlight. Eq. (1.11) therefore shows that heterodyne detection provides a form of amplification of the sunlight power by a gain of P_L .

1.2.4 Lock-in amplifier

In LHR, lock-in amplifier [12,13] is usually used for sensitive measurement (c.f. Fig. 1.1). The sunlight is modulated through a mechanical chopper [6,14] in free-space configuration or an optical switch [15] in fiber-coupling configuration at a modulation frequency ω_{ref} . LIA,

referenced to this frequency ω_{ref} , only detects the heterodyne signal with frequencies at the reference frequency using phase sensitive detection (PSD), noises at other frequencies are removed by a low-pass filter (with a time constant RC) in the PSD and weak heterodyne signal is then extracted from noise at this reference frequency.

The output of the LIA is proportional to the integrated P_{HET} through the transfer function of the low-pass filter in the LIA, $H(j\omega_{\text{IF}})$ as follows [6] :

$$S(\omega) \propto P_{\text{HET}} \cdot H(j\omega_{\text{IF}}) \quad (1.12)$$

As a basic approximation, we consider the RC filter model, its transfer function is well approximated by :

$$H(j\omega_{\text{IF}}) = \frac{1}{1 + j\omega_{\text{IF}}\tau} \quad (1.13)$$

where the time constant $\tau = RC$ of the low-pass filter, and the corresponding cut-off frequency $f_c = \omega_c / 2\pi = 1 / (2\pi\tau)$. Eq. (1.12) can thus be expressed by :

$$S(\omega) \propto P_{\text{HET}} \cdot H(j\omega_{\text{IF}}) \propto 2 \cdot \left(\frac{\eta \cdot e}{h \cdot \nu} \right)^2 \cdot \frac{G^2}{1 + j\omega_{\text{IF}}\tau} \cdot P_s(\omega) P_L(\omega_L) \quad (1.14)$$

Therefore, heterodyne detection allows an "amplification" of the weak incoming signal (although there is no optical amplification involved). The beat signal at the intermediate frequency within the bandwidth of the photomixer contains all spectral information, and is processed further with a RF receiver. Atmospheric species absorption spectrum can thus be recovered by scanning the LO frequency across the absorption feature.

1.3 Heterodyne efficiency

The heterodyne signal given in Eq. (1.7) is established for the ideal case of monochromatic plane waves, phase front perfectly aligned, beam spot size fully matched, and perfectly co-aligned onto the photomixer surface with their polarization state matched [16]. The general form of the heterodyne efficiency is given in Eq. (1.15), which bears similarity to overlap integrals, with the added dependence on quantum efficiency of the photomixer η , including its spatial distribution dependence [16,17].

$$\eta_{\text{het}} = \frac{\left| \int_0^{r_0} \eta(r) \cdot E_s(r) \cdot E_L^*(r) dr \right|^2}{\int_0^{r_0} \eta(r) \cdot E_L(r) \cdot E_L^*(r) dr \cdot \int_0^{r_0} E_s(r) \cdot E_s^*(r) dr} \quad (1.15)$$

where $E_L(r)$ and $E_S(r)$ are the LO and the sunlight field amplitude distributions on the photomixer with a radius of r_0 , respectively, and $\eta(r)$ is photomixer response distribution.

Therefore, the heterodyne efficiency of photomixing of the sunlight beam and the LO beam is strongly conditioned by three main criteria influencing each other including [17-20] :

- (1) Spatial distribution of the beams being mixed;
- (2) Polarization-sensitive photomixing;
- (3) Coupling of the mixed beams to the mixer.

1.3.1 Spatial distribution of the beams being mixed

The effective photomixing efficiency depends explicitly on the spatial distribution of the beams being mixed. The complete theoretical analysis of this issue has been addressed by S. C. Cohen [17] and for more particular geometries by K. Tanaka [19]. Let us take S. C. Cohen's results in the case closest to what will be ours, namely, an incoherent solar beam having an uniform distribution and a Gaussian LO beam which is linearly polarized [17].

1.3.1.1 Beam spot size

In quasi-optics, a Gaussian beam is a beam of monochromatic electromagnetic radiation whose transverse magnetic and electric field amplitude profiles are given by the Gaussian function. It implies a Gaussian intensity (irradiance) profile. Mathematical expression for the electric field amplitude is a solution to the paraxial Helmholtz equation [21]. Assuming polarization in the x direction and propagation in the +z direction, the electric field in complex notation is given by [21] :

$$E(r, z) = A_0 \cdot \hat{x} \cdot \frac{w_0}{w(z)} \cdot \exp\left(\frac{-r^2}{w(z)^2}\right) \cdot \exp\left(-i\left(k \cdot z + k \frac{r^2}{2 \cdot R(z)} - \Psi(z)\right)\right) \quad (1.16)$$

where \hat{x} is the unit vector, r is the radial distance from the center axis of the beam, z is the axial distance from the beam waist, i is the imaginary unit, $k = 2\pi/\lambda$ is the wave number (in radians per meter) for a wavelength λ , $A_0 = E(0,0)$, the electric field amplitude (and phase) at the origin at time 0, $w(z)$ is the Gaussian beam width at which the field amplitudes fall to $1/e$ of their axial values, at the plane z along the beam, $w_0 = w(0)$ is the waist size at $z = 0$, $R(z)$ is the radius of curvature of the beam's wavefronts at z , and $\psi(z)$ is the Gouy phase at z , an extra phase term beyond that attributable to the phase velocity of light. Fig. 1.9 shows a Gaussian intensity profile.

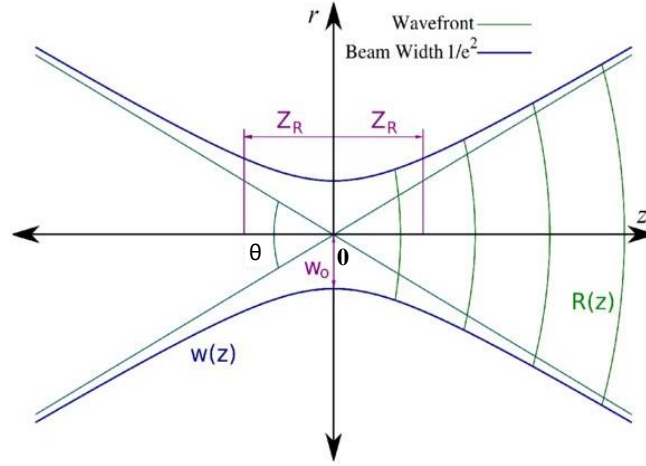


Figure 1.9 Gaussian beam width $w(z)$ as a function of the distance z along the beam. w_0 : beam waist; r : radial distance from the center axis of the beam; $R(z)$: radius of curvature of the beam's wavefronts at z ; z_R : Rayleigh range; θ : full angle divergence.

At a position z along the beam (measured from the waist), the spot size parameter $w(z)$ is given by [21]:

$$w(z) = w_0 \cdot \sqrt{1 + \left(\frac{z}{z_R}\right)^2} \quad (1.17)$$

where $z_R = \frac{\pi \cdot w_0^2}{\lambda}$ is called the Rayleigh range.

The curvature of the wavefronts is zero at the beam waist and also approaches zero as $z \rightarrow \pm\infty$. It is equal to $1/R$ where $R(z)$ is the radius of curvature as a function of position along the beam, given by [21] :

$$R(z) = z \left[1 + \left(\frac{z_R}{z}\right)^2 \right] \quad (1.18)$$

From Eqs. (1.17) and (1.18), the curvature of the wavefronts can be expressed by :

$$R(z) = \frac{\pi \cdot w^2(z)}{\lambda \cdot \sqrt{n^2 - 1}} \quad (1.19)$$

where $n = \frac{w(z)}{w_0}$.

Consider the wavefronts of two Gaussian beams (w_1, w_2 and R_1, R_2) couple on a plan P (Fig. 1.10) :

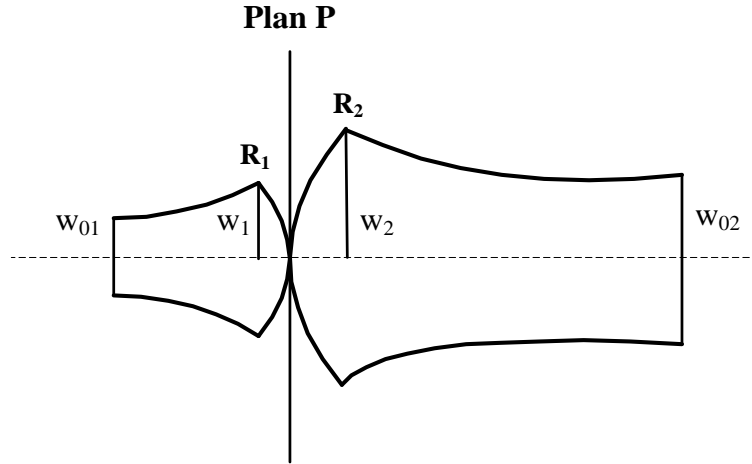


Figure 1.10 Coupling wavefronts of two Gaussian beams (R_1 , R_2 are the curvatures of the wavefronts of two Gaussian beams).

The coupling efficiency of two Gaussian beams is given by [20] :

$$K = 4 \cdot \left[\left(\frac{w_2}{w_1} + \frac{w_1}{w_2} \right)^2 + \left(\frac{\pi \cdot w_1 \cdot w_2}{\lambda} \right)^2 \cdot \left(\frac{1}{R_1} - \frac{1}{R_2} \right)^2 \right]^{-1} \quad (1.20)$$

In heterodyne experiment, the wavefronts of a Gaussian beam (w_1 , R_1) and a plane beam (w_2 , R_2) couple on a plan P (Fig. 1.11).

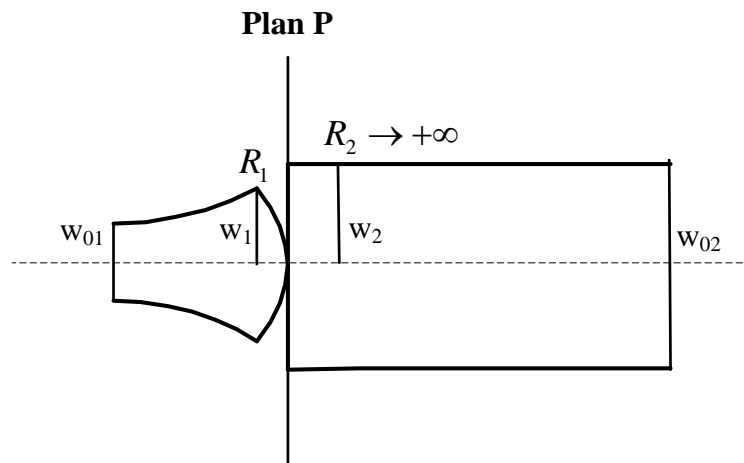


Figure 1.11 Coupling wavefronts of a Gaussian beam and a plane beam (R_2 is the curvature of the wavefront of the plane beam with $R_2 \rightarrow +\infty$).

From this perspective, the curvature R_2 of the wavefront approaches $+\infty$, so the coupling efficiency of a Gaussian beam and a plane beam can be written as :

$$K = 4 \cdot \left[\left(\frac{w_2}{w_1} + \frac{w_1}{w_2} \right)^2 + \left(\frac{w_2}{w_1} \right)^2 \cdot (n_1^2 - 1) \right]^{-1} \quad (1.21)$$

where $n_1 = \frac{w_1}{w_{01}}$ for $R_1(z) = \frac{\pi \cdot w_1^2(z)}{\lambda \cdot \sqrt{n_1^2 - 1}}$.

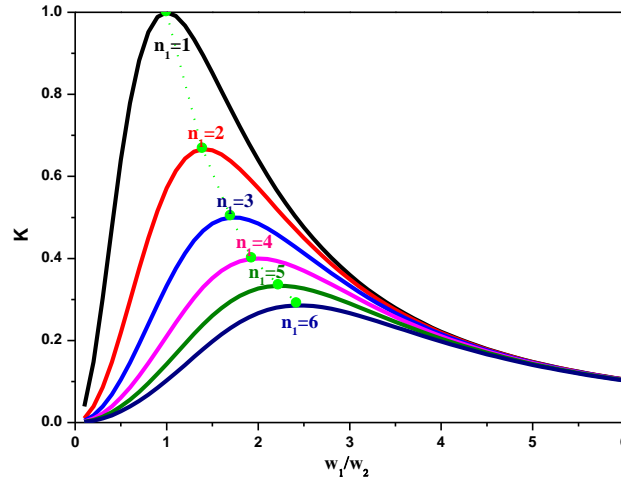


Figure 1.12 Coupling efficiency of a Gaussian beam with a plane beam.

The calculation of the coupling efficiency between a Gaussian beam and a plane beam is shown in Fig. 1.12. The maximum coupling efficiency K can be obtained when :

$$w_1 = w_2 \quad (n_1=1) \quad (1.22)$$

The condition for maximum coupling efficiency requires $w_1=w_2$ and the maximum coupling efficiency decreases as the spot size of the Gaussian beam increases, i.e. the increase of n_1 (w_1/w_{01} , Fig.1.12 *green dot*). Moreover, a larger n_1 needs a larger value of w_1/w_2 for obtaining the maximum coupling efficiency.

Therefore, for the purpose of high-efficiency heterodyne mixing of two light beams, it is necessary to make the beam sizes of the sunlight and the LO as close as possible.

1.3.1.2 Phase front alignment

The quality of the superposition of the two beams on the photomixer greatly has a significant impact on the mixing efficiency. In order to obtain a maximum light-induced photocurrent, the iso-phase planes of the solar radiation and the LO light must coincide with each other as well as the photosensitive surface of the photomixer i. e. the wavefronts of the sunlight field and the LO field must be confused such that the photocurrents induced are in phase.

The following is an analysis of the influence of the misalignment of the two beams on the coherent detection. It is assumed that both the sunlight and the LO are plane waves, and there is an angle Θ between their wavefronts, as shown in the Fig.1.13.

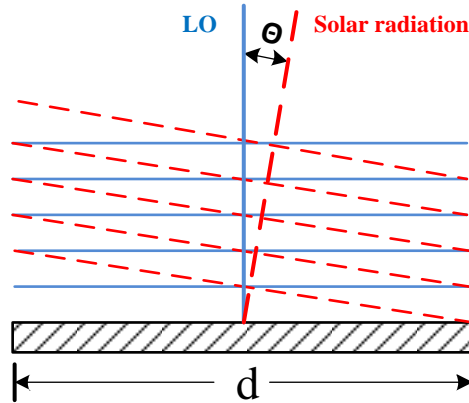


Figure 1.13 Photomixing illuminated by the solar radiation and the LO light. Phase fronts of the both beams are normal to the propagation direction.

It is assumed that the photosensitive surface of the photomixer is a square having a side length of d . In the analysis, it is assumed that the LO beam is incident in a direction perpendicular to the surface of the photomixer, so that the LO field can be written as :

$$E_L(t) = A_{L0} e^{i\omega_L t} \quad (1.23)$$

The sunlight wavefront has a mismatch angle with the LO wavefront, the beam is obliquely incident on the surface of the photomixer, and the sunlight field can be written as :

$$E_S(t) = A_{S0} e^{i\omega_S t + k \sin \Theta \cdot x} \quad (1.24)$$

let $\beta = k \sin \Theta$, then the above formula is written as :

$$E_S(t) = A_{S0} e^{i\omega_S t + \beta \cdot x} \quad (1.25)$$

The total electric field incident on the surface of the photomixer is :

$$E(t) = E_S(t) + E_L(t) \quad (1.26)$$

and the instantaneous IF photocurrent generated by the photomixer (c.f. Section 1.2.1) is written by :

$$i_{IF}(t) \propto \iint_{\frac{d}{2}, \frac{d}{2}} 2A_{L0} A_{S0} e^{i(\omega_L - \omega_S)t + \beta \cdot x} dx dy$$

$$= d^2 \cdot A_{L0} A_{S0} e^{i(\omega_L - \omega_S)t} \cdot \frac{\sin \frac{d \cdot \beta}{2}}{\frac{d \cdot \beta}{2}} \quad (1.27)$$

Because $\beta = (2 \cdot \pi / \lambda) \cdot \sin \Theta$, the magnitude of the instantaneous IF photocurrent is related to the mismatch angle Θ . Obviously when the sinc function γ :

$$\gamma = \frac{\sin \frac{d \cdot \beta}{2}}{\frac{d \cdot \beta}{2}} = 1 \quad (1.28)$$

i.e. $\Theta = 0$, the instantaneous IF photocurrent reaches a maximum value.

In practice, the mismatch angle Θ is difficult to adjust to 0. In order to get the maximum IF output as possible, it is highly desirable to set $\Theta = 0$ as possible. To satisfy this condition, it would be:

$$\frac{d \cdot \beta}{2} \ll 1 \quad (1.29)$$

i.e. $\sin \Theta \ll \frac{\lambda}{\pi \cdot d} \quad (1.30)$

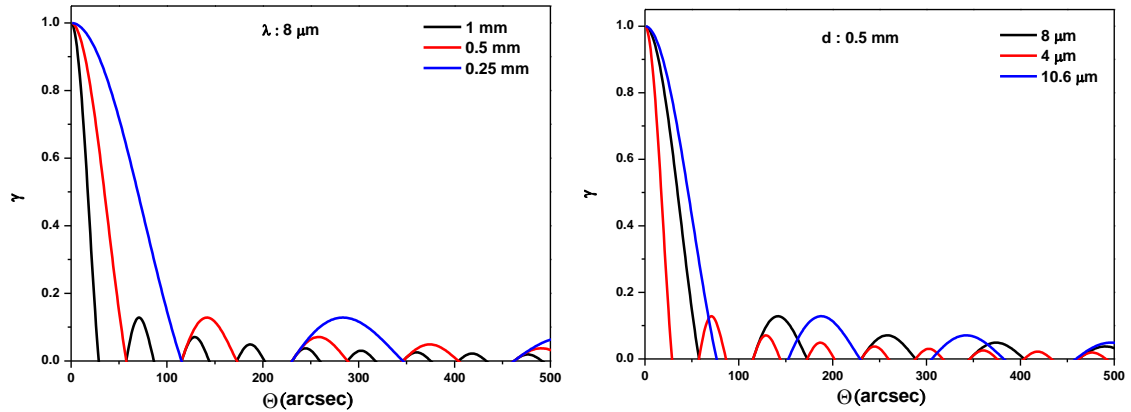


Figure 1.14 *left*: γ as a function of the mismatch angle Θ for several values d (at $\lambda=8 \mu\text{m}$); *right*: γ as a function of mismatch angle Θ for several values of λ (with $d=0.5 \text{ mm}$).

The effect of the mismatch angle on the output of the optical heterodyning is plotted in the Fig.1.14. As can be seen, the photomixing efficiency dramatically decreases with increasing the mismatch angle. A photomixer with a smaller size has a larger mismatch angle and vice versa (Fig. 1.14 *left*). The shorter the wavelength is, the stricter the angular requirement is, i.e. smaller mismatch angle is needed (Fig. 1.14 *right*). Therefore, optimal spatial alignment for heterodyne detection is highly desired. Due to this strict spatial

alignment requirement, stray light or background radiation that do not meet this requirement will not contribute to the optical heterodyning, heterodyne detection exhibits thus a good spatial filtering performance.

1.3.2 Polarization-sensitive photomixing

It is well known that the heterodyne detection is sensitive to polarization due to the fact that the beat occurs when the field component of the sunlight beam is parallel to the polarization of the LO beam [23,24]. Since we use an unpolarized/incoherent sunlight, optical power of sunlight that can contribute to the heterodyne signal is thus halved.

1.3.3 Coupling of the mixed beams to the mixer

The last criteria is the spatial distribution of the mixed light beams on the photomixer (Fig. 1.15). That is, the focusing full-angle 2θ of the incident beam should be less than the FoV of the photomixer, and the focused beam size $2\omega_0$ on the photomixer should be less than its optical receiving area.

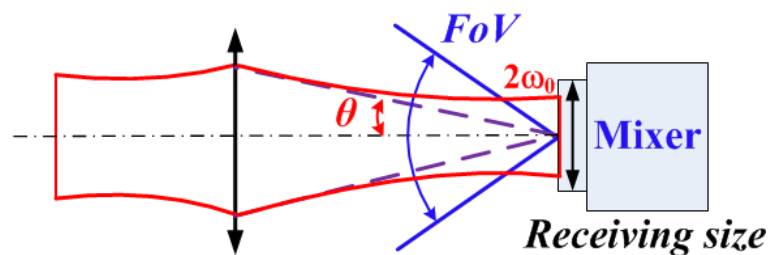


Figure 1.15 Spatial distribution of the incident beams on the photomixer.

1.4 Noise sources

SNR (signal-to-noise ratio) is the most important parameter for evaluation of the LHR sensitivity. It can be affected by system noises at the intermediate frequency. All noise currents are referred to the photomixer. The noise sources are of three types : those which are independent of LO power P_L (see 1.4.1 below), those which depend on LO power P_L (see 1.4.2 below), and those which depend on signal power P_S (see 1.4.3 below).

1.4.1 Detection chain noise

In a heterodyne system, the detection chain noises originating from a photomixer and preamplifiers, which are independent of the LO laser power (P_L), include : (1) Johnson noise, (2) Background noise, (3) Dark noise.

1.4.1.1 Johnson noise

Johnson noise is produced regardless of an applied voltage, and is generated by the random thermal agitation of electrons inside a conductor of photomixer and amplifier at equilibrium [25]. The Johnson noise in the receiver band is expressed by the mean-square noise current $\langle i_J^2 \rangle$:

$$\langle i_J^2 \rangle = 4 \cdot k \cdot B_0 \cdot \left(\frac{T_M}{R_M} + \frac{T_A}{M \cdot R_A} \right) \quad (1.31)$$

where $k = 1.38 \times 10^{-23}$ J/K is the Boltzmann; R_M and R_A are the load resistance of the photomixer and the resistance of the amplifier, respectively; T_M and T_A are the noise temperatures of the photomixer and the amplifier, respectively; M is a parameter (≤ 1) expressing an impedance mismatch between the photomixer and the amplifier [26].

When the photomixer is cooled and its Johnson noise is negligible compared with the noise from the amplification system. Eq. (1.31) can thus become :

$$\langle i_J^2 \rangle = 4 \cdot k \cdot B_0 \cdot \frac{T_A}{M \cdot R_A} \quad (1.32)$$

1.4.1.2 Background noise

Thermal radiation outside of the receiving bandwidth of the heterodyne receiver, but inside the total spectral range over which the photomixer will give a photocurrent response. On the other hand, the thermal radiation inside the receiving bandwidth of the heterodyne receiver, but outside the FoV of the heterodyne receiver will induce the photomixer to produce noise currents. It follows that the optical power spectrally and spatially outside the heterodyne receiver will affect the photomixer and generate a photocurrent. This photocurrent will not be amplified by the heterodyne detection but it provides a continuous background noise to the

detected signal. The background noise can be expressed by the mean-square noise current $\langle i_{BG}^2 \rangle$:

$$\langle i_{BG}^2 \rangle = 2 \frac{\eta \cdot e^2}{h \cdot \nu} \cdot P_B \cdot B_0 \quad (1.33)$$

where h is the Planck constant, ν is the frequency, η stands for the quantum efficiency, e is the electric charge, B_0 is the bandwidth of the photomixer, and P_B is the thermal radiation power radiating onto the photomixer.

The influence of the background noise can be reduced by the addition of spectral and spatial filters in the optical path of the thermal source and the condition $P_B \ll P_L$ is then achieved. Therefore, the background noise ($\propto P_B$) can be rendered negligible compared with laser induced-noise ($\propto P_L$, see 1.4.2).

1.4.1.3 Dark current noise

Dark current noise is a constant current which is due to the random generation of electrons and holes within the depletion region of the photomixer when no photons are incident on the photomixer [27]. The dark current noise in the photomixer is expressed by the mean-square noise current $\langle i_{DK}^2 \rangle$:

$$\langle i_{DK}^2 \rangle = 2 \cdot e \cdot i_{DK} \cdot B_0 \quad (1.34)$$

where i_{DK} is the average dark current of the photomixer.

Typically, dark current noise can be significantly reduced at low temperature and therefore can be ignored.

1.4.2 Laser-induced noise

In a heterodyne system, laser-induced noises, which depend on the laser power (P_L), include : (1) Laser-induced shot noise, (2) Coherently detected thermal noise, (3) Laser excess noise.

1.4.2.1 Laser-induced shot noise

Shot noise, also called quantum noise, is caused by fluctuations of the detected photons, which obeys Poisson statistic. In electronics shot noise originates from the discrete nature of electric charge, and in photon counting in optical devices, it is associated with the particle nature of light.

In a LHR system, laser-induced shot noise arises due to fluctuations in the rate of arrival of LO photons, but an expression for it can be obtained by considering the shot noise in the LO radiation-induced current in the photomixer [26]. This current is dominated by i_{dc} , which is the response of the photomixer to the incident LO power, so that the mean square laser-induced shot noise current $\langle i_{LSN}^2 \rangle$ is proportional to the LO power on the photomixer and is given by [11,26,28] :

$$\langle i_{LSN}^2 \rangle = 2 \cdot \left(\frac{\eta \cdot e^2}{h \cdot \nu} \right) \cdot P_L \cdot B_0 = 2 \cdot e \cdot i_{dc} \cdot B_0 \quad (1.35)$$

and
$$i_{dc} = \frac{\eta \cdot e}{h \cdot \nu} \cdot P_L \quad (1.36)$$

where h is the Planck constant, ν is the frequency, η stands for the quantum efficiency, e is the electric charge, P_L is the LO power, and B_0 is the bandwidth of the photomixer.

1.4.2.2 Coherently detected thermal noise

Radiation power from any unwanted thermal source (e.g. emission from the atmosphere in a ground-based experiment) located in the FoV of the heterodyne receiver is coherently detected and amplified by the usual heterodyne "amplification" process if within the bandwidth of the heterodyne receiver [26]. In this case, the coherently detected thermal noise must also be considered. For a thermal source of temperature T_B filling the FoV of the heterodyne receiver, the coherently detected thermal noise has the same expression as heterodyne signal (c.f. Eq. (1.10)) and it can be expressed by the mean-square noise current $\langle i_{CDT}^2 \rangle$ [11,26] :

$$\langle i_{CDT}^2 \rangle = 2 \left(\frac{\eta \cdot e}{h \cdot \nu} \right)^2 \cdot P_{TB} \cdot P_L \quad (1.37)$$

$$P_{TB} = 2h \cdot \nu \cdot \delta_B \cdot B_0 \quad (1.38)$$

and
$$\delta_B = \left(\exp \left(\frac{h \cdot \nu}{k \cdot T_B} \right) - 1 \right)^{-1} \quad (1.39)$$

Substituting Eqs. (1.38) and (1.39) into Eq. (1.37), then :

$$\langle i_{CDT}^2 \rangle = \frac{4 \cdot \eta^2 \cdot e^2}{h \cdot \nu} \cdot \delta_B \cdot P_L \cdot B_0 \quad (1.40)$$

where h is the Planck constant, ν is the frequency, η stands for the quantum efficiency, e is the electric charge, k is the Boltzmann constant, P_L is the LO power, P_{TB} is the radiation power from any unwanted thermal source, and B_0 is the bandwidth of the photomixer.

The contribution from the laser-induced shot noise (Eq. (1.35)) and the coherently detected thermal noise (Eq. (1.40)) measured at the photomixer output can thus be expressed by :

$$\langle i_{LSN}^2 \rangle + \langle i_{CDT}^2 \rangle = \frac{2 \cdot \eta \cdot e^2}{h \cdot \nu} \cdot P_L \cdot B_0 \cdot (1 + 2 \cdot \eta \cdot \delta_B) \quad (1.41)$$

if $h\nu \gg kT_B$, then $\delta_B \approx 0$, the laser-induced shot noise (quantum noise) dominates the coherently detected thermal noise, and vice versa.

In an 8 μm EC-QCL-based LHR system, the temperature of the thermal source T_B (Eq. 1.39) is usually equal to the room temperature (300 K), the radiation frequency ν is 3.75×10^{13} Hz and the quantum efficiency of the photomixer η is 0.5. In Eq. (1.41), the term $2 \cdot \eta \cdot \delta_B$ due to the coherently detected thermal noise is thus calculated to be 0.0024 which is far smaller than the term '1' resulted from the laser-induced shot noise. Therefore, coherently detected thermal noise can be neglected compared to the laser-induced shot noise in the 8 μm EC-QCL-based LHR system.

1.4.2.3 Laser excess noise

Laser excess noise depends on the transmitted laser power within the measurement bandwidth centred on the detection frequency. Both mode competition and optical feedback to the laser due to scattering from components in the optical system influence the laser excess noise. The mean square laser excess noise current $\langle i_{LEN}^2 \rangle$ is proportional to the square of the LO power on the photomixer [29] and can be expressed approximately as :

$$\langle i_{LEN}^2 \rangle \propto \left(\frac{\eta \cdot e}{h \cdot \nu} \right)^2 \cdot P_L^2 \cdot B_0 \quad (1.42)$$

where h is the Planck constant, ν is the frequency, η stands for the quantum efficiency, e is the electric charge, P_L is the LO power, and B_0 is the bandwidth of the photomixer.

1.4.3 Signal-induced noise

In a heterodyne system, the signal-induced noises, which depend on the source power (P_S), include : (1) Signal-induced shot noise, (2) Signal excess noise.

1.4.3.1 Signal-induced shot noise

In a LHR system, signal-induced shot noise arises due to fluctuations in the rate of arrival of source photons and it can be obtained by considering the shot noise in the source radiation-induced current in the photomixer [26]. This current is dominated by i_{dc}^S , which is the response of the photomixer to the incident source power, so that the mean square shot noise current $\langle i_{SSN}^2 \rangle$ is proportional to the source power on the photomixer and is given by [16,26] :

$$\langle i_{SSN}^2 \rangle = 2 \cdot \left(\frac{\eta \cdot e^2}{h \cdot \nu} \right) \cdot P_S \cdot B_0 = 2 \cdot e \cdot i_{dc}^S \cdot B_0 \quad (1.43)$$

and
$$i_{dc}^S = \frac{\eta \cdot e}{h \cdot \nu} \cdot P_S \quad (1.44)$$

where h is the Planck constant, ν is the frequency, η stands for the quantum efficiency, e is the electric charge, P_S is the source power, and B_0 is the bandwidth of the photomixer.

1.4.3.2 Signal excess noise

The signal excess noise depends on the transmitted source power within the measurement bandwidth. The mean square signal excess noise current $\langle i_{SEN}^2 \rangle$ is proportional to the square of the source power on the photomixer and is given by :

$$\langle i_{SEN}^2 \rangle \propto \left(\frac{\eta \cdot e}{h \cdot \nu} \right)^2 \cdot P_S^2 \cdot B_0 \quad (1.45)$$

where h is the Planck constant, ν is the frequency, η stands for the quantum efficiency, e is the electric charge, P_S is the source power, and B_0 is the bandwidth of the photomixer.

Comparing Eq. (1.35) with Eq. (1.43) and Eq. (1.42) with Eq. (1.45), for $P_S \ll P_L$:

$$\langle i_{SSN}^2 \rangle \ll \langle i_{LSN}^2 \rangle \quad (1.46)$$

and
$$\langle i_{SEN}^2 \rangle \ll \langle i_{LEN}^2 \rangle \quad (1.47)$$

Therefore, if LO power is high enough, the signal-induced noise can be rendered negligible.

In order to enhance sensitivity of the LHR system, i.e. to reach a shot-noise-limited performance, suppression of the laser excess noise (1.4.2.3) or/and reduction of the Johnson noise (1.4.1.1) are the best strategies. The Johnson noise (1.4.1.1) can be reduced by selecting

an appropriate detector element with a low-noise preamplifier. The laser excess noise (1.4.2.3), related to the LO power, optical feedback and mode competition, can thus be controlled by adjusting LO power. Meanwhile, to obtain the laser-induced shot-noise-limited performance in LHR system, it is necessary to increase P_L so that the Johnson noise (1.4.1.1) is far smaller than the laser-induced shot noise (1.4.2.1), that is (using Eqs. (1.32) and (1.35)) :

$$\langle i_J^2 \rangle \ll \langle i_{LSN}^2 \rangle \quad (1.48)$$

$$\text{i.e.} \quad 4 \cdot k \cdot B_0 \cdot \frac{T_A}{M \cdot R_A} \ll 2 \cdot \left(\frac{\eta \cdot e^2}{h \cdot \nu} \right) \cdot P_L \cdot B_0 \quad (1.49)$$

then the required lowest limit on P_L is given by :

$$P_L > \frac{2 \cdot k \cdot h \cdot \nu \cdot T_A}{\eta \cdot e^2 \cdot M \cdot R_A} \quad (1.50)$$

With given parameters in an 8 μm EC-QCL-based LHR system, i.e. $\nu = 3.75 \times 10^{13}$, $\eta = 0.5$, $M = 1$, $R_A = 50 \Omega$ and $T_A = 300 \text{ K}$, P_L must be greater than about 0.32 mW to ensure laser-induced shot-noise-limited operation. Meanwhile, LO power has an additional caveat that this power needs not to saturate the photomixer preamplifier either [16].

Based on the above introduction of the noise sources we are now discussing on instrument SNR and its sensitivity in the following section.

1.5 Instrument SNR and sensitivity (limit of detection, LoD)

To characterize the performance of a developed LHR, a blackbody source (with high cavity emissivity of ~ 0.99) is usually used. In this case, the BB source power P_S received by the LHR system can be calculated by [5] :

$$P_S = \frac{1}{2} \cdot \kappa \cdot I(\nu, T_S) \cdot \lambda^2 \cdot 2 \cdot B_0 \quad (1.51)$$

$$\text{and} \quad I(\nu, T) = \frac{2 \cdot h \cdot \nu^3}{c^2} \cdot \delta_S, \text{ and } \delta_S = \left(\exp\left(\frac{h \cdot \nu}{k \cdot T_S}\right) - 1 \right)^{-1} \quad (1.52)$$

From Eqs. (1.51) and (1.52), the received source power P_S can be expressed by :

$$P_S = 2 \cdot \kappa \cdot h \cdot \nu \cdot B_0 \cdot \delta_S \quad (1.53)$$

where κ is the overall optical coupling efficiency defined as the fraction of the incoming blackbody radiation passed by all the optical components in the instrument, which mainly

accounts for transmission efficiency of the optics. $I(\nu, T)$ is the Planck equation (spectral radiance) for a blackbody at temperature T_S , and λ^2 is the throughput of a single spatial mode [5]. The one-half factor gives reason for heterodyne detection is inherently a polarization dependent technique [30].

The heterodyne power obtained in the LHR system (c.f. Eq. (1.10)) is expressed by [9] :

$$\langle i_{IF}^2 \rangle = 2 \left(\frac{\eta \cdot e}{h \cdot \nu} \right)^2 \cdot P_S \cdot P_L \quad (1.54)$$

The ideal laser-induced shot-noise-limited SNR of the LHR system at the output of the photomixer preamplifier is given by :

$$SNR = \frac{\langle i_{IF}^2 \rangle}{\langle i_{LSN}^2 \rangle} = \frac{\eta \cdot P_S}{h \cdot \nu \cdot B_0} = 2 \cdot \eta \cdot \kappa \cdot \delta_S \quad (1.55)$$

From Eq. (1.55), the final SNR of the LHR signal at the output of the RF filter with the bandwidth $B/2$ ($B < B_0$) and an integration time τ is given by [9,26] :

$$SNR_{LHR} = \frac{\langle i_{IF}^2 \rangle_{B_0=B/2}}{\langle i_{LSN}^2 \rangle_{B_0=B}} \cdot \sqrt{B \cdot \tau} = \frac{\eta \cdot P_S}{h \cdot \nu} \cdot \sqrt{\frac{\tau}{B}} = \eta \cdot \kappa \cdot \delta_S \cdot \sqrt{B \cdot \tau} \quad (1.56)$$

where τ is often the time constant in case using a LIA, the theoretical SNR increases with τ .

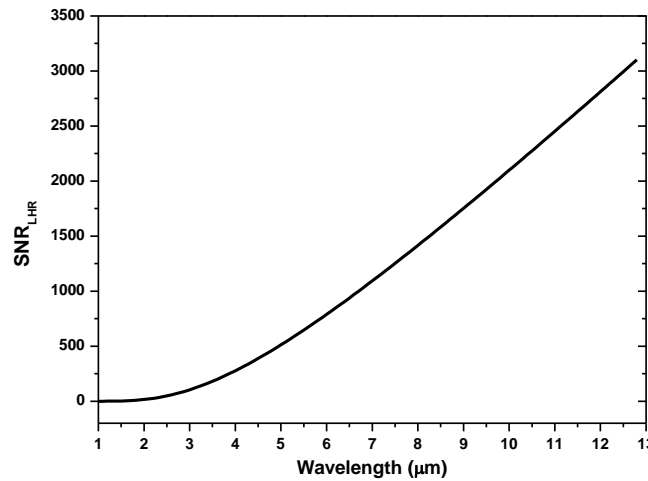


Figure 1.16 Plot of SNR for an ideal LHR vs. wavelength, calculated with a quantum efficiency η of 0.5, a temperature of blackbody radiation T of 1273 K, a bandwidth of the instrument B of 485 MHz, an integration time τ of 1 s, and an overall optical coupling efficiency of the blackbody radiation κ of 0.4.

Fig.1.16 shows ideal SNR of a LHR as a function of wavelength with 1273 K blackbody radiation, 485 MHz spectral resolution, 0.5 quantum efficiency, 1 s integration time and 0.4 overall optical coupling efficiency of the blackbody radiation. As can be seen, under this

condition, the SNR of the LHR increases with the wavelength, i.e. the mid-IR is theoretically more favorable than in the near infrared. In practice, optical losses, instabilities of the solar image on the photomixer, and atmospheric effects degrade this SNR. In LHR, in order to improve the SNR, pass-band of the RF filter must be carefully chosen to filter out low frequency noise. In addition, according to the analysis in Section 1.3.1, making spot sizes of two beams as close as possible and phase front misalignment angle as small as possible can improve effectively heterodyne efficiency (Eq. (1.15)), thus increase the actual SNR.

A noise equivalent power (NEP in W/Hz) is introduced as a measure of the sensitivity of a LHR system. Considering the source power before post-detection, the NEP corresponds to the P_S that gives a SNR of unity, i. e. Eq. (1.55) is equal to 1, in a one hertz output bandwidth [9,30,31] :

$$NEP = \frac{P_S|_{SNR=1}}{B_0} = \frac{h \cdot \nu}{\eta} \quad (1.57)$$

The sensitivity of the LHR system in terms of minimum detectable sunlight power can be defined by the limit of detection (LoD) [32]. From Eqs. (1.53) and (1.56), the LoD, $P_{S,\min}$ (in W) of the LHR can be expressed by [7,30] :

$$P_{S,\min} = \frac{P_S}{SNR_{LHR}} = \frac{h \cdot \nu}{\eta} \sqrt{\frac{B}{\tau}} \quad (1.58)$$

Assuming a quantum efficiency of 0.5 and an integration time of 1 ms, the $P_{S,\min}$ for a 8 μm QCL-based LHR at different resolutions is shown in Fig. 1.17.

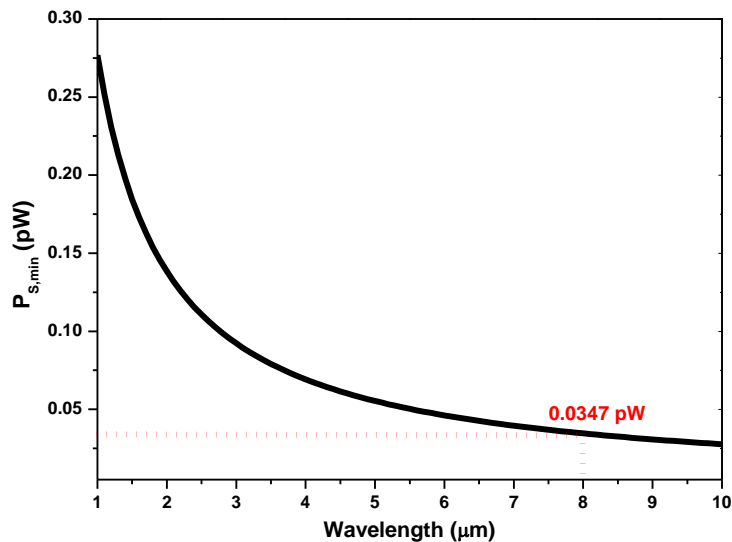


Figure 1.17 Heterodyne radiometer sensitivity to thermal radiation (bandwidth of the LHR (B): 485 MHz; integration time (τ):1 ms; quantum efficiency (η): 0.5).

When the atmosphere is transparent at a frequency corresponding to a wavelength near 8 μm , with a 485 MHz bandwidth and a 1 ms integration time, the corresponding theoretical sensitivity of the LHR to source radiation is about 0.0347 pW obtained from Fig. 1.17.

1.6 Extraction of heterodyne signal using a lock-in amplifier

In a LHR system, the heterodyne signal resulted from photomixing of a broadband incoherent sunlight with a coherent laser LO in a photomixer is proportional to the product of the intensities of the sunlight and LO. The heterodyne signal's frequency is the difference frequency between the sunlight and LO frequencies at RF frequency. Molecular spectral absorption information in the sunlight can be extracted by recording the heterodyne signal by scanning the LO frequency. The heterodyne signal can be detected with the help of lock-in amplifier.

LIA is an effective device capable of recovering weak signal buried in noise [33,34] through removing the $1/f$ noise by using modulation techniques to shift the input signal away from the base band and perform the detection at a relatively high frequency domain [35]. This is usually realized by modulating the input signal at a specific reference frequency. Phase sensitive detection is then carried out at this reference frequency for the demodulation of the modulated signal within a narrow lock-in pass-band to remove $1/f$ noise [12]. A low-pass filter with an appropriate cut-off frequency is used to extract the mean value of the amplified signal. Meanwhile, both of heterodyne spectral line-shape and spectral line center will be affected by the low-pass filter, which is determined by the LIA time constant. The details related to this issue will be discussed in the following chapters.

In LHR, the sunlight radiation modulated with a light modulator (such as mechanical chopper or optical switch) at a modulation frequency is synchronously detected by a LIA for demodulation.

The most reported LHRs using LIAs for efficiently extracting the heterodyne signal are shown in Fig. 1.18.

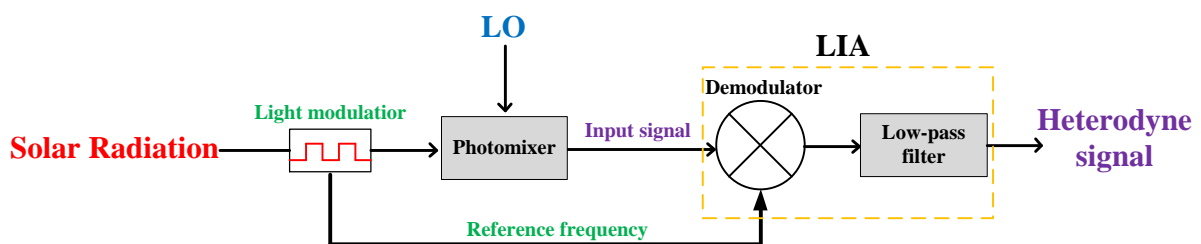


Figure 1.18 Schematic diagram of a LHR using a LIA.

In general, heterodyne signal can also be extracted using digital signal processing (DSP). AC-coupling part of the output signal from the photomixer includes total noise of the LHR system (such as detection chain noise and laser-induced noise) and heterodyne signals. In this way, a high-speed acquisition card is used to directly digitalize the output signal from the photomixer, and the heterodyne signal (σ_{Het}^2 related to P_{HET}) is extracted by subtracting the variance of the system total noises (σ_{Noise}^2) (when there is no sunlight injection) from the variance of the heterodyne signal plus system total noise (σ_{Sum}^2) (when there is sunlight injection) using DSP, that is [36] :

$$\sigma_{\text{Het}}^2 = \sigma_{\text{Sum}}^2 - \sigma_{\text{Noise}}^2 \quad (1.59)$$

1.7 Comparing the LHR with a Fourier Transform Spectrometer

It is interesting to briefly compare the LHR with a Fourier transform spectrometer, which should have large optical path differences in order to achieve a high spectral resolution (e.g. a Bruker IFS 125HR FTS (an optical path difference of 256 cm) with a spectral resolution of 0.02 cm^{-1}).

The SNR of a FTS can be expressed as [37] :

$$SNR_{\text{FTS}} = \frac{I(\nu, T) \cdot U \cdot \xi \cdot B \cdot D^* \cdot \sqrt{\tau}}{\sqrt{A_D}} \quad (1.60)$$

where U is the FTS throughput, ξ is the efficiency, B is the resolution, D^* is the detectivity, and A_D is the physical area of the detector element. Dividing the SNR_{LHR} (Eq. (1.56)) by the SNR for the FTS, quantitative comparison between them can be realized by :

$$\frac{SNR_{\text{LHR}}}{SNR_{\text{FTS}}} = \left(\frac{1}{2 \cdot h \cdot c} \cdot \frac{\sqrt{A_D}}{U \cdot \xi \cdot D^*} \cdot \eta \cdot \kappa \right) \cdot \frac{\lambda^3}{\sqrt{B}} \quad (1.61)$$

The term in the bracket is a constant related to the system parameters, and the term out of the bracket shows that LHR is more preferable at longer wavelength and higher resolution (smaller B). Typical specifications for a commercial FTS operating at a wavelength of $10 \text{ }\mu\text{m}$, are : $A_D = 1 \text{ mm}^2$, $U = 0.01 \text{ cm}^2 \text{ sr}$, $\xi = 0.1$, and $D^* = 8 \times 10^{10} \text{ cm} \sqrt{\text{Hz}} \text{ W}^{-1}$, and assuming an ideal LHR with a quantum efficiency η of 1 and an overall optical coupling efficiency of the source radiation κ of 1, the quantitative comparison between them in the resolution ranging from 30 MHz to 360 MHz is plotted in Fig.1.19. It shows that with the given conditions, an

ideal LHR at wavelengths longer than 7.7 μm and resolutions below 200 MHz has a greater SNR than a FTS.

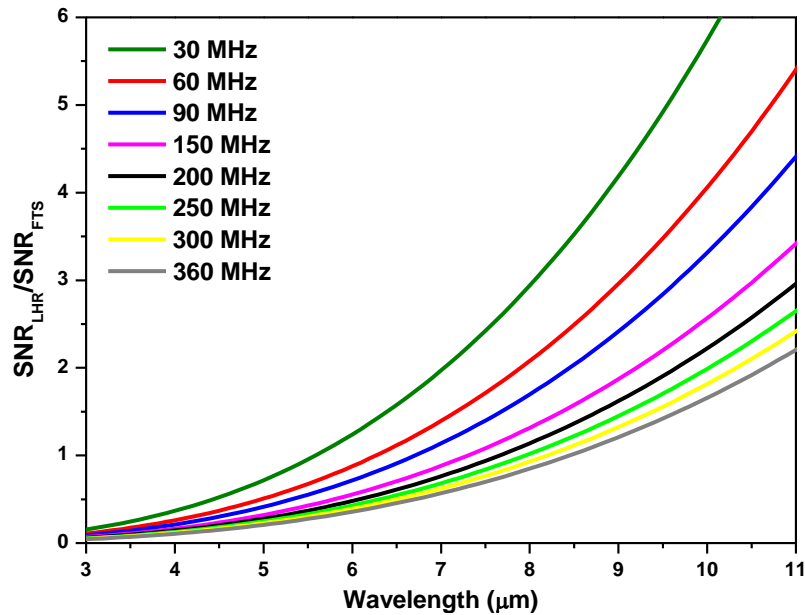


Figure 1.19 Quantitative comparison between SNR_{LHR} and SNR_{FTS} .

1.8 From atmospheric column absorption spectrum to vertical profile concentration

The atmospheric transmission spectrum obtained by the ground-based measurement (Fig. 1.20 (b)) is the integrated transmission spectrum from all species along the optical path in the atmosphere (Fig. 1.20 (a)). The measured atmospheric transmission spectrum contains information on the height distribution of the absorber up to altitudes (typically 35 km) [38] at which Doppler effects overwhelm pressure broadening. It is possible to retrieve trace gas abundance at different altitudes (Fig. 1.20 (c)) using a retrieval algorithm, given a decent knowledge of additional atmospheric parameters, such as solar angle, atmospheric temperature and pressure, atmospheric composition, and refractive index [2].

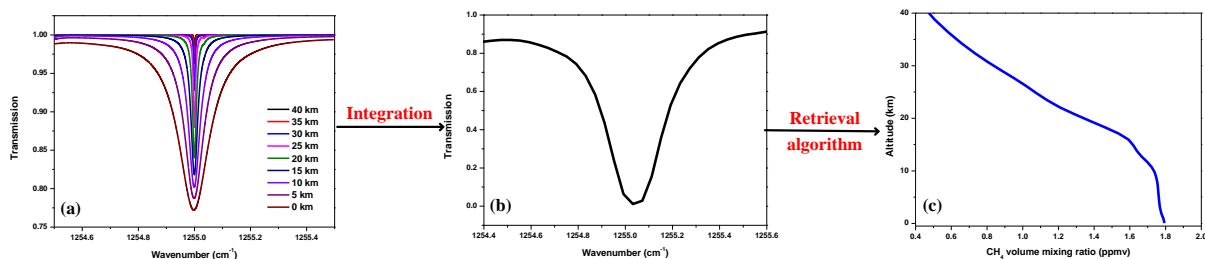


Figure 1.20 (a) Calculated CH_4 absorption spectra at different altitudes in the infrared range of 1254.5-1255.5 cm^{-1} ; (b) Atmospheric transmission spectrum of CH_4 obtained by integrating spectra in (a); (c) Vertical concentration profile of atmospheric CH_4 at the location of TCCON-Paris station (WACCM model (Whole Atmosphere Community Climate Model) [39]). (Note : all Figures here are only used for schematic diagrams).

1.8.1 Retrieval principle

The retrieval algorithm is generally composed of two parts : atmospheric radiative transfer forward model and inversion method in atmospheric vertical profile .

1.8.1.1 Atmospheric radiative transfer forward model

In order to retrieve vertical concentration profiles of atmospheric trace gases, atmospheric radiative transfer equation (RTE) has to be applied. Because an exact analytic solution for RTE in most of the cases cannot be found under realistic atmospheric medium and multiple-scattering effects, a radiative transfer forward model has to be developed to get the analytic solution. The most known forward models are 6sSecond Simulation of the Satellite Signal in the Solar Spectrum (6S) [40], MODerate resolution TRANsmittance code (MODTRAN), and Line-By-Line Radiative Transfer Model (LBLRTM) based on Fast Atmospheric Signature CODE (FASCODE), etc [41].

The spectrum measured by the ground-based measurement has a high spectral resolution ($\sim 0.001 \text{ cm}^{-1}$), the forward model used for calculating an atmospheric theoretical spectrum should have a same or higher spectral resolution than the measured spectrum. Therefore, LBLRTM with a higher spectral resolution of less than 0.001 cm^{-1} [42,43] is desirable.

1.8.1.2 Inversion method in atmospheric vertical profile

The data retrieval is performed employing the optimal estimation method (OEM), introduced by C. D. Rodgers [48,49], in which the Bayesian statistics theorem is used to find the Gaussian probability distribution function (PDF) of the state of interest. The atmospheric transmission spectrum of the solar radiance can be calculated using a radiative transfer model $F(x)$, called forward model, which describes the instrumental output by considering the atmospheric transmission spectrum of the solar radiance and the instrumental model. The relationship between pre-processed measured data and the atmospheric state vectors is described as :

$$y = F(x, a, b, c) + \varepsilon \quad (1.62)$$

Where y is the measurement vector, i.e. atmospheric transmission spectrum measured with the ground-based measurement; x is the state vector, considered in the forward calculation; ε is the measurement error vector; A second order polynomial baseline (with coefficients of a , b and c) represents the non-selective absorption and uncorrected power contributions in the target spectral region [50].

To solve for x in Eq. (1.62), the OEM data retrieval algorithm uses an iterative Levenberg-Marquardt [51-53] approach to minimize the cost function, χ^2 , which is a measure of the convergence of the fit with the measured data and the a priori knowledge, as defined in the following equation [54] :

$$\chi^2 = (y - F(x_i))S_\varepsilon^{-1}(y - F(x_i))^T + (x_a - x_i)S_a^{-1}(x_a - x_i)^T \quad (1.63)$$

where x_a is a priori state vector with an a priori covariance matrix S_a based on the error definitions, x_i is the state vector at the i th iteration, and S_ε is the measurement error covariance matrix based on the standard deviation of the measurement vector. The iterative state vector x_{i+1} is calculated using the following equation :

$$x_{i+1} = x_i + \left[(1 + \lambda)S_a^{-1} + K_i^T S_\varepsilon^{-1} K_i \right]^{-1} \times \left[K_i^T S_\varepsilon^{-1} (y_i - F(x_i)) + S_a^{-1} (x_a - x_i) \right] \quad (1.64)$$

where K is the Jacobian matrix (or weighting functions) describing the sensitivity of the forward model to the state vector, and λ is the LM parameter.

A flow chart for data retrieval is shown in Fig. 1.21, with the inputs of atmospheric parameters (i.e. vertical profiles of pressure, temperature, H₂O continuum, and atmospheric species) [44,45], the spectroscopic parameters (i.e. line position, line intensity, pressure line shift, and broadening parameters [46] those can be taken from the HITRAN 2016 database), the instrument parameters (i.e. noise performance, gain, and the ILS function), *a priori* state vector (i.e. an initial guess for the vertical profiles of target species that can be taken from ECMWF (European Center for Medium Range Weather Forecasts) [47] or WACCM), and solar position (i.e. zenith angle for ray trace path calculation), the atmospheric transmission spectrum of the solar radiance (y_0) combined with a baseline and the corresponding weighting function (K) are calculated by the forward model. In the inversion model (OEM), given the measured and pre-processed measured spectrum (y), the a priori covariance matrix (S_a), and the error covariance matrix (S_ε), the forward model is iteratively called to minimize the cost function χ^2 (Eq. (1.63)) following LM algorithm (Eq. (1.64)). In a well-conditioned retrieval, the ultimate cost function (χ^2) should be close to the number of the measurement vector and the inversion program will yield a vertical concentration profile of target gas in the atmospheric column.

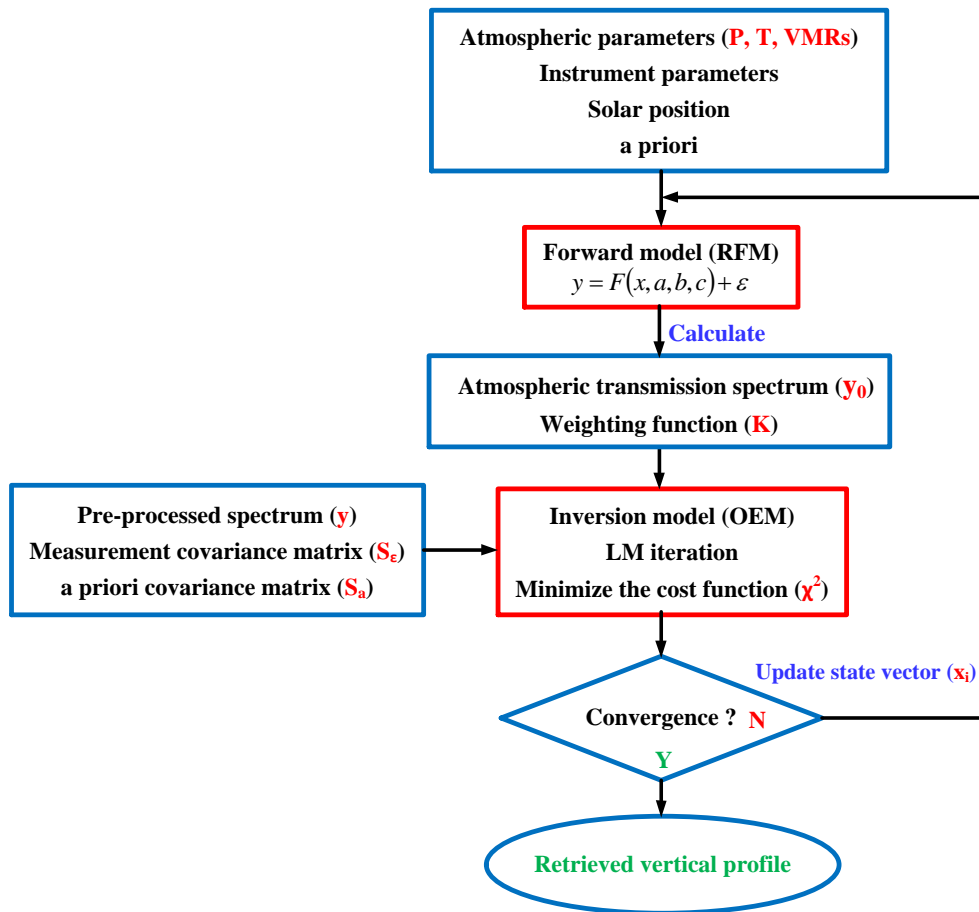


Figure 1.21 Flow chart of the data retrieval. VMRs : volume mixing ratios; LM : Levenberg-Marquardt [50].

1.8.2 Baseline treatment

The solar spectra obtained by the measurement system include system background baseline, in order to obtain an absolute atmospheric absorption spectrum for retrieving vertical profile, the system background baseline should be determined.

In case of known regular laser scanning waveform (sine waveform or rectangular waveform), the baseline in the absence of absorption can be estimated

(1) by selecting spectral points excluding absorption peaks and fitting these points with polynomial function;

(2) by fitting a baseline from near-by, non-absorbing wavelengths [14];

(3) in case of LHR baseline treatment, using a wavelength-modulated (WM) LO laser can (i) provide baseline-free spectra, a superior SNR (so lower limits of detection), and better precision and consistency than the conventional approach; (ii) open the door for cost-efficient wide spectral range LHR in the near future [55,56].

1.8.3 Vertical resolution

One of the basic parameters in an algorithm for atmospheric profile retrieval concerns the vertical resolution that is a measure of the smallest altitude over which an independent information can be obtained by the measurement system. In order to estimate the vertical resolution of the measurement system, an important quantity of the retrieval describing the sensitivity of the retrieved state x to the true state vector x_t , i.e. averaging kernel (AK) matrix A is considered [57] :

$$A = \frac{\partial x}{\partial x_t} = \left[(S_a^{-1} + K^T S_\varepsilon^{-1} K)^{-1} K^T S_\varepsilon^{-1} \right] K \quad (1.65)$$

Width of the AK can provide the vertical resolution of the measurement system at a certain altitude and it can be quantified using a spread function, which is well defined by G. Backus and F. Gilbert [58] and expressed by :

$$s(z) = 12 \frac{\int (z - z')^2 A^2(z, z') dz'}{\left(\int A(z, z') dz' \right)^2} \quad (1.66)$$

Substituting Eq. (1.65) into Eq. (1.66), the width of the AK at altitude z can be estimated [57], therefore the vertical resolution of the retrieval is obtained.

The vertical resolution is closely associated with SNR and spectral resolution of the measurement system [59]. The system SNR influences the error covariance matrix S_ε which is used for estimating the width of AK (c.f. Eq. (1.65)), thereby influencing the vertical resolution estimated by the width of AK. The spectral resolution of the measurement system influences the width of the weighting function (K) used in the retrieval algorithm, thereby affecting the vertical resolution generated by the algorithm. In addition, as the spectral resolution increases (instrument bandwidth (B) decreases), the SNR decreases (c.f. Eq. (1.56)). In a realistic measurement system, a compromise between the spectral resolution and SNR should be made to achieve a vertical resolution as high as possible.

Conclusion

In this chapter, the principle of LHR has been presented. Through heterodyne detection, atmospheric absorption spectrum can be recovered by scanning the LO frequency across the absorption feature. Then, the heterodyne efficiency of two light beams in free-space LHR dependant on three optical criteria has been discussed in detail. The high heterodyne efficiency of the LO beam and sunlight beam can be obtained when phase fronts are perfectly

aligned, beam spot sizes are fully matched, and beams are perfectly co-aligned onto the photomixer surface with their polarization state matched. Based on the analysis of the three major noise sources in a LHR, the LO power conditions for shot-noise-dominated heterodyne detection, shot-noise-dominated SNR and the corresponding instrument sensitivity have been discussed. SNR comparison of instrumental performance in terms of SNR between the LHR and the FT-IR has been made and it illustrates that the theoretical SNR of the LHR is more preferable over that of the FT-IR instrument at longer wavelengths and higher spectral resolutions with the given system condition. At the end of this chapter, vertical profile retrieval algorithm for retrieving vertical concentration profile from the measured atmospheric spectrum as well as the vertical resolution have been briefly described.

In the next chapter, practical instrumental considerations and the specifications of the devices involved in the LHR will be introduced and discussed.

References

- [1] D. Crisp, B. M. Fisher, C. O'Dell, C. Frankenberg, R. Basilio, H. Bösch, L. R. Brown, R. Castano, B. Connor, N. M. Deutscher, A. Eldering, D. Griffith, M. Gunson, A. Kuze, L. Mandrake, J. McDuffie, J. Messerschmidt, C. E. Miller, I. Morino, V. Natraj, J. Notholt, D. M. O'Brien, F. Oyafuso, I. Polonsky, J. Robinson, R. Salawitch, V. Sherlock, M. Smyth, H. Suto, T. E. Taylor, D. R. Thompson, P. O. Wennberg, D. Wunch, and Y. L. Yung. The ACOS CO₂ retrieval algorithm-Part II : Global XCO₂ data characterization, *Atmos. Meas. Tech.* 2012, **5**, 687-707.
- [2] A. Kuze, H. Suto, K. Shiomi, T. Urabe, and M. Nakajima. Level 1 algorithms for TANSO on GOSAT : processing and on-orbit calibrations, *Atmos. Meas. Tech.* 2012, **5**, 2447-2467.
- [3] A. E. Siegman. The antenna properties of optical heterodyne receivers, *Appl. Opt.* 1966, **5**, 1588-1594.
- [4] T. Kostiuik and M. J. Mumma. Remote sensing by IR heterodyne spectroscopy, *Appl. Opt.* 1983, **22**, 2644-2654.
- [5] D. Weidmann, W. J. Reburn, and K. M. Smith. Ground-based prototype quantum cascade laser heterodyne radiometer for atmospheric studies, *Rev. Sci. Instrum.* 2007, **78**, 073107.
- [6] H. R. Melroy, E. L. Wilson, G. B. Clarke, L. E. Ott, J. Mao, A. K. Ramanathan, and M. L. McLinden. Autonomous field measurements of CO₂ in the atmospheric column with the miniaturized laser heterodyne radiometer (Mini-LHR), *Appl. Phys. B* 2015, **120**, 609-615.
- [7] R. T. Menzies. In laser monitoring of the atmosphere edited by E. D. Hinkley, Springer, Berlin, 1976.
- [8] T. Tsai. External cavity quantum cascade lasers for spectroscopic applications (Doctoral dissertation), Princeton, NJ : Princeton University, 2012.
- [9] D. Weidmann. Radiometrie heterodyne infrarouge par diode laser accordable (Doctoral dissertation), Reims University, Reims, France, 2002.
- [10] D. Whitlow. IF / LO Subsystems, Research Experiences for Undergraduates (REU), 2011.
- [11] B. Parvitte, V. Zéninari, C. Thiébeaux, A. Delahaigue, D. Courtois. Infrared laser heterodyne systems, *Spectrochimica Acta Part A* 2004, **60**, 1193-1213.
- [12] SRS : About Lock-in amplifiers. Available online: <http://www.thinksrs.com/downloads/PDFs/ApplicationNotes/AboutLIAs.pdf>.

- [13] J. Masciotti, J. Lasker, A. Hielscher. Digital lock in detection for discriminating multiple modulation frequency with high accuracy and computational efficiency. *IEEE Trans. Instrum. Meas.* 2008, **57**, 182-189.
- [14] E. L. Wilson, M. L. McLinden, and J. H. Miller. Miniaturized laser heterodyne radiometer for measurements of CO₂ in the atmospheric column, *Appl. Phys. B* 2014, **114**, 385-393.
- [15] E. L. Wilson, A. J. DiGregorio, V. J. Riot, M. S. Ammons, W. W. Bruner, D. Carter, J. Mao, A. Ramanathan, S. E. Strahan, L. D. Oman, C. Hoffman, and R. M. Garner. A 4 U laser heterodyne radiometer for methane (CH₄) and carbon dioxide (CO₂) measurements from an occultation-viewing CubeSat, *Meas. Sci. Technol.* 2017, **28**, 035902.
- [16] H. Niwuwenhuijzen. Photo-electric mixing of coherent and incoherent light, *Bull. Astr. Inst. Netherlands*, 1967, **19**, 391-404.
- [17] S. C. Cohen. Heterodyne detection : phase front alignment, beam spot size, and detector uniformity, *Appl. Opt.* 1975, **14**, 1953-1959.
- [18] O. Andrade and B. J. Rye. Tolerances in optical mixing, *J. Phys. D. Appl. Phys.* 1974, **7**, 280-291.
- [19] K. Tanaka and N. Ohta. Effects of tilt and offset of signal field on heterodyne efficiency, *Appl. Opt.* 1987, **26**, 627-632.
- [20] D. Fink. Coherent detection signal-to-noise, *Appl. Opt.* 1975, **14**, 689-690.
- [21] M. A. Bandres and J. C. Gutiérrez-Vega. Ince-Gaussian beams, *Opt. Lett.* 2004, **29**, 144-146.
- [22] W. Chen, R. Rocquet, J. Burie, and D. Boucher. Gaussian optical design of a submillimeter-wave and far-infrared laser sideband heterodyne spectrometer, *Int. J. IR & Milli. Waves* 1997, **18**, 217-232.
- [23] A. E. Siegman. The antenna properties of optical heterodyne receivers, *Proc. IEEE* 1966, **54**, 1350-1356.
- [24] A. Waksberg. Field of view increase for optical heterodyne receivers, *Int. J. IR & Milli. Waves* 1999, **20**, 1059-1071.
- [25] J. B. Johnson. Thermal agitation of electricity in conductors, *Phys. Rev.* 1928, **32**, 97-109.
- [26] T. G. Blaney. Signal-to-noise ratio and other characteristics of heterodyne radiation receivers, *Space Sci. Rev.* 1975, **17**, 691-702.
- [27] R. Hui and M. O'Sullivan. Fiber optic measurement techniques, *ScienceDirect*, 2009,

ISBN: 978-0-12-373865-3, <https://doi.org/10.1016/B978-0-12-373865-3.X0001-8>.

- [28] R. L. Passmore. The development of an infrared laser heterodyne radiometer to search for methane in the atmosphere of Mars, Second Year Report, 2010.
- [29] Y. Wang, M. Nikodem, and G. Wysocki. Cryogen-free heterodyne-enhanced mid-infrared Faraday rotation spectrometer, *Opt. Express* 2013, **21**, 740-755.
- [30] M. M. Abbas, M. J. Mumma, T. Kostiuik, and D. Buhl. Sensitivity limits of an infrared heterodyne spectrometer for astrophysical applications, *Appl. Opt.* 1976, **15**, 427-436.
- [31] Relative intensity noise of distributed feedback laser, Application note, eagleyard Photonics GmbH, Berlin, Germany.
- [32] R. T. Menzies and M. T. Chahine. Remote atmospheric sensing with an airborne laser absorption spectrometer. *Appl. Opt.* 1974, **13**, 2840-2849.
- [33] J. H. Scofield. Frequency domain description of a lock-in amplifier, *Am. J. Phys.* 1994, **62**, 129-133.
- [34] G. Wang, S. Rebou, J. Choque, E. Fertein, and W. Chen. Circular regression-based dual-phase lock-in amplifier for coherent recovery of weak signal, *Sensors* 2017, **17**, 2615-2630.
- [35] R. Burdett. Handbook of measuring system design; John Wiley and Sons Inc.: Chichester, UK, 2005.
- [36] A. Klimchuk, A. Nadezhdinskii, Ya. Ponurovskii, Yu. Shapovalov, and A. Rodin. On the possibility of designing a high-resolution heterodyne spectrometer for near-IR range on the basis of a tunable diode laser, *Quantum Electron.* 2012, **42**, 244-249.
- [37] P. R. Griffiths and J. A. de Haseth. Fourier transform infrared spectrometry, Wiley, New York, 1986.
- [38] R. T. Menzies and R. K. Seals. Ozone monitoring with an infrared heterodyne radiometer, *Science* 1977, **197**, 1275-1277.
- [39] <https://www.acom.ucar.edu/waccm/forecast/>
- [40] E. F. Vermote, D. Tanre, J. L. Deuze, M. Herman, J. J. Morcrette, and S. Y. Kotchenova. Second Simulation of a Satellite Signal in the Solar Spectrum-Vector (6SV), 6S User Guide Version, 2006, Available online at : http://6s.ltdri.org/files/tutorial/6S_Manual_Part_1.pdf.
- [41] F. Callieco and F. Dell'Acqua. A comparison between two radiative transfer models for atmospheric correction over a wide range of wavelengths, *Int. J. Remote Sens.* 2011, **32**, 1357-1370.

- [42] S. A. Clough, M. W. Shephard, E. J. Mlawer, J. S. Delamere, M. J. Iacono, K. Cady-Pereira, S. Boukabara, and P. D. Brown. Atmospheric radiative transfer modeling : a summary of the AER codes, Short Communication, *J. Quant. Spectrosc. Radiat. Transfer* 2005, **91**, 233-244.
- [43] S. A. Clough and M. J. Iacono. Line-by-line calculations of atmospheric fluxes and cooling rates II: Application to carbon dioxide, ozone, methane, nitrous oxide, and the halocarbons, *J. Geophys. Res.* 1995, **100**, 16519-16535.
- [44] <http://www.ecmwf.int>.
- [45] S. A. Clough, M. W. Shephard, E. J. Mlawer, J. S. Delamere, M. J. Iacono, K. Cady-Pereira, S. Boukabara, and P. D. Brown. Atmospheric radiation transfer modelling: A summary of the AER codes, short communication, *J. Quant. Spec. Radiat. Transfer* 2005, **91**, 233-244.
- [46] L. S. Rothman, I. E. Gordon, A. Barbe, D. C. Benner, P. F. Bernath, M. Birk, V. Boudon, L. R. Brown, A. Campargue, J. P. Champion, K. Chance, R. R. Gamache, A. Goldman, D. Jacquemart, I. Kleiner, N. Lacome, W. Lafferty, O. V. Naumenko, A. V. Nikitin, J. Orphal, V. I. Perevalov, A. Perrin, A. Predoi-Cross, C. P. Rinsland, M. Rotger, M. Simeckova, M. A. H. Smith, K. Sung, S. A. Tashkun, J. Tennyson, R. A. Toth, A. C. Vandaele, J. V. Auwera. The HITRAN 2008 molecular spectroscopic database, *J. Quant. Spec. Radiat. Transfer* 2009, **110**, 533-572.
- [47] European Centre for Medium-range Weather Forecasts, “ECMWF data archive services,” <http://www.ecmwf.int/products/data/archive/>.
- [48] C. D. Rodgers. A general error analysis for profile retrieval, *RSRM87*, Advances in remote sensing retrieval methods, Deepak, 1987, 285-297.
- [49] C. D. Rodgers. Characterization and error analysis of profile retrieved from remote sensing measurements, *J. Geophys. Res.* 1990, **95**, 5587-5595.
- [50] J. Wang, G. Wang, T. Tan, G. Zhu, C. Sun, Z. Cao, X. Gao, and W. Chen. Mid-infrared laser heterodyne radiometer (LHR) based on a 3.53 μm room-temperature interband cascade laser, *Opt. Express* 2019, **27**, 9610-9619.
- [51] K. Levenberg. A method for the solution of certain non-linear problems in least squares, *Q. Appl. Math.* 1944, **2**, 164-168.
- [52] D. W. Marquardt. An algorithm for the least-squares estimation of nonlinear parameters, *J. Soc. Indust. Appl. Math.* 1963, **11**, 431-441.
- [53] H. D. Mittelmann. The least squares problem. <http://plato.asu.edu/topics/problems/nlolsq.html>, Jul. 2004. [Accessed on 4 Aug. 2004].

- [54] D. Weidmann, W. J. Reburn, and K. M. Smith. Retrieval of atmospheric ozone profiles from an infrared quantum cascade laser heterodyne radiometer : results and analysis, *Appl. Opt.* 2007, **46**, 7162-7171.
- [55] P. Mart ín-Mateos, O. E. Bonilla-Manrique, and C. Guti érez-Escobero. Wavelength modulation laser heterodyne radiometry, *Opt. Lett.* 2018, **43**, 3009-3012.
- [56] P. Mart ín-Mateos, A. Genner, H. Moser, and B. Lendl. Implementation and characterization of a thermal infrared laser heterodyne radiometer based on a wavelength modulated local oscillator laser, 2019, **27**, 15575-15584.
- [57] C. D. Rodgers. Inverse methods for atmospheric sounding : Theory and Practice, vol. 2 of Atmos. Oceanic Planet. Phys. World Sci. Hackensack, NY, 2000.
- [58] G. Backus and F. Gilber. Uniqueness in the inversion of inaccurate gross earth data, *Philos, Trans. Royal. Soc. A*, 1970, **266**, 123-192.
- [59] F. Wang, J. Li, T. J. Schmit, and S. A. Ackerman. Trade-off studies of a hyperspectral infrared sounder on a geostationary satellite, *Appl. Opt.* 2007, **46**, 200-209.

Chapter 2 Mid-IR LHR instrumental consideration and configuration

Objective

In this chapter, practical instrumental considerations and specifications of the devices involved in our mid-IR LHR system (Fig. 2.1) are introduced and discussed.

Two systems for sunlight collection to the LHR receiver, including : (1) free-space telescope system, and (2) fiber coupling system, will be presented as well.

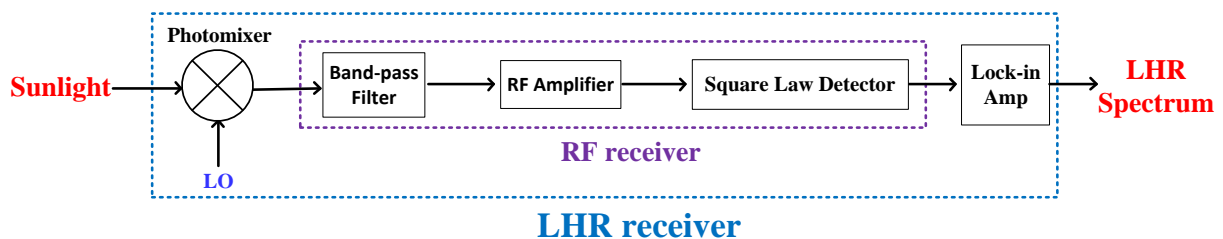


Figure 2.1 Schematic diagram of a typical LHR system.

2.1 Key devices involved in a mid-IR LHR

2.1.1 Sun-tracker

Sun-tracker system is usually used in a LHR instrument to real-time follow the movement of the Sun for sunlight collection. The tracking mechanism of a sun-tracker is generally depicted in Fig. 2.2. The sun-tracker mainly composes of a servo system (including a 4-quadrant detector [1] (or a camera [2]) and a servo control loop), a zenith stepping motor (adjusting zenithal angle θ_2) and an azimuth stepping motor (adjusting azimuthal rotation angle θ_1).

During initial operation, the zenith and azimuth stepping motors coarsely point the tracker to the calculated position of the Sun (through a solar position algorithm based on the local GPS coordinates and time of day). Then a 4-quadrant detector generates an error signal as a result of an unbalanced solar power distribution and different sunlight beam shapes on four identical photodiodes which compose the 4-quadrant detector [3]. The servo control loop uses this error signal to drive the two stepping motors to center the Sun's spot on the center of the 4-quadrant photodetector with the help of an optical system consisting of two elliptical plane mirror 1 (M1) and mirror 2 (M2), as indicated in Fig. 2.2, in the sun-tracker. The zenithal and

azimuthal angles are considered correct when the center of the Sun's spot is consistent with the center of the 4-quadrant photodiode.

Accurate and precise tracking of the Sun is required for remote sensing of the atmosphere in order to avoid significant bias at the data retrieval stage. Indeed, the retrieval of vertical profile of trace gas from an observed solar transmission spectrum is highly sensitive to the effective air mass sounded [4]. For LHR measurement it is also necessary to keep a stable sunlight power. So the center of the Sun's spot must be perceived on the servo system for a precise tracking, that is, the FoV of the sun-tracker is larger than the Sun's angular diameter ($\alpha = 9 \text{ mrad}$), as shown in Fig. 2.2. Therefore, a sun-tracker with a high tracking accuracy and a large FoV is preferable.

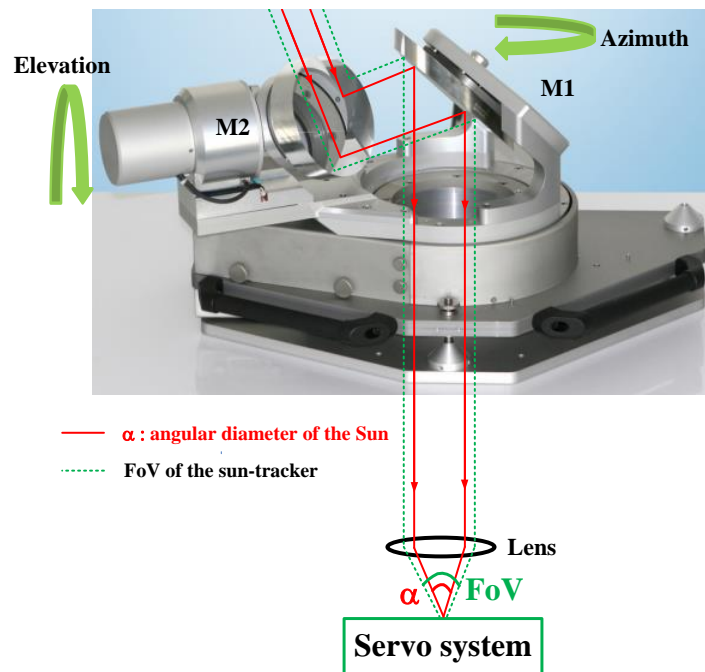


Figure 2.2 Schematic of sun tracker.

Three kinds of sun-trackers commercially available can be potentially used :

(1) Cimel sunphotometer (CSPHOT-CE318)

CSPHOT-CE318 sun-photometer (Fig. 2.3 left) is a multi-channel, automatic sun-and-sky scanning radiometer with a tracking accuracy of 0.1° and a FoV of 1.2° (determined by the design of the internal sun-viewing-collimator, as shown in Fig. 2.3 left). A 4-quadrant detector precisely updates, with the help of a feedback control loop, the sun-tracker's position. Wilson and co-worker from NASA installed sunlight collection optics for the LHR (Fig. 2.3 right) on the sun-tracker, and the optical axis of the sunlight collection optics is parallel to

that of the sun-viewing-collimator. They used this sun-photometer as sun-tracker to follow the Sun in order to collect sunlight for their near-IR-LHR system (Fig. 2.3 *right*) [5].



Figure 2.3 *left*: CSPHOT sun-photometer; *right*: sunlight collection optics (circled by *green dotted line*) installed on the CSPHOT sun-photometer, involved in NASA's near-IR-LHR setup.

(2) Bruker A547N Solar Tracker

The Bruker A547N Solar Tracker consists of an optical collection system including two plane elliptical mirrors (M1 and M2) held in 45 degrees relative to the vertical (Fig. 2.4), facing each other. The sunlight is reflected into the servo system and spectrometer for applications by these two mirrors.

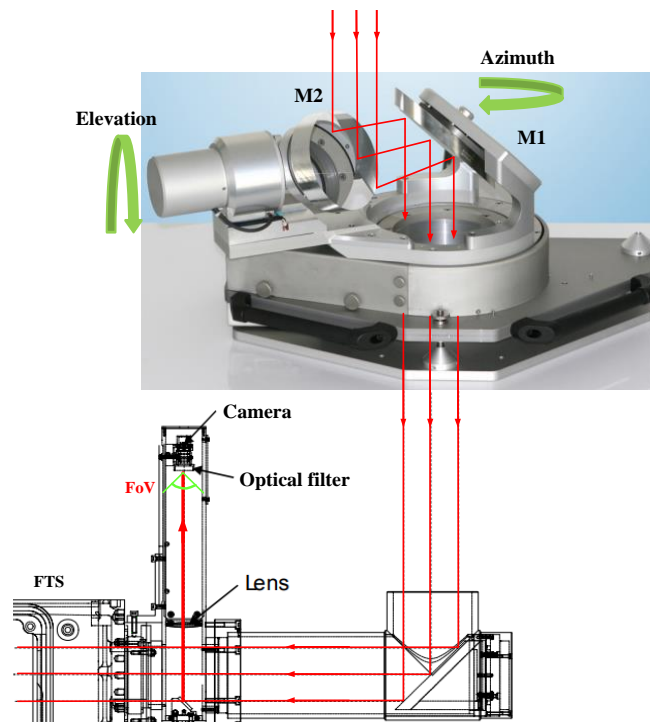


Figure 2.4 Bruker A547N Sun tracker. M1, M2 : mirror 1 and mirror 2.

The Sun's spot is observed by a camera. An image processing software (called CamTracker [2]) calculates the position of the center of the Sun related to the input aperture of the collection system, and provides feedback signal to the sun-tracker stepping motors to point the optical system to the Sun center with a tracking accuracy of 0.0167° . This kind of sun-tracker with a NA (Numerical Aperture) of 0.0087° is mostly designed for Bruker's FT-IR spectrometer for ground-based measurements of trace gases in the atmospheric column.

(3) EKO sun-tracker

EKO sun-tracker (Model STR-21G, EKO Instruments CO, LTD) provides a FoV of 30° with a tracking accuracy of 0.01° (Fig. 2.5).

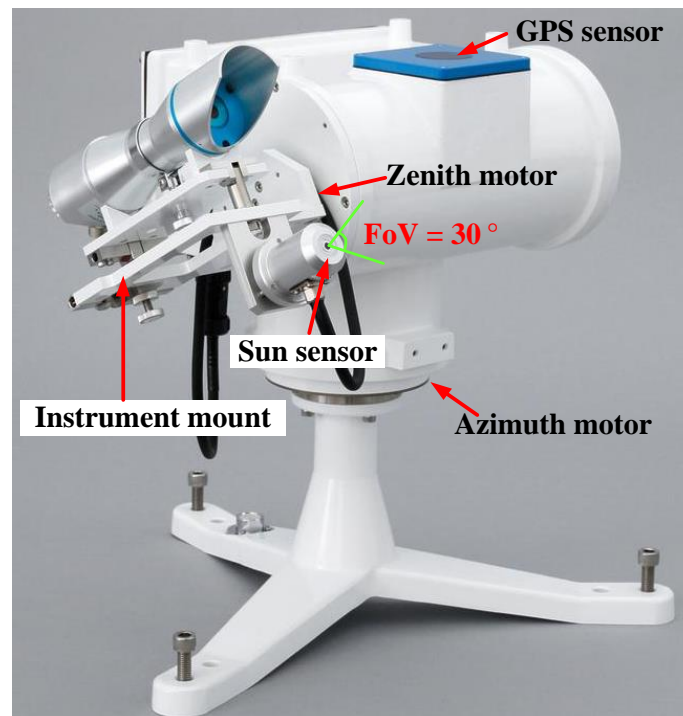


Figure 2.5 EKO sun-tracker (model STR-21G).

The sun-tracker can be operated in two modes to follow the Sun's movement : (1) Calculation mode : when the sun-tracker is just starting up or the Sun is absent, tracking mode automatically changes to the calculation mode which will coarsely calculate the Sun's position (including zenith and azimuth angles) based on the received information from the GPS sensor on latitude, longitude, date and time. (2) Sun-sensor mode : once the Sun is within the FoV of the sun-tracker, tracking mode switches to this mode. A 4-quadrant detector and an internal learning track function will accurately detect the Sun's radiation (and hence its position) and will compensate for misalignment of the sun-tracker to the Sun

position with the help of a closed-loop control system of the sun-sensor, even if the tracker is not oriented or levelled properly. In general, in order to maintain the highest tracking accuracy possible, two tracking modes will be automatically switched according to the solar radiation conditions.

This sun-tracker is equipped with an adjustable instrument mount which allows fine optical alignment of the optical setup installed on this mount for sunlight collection.

Based on the specifications of above three kinds of sun-trackers, summarized in Table 2.1, the EKO sun-tracker is selected for use in the present work to collect sunlight with a higher tracking accuracy and lower price.

Table 2.1 Specifications of three commercially available sun-trackers.

	Cimel CSPHOT	Bruker A547N	EKO STR-21G
FoV	1.2°	45°	30°
Tracking accuracy	0.1°	0.0167°	0.01°
Portability	Yes	No	Yes
Price	~ 25000 USD	~ 20000 USD	~ 14000 USD

2.1.2 IR blackbody sources

Blackbody sources with stable radiation are highly requested for the development and the performance characterization of LHR. In our experiments, an Oriel® blackbody source (Model 67030, Newport Inc.) and an IR blackbody emitter (Model IR-Si217, Hawkeye Technologies Inc.) are respectively used.

(1) Oriel® blackbody (Fig. 2.6 *left*) is a highly uniform and temperature stabilized infrared radiation source, calibrated to a NIST (National Institute of Standards and Technology, USA) standard. The major functional components of the blackbody are cavity, heater and dual thermocouples (Fig. 2.6 *right*). A ceramic sealed heater coil uniformly heats a stainless steel cavity cylinder to provide blackbody radiation. The cavity is manufactured from special stainless steel and processed to have a uniform and high emissivity coating which allows it to produce an effective emissivity very near unity. An 8-position aperture wheel provides 7 different apertures and 1 open position. The aperture size is adjusted to be 15.2, 10.2, 5.1, 2.5, 1.3, 0.64, and 0.32 mm in diameters, respectively.

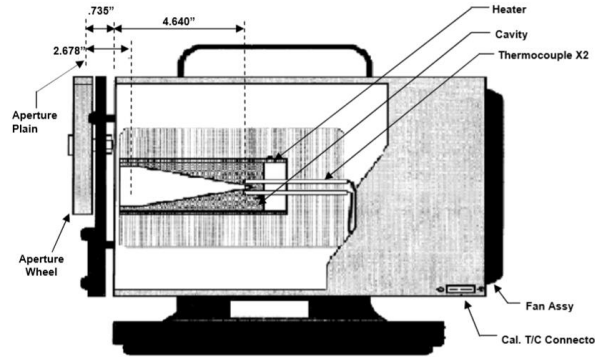


Figure 2.6 *left*: blackbody source (Oriel® Model 67030, Newport Inc.); *right*: major components of the 67030 blackbody source.

Temperature of the blackbody can be adjusted with a digital temperature controller with a precision of 0.1 °C from 50 to 1050 °C. Typical irradiance spectra of the blackbody at different temperatures are shown in Fig. 2.7 (a). Fig. 2.7 (b) shows the emissivity of the blackbody at 1000 °C with an aperture of 0.5 inch (12.7 mm). The emissivity in the range of 2-10 μm is close to 1. This blackbody is an ideal standard blackbody source for the development of an infrared LHR instrument.

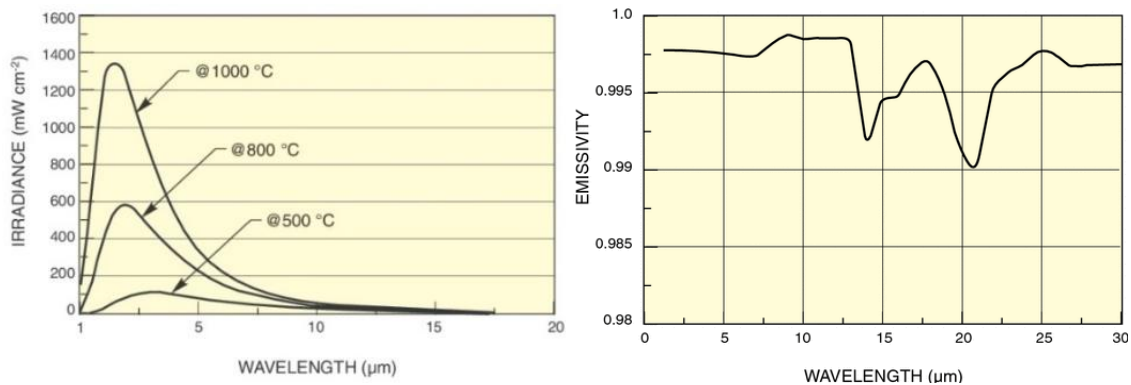


Figure 2.7 (a) Typical irradiance spectra of the used blackbody at different temperatures; (b) Emissivity of the blackbody at 1000 °C from a 0.5 inch (12.7 mm) aperture.

A digital temperature controller is used to provide fast stable temperature control via a PID (proportional, integral and derivative) system and prevents excessive settling time and temperature overshoot. All operating parameter adjustments, temperature and indicators are adjusted and displayed through the temperature controller. A GPIB/IEEE-488 port is available for interface with computer.

(2) IR-Si217 infrared emitter (Fig. 2.8 *left*) is a robust, efficient and very economic infrared emitter. It features true blackbody radiation characteristics with low power

consumption, high emissivity (0.8) and a long lifetime. It is manufactured using a patented silicon carbide material. The used IR emitter is packaged in a compact aluminium block with an emission size of 4.4×6.0 mm (Fig. 2.8 *right*). It is operated in DC power mode with an operating current and voltage around 1.5 A and 7 V, respectively, which results in an operating temperature of about 1385 °C providing an optical output power of about 800 mW over all spectral region (1-20 μm).

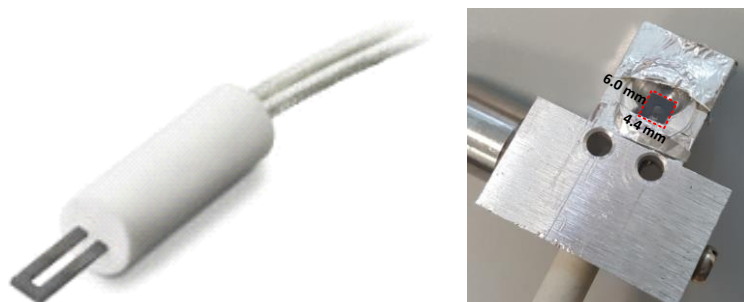


Figure 2.8 *left*: emitter source IR-Si217; *right*: packaged emitter source with a CaF₂ window.

Fig. 2.9 shows calculated spectral radiances of the used two blackbody sources based on the Planck's law. As can be seen, two blackbodies have almost the same spectral radiance at 8 μm. IR-Si217 infrared emitter exhibits the unique advantage for field applications owing to its compact size and very low cost.

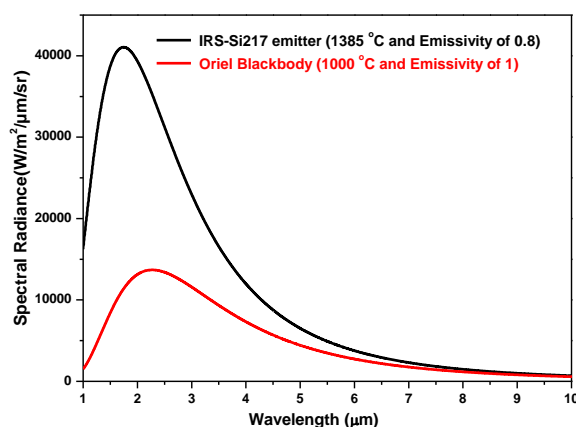


Figure 2.9 Spectral radiances of an Oriel blackbody source (Model 67030, Newport Inc.) operating at 1000 °C with an emissivity of 1 (red curve) and an IR-Si217 infrared emitter operating at 1385 °C with an emissivity of 0.8 (black curve).

2.1.3 Local oscillator (LO)

The LO is the key device for a high-performance LHR. The characteristics of the laser source used as the LO determine the working spectral range (and thus the target molecule being

measured) and the performance of the LHR. The following laser properties should be considered : emission frequency, output power, emission line width, frequency stability, single-mode tunability, and wavelength-dependent baseline.

In our LHR setup, a continuous wave (CW) external-cavity quantum cascade laser (EC-QCL) operating in the mid-IR around 8 μm (1250 cm^{-1}) is used as the LO. The EC-QCL (TLS-41000-MHF, Daylight solutions Inc.), shown in Fig. 2.10 (*left*), is controlled with a specific controller (Model 1001-TLC, Daylight solutions Inc.) and continuously tunable in frequency from 1223 to 1263 cm^{-1} ($7.91\text{-}8.17\ \mu\text{m}$) through its external-cavity tuning. The laser provides optical output powers of more than 60 mW over 40 cm^{-1} spectral coverage (Fig. 2.10 *right*) with a power fluctuation less than 1% r.m.s (root-mean-square, the square root of the average of the squared power fluctuations) over 5 minutes, according to the manufacturer.

Wavenumber accuracy of the laser is $\pm 0.5\text{ cm}^{-1}$ (uni-directional) with a laser emission line width of 5 MHz, resulting in a laser resolving power ($\Delta\nu/\nu$) of about 10^7 . The full spectral scan can be realized by varying cavity grating angle of the EC-QCL with a step of 0.01 cm^{-1} in automatic or manual step mode via the controller. Fine frequency scan over $\sim 1\text{ cm}^{-1}$ (at a rate of up to 60 Hz) can be achieved using a sine-wave signal. The sine-wave signal from a function generator is firstly amplified with a piezoelectric transducer (PZT) driver (3-Axis Piezo Controller Model MDT690, Thorlabs) to about 100 V and then applied to the PZT element of the EC-QCL to modulate the external-cavity grating angle and hence the external-cavity length. Sine-waveform is used for laser frequency scan in order to avoid rapid changes in the scan direction (such as in case of the use of a sawtooth or triangular ramp signal) which will cause excitation of mechanical vibrations, rendering the laser output unstable and result in permanent laser damage.

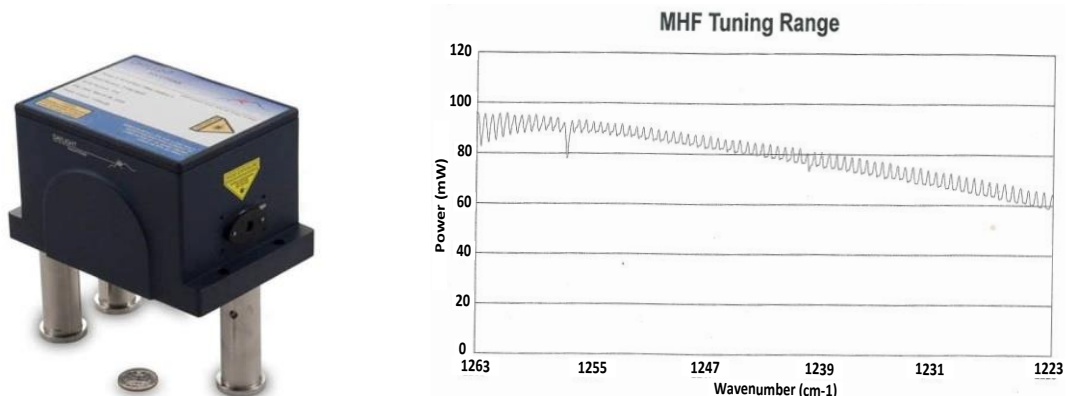


Figure 2.10 *left*: CW Mode Hop-Free EC-QCL (Model CW-MHF 41000, Daylight Solution, Inc.); *right*: wide tuning of 1223 to 1263 cm^{-1} with output power of $\sim 60\text{ mW}$ at 1223 cm^{-1} and more than 80 mW at $\geq 1247\text{ cm}^{-1}$.

When the LO laser frequency is appropriately scanned across the target molecular absorption line, the changes in the resulting RF beat signal amplitude correspond to the molecular absorption feature that is thus restituted from the total absorption of the sunlight by all molecules in presence in the atmosphere.

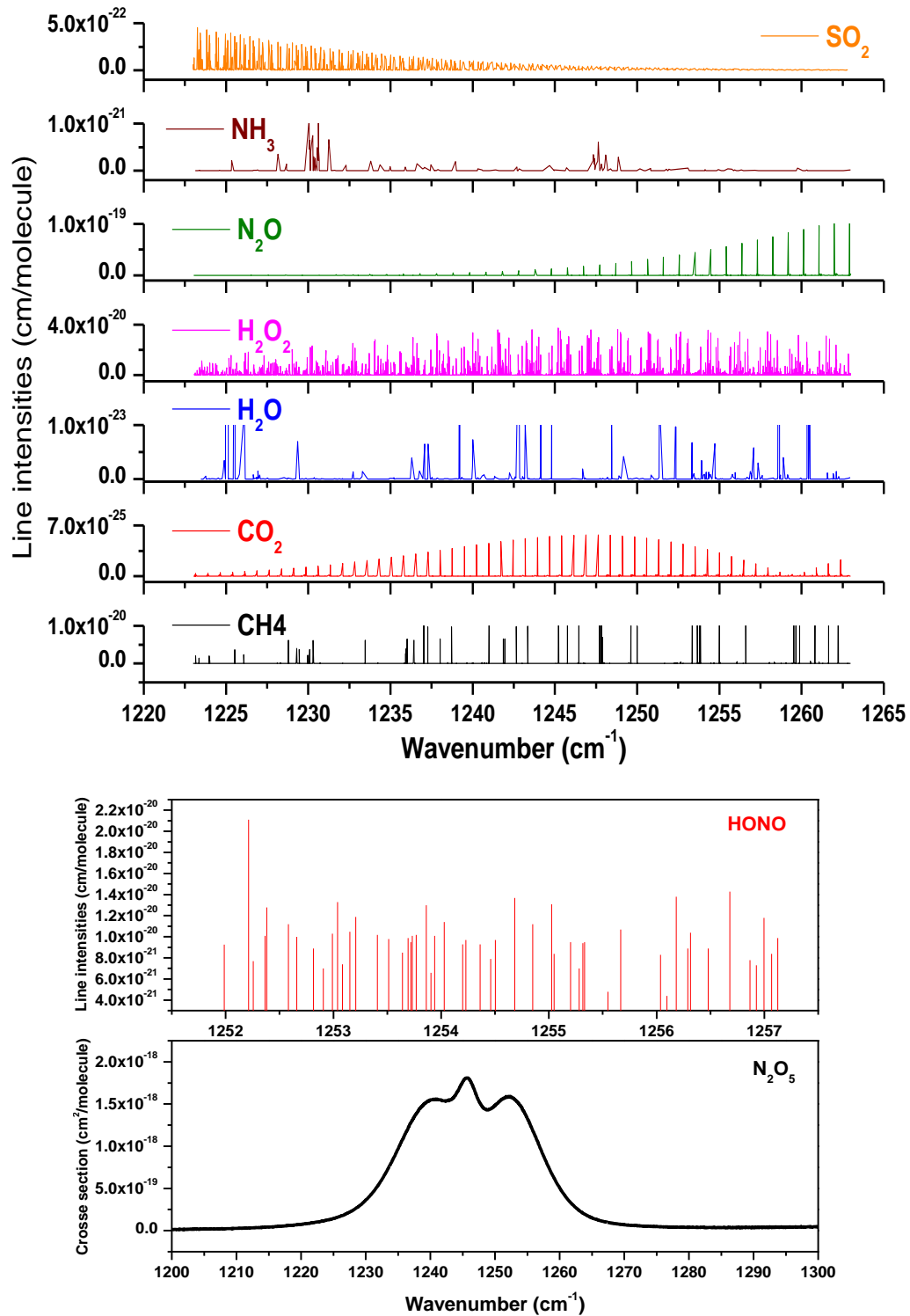


Figure 2.11 upper: detectable molecules in the spectral coverage region of the EC-QCL used in the present work, based on the HITRAN database [6]; lower: absorption spectra of HONO [8] and N₂O₅ [7].

Wide tuning range of more than some tens of cm^{-1} of the used EC-QCL as the LO is interesting, which offers the capacity of our LHR instrument to monitor multi-species or/and broadband absorption/emission. Fig. 2.11 shows major molecules present in the frequency tuning region of the used EC-QCL (based on the HITRAN database [6], the GEISA database [7] and our laboratory measurements [8]).

The performance of the EC-QCL source, in term of laser emission line width, single mode wavelength tunability and wavelength-dependent baseline, has been evaluated via concentration measurement of N_2O produced in a chemical catalytical reaction process (described in Chapter 3).

2.1.4 Photomixer

Photomixer used for mixing LO radiation and sunlight to generate a heterodyne signal is a core component of the LHR. In order to sensitively detect weak mid-IR sunlight intensity (in the range of μW) with high SNR, the responsivity and the detectivity of the photomixer with a lower noise density must be as high as possible. Meanwhile, a photomixer with a wider bandwidth can provide not only a faster response time but also a high flexibility for the choice of filter pass-band of the RF receiver. In addition, a DC component output of the photomixer can be used to monitor baseline variation in heterodyne signal (mainly due to the variation in the LO power). Therefore a photomixer with both DC (for monitoring LO power variation) and AC (for heterodyne RF signal) components, which can be separated through a bias-T at the photomixer output, would be a favorable option. Currently, two photodetectors are potentially suitable for use as photomixer for 8- μm LHR.

(1) DC-coupled photovoltaic detector PVMI-4TE-8 (VIGO System S.A.) equipped with a four-stage thermoelectrical cooler and integrated with a preamplifier (MIP-DC-250M-F-M4) (Fig. 2.12 *left*). It has a FoV of 35° .

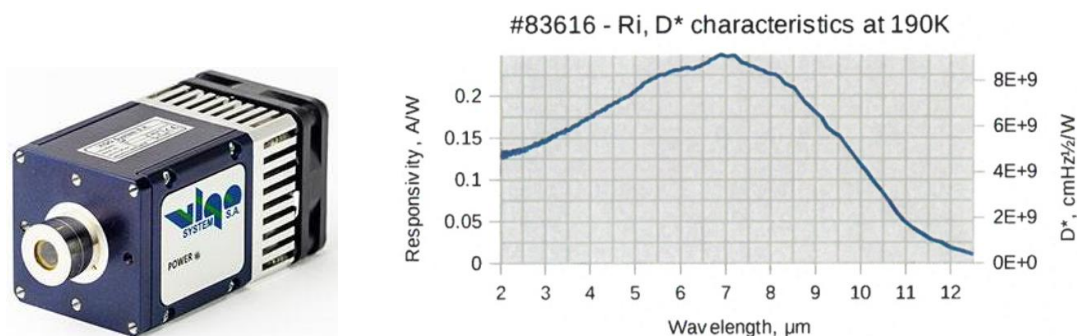


Figure 2.12 *left*: PVMI-4TE-8 VIGO detector; *right*: detector current responsivity and detectivity vs. wavelength.

The upper 3 dB cut-off frequency is 195 MHz with a current responsivity of 0.226 A/W and a detectivity of $8.3\text{E}+9 \text{ cmHz}^{1/2}/\text{W}$ (at $\lambda=8 \text{ }\mu\text{m}$), as shown in the Table 1. Fig. 2.12 (right) shows its typical spectral performance.

(2) AC-coupled fast photovoltaic detector PVI-4TE-10.6 (VIGO System S.A.), four-stage thermoelectric cooled with a FoV of 35° (Fig. 2.13 left). The upper 3 dB cut-off frequency is 800 MHz with a current responsivity of 4.2 A/W and a detectivity of $5\text{E}+9 \text{ cmHz}^{1/2}/\text{W}$ (at $\lambda=8 \text{ }\mu\text{m}$). The integrated preamplifier exhibits an electronic pass-band of 1 kHz-500 MHz. Fig. 2.13 (right) shows its typical performance.

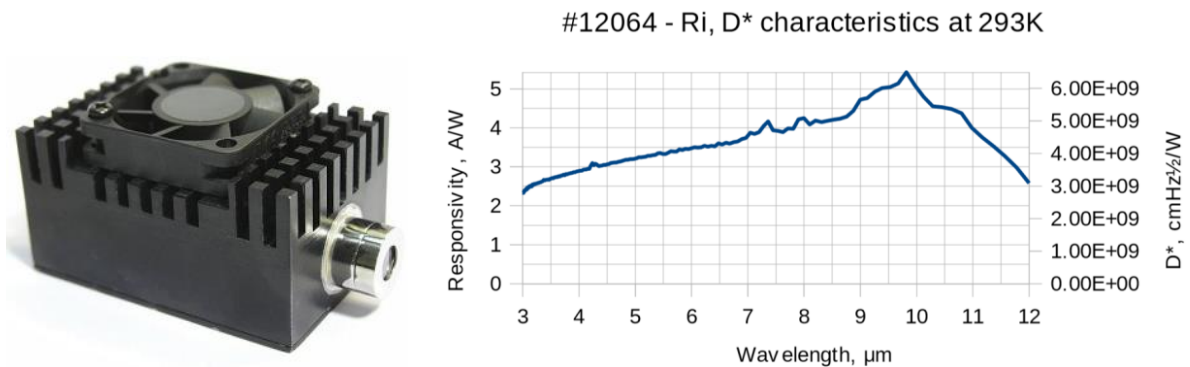


Figure 2.13 left: PVI-4TE-10.6 VIGO detector; right: detector current responsivity and detectivity vs. wavelength.

Main specifications of above two photomixers are summarized in Table 2.2. Comparing their specifications, the DC-coupled PVMI-4TE-8 detector has a lower current responsivity (of 0.226 A/W) and a higher output voltage noise density of $250 \text{ nV}/\sqrt{\text{Hz}}$. Based on these two parameters, the AC-coupled fast PVI-4TE-10.6 detector with a higher responsivity (4.2 A/W) and a lower output voltage noise density of $120 \text{ nV}/\sqrt{\text{Hz}}$ is selected for use as photomixer in our LHR system though there is not a DC component output for monitoring LO power variation.

Table 2.2 Specifications of IR photomixers for LHR application.

VIGO detector	PVI-4TE-10.6	PVMI-4TE-8
Active Area	0.5*0.5 mm ²	1*1 mm ²
Window	BaF2 (3 deg wedged)	BaF2 (wedged)
Wavelength Range	3 to 12 μm	2 to 12 μm
Transimpedance @ R _{LOAD} = 50 Ω	6.0E+3 V/A	1.15E+4 V/A
Detectivity ±20% @ 8 μm	5.0 E+09 cm \sqrt{Hz} /W	8.3 E+09 cm \sqrt{Hz} /W
Current Responsivity ±20% @ 8 μm	4.2 A/W	0.226 A/W
Voltage Responsivity @ 8 μm	2.52E+4 V/W	2.55E+3 V/W
Output Voltage Noise Density	120 nV/ \sqrt{Hz}	250 nV/ \sqrt{Hz}
Immersion Type / FOV	Hyperhemispherical / 35°	Hyperhemispherical / 35°
Dynamic Resistance	150 Ω	1410 Ω
Thermistor Resistance	320 kΩ	470 kΩ
Reverse Bias Voltage	650 mV	0 V
Stability of Temperature	0.01 K	0.01 K (estimated)

2.1.5 RF receiver

Heterodyne signal at radio frequency from the photomixer is further processed by a back-end electronic RF receiver containing band-pass filter, RF amplifiers and a square law detector, as shown in Fig. 2.1.

2.1.5.1 Band-pass filter

Spectral resolution of the LHR system is in general determined by the bandwidth of the used band-pass filter, which may be easily changed to meet the spectral resolution requirements of particular measurements. Bandwidth and the cut-off frequency of the filter can be adjusted according to the noise density spectrum in the beat note, analyzed using a signal analyser (N9000B, CXA X-Series, Keysight, Inc). Appropriate selection of their values can not only provide the requested spectral resolution, but also effectively remove noises resulting from the LO laser and electronic components. Various combinations of filters with different pass-

bands, connected in cascade at the output of the photomixer, are applied to optimize the LHR performance. The filters available for the present LHR development are listed in Table 2.3.

Table 2.3 Pass-bands of RF filters available for the present work.

Model	BLP-300+	BLP-550+	BLP-800+	BBP-30+	BHP-25+	BBP-70+	BHP-150+	BHP-175+	BHP-200+	BHP-250+
Pass-band (MHz)	DC-270	DC-520	DC-720	27-33	27.5-800	63-77	133-270	160-270	185-270	225-270

2.1.5.2 RF amplifier

In the current RF receiver, 2 low-noise amplifiers (Model ZFL-500LN+, Mini-Circuits®), with a gain of 24 dB and a pass-band of 0.1-500 MHz each (Fig. 2.14 *left*), are used for amplification of the RF beat signal. Fig. 2.14 (*right*) shows the noise figure (NF) of the selected amplifiers, which characterizes the degradation in SNR by the amplifier and is expressed by :

$$NF = 10 \log_{10} \left(\frac{SNR_{IN}}{SNR_{OUT}} \right) \quad (2.1)$$

where SNR_{IN} and SNR_{OUT} are the SNR at the input and output of the amplifier, respectively. It would be preferred to select an amplifier with a higher gain, a pass-band covering the bandwidth of the RF signal, and a NF as low as possible.

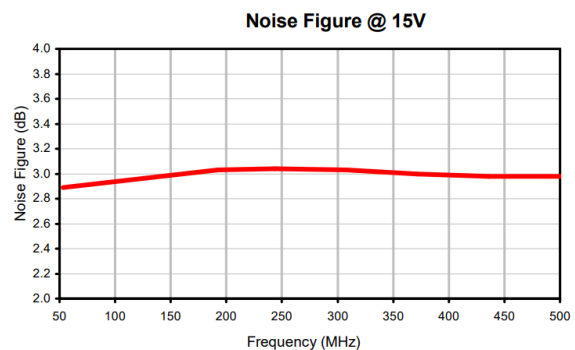


Figure 2.14 *left*: RF amplifier (ZFL-500LN+); *right*: Noise Figure vs. frequency.

2.1.5.3 Square law detector

In order to rectify the RF beat signal, a square law detector is used, which plays a role of envelope detection. The filtered and amplified RF beat signal is passed to a Schottky diode (Model 8472B, Keysight Inc.), as called square law detector because its output is proportional

to the square of the amplitude of the input beat signal (c.f. Fig. 2.15 lower, left). The used square law detector is a low-barrier Schottky diode (LBSD) specially fabricated with low origin resistance and low junction capacitance to cover DC to 18 GHz frequency range (Fig. 2.15 upper).

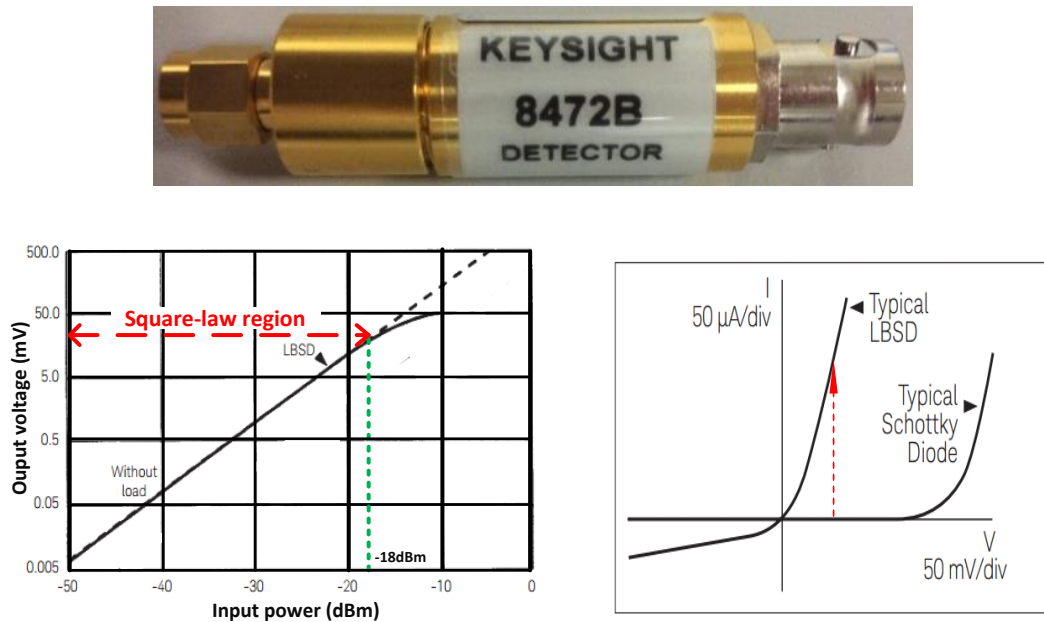


Figure 2.15 upper: Keysight 8472B schottky diode; lower: typical detector's square-law response (left) and diode V/I characteristics (right).

LBSD is widely used for continuous-wave or pulsed power detection and frequency response test of microwave components. This diode detector does not require a DC bias, making it very easy for use. It also offers very good ruggedness and burnout protection, easy for integration with other circuit elements to minimize stray reactance and optimize broadband performance. In the square-law region (Fig. 2.15 lower, left), the diode detector typically operates within 0.5 dB of square-law from the tangential signal sensitivity level up to -18 dBm. Fig. 2.15 lower (right) shows the characteristic transmission curves of a typical Schottky diode detector and a LBSD. As can be seen, the LBSD has a higher voltage transmission coefficient, i.e. higher sensitivity. LBSD provides also improved broadband flatness and smaller standing wave ratio (SWR) over point-contact Schottky diode.

Two commercially available LBSDs (low-barrier Schottky diode Keysight 8472B and zero-bias Schottky diode Herotek DHM020BB) are compared and their specifications are summarized in Table 2.4. The Keysight 8472B exhibits better performance, in terms of broader frequency range, smaller frequency response, smaller SWR (i.e. smaller uncertainty of power measurement) and smaller noise, except from its smaller low-level sensitivity.

Table 2.4 Specifications of Keysight 8472B and Herotek DHM020BB schottky diodes.

Model	Frequency range	Frequency response	Low-level sensitivity*	Noise	Maximum input power	SWR
Keysight 8472B	0-18 GHz	±0.2 dB	> 0.5 mV/μW	< 50 μV	200 mW	1.2
DHM020BB	100 kHz-2 GHz	±0.3 dB	1.0 mV/μW	< 100 μV	200 mW	1.3

* Note : Schottky diodes are designed to rectify very low levels of RF power to produce a DC output voltage proportional to the RF power. Therefore, the sensitivity of Schottky diodes is usually defined as low level sensitivity [9].

2.1 6 Lock-in amplifier

In order to improve the SNR of the LHR signal, lock-in amplifier is usually used. The key specifications of the used analog lock-in amplifier (Model 5110, AMETEK, Inc.) are listed in Table 2.5.

In order to perform phase-sensitive LIA detection, sunlight is mechanically modulated using a chopper. To avoid any truncation of sunlight by chopper slot aperture, sunlight beam size should be smaller than the slot aperture of the chopper. In our designed LHR system, the shaped sunlight beam size is about 12.5 mm. Therefore, a 10-slot blade with a widest aperture of about 13 mm is usable. An optical chopper (Model MC1F10HP, Thorlabs, Inc.) is used. It provides chopping frequencies ranging from 20 Hz to 1 kHz, with a frequency fluctuation of 20 ppm/°C. As presented in Section 2.4, the used photomixer is AC-coupled with a frequency range of 1 kHz to 500 MHz, the chopper modulation frequency is set to 1 kHz to match the pass-band of the photomixer.

Table 2.5 Specifications of lock-in amplifier (Model 5110, AMETEK, Inc.).

Frequency response	Voltage sensitivity	Minimum detection sensitivity	Input impedance	Time constant	Dynamic reserve*	Octave roll-off
0.5 Hz-100 kHz	100 nV-1V	100 nV	1 MΩ//30 pF	1 ms-300 s	105 dB	6/12 dB

* Note : Dynamic reserve (the ratio by which input noise voltages may exceed the full-scale sensitivity value without causing overload) : ≤105 dB (high reserve), ≤ 85 dB (Normal), and ≤65 dB (high stability), respectively.

Time constant τ (in [s]), related to the low-pass (LP) filter cut-off frequency in the LIA, is a very critical parameter for the use of LIA, which impacts on noise suppression and absorption line-shape. The cut-off frequency (f_c) of the LP filter is driven by the LIA time

constant τ as $f_c \approx 1/2\pi\tau$ [10]. Longer time constant τ can significantly filter out the noise, but it also results in blueshift of the spectral line center (shifting to the frequency scan direction / decrease in wavelength) and distort the line-shape (becoming broadened and asymmetric) [10,11].

The frequency shift $\delta\nu$ can be approximately expressed by [12] :

$$\delta\nu = \frac{d\nu}{dt} \tau = \nu_{sc} \tau \quad (2.2)$$

where $d\nu/dt = \nu_{sc}$ (in $[\text{cm}^{-1}/\text{s}]$) is the frequency scanning speed, for frequency scan in continuous mode, it is the ratio of the frequency scanning range $\Delta\nu_{\text{scan}}$ to the scanning period T (in $[\text{s}]$) that is the reciprocal of the scanning frequency.

In order to avoid this unwanted effect, the LIA time constant τ has to be appropriately chosen with respect to the time ΔT_{scan} needed for scanning through the halfwidth $\Delta\nu_{\text{HWHM}}$ of the absorption line profile, which depends upon the frequency scanning speed ν_{sc} . Simulations of the impact of τ have been performed in order to find optimal τ with respect to the experimentally applied frequency scanning speed. The effective transfer function of a LIA can be equivalent to a LP filter [13], as shown in Figure 2.16.

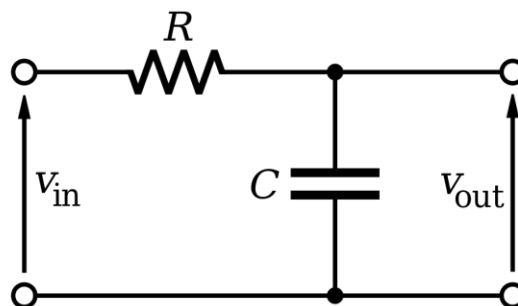


Figure 2.16 Effective transfer function of a LIA. R is the resistor; C is the capacitor.

According to Kirchhoff's Laws and the definition of capacitance :

$$V_{in}(t) - V_{out}(t) = RC \cdot \frac{dV_{out}(t)}{dt} \quad (2.3)$$

where R is the resistance; C is the capacitance. For simplicity, assuming that samples of the input and output are taken at evenly spaced points in time separated by Δt , Eq. (2.3) can be expressed in terms of V_{out} at time k, V_{in} at time k and V_{out} at time k-1 :

$$V_{in}(k) - V_{out}(k) = RC \cdot \frac{V_{out}(k) - V_{out}(k-1)}{\Delta t} \quad (2.4)$$

Rearranging terms in Eq. (2.4) gives a recurrence relation :

$$V_{out}(k) = V_{in}(k) \cdot \left(\frac{\Delta t}{RC + \Delta t} \right) + V_{out}(k-1) \cdot \left(\frac{RC}{RC + \Delta t} \right) \quad (2.5)$$

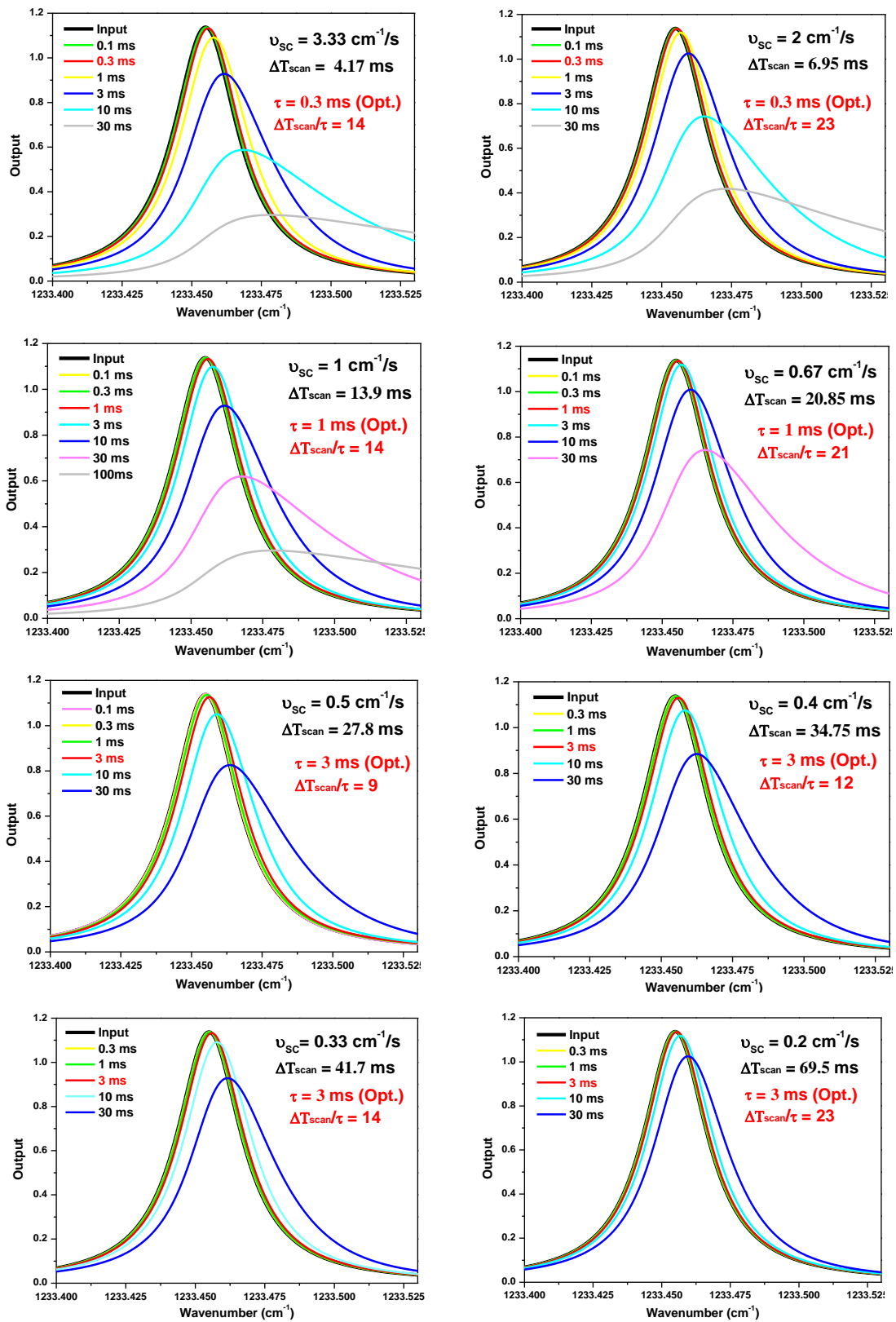
The first term on the right side of Eq. (2.5) is the contribution from the input, and the second term is the inertia from the previous output. This differential model of the LP filter described in Eq. (2.5) provides a way to determine the output data based on the input and the previous output values.

Based on Eq. (2.5), the effect of the LP filter is simulated by using a pseudocode algorithm with the help of Matlab. In the simulation, V_{in} is a Hitran simulation spectrum of CH_4 around 1233.45 cm^{-1} , and V_{out} is the simulation outputs resulting from different parameters : scanning period T , scanning speed v_{sc} , scanning time ΔT_{scan} and time constant τ (see Table 2.6).

Table 2.6 Simulation of the effect of the LP filter on absorption line-shape with different τ .

Halfwidth $\Delta v_{\text{HWHM}} [\text{cm}^{-1}]$	0.014	0.014	0.014	0.014	0.014	0.014	0.014	0.014	0.014	0.014
Scanning range $\Delta v_{\text{scan}} [\text{cm}^{-1}]$	1	1	1	1	1	1	1	1	1	1
Scanning period T [s]	0.3	0.5	1	1.5	2	2.5	3	5	10	30
Scanning speed $v_{sc} [\text{cm}^{-1}/\text{s}]$ $= \Delta v_{\text{scan}} / T$	3.33	2	1	0.67	0.5	0.4	0.33	0.2	0.1	0.033
Scanning time $\Delta T_{\text{scan}} [\text{ms}]$	4.17	6.95	13.9	20.85	27.8	34.75	41.7	69.5	139	417
τ [ms]	0.1	0.1	0.1	0.1	0.1	0.3	0.3	0.3	1	1
	0.3	0.3	0.3	0.3	0.3	1	1	1	3	3
	1	1	1	1	1	3	3	3	10	10
	3	3	3	3	3	10	10	10	30	30
	10	10	10	10	10	30	30	30	100	100
	30	30	30	30	30	-	-	-	-	300
	-	-	100	-	-	-	-	-	-	-

Simulation results for frequency scan in continuous mode are shown in Fig. 2.17.



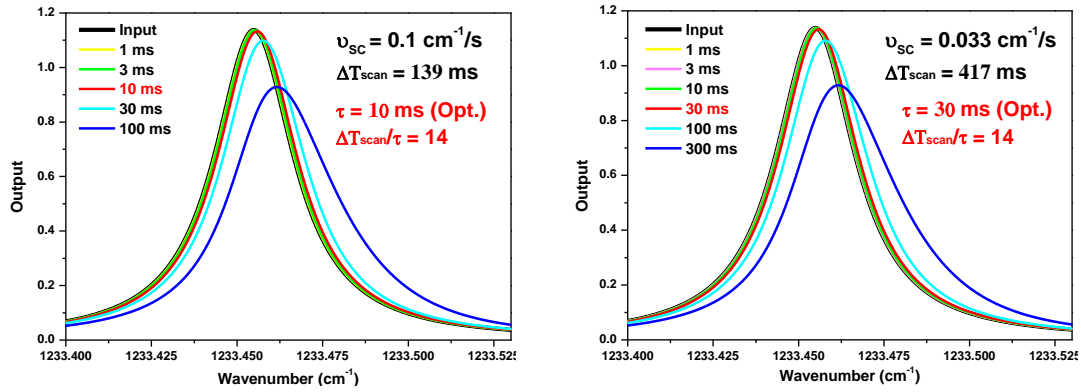


Figure 2.17 Simulation output spectra from the LP filter using different parameters (see Table 2.6). Condition of the Hitran simulation spectrum (input : *black*) : absorption line center: 1233.45 cm^{-1} , pressure: 250 mbar, concentration: 0.1, and length of the absorption cell: 13 cm.

As can be seen from Fig. 2.17, when the scanning time ΔT_{scan} ($\Delta v_{\text{HWHM}} / v_{\text{sc}}$) is 9-23 times of time constant τ , the output spectrum (*red*) is consistent with the input spectrum (*black*). The scanning time ΔT_{scan} (Table 2.6 in *blue bold*) as a function of the time constant τ (Table 2.6 in *red bold*) is plotted (Fig. 2.18 *square dot*). The mathematical relationship between the time constant τ and the scanning time ΔT_{scan} is obtained from a linear fit ($r^2=99.25$), as shown in Fig. 2.18 :

$$\Delta T_{\text{scan}} = \frac{\Delta v_{\text{HWHM}}}{v_{\text{sc}}} \approx 14 \cdot \tau \quad (2.6)$$

Based on Eq. (2.6), with respect to the given frequency scanning speed in the continuous mode and to the halfwidth of the spectrum to scan, the reasonable scanning time ΔT_{scan} should be approximately 14 times of the LIA time constant τ in order to efficiently reduce the noise without significant shift and distortion of the line-shape.

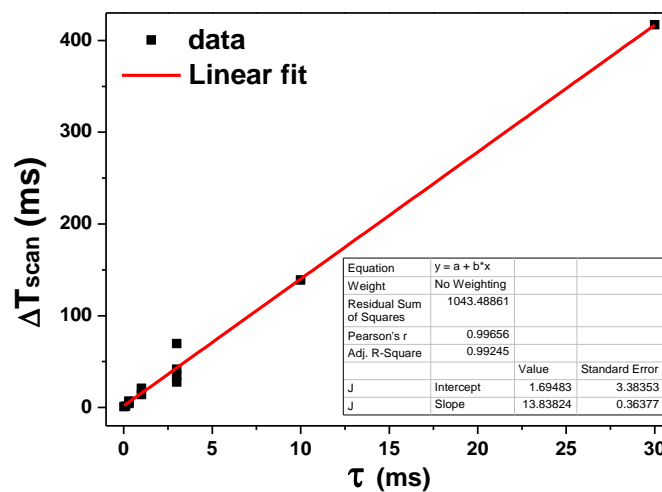


Figure 2.18 Plot of the time constant vs. ΔT_{scan} , associated with a linear fit.

In case of scanning laser frequency in point-by-point tuning mode, time-domain function characteristic of the low-pass filter at time k could be considered as follows :

$$V_{out}(t) = V_{in}(t) \cdot (1 - \exp(-t/\tau)) \quad (2.7)$$

Plot of $V_{out}(t)$ versus $V_{in}(t)$ with time constant τ is shown in Fig. 2.19. As can be seen, when the time is 2.5 times time constant (τ), $V_{out}(t)$ is 91.8% of the input $V_{in}(t)$, while when the time is 6 times time constant (τ), $V_{out}(t)$ is 99.8% of the input $V_{in}(t)$.

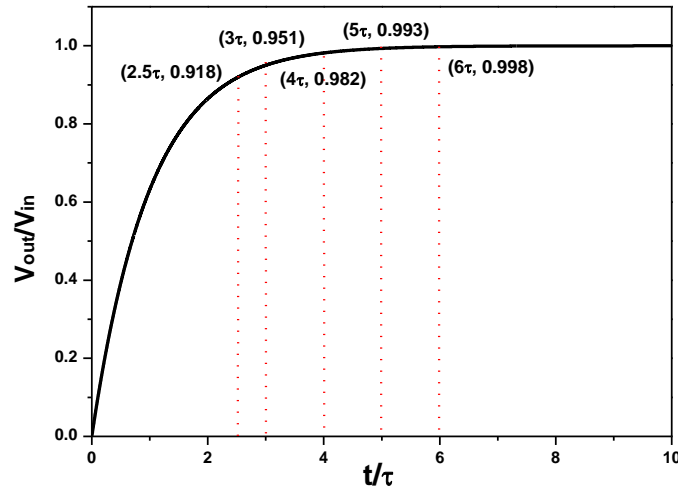


Figure 2.19 Plot of $V_{out}(t)$ vs. $V_{in}(t)$ in point-by-point frequency tuning mode.

Therefore, when tuning laser frequency in point-by-point mode, a time interval (i.e. the time between two sampling points) longer than ~ 6 times of the LIA time constant τ has to be used to avoid deformation of line-shape of the spectrum [14,15].

2.2 LHR configurations

The devices involved in a LHR have been introduced and characterized in the previous section, configurations of the PoC of mid-IR LHR being developed are discussed in this section. Fig. 2.20 shows two configurations used in the present work for the development of a LHR deployable for in situ ground-based measurements of vertical concentration profiles of atmospheric trace gases : (1) using heliostat located on a roof terrace (University Paris VI) to direct sunlight through a free-space telescope system to a developed LHR receiver which allows us to test, characterize and improve its performance in the first stage of the LHR development; (2) using an EKO sun-tracker to couple sunlight through a fiber to the LHR receiver, which makes the LHR truly transportable for in situ measurement anywhere.

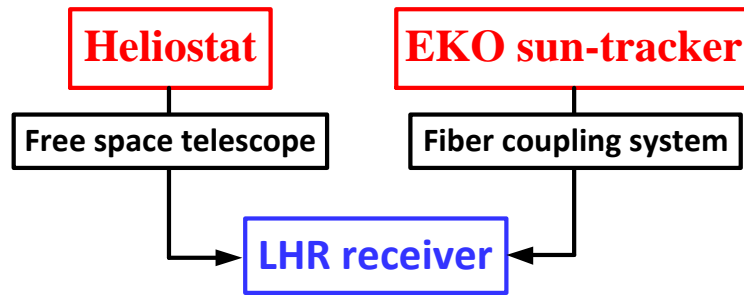


Figure 2.20 Scheme of the LHR configurations involved in the present work.

2.2.1 Sunlight collection using a free-space telescope cage system

In order to well couple the sunlight coming from the heliostat (c.f. Chapter 4.3.1), a Thorlabs 60 mm cage assembly system is used to realize a free-space telescope (Fig. 2.21).

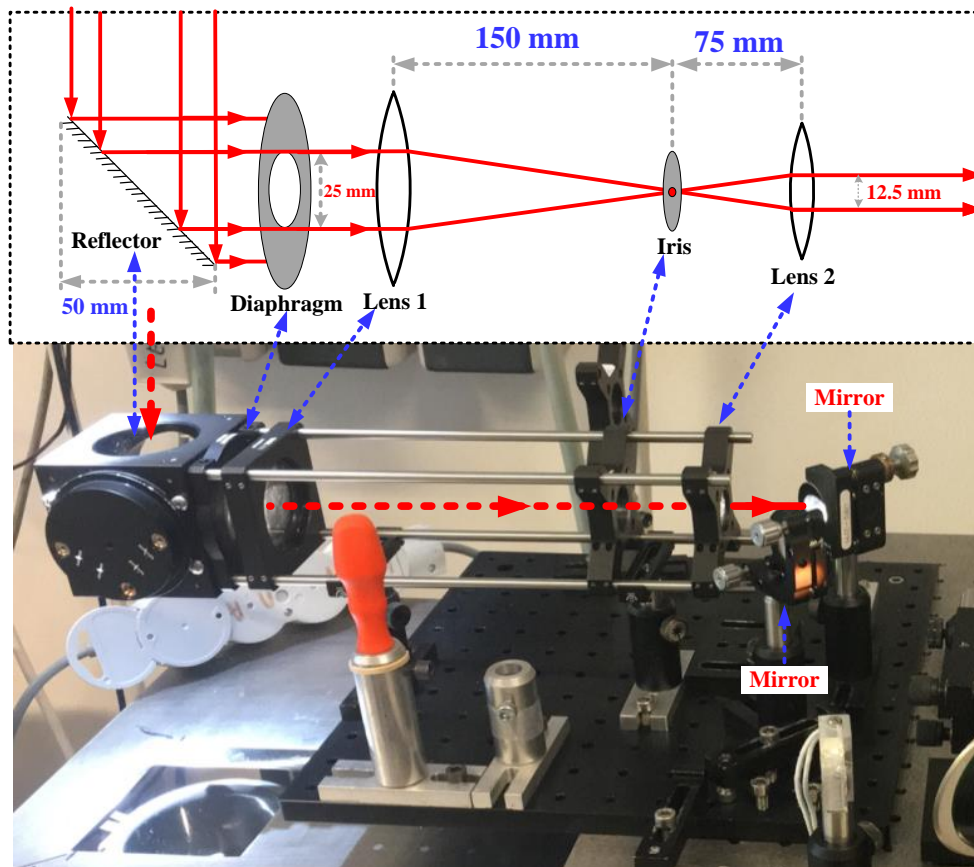


Figure 2.21 *upper*: schematic of a free-space telescope cage system for coupling sunlight; *lower*: photo of the developed telescope cage system. Lens 1 : $f_1 = 150$ mm, $D_1 = 50$ mm; Lens 2 : $f_2 = 75$ mm, $D_2 = 25.4$ mm.

For LHR measurement it is preferable to collect as much sunlight radiation as possible, therefore, a mirror reflector with a large aperture diameter of 50 mm is used to well collect sunlight from the heliostat (with a clear aperture of 78 mm) and then direct the collected

sunlight to the LHR receiver. Whereas, if the sunlight beam size is too large, the focused beam size as well as the focusing angle by a lens will exceed the size and FoV of the used photomixer. In order to match the requirement for the size and FoV of the used photomixer (c.f. Chapters 1.3.3 and 2.2.1.2), the incoming sunlight with a beam size of 25 mm for heterodyne detection is chosen. A telescope in combination with an adjustable diaphragm (LCP50S) is designed to constrain the sunlight beam size while keeping enough sunlight power. The adjustable diaphragm located in front of the telescope is used as aperture stop for the lens 1, and the amount of reflected sunlight admitted is controlled by the opening diameter of the diaphragm.

Fig. 2.21 (*upper*) shows that the sunlight (considered as plane beam) is collected and size-initialized by the mirror reflector to a beam size of 50 mm, then the collected sunlight is size-controlled by the adjustable diaphragm to a beam size of 25 mm as required. The sunlight is further shaped through a telescope consisted of two CaF₂ lenses for gathering sunlight power. Iris 2, located at the focal point of the two CaF₂ lenses, is used as a field stop to eliminate the stray light. The developed free-space telescope system based on a Thorlabs 60 mm cage assembly system is shown in Fig. 2.21 (*lower*).

Sunlight beam emerging from lens 2 is directed to a beam splitter on which it is superimposed with the LO beam. The free-space telescope system with a 50 mm diameter mirror reflector collecting sunlight radiation at 8 μm provided a FoV of ~0.2 mrad (0.011°) for LHR system.

2.2.1.1 Sunlight beam contraction and laser beam expander

The LO beam (Gaussian beam) from the EC-QCL has a pre-collimated size of 2.5 mm that is 10 times smaller than the sunlight beam size of 25 mm, which results in a beam coupling efficiency K of only 3.92% (c.f. Eq. (1.22)). In order to realize high-efficiency mixing of two light beams, it is necessary to match the beam size of the collimated sunlight to that of the collimated LO beam as close as possible (c.f. Chapter 1.3.1.1).

A 2× beam contraction of sunlight to reduce the sunlight beam size by a factor of 2 and a 5× beam expander to enlarge LO beam size by a factor of 5 are designed, which can make two light beams having the same beam size of about 12.5 mm, so as to ensure a maximum beam coupling efficiency. A sunlight beam contraction and a laser beam expander systems are designed using Kaplerian Telescopes. Kaplerian beam contraction/expander design consideration can be expressed by the following equations :

$$\text{Magnification power} = \frac{f_2}{f_1} \quad (2.8)$$

$$\text{Optical track length of the telescope} = f_1 + f_2 \quad (2.9)$$

where f_1 and f_2 are the focal length of two positive lenses, respectively. Design using two positive lenses meets the magnification requirements (Eq. (2.8)) without exceeding the designed overall system size (30 cm × 30 cm determined by Eq. (2.9)). As illustrated further, these equations are first order equations, lens thickness and focus optimization might cause slight deviation from these ideal values.

Lens clear aperture also needs to be taken into account during the selection, as the lens size must be two times the incoming beam size in order to avoid any beam truncation.

(1) Design of a 2× Kaplerian beam contraction and a 5× Kaplerian beam expander

A two-singlet Kaplerian telescope involving two lenses of $f_1=150$ mm and $f_2=75$ mm with a reasonable system size less than 300 mm long is designed for the 2× beam contraction. Regarding the 5× beam expander, a Kaplerian telescope system using two lens of $f_1=20$ mm and $f_2=100$ mm is realized to meet the expander requirement.

It's worth noting, in a two singlet Kaplerian telescope system, wavefront quality would increase with increasing optical track, i.e. a combination of a 20-mm and a 100-mm lens would have a better wavefront quality than that of the combination of a 10-mm and a 50-mm lens for the same magnification power. In addition, the quality of the wavefront is improved by using a lens with a plane surface, such as plano-convex or plano-concave, rather than one with curvature on both surfaces. With plano lenses and a Kaplerian layout, orienting the convex surface towards the input beam tends to avoid the laser damage from the first plano surface, even if it's anti-reflection coated.

As the maximum beam size is also limited by the clear aperture of the lens, a 50 mm diameter plano-convex lens with 150 mm focal length, (lens 1, #89-169, Edmund Inc.) and a 25.4 mm diameter bi-convex lens with 75 mm focal length (lens 2, LB5247, Thorlabs Inc.) are used to construct a 2× beam contraction Keplerian telescope. A 12.7 mm diameter plano-convex lens with 20 mm focal length (lens 3, LA5317, Thorlabs Inc.) and a 25.4 mm diameter plano-convex lens with 100 mm focal length (lens 4, LA5817, Thorlabs Inc.) are used to realize a 5× Kaplerian beam expander.

(2) Design optimization using Zemax

Because of using stock lenses, the only variable involved in Zemax lens data editors for the design is the distance between two lenses, i.e. the value of the thickness of surface 3 as shown in Tables 2.7 and 2.8. Figs. 2.22 and 2.23 show the lens layout of the beam contraction and expander in a confocal mode, respectively.

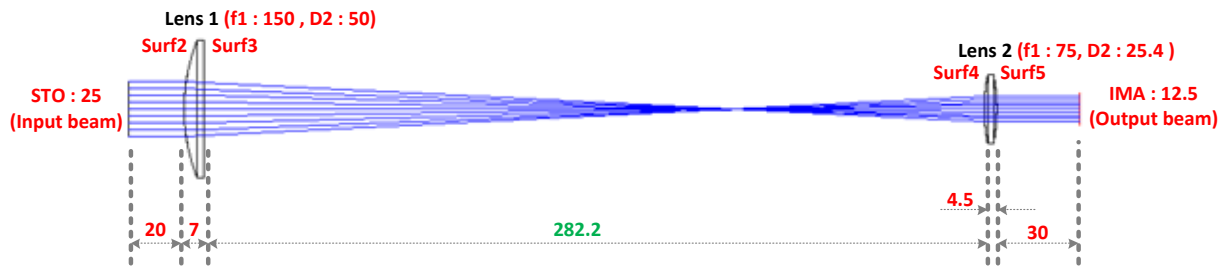


Figure 2.22 Beam contraction layout (surf : surface of lens, f : focal length, D : lens diameter, STO : Stop surface, IMA : Image surface). All dimensions are in [mm].

Table 2.7 Lens data editor of the beam contraction.

Surf>Type	Comment	Radius	Thickness	Glass	Semi-Diameter
OBJ	Standard	Infinity	Infinity		0.000000
STO*	Standard	Infinity	STO-Surf2: 20.000000		Input beam: 12.500000 U
2*	Standard	69.300000	Surf2-Surf3: 7.000000	Lens 1 material: CAF2	Lens 1: 25.000000 U
3*	Standard	Infinity	Surf3-Surf4: 282.202272 V		25.000000 U
4*	Standard	64.400000	Surf4-Surf5: 4.500000	Lens 2 material: CAF2	Lens 2: 12.700000 U
5*	Standard	-64.400000	Surf5-IMA: 30.000000		12.700000 U
IMA	Standard	Infinity	-		Output beam: 6.250000 U

Note : Thickness indicates relative distance between two surfaces. The setting variables are radius, thickness, glass and semi-diameter, respectively. The optimal distance between two lenses for the beam contraction is highlighted in a green frame.

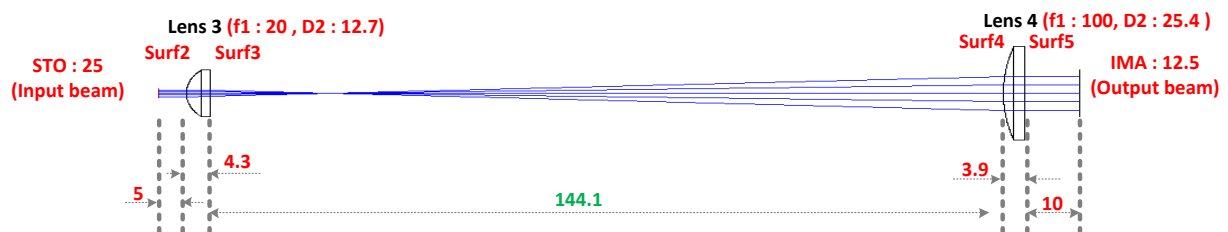


Figure 2.23 Beam expander layout (surf : surface of lens, f : focal length, D : lens diameter, STO : Stop surface, IMA : Image surface). All dimensions are in [mm].

Table 2.8 Lens data editor of the beam expander.

Surf:Type	Comment	Radius	Thickness	Glass	Semi-Diameter
OBJ	Standard	Infinity	Infinity		0.000000
STO*	Standard	Infinity	STO-Surf2: 5.000000		Input beam: 1.250000 U
2*	Standard	8.700000	Surf2-Surf3: 4.300000	Lens 1 material: CAF2	Lens 1: 6.350000 U
3*	Standard	Infinity	Surf3-Surf4: 144.100000 V		6.350000 U
4*	Standard	43.400000	Surf4-Surf5: 3.900000	Lens 2 material: CAF2	Lens 2: 12.700000 U
5*	Standard	Infinity	Surf5-IMA: 10.000000		12.700000 U
IMA	Standard	Infinity	-		Output beam: 6.250000 U

Note : Thickness indicates relative distance between two surfaces. All setting variables are radius, thickness, glass and semi-diameter, respectively. The optimal distance between two lenses for the beam contraction is highlighted in a green frame.

The distance between two lenses is optimized in two systems using Zemax in order to obtain the same emerging beam size of 12.5 mm (c.f. IMA semi-diameter in Tables 2.8 and 2.9) in both systems. 25 mm and 2.5 mm (c.f. STO semi-diameter in Tables 2.8 and 2.9, respectively) are set as input beam sizes with normal incident angle for sunlight beam contraction and for laser beam expander.

After optimization of the distance between two lenses (so called the thickness of surface 3), optimal distance between two lenses for the beam contraction and the beam expander are 282.2 mm and 144.1 mm, respectively.

2.2.1.2 Coupling of sunlight and LO beams to the mixer

According to the last criteria mentioned in chapter 1.3.3, the focusing angle 2θ (Fig. 2.24) of the light beam on the detector should be less than the FoV of the detector (35°), and the focused size $2\omega_0$ would be less than the optical receiving area of the detector ($0.5 \text{ mm} \times 0.5 \text{ mm}$). These parameters are both dependent upon the incoming sunlight beam size.

After optimization of beam expander and beam contraction with Zemax sequential mode, two optimal designs are integrated into Zemax non-sequential mode to make a final simulation and optimization of the entire system related with the optimal position. The lens editor and system layout are shown in Table 2.9 and Fig. 2.24, respectively. The optimal distance between the focusing lens and the photomixer detector is 52.3 mm.

Table 2.9 The Lens editor.

Object Type	Comment	Material	X position	Y position (Vertical)	Z position (Horizontal)	Tilt About X (in degree)
1	Source Ellipse	LASER	0.000000	120.000000	380.000000	180.000000
2	Standard Lens	Lens 3 : LA5317	0.000000	120.000000	320.000000	180.000000
3	Standard Lens	Lens 4 : LA5817	0.000000	120.000000	175.926504	180.000000
4	Standard Lens	Mirror 1 : PF10-03-M01	0.000000	120.000000	130.000000	45.000000
5	Standard Lens	Mirror 2 : PF10-03-M01	0.000000	60.000000	130.000000	135.000000
6	Standard Lens	Mirror 3 : PF10-03-M01	0.000000	60.000000	340.000000	0.000000
7	Source Ellipse	Sunlight	0.000000	0.000000	0.000000	0.000000
8	Standard Lens	Lens 1 : #89-169	0.000000	0.000000	20.000000	0.000000
9	Standard Lens	Lens 2 : LB5247	0.000000	0.000000	302.200000	0.000000
10	Standard Lens	Splitter. POB	0.000000	0.000000	340.000000	135.000000
11	Standard Lens	Lens 5 : LA5370	0.000000	0.000000	360.000000	0.000000
12	Detector Rect	VIGO		0.000000	412.300000	0.000000

Note : Y and Z positions both indicate relative distance between two objects. The optimal distance between the focusing lens and the photomixer detector is 52.3 mm, which is equal to the relative distance between Object 11 (360.0 mm) and Object 12 (412.3 mm).

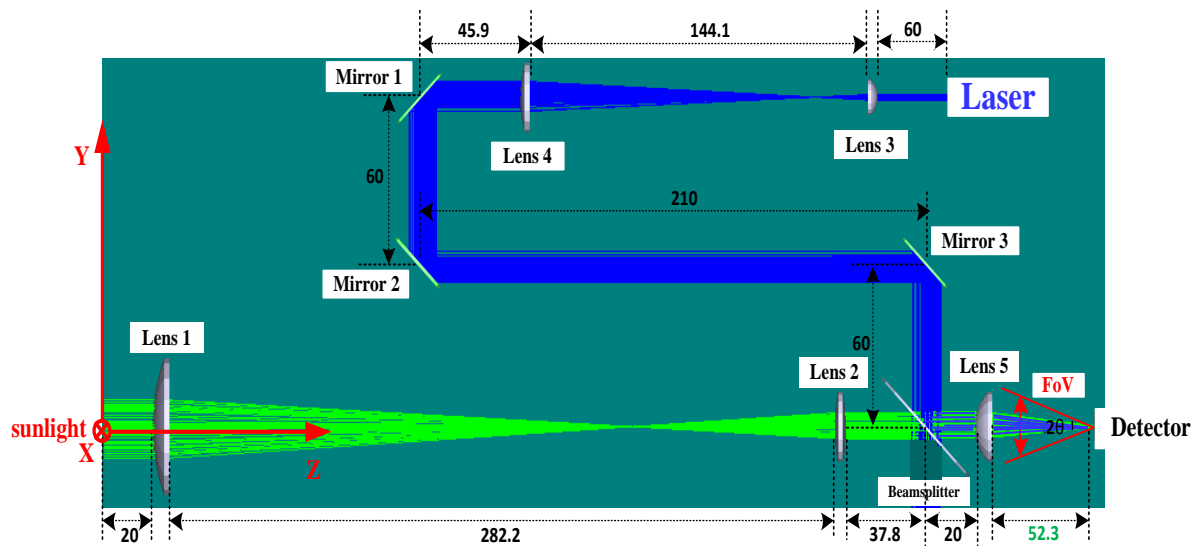


Figure 2.24 Optical layout of a free-space coupling mid-IR LHR (All size parameters are in [mm]).

In order to make sure that the size and the focusing angle 2θ of the beams emerging from lens 5 are both smaller than the optical area ($0.5 \text{ mm} \times 0.5 \text{ mm}$) and the FoV (35°) of the VIGO photomixer, the size and the focusing angle 2θ of the emerging beams are studied as a function of the incident sunlight size. The results are shown in Figs. 2.25 and 2.26, respectively. The emerging beam size decreases as the sunlight size decreases, and its focusing angle decreases with the sunlight size. Meanwhile, the distance between two lenses of the sunlight beam contraction as a function of the sunlight size is built, as shown in Fig. 2.27. It would be practical to adjust the distance between two lenses, given the sunlight size.

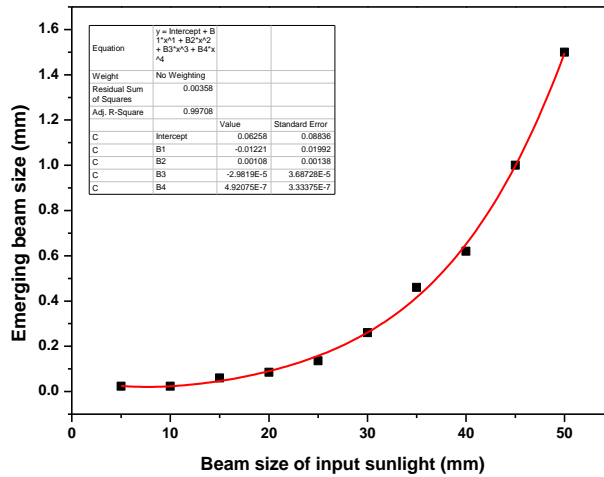


Figure 2.25 Emerging beam size after lens 5 as a function of the sunlight size.

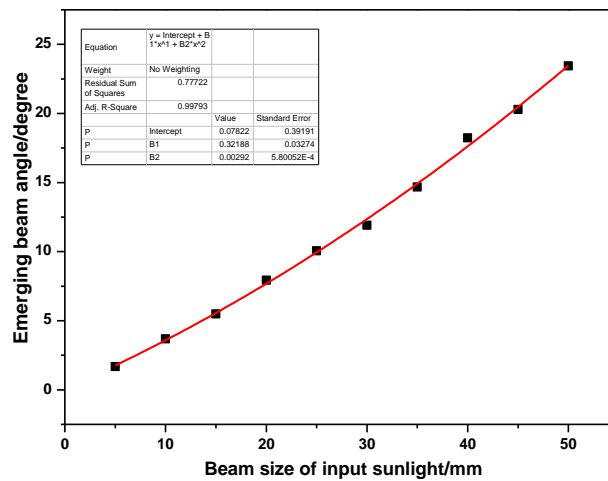


Figure 2.26 Focusing angle of the emerging beam by lens 5 as a function of the sunlight size.

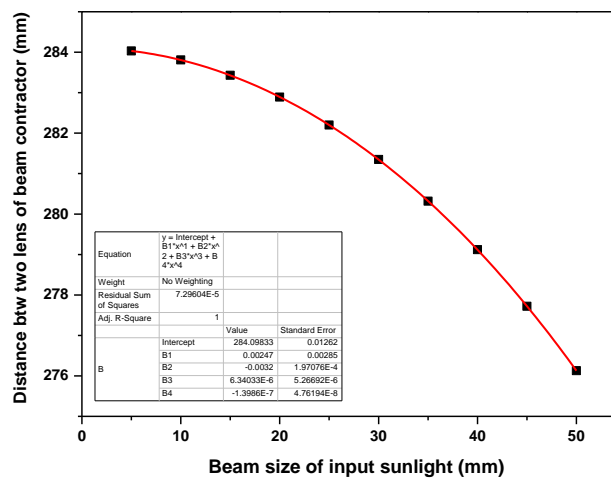


Figure 2.27 Distance needed between two lenses ($f_1=150$ mm and $f_2=75$ mm) for the beam contraction as a function of the sunlight size.

However, in a heterodyne system, collecting more sunlight energy is highly desired for sensitive remote sensing. Therefore, a trade-off between sunlight beam size and the emerging beam size has to be made. An incident sunlight size of 25 mm is chosen in the present work, the resulting emerging beam size and the focusing angle 2θ after lens 5 are 0.16 mm and 10.1° , respectively, based on the simulation. They meet both the requirement of being smaller than the VIGO photomixer's parameters mentioned above : detector size = $0.5 \text{ mm} \times 0.5 \text{ mm}$ and FoV = 35° .

2.2.2 Sunlight collection using a fiber coupling system

2.2.2.1 Description of a fiber coupling system for sunlight collection

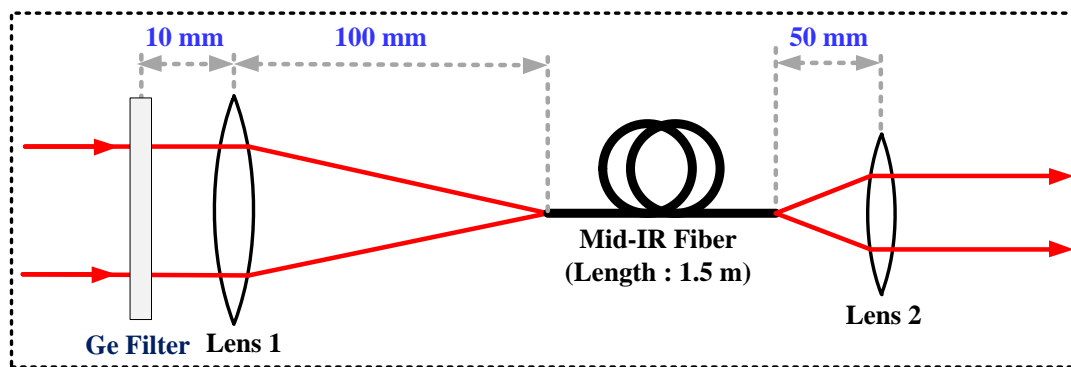


Figure 2.28 Schematic of the fiber system for sunlight coupling.

A portable EKO sun-tracker is used for the development of a fully transportable LHR. A mid-IR fiber is employed to couple solar radiation to the LHR receiver (Fig. 2.28). The mid-IR fiber coupling system, installed on the sun-tracker, includes lens 1 (in CaF_2 , $f_1=100 \text{ mm}$, $D_1=25.4 \text{ mm}$), associated with a Ge-filter to filter out radiation out of the spectral region of interest to minimize shot noise resulting from the signal source. Sunlight is focused by lens 1 into a polycrystalline fiber ($\text{NA}=0.3$ corresponding to an acceptance half-angle θ of 17.46° that is bigger than the half focusing angle of 7.47° of lens 1). The beam emerging from the fiber is collimated with lens 2 (in CaF_2 , $f_2=50 \text{ mm}$, $D_1=12.7 \text{ mm}$) and directed, in free-space, toward a beam splitter on which it is superimposed with the LO beam.

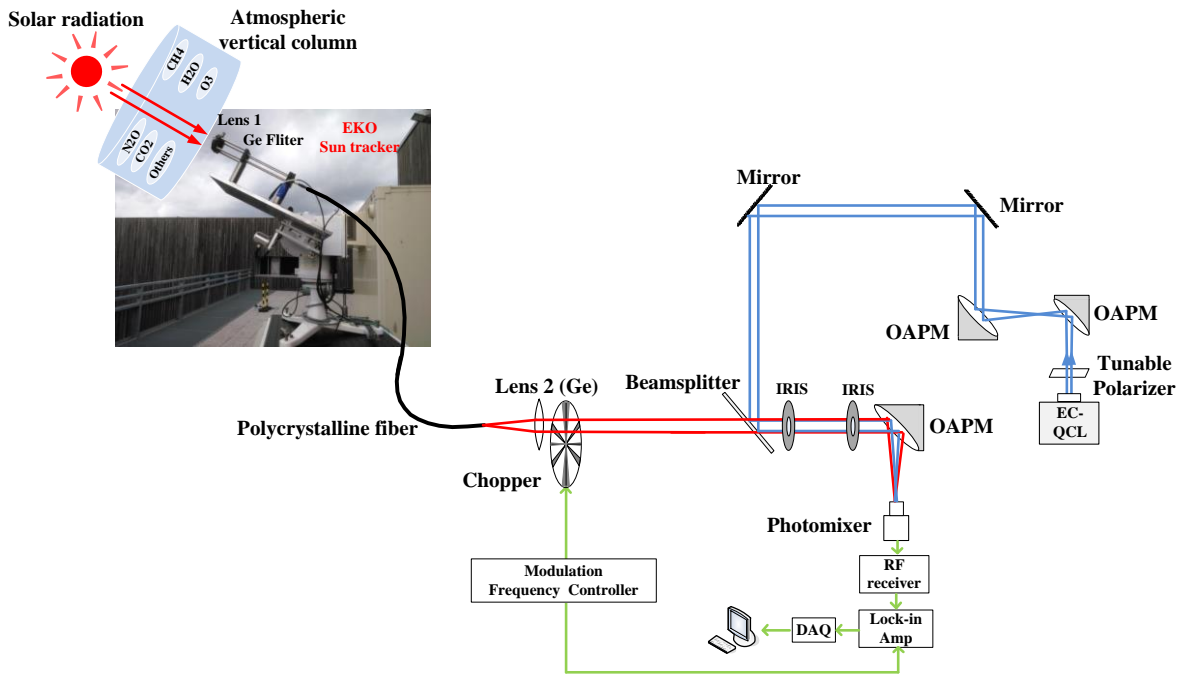


Figure 2.29 Schematic of a fully transportable LHR involving a mid-IR fiber coupling sunlight system.

The schematic of a full transportable LHR prototype involving a mid-IR fiber coupling sunlight system is shown in Fig.2.29. The sunlight is coupled to the LHR through the fiber coupling system as shown in Fig.2.28. The emerging sunlight from lens 2 is first amplitude modulated with a chopper, and then directed to a beam splitter. The transmitted light is overlapped with the LO beam from the EC-QCL. The mixed beams are focused and injected into the VIGO photomixer, the output signal from the VIGO photomixer is processed by the RF receiver.

The fiber used for sunlight-coupling (Fig. 2.30 *left*) is a polycrystalline infrared (PIR) fiber (PIR900/1000-150-TI/SMA-TI/SMA-PE32, art photonics Inc.). The PIR-fiber is non-toxic, very flexible, transparent across a broad spectral range of 3-18 μm with high transmittance and a large NA (0.3), as shown in Fig. 2.30 (*right*), suitable for laser power of up to 40 W (CW), and capable of operating over a temperature range of -50-140 $^{\circ}\text{C}$ without aging effect.

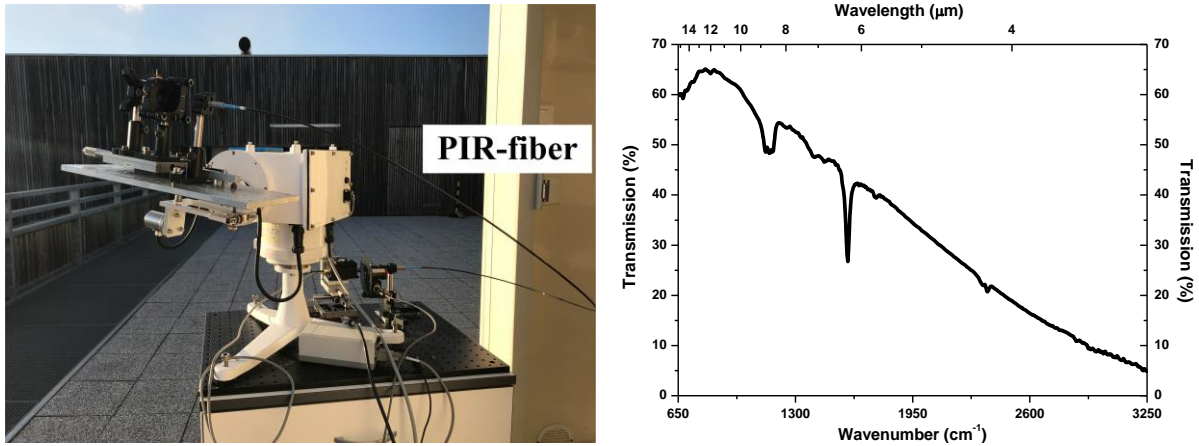


Figure 2.30 *left*: polycrystalline IR-fiber coupling system; *right*: transmission spectra of the PIR fiber.

Table 2.10 Specifications of the PIR fiber.

Fiber Specification	
Core diameter [μm]	860 ± 20
Minimum bend radius [mm]	150
Transmission Range [μm]	3 - 18
Core material	$\text{AgCl}_{0.25} \text{Br}_{0.75}$
Cladding material	$\text{AgCl}_{0.50} \text{Br}_{0.50}$
Core refractive index	2.15
Effective NA	0.30 ± 0.03
Operating temperature [$^{\circ}\text{C}$]	$-50 < T < 140$
Maximum transmitted Power [W]	40 (CW)
Length [m]	1.5 ± 0.05

2.2.2.2 Test of the fiber coupling and sun-tracking performance

In order to test the coupling ability of the polycrystalline IR-fiber as well as to test the sun-tracker performance, measurement of the sunlight radiation was carried out over 5 hours on the roof of the IRENE (Innovation Recherche en Environnement) platform in Dunkerque ($51.05^{\circ}\text{N}/2.34^{\circ}\text{E}$).

In this test, two operation modes of the EKO sun-tracker were tested to obtain information on latitude, longitude, date and time. One is "GPS mode", which can automatically achieve such geographical location and time information through a built-in GPS sensor. The other is "manual mode", in which such information should be set manually via a specific software “STRconfig”, as shown in Fig. 2.31.

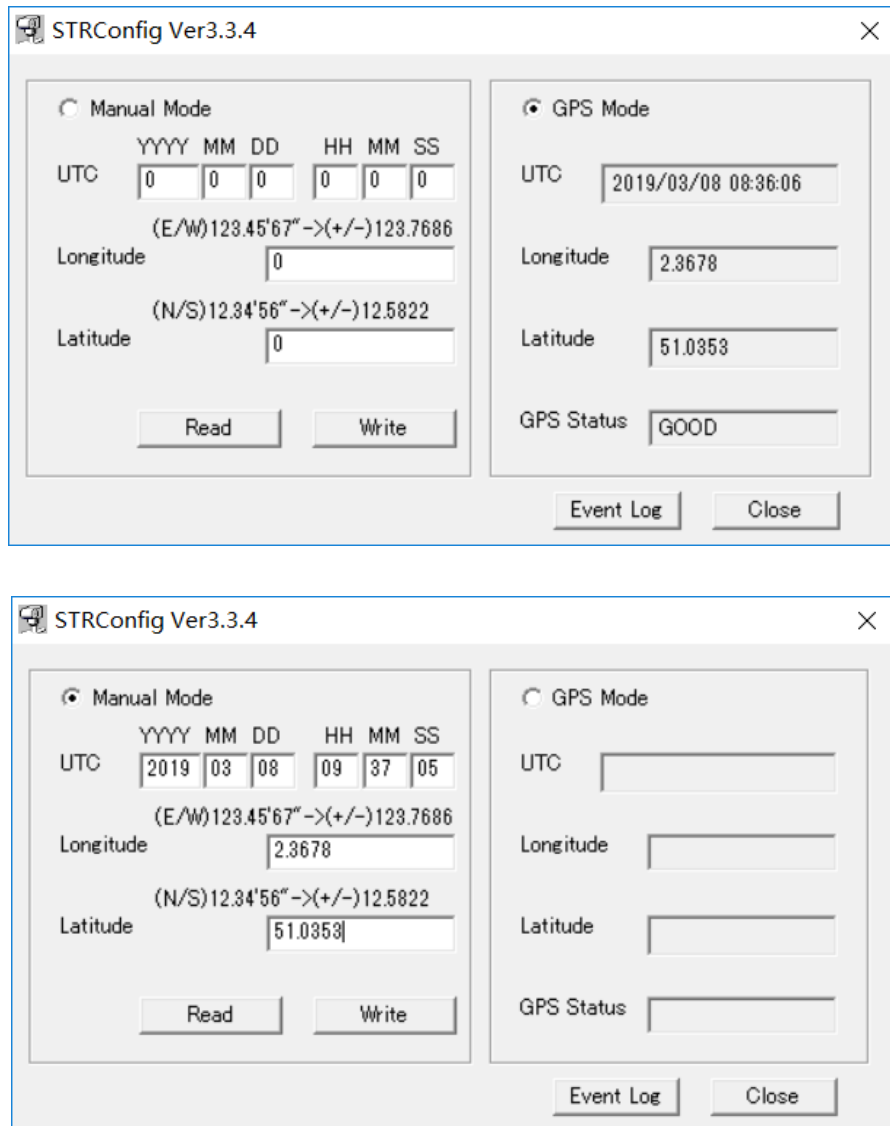


Figure 2.31 “STRConfig” Setting screen : GPS mode (*upper*) and manual mode (*lower*).

Fig. 2.32 shows the sunlight radiation measured from 11:40 to 16:40 (blue curve) in comparison with the global solar radiation data (black curve) recorded at the same date and the same place with a "Davis Vantage Pro2". Global solar radiation represents the total amount of solar energy received at the Earth’s surface (W/m^2). This can account for 50%, 43%, and 7% of the visible (0.4-0.76 μm), the infrared ($>0.76 \mu m$), and the ultraviolet (<0.4

μm) spectral regions, respectively. As can be seen, the trends of the two curves are roughly the same. In addition, the measured mid-IR solar radiation is around 38% of the global solar radiation, the difference from empirical value (43%) is mainly resulted from the PIR-fiber transmission of about 54% and optical coupling of the sunlight to the fiber. This experiment confirms the coupling ability of the polycrystalline IR-fiber and the tracking performance of the sun-tracker.

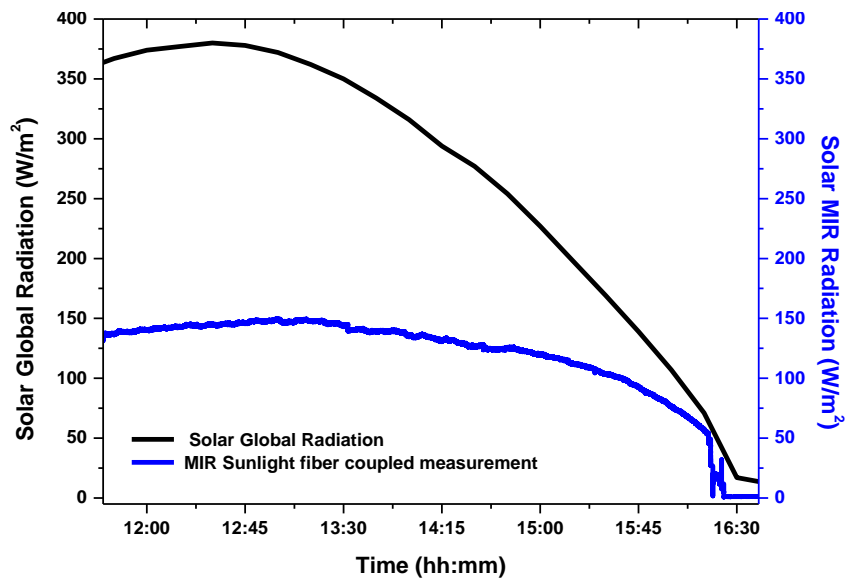


Figure 2.32 Measured sunlight intensities (blue curve) in comparison with a reference from a "Davis Vantage Pro2" weather station (black curve). Note : conversion from the measured intensity (in [V]) to the radiation (in $[\text{W}/\text{m}^2]$) is given in Appendix 3.

Conclusion

In this chapter, instrumental considerations and device specifications for design of a LHR, such as sun-tracker, blackbody, LO laser, photomixer, RF receiver (amplifier, band-pass filter, and square law detector), and LIA are introduced. Two sunlight collection configurations including free-space telescope cage system adapted to a heliostat and mid-IR fiber coupling system adapted to an EKO sun-tracker are considered and designed. The polycrystalline mid-IR fiber coupling sunlight system is tested and evaluated, which confirms the fiber coupling ability and the tracking performance of the sun-tracker.

Two LHR prototypes have been developed during this PhD works for field measurements : (1) a proof of concept mid-IR LHR involving a free-space cage system for sunlight coupling, and (2) a fully transportable LHR involving a polycrystalline IR-fiber coupling sunlight system.

References

- [1] C. Y. Lee, P. C. Chou, C. M. Chiang, and C. F. Lin. Sun tracking systems: a review, *Sens. (Basel)*, 2009, **9**, 3875-3890
- [2] M. Gisi, F. Hase, S. Dohe, and T. Blumenstock. Camtracker : A new camera controlled high precision solar tracker system for FTIR-spectrometers. *Atmos. Meas. Tech.* 2011, **4**, 47-54.
- [3] M. Mammez, R. Vallon, F. Polak, B. Parvitte, and V. Zéinari. Design and implementation of a heliostat for atmospheric spectroscopy, *Infrared Phys. Technol.* 2019, **97**, 235-243.
- [4] A. Hoffmann, N. A. Macleod, M. Huebner, and D. Weidmann. Thermal infrared laser heterodyne spectroradiometry for solar occultation atmospheric CO₂ measurements, *Atmos. Meas. Tech.* 2016, **9**, 5975-5996.
- [5] E. L. Wilson, M. L. McLinden, and J. H. Miller. Miniaturized laser heterodyne radiometer for measurements of CO₂ in the atmospheric column, *Appl. Phys. B* 2014, **114**, 385-393.
- [6] L. S. Rothman, I. E. Gordon, A. Barbe, D. C. Benner, P. F. Bernath, M. Birk, V. Boudon, L.R. Brown, A. Campargue, J. P. Champion, K. Chance, R. R. Gamache, A. Goldman, D. Jacquemart, I. Kleiner, N. Lacome, W. Lafferty, O. V. Naumenko, A. V. Nikitin, J. Orphal, V. I. Perevalov, A. Perrin, A. Predoi-Cross, C. P. Rinsland, M. Rotger, M. Simeckova, M. A. H. Smith, K. Sung, S. A. Tashkun, J. Tennyson, R. A. Toth, A.C. Vandaele, and J. Vander Auwera. The HITRAN 2008 molecular spectroscopic database, *J. Quant. Spectrosc. Radiat. Transf.* 2009, **110**, 533-572.
- [7] C. A. Cantrell, J. A. Davidson, A. H. Mcdaniel, R. E. Shetter, and J. G. Calvert. Infrared absorption cross sections for N₂O₅, *Chem. Phys. Lett.* 1988, **148**, 358-363.
- [8] X. Cui, F. Dong, M. W. Sigrist, Z. Zhang, B. Wu, H. Xia, T. Pang, P. Sun, E. Fertein, and W. Chen. Investigation of effective line intensities of trans-HONO near 1255 cm⁻¹ using continuous-wave quantum cascade laser spectrometers, *J. Quant. Spectrosc. Radiat. Transfer* 2016, **182**, 277-285.
- [9] Application note (Skyworks Solutions, Inc.) : Mixer and detector diodes, 200826 Rev. A. Skyworks proprietary information, August 19, 2008.
- [10] I. Pelant and J. Valenta. Luminescence spectroscopy of semiconductors, Oxford Scholarship Online, 2012.

- [11] S. Brodersen. Noise filter effects in recording spectroscopes, *J. Opt. Soc. Am.* 1953, **43**, 1216-1220.
- [12] W. Demtröder. *Laser spectroscopy : basic concepts and instrumentation*, Springer-Verlag Berlin Heidelberg, 1996.
- [13] D. Weidmann. *Radiometrie heterodyne infrarouge par diode laser accordable* (Doctoral dissertation), Reims University, Reims, France, 2002.
- [14] T. Tsai, R. A. Rose, D. Weidmann, and G. Wysocki. Atmospheric vertical profiles of O₃, N₂O, CH₄, CCl₂F₂, and H₂O retrieved from external-cavity quantum-cascade laser heterodyne radiometer measurements, *Appl. Opt.* 2012, **51**, 8779-8792.
- [15] J. Wang, G. Wang, T. Tan, G. Zhu, C. Sun, Z. Cao, X. Gao, and W. Chen. Mid-infrared laser heterodyne radiometer (LHR) based on a 3.53 μm room-temperature interband cascade laser, *Opt. Express* 2019, **27**, 9610-9619.

Chapter 3 Performance evaluation of the local oscillator being used

Objective

This chapter will present the evaluation of the performance of an external-cavity quantum cascade laser (EC-QCL) that will be used as a local oscillator (LO) in our mid-IR LHR system. The performance was evaluated, in terms of laser emission line width, single mode wavelength tunability, stabilization of the LO source and wavelength-dependent baseline, via real-time monitoring of nitrous oxide (N_2O) produced in a chemical catalysis process. This work was carried out in collaboration with the « Unité de Chimie Environnementale et Interactions sur le vivant (UCEIV) » of the ULCO.

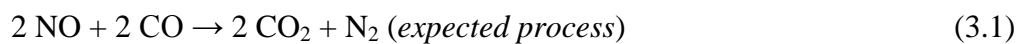
In the context of climate change mitigation, reuse of carbon dioxide (CO_2) represents a great interest for applications in chemical industry and power generation. For this purpose, CO_2 must be purified. Combustion processes lead to high amounts of CO_2 but still with impurities and also accompanied by toxic gases (mainly NO and CO). A catalytic reduction process of NO (to N_2) while oxidizing CO into CO_2 is a promising method to purify the CO_2 in combustion processes. However, nitrous oxide (N_2O), having a global warming potential of 300 times greater than CO_2 , may be a by-product from this process. It is therefore necessary to optimize the chemical reaction conditions to minimize N_2O production.

3.1 Introduction

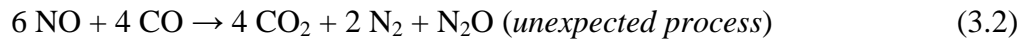
The characteristics of a laser source used as a LO largely determine the performance of a LHR instrument. The laser source should primarily fulfill the following requirements : narrow laser emission line width (for high spectral resolution and hence high spatial resolution in LHR measurements), single-mode emission and mode-hop free wavelength tunability (high precision spectroscopic measurement), as well as a wavelength-dependent baseline as smooth as possible (for high quality spectral normalization). Performance of the external-cavity quantum cascade laser (EC-QCL) being used as a LO was evaluated via the concentration measurement of trace gas N_2O produced during a chemical catalysis process of carbon dioxide (CO_2) purification.

CO_2 is responsible for 55-60% of anthropogenic radiative forcing on global warming. To reduce CO_2 injected into the atmosphere, reuse of CO_2 is a promising and alternative solution,

because CO₂ is a valuable industrial gas for chemical industrial applications and power generation [1]. For this purpose, CO₂ should be as pure as possible. Purification of CO₂ can be performed through the oxyfuel-combustion which allows one to obtain a rich CO₂ stream with the highest purity (80%-98%) [2]. In an oxyfuel system, the combustion flow consists of O₂ and CO₂. This Process emits also water vapor (H₂O), unburned components such as carbon monoxide (CO) generated by incomplete combustion and nitrogen monoxide (NO) due to the oxidation of nitrogen (N₂) included in the fuel. Purifying CO₂ in an exhaust flow from the oxyfuel-combustion can be realized through the reduction of NO to N₂ by oxidizing CO into CO₂ over catalysts [2], as shown in Eq. (3.1) below [4] :



However, products from the chemical process above is, like any chemical reaction, depending upon the reaction conditions (quantity of NO and CO, temperature, pressure, presence of oxygen and water vapor or not), kind of catalyst (active phase, metal dispersion, support type) and synthesis method, etc. N₂O may be a by-product from the above NO-CO reaction [3] :



As N₂O is a very powerful greenhouse gas with a global warming potential of 300 times greater than CO₂, it is therefore necessary to optimize the catalytic reaction conditions to minimize the N₂O production.

In the present work, tunable diode laser absorption spectroscopy (TDLAS) technique is applied to in situ monitor the production of N₂O during the catalytic reaction of NO with CO.

3.2 Experimental details

3.2.1 N₂O monitoring by long optical path absorption spectroscopy

The experimental setup is shown in Fig. 3.1. A continuous-wave EC-QCL (TLS-41000-MHF, Daylight solutions Inc.), being used as a LO in our mid-LHR experiment, is coupled to a modified-Herriot multi-pass cell. The EC-QCL frequency is scanned across an appropriate N₂O absorption line to determine its concentration-dependent integrated absorbance by fitting the experimental absorption spectrum to a Voigt profile model. The fine frequency tuning of the EC-QCL is realized by applying a 50 Hz sine-wave signal (with an amplitude of +3.0 V_{PP} and an offset of +1.6 V_{DC}) from a function generator to the PZT (Piezoelectric ceramic

transducer) element of the external cavity of the EC-QCL. As shown in Fig. 3.1 (left), 10% reflected laser beam is sent to a Fabry-Perot etalon for laser frequency calibration, and 90% transmitted laser beam is directed into the multi-pass cell to probe long optical path absorption of N₂O.

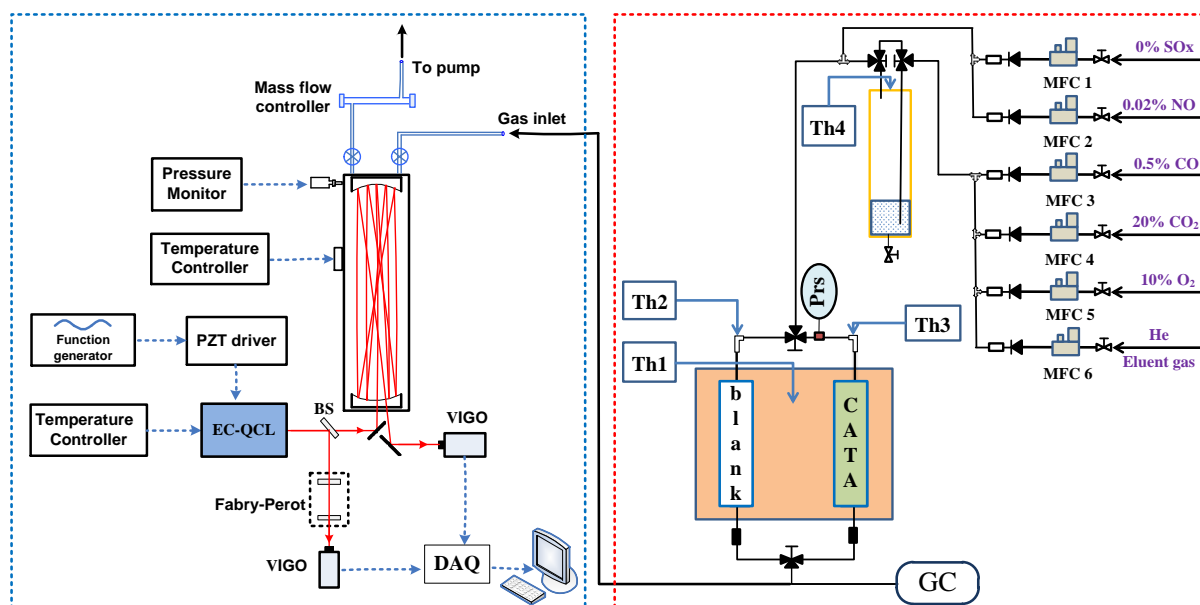


Figure 3.1 Experimental setup used for N₂O monitoring of a chemical catalysis reaction of NO with CO. BS: beam splitter; GC: gas chromatograph; MFC 1, 2, 3, 4, 5, 6: mass flow controllers; Th 1: thermocouple in the oven, Th 2: thermocouple in the blank, Th 3: thermocouple in the reactor, Th 4: thermocouple in the saturator; Prs: pressure sensor; VIGO: thermoelectrically cooled infrared photovoltaic detector; DAQ: data acquisition card.

The used 3.2 L modified-Herriot multi-pass cell (New Focus, Model 5612) is formed with two high reflectivity mirrors (separated by ~55 cm). Laser light enters and exits the multi-pass cell through a common hole equipped with a wedged coupling window at the front of the cell. In the present work, 90 passes were made between the mirrors resulting in an effective optical path length of 50 m. The exiting laser beam from the multi-pass cell is focused into a thermoelectrically cooled infrared photovoltaic detector (PVI-4TE-10.6, VIGO System S.A). A National Instruments data acquisition card (PCI 6251, NI Inc.), controlled with a LabVIEW program, is used for data sampling and acquisition. The recorded data is digitalized and transferred to a laptop for further data processing to retrieve N₂O concentration.

3.2.2 Selection of a N₂O absorption line for sensitive and selective concentration measurement

High spectral resolution is required in spectroscopic measurement for discrimination of the target gas absorption from absorptions of other interfering species. Careful selection of appropriate absorption line(s) well isolated from other interference absorptions was performed. Fig. 3.2 shows a simulation spectrum of the selected N₂O absorption line (centered at 1261.0598 cm⁻¹ with a line intensity of 9.677E-20 cm/molecule), based on the HITRAN database [5]. The simulation was calculated using 300 ppbv (parts per billion by volume) N₂O in a 50-m long absorption cell at 120 mbar. Meanwhile, potential interferences from 450 ppmv (parts per million by volume) CO₂ and 1% H₂O vapor were taken into account in the simulation. As can be seen in Fig. 3.2, this selected line is well isolated and spectral interference free from CO₂ and H₂O. It is a good tradeoff between the required sensitivity and selectivity for quantitative measurement of N₂O by direct absorption spectroscopy in a 50-m long optical path at 120 mbar.

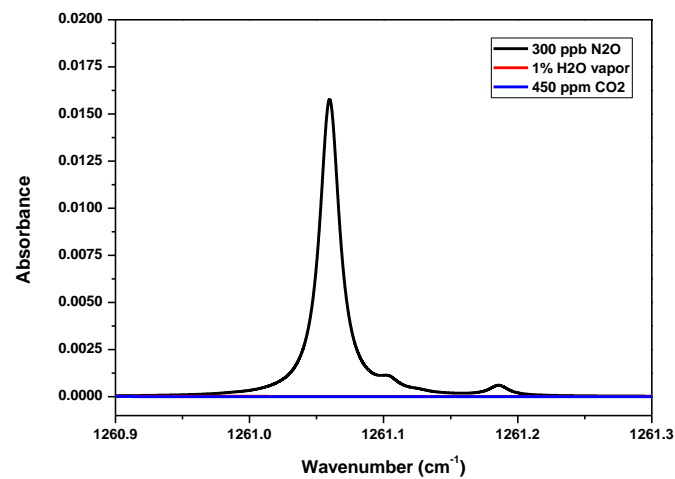


Figure 3.2 Simulation spectra of 300 ppbv N₂O, 1% H₂O, and 450 ppmv CO₂ absorptions in a multi-pass cell ($L_{\text{eff}}=50$ m) at 120 mbar.

3.2.3 Frequency metrology and N₂O absorption spectrum retrieval

The N₂O absorption signal was recorded versus the data point number when scanning the EC-QCL frequency around 1261.0598 cm⁻¹ using PZT scan mode. For the conversion of this absorption signal (a) to an absorption spectrum (d) (Fig. 3.3), interference fringes from a home-made Fabry-Perot etalon with a free spectral range (FSR) of 1 GHz (~0.0333 cm⁻¹) were recorded (b) and used to determine the relationship between the data point number and

the corresponding frequency in wavenumber (c). The absolute frequency was determined with the help of the N₂O absorption frequency provided by the HITRAN database [5].

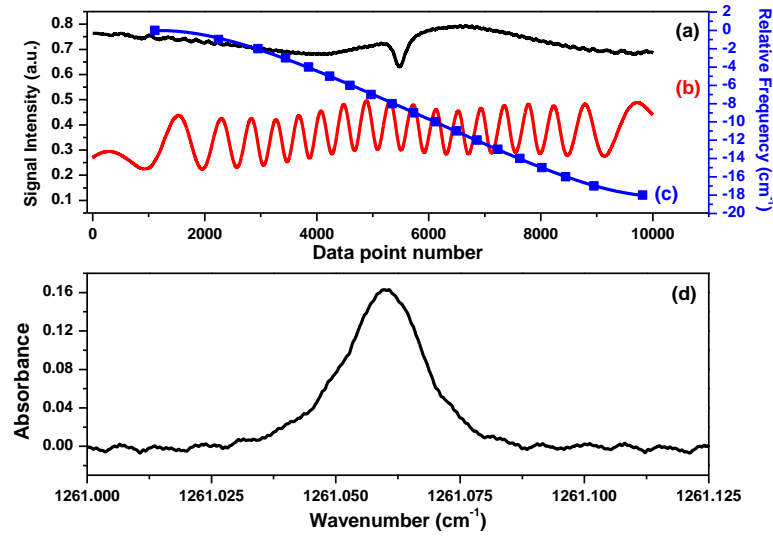


Figure 3.3 Absorption signal of 5 ppmv N₂O at 120 mbar (a) and its absorption spectrum (d), obtained using the relative wavenumber calibration curve (c) which allows one to convert “data point number” into “wavenumber” through the FSR of the used etalon (b).

3.2.4 N₂O concentration retrieval

N₂O concentration can be determined based on the Beer-Lambert law using known spectral parameters (such as absorption frequency, line intensity, etc.). In the present work, the N₂O concentration was deduced from a calibration curve of concentrations vs. integrated absorbances (over the scanned spectral range [6]). For this purpose, N₂O samples with different standard concentrations were produced using a high-precision gas dilutor (Model PPA 2000M, Calibrage Inc.).

A N₂O cylinder with a standard concentration of 1000 ppmv ($C_{initial}$) with different flow rates D_1 was mixed with N₂ gas (at a fixed flow rate D_2) in the gas dilutor. The concentration of the diluted N₂O (C_{final}) was calculated using the following equations :

$$C_{final} = C_{initial} / K \quad (3.3)$$

$$K = (D_1 + D_2) / D_1 \quad (3.4)$$

where K is the dilution factor, and D_2 is fixed at a constant rate of 2086 ml/min. Different N₂O concentrations were produced at 0.24, 0.51, 0.99, 1.46, 2.01, 2.48, 3.37 and 5.03 ppmv for calibration in the present work. The relevant settings and the obtained final concentrations are presented in Table 3.1.

Table 3.1 Relevant settings and the diluted concentration.

D ₁ [ml/min]	K	C _{initial} [ppmv]	C _{final} [ppbv]
0.50	4173.0	1000	239.64
1.06	1968.9	1000	507.89
2.06	1013.6	1000	986.56
3.06	682.7	1000	1464.77
4.20	497.7	1000	2009.38
5.16	405.3	1000	2467.53
7.06	296.5	1000	3373.05
10.55	198.7	1000	5032.08

The multi-pass cell was initially rinsed with pure nitrogen (N₂) before the measurements of N₂O. The ambient N₂O absorption spectra centered at 1261.0598 cm⁻¹ and N₂O at different concentrations produced by dilution were recorded at 120 mbar, as shown in Fig. 3.4 (a). The relationship between the integrated absorbance A_I obtained from nonlinear least-square fitting of Voigt profile and the corresponding N₂O concentration (Fig. 3.4 (b)) was obtained from a linear fit (r²=99.6) which allowed us to express N₂O concentration from the measured A_I through this calibration slope *k* :

$$C_{N_2O} = \frac{A_I}{k} \quad (3.5)$$

where $k = 7.7656E-4$.

Based on this calibration formula, the ambient N₂O concentration was determined to be about 325±7 ppbv. The total relative uncertainty of about 4% is mainly attributed to the uncertainties in the linear fit ($\Delta k/k < 2\%$) and in the Voigt profile fitting ($\Delta A_I/A_I < 2\%$).

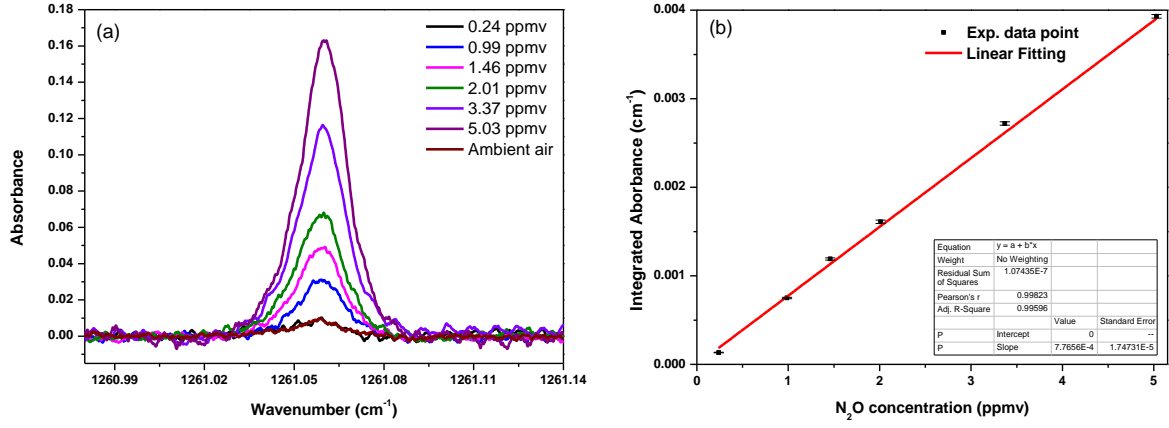


Figure 3.4 (a) N₂O absorption spectra at different concentrations at 120 mbar; (b) Plot of the integrated absorbance vs. concentration, associated with a linear fit. Error bars are one standard deviation of the integrated absorbance from Voigt profile fit.

3.2.5 Laser line width evaluation

The line width of the EC-QCL emission being used as a LO plays a key role in the spectral resolution of the LHR. This parameter was evaluated in the present work using spectroscopic method. As shown in Fig. 3.5, Voigt profile was fitted to an experimental absorption line of 6.13 ppm N₂O at a pressure of 120 mbar. In Voigt fit, the line width w_L is resulted from pressure induced collision broadening (Lorentzian line width, Δv_L), while the line width Δw_G is the convolution of the Gaussian line width (Δv_G) due to Doppler effect and the line broadening related to instrument function (laser line width, Δv_{LA}). The Voigt line width (Δv_V) can be expressed as follows [11] :

$$\Delta v_V = 0.5346\Delta w_L + (0.2166\Delta w_L^2 + \Delta w_G^2)^{1/2} = 0.5346\Delta v_L + \sqrt{0.2166\Delta v_L^2 + (\Delta v_G^2 + \Delta v_{LA}^2)} \quad (3.6)$$

where the Lorentz line width, Δv_L (FWHM, for Full Width at Half Maximum) was calculated to be 0.017035 cm⁻¹ [5] at 120 mbar. The Gaussian line width, Δv_G of 0.00236 cm⁻¹ was calculated from Eq. (3.7) [9] :

$$\Delta v_G = 7.16 \cdot 10^{-7} \cdot \nu_0 \sqrt{\frac{T}{M}} \quad (3.7)$$

with ν_0 the absorption center frequency (1261.0598 cm⁻¹), T the working temperature (300 K), and M the molecular mass (44 g/mole).

Based on the fitted Δw_G value of 0.00238 cm⁻¹, the laser line width Δv_{LA} can be given approximately by [10] :

$$\Delta v_{LA} = \sqrt{\Delta w_G^2 - \Delta v_G^2} \quad (3.8)$$

A laser line width (FWHM) of 9.2 MHz (0.000307 cm^{-1}) was experimentally deduced, which corresponds to a laser resolving power ($v_{LASER}/\Delta v_{LA}$) of about 10^7 . This result demonstrates that the EC-QCL is very suitable for use as a LO in the LHR system being developed and it could ensure the high spectral resolution requirement ($\Delta v_{LA} \leq$ conventional electronic filter bandwidth ranging from ~ 10 MHz to some tens of MHz).

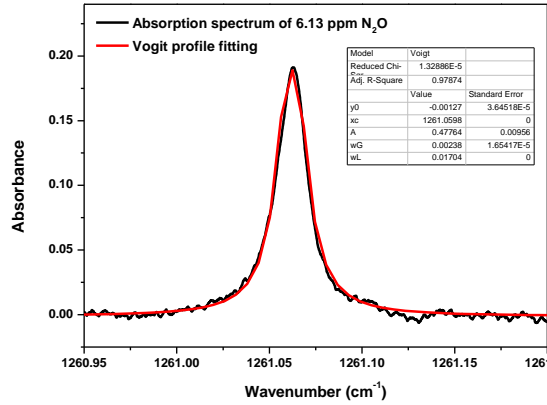


Figure 3.5 Absorption spectrum of 6.13 ppmv N_2O (black curve) at 120 mbar, accompanied with a Voigt profile fit (red curve).

3.2.6 Measurement precision and limit of detection (LoD)

Stability of an analytical instrument is an important parameter that affects the detection sensitivity and the measurement precision. Signal averaging is usually used to improve the detection sensitivity and the measurement precision. However, due to the instability of the instrument (such as changes in light intensity, laser wavelength shifts and detector dark noise drifts, temperature drifts, moving fringes, changes in background spectra, etc.), any actual system is only stable for a limited time, i.e. an optimal averaging time should be determined via an Allan variance analysis [7] in order to determine the max. averaging number, i.e. the best measurement precision.

Time series measurements of 1 ppmv N_2O absorption spectra were carried out for the Allan variance analysis to determine the optimal averaging time. 9000 consecutive direct absorption spectra of N_2O were experimentally recorded, with an acquisition time of 0.2 s per spectrum. Fig. 3.6 plots an Allan deviation as a function of the averaging time [8] based on the time series measurements of N_2O absorption spectra. The decaying slope (red dashed line) shows the efficient white noise reduction by signal averaging within a maximum averaging

time (system stability time) of about 236 s, which is mainly limited by the temperature and current stability of the QCL controller, but also constrained by other factors : stability of the optical setup (optical cell), or of the injected gas mixture. The corresponding measurement precision is 5.2 ppbv, leading to a relative uncertainty in measurement precision of 0.5%. After 236 s, the Allan deviation increases (blue dashed line), i.e. the instabilities of the instrumental system nevertheless counterbalances the noise reduction given by time-consuming average.

It's worth noting that this max. stabilization time of 236 s evinces also that the stability time of the used EC-QCL is at least as good as 236 s, which is very suitable for acquisition of LHR spectra (~ minute per spectrum).

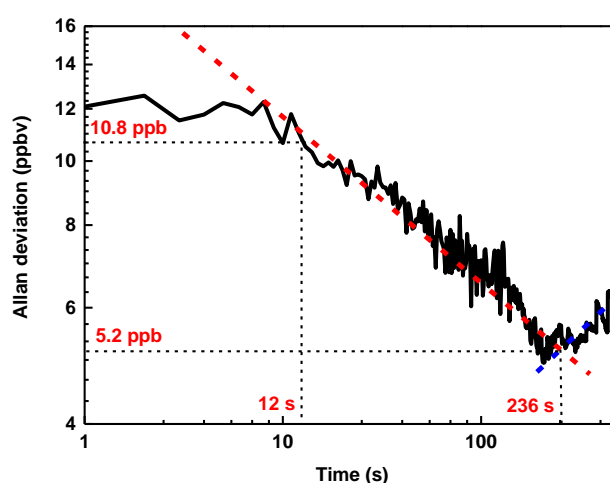


Figure 3.6 Allan deviation plot.

In the present work on monitoring a chemical reaction, a measurement precision of 10.8 ppbv (corresponding to a relative precision uncertainty of 1.1%) in 12 s was used to real-time track N_2O production.

Fig. 3.7 shows an experimental absorption spectrum of N_2O ($A_v=240$ in 12 s) in air at a pressure of 120 mbar, which resulted in a N_2O concentration of 325 ppbv. Based on the signal-to-noise ratio ($SNR \approx 10$) deduced from the residual of the Voigt profile fit to the experimental absorption spectrum of ambient N_2O , a 1σ ($SNR=1$) limit of detection was determined to be 32.5 ppbv in 12 s.

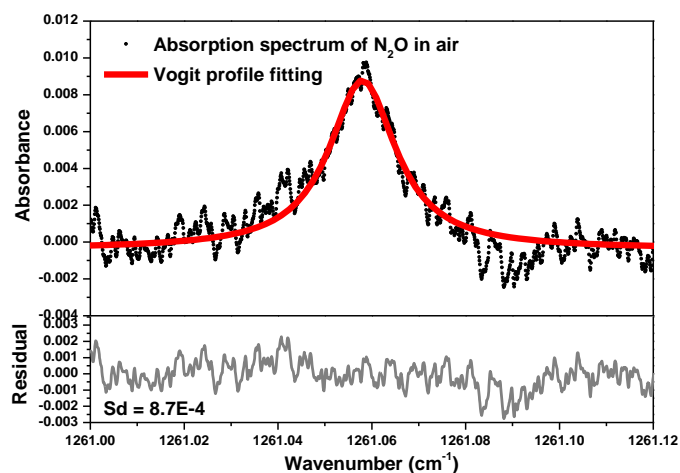


Figure 3.7 *upper panel*: absorption spectrum of N_2O in air (black curve) at 120 mbar, accompanied with a Voigt profile fit (red curve); *lower panel*: fit residual.

3.3 Experimental results and discussions

Fig. 3.8 (*left*) shows the experimental setup of the studied catalytic reaction. Reactant gases composed of 20% CO_2 , 10% O_2 , 0.5% CO , 0.02% NO and He (eluent gas) with a total flow rate of 200 mL/min. The products of CO_2 and N_2 from the catalytic reduction of NO by oxidizing CO were analyzed by an on-line gas chromatography (TranceGC 1300 XXL, Global Analyzer Solutions G.A.S, Inc.), NO was analyzed with a NO analyzer (Xentra 4900C, Servomex Inc.), NO_2 was measured with the same NO analyzer after conversion of NO_2 to NO by a converter BÜNOx (Bühler Technologies Inc.), while N_2O was monitored by the EC-QCL-based laser sensor as discussed above (Fig. 3.8 *right*).

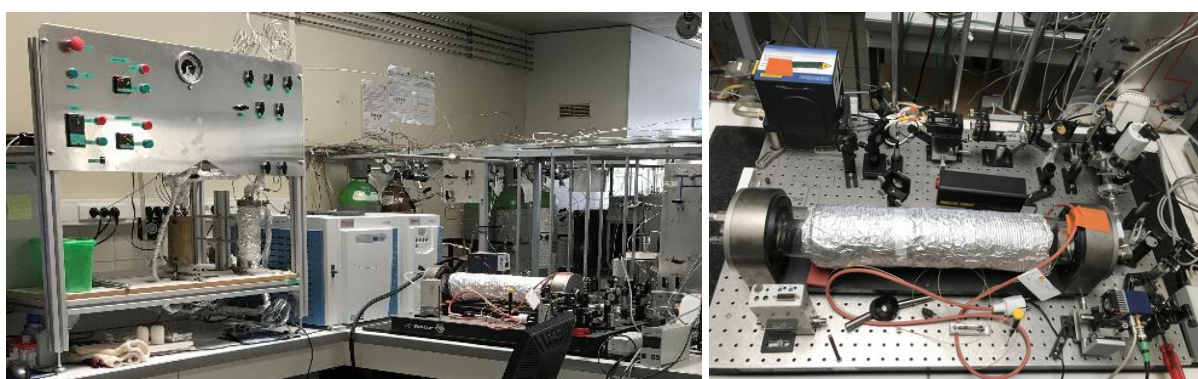


Figure 3.8 *left*: experiment of catalytic reaction of NO with CO to purify CO_2 in exhaust gas flow from oxyfuel-combustion; *right*: EC-QCL-based sensor of N_2O .

3.3.1 N₂O evolution in catalytic reaction of NO with CO

The catalytic reaction of NO with CO over a Pt/SiO₂ catalyst in the temperature range of 50-500 °C was performed, N₂O production was real-time monitored and analyzed using the developed EC-QCL sensor.

A typical N₂O absorption spectrum recorded during the process of NO reaction with CO over a Pt/SiO₂ catalyst at 190 °C is shown in Fig. 3.9. It was recorded at a pressure of 120 mbar in the multi-pass cell with 240 spectral averages in 12 s.

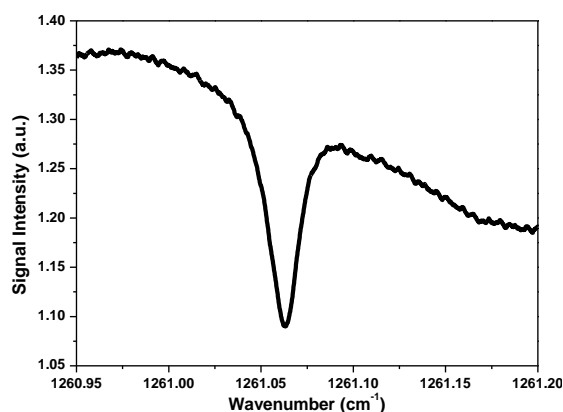


Figure 3.9 Absorption spectrum of 6.13 ppmv N₂O during a catalytic reaction of NO with CO over a Pt/SiO₂ catalyst at 190 °C at 120 mbar.

Fig. 3.10 shows time series measurement (with a step of 1 °C from 50 to 500 °C) of N₂O concentrations produced during the NO-CO reaction over the Pt/SiO₂ catalyst. A max. concentration of ~6.1 ppmv N₂O was observed at 190 °C.

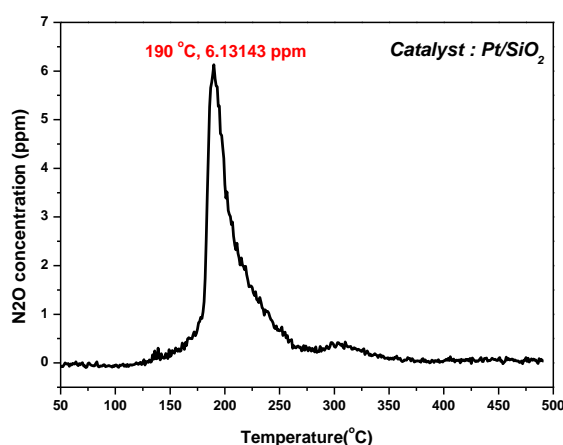


Figure 3.10 Time series measurement of N₂O concentration during a NO-CO reaction over a Pt/SiO₂ catalyst vs. temperature.

Based on the real-time monitoring of N₂O concentration, optimal catalytic reaction condition for zero N₂O production was experimentally determined [12].

Conclusion

In this chapter, the performance of an EC-QCL, that will be used as a LO in the LHR system, was evaluated in terms of laser emission line width, single-mode wavelength tunability, stabilization of the LO source and wavelength-dependent baseline. Based on the analysis of the measured N₂O absorption spectra, the EC-QCL emission line width of 9.2 MHz was deduced. A stable operation time of the LO as good as 236 s was estimated using Allan variance analysis, it is suitable for LHR measurement of molecular absorption spectrum. The EC-QCL is mode-hop free continuously tunable with a smooth baseline. In fact, in a LHR instrument, spectral baseline is mainly determined by the laser (LO) power variation when scanning the laser wavelength across the target molecular absorption feature. It's thus highly desirable to have a laser power induced spectral baseline as smooth as possible in order to obtain high quality retrieval of atmospheric LHR spectrum.

This work allowed us not only to evaluate the spectral performance of the EC-QCL for use as a LO in our mid-IR LHR instrument being developed, but also to demonstrate the potential of the EC-QCL for in-situ, real time and direct monitoring (without any sample preparation) of chemical catalysis process

References

- [1] M. Tahir and N. S. Amin. Recycling of carbon dioxide to renewable fuels by photocatalysis : Prospects and challenges, *Renew Sust. Energ. Rev.* 2013, **25**, 560-579.
- [2] C. Iloeje, R. Field, and A. F. Ghoniem. Modeling and parametric analysis of nitrogen and sulfur oxide removal from oxy-combustion flue gas using a single column absorber, *Fuel* 2015, **160**, 178-188.
- [3] K. Skalska, J. S. Miller, and S. Ledakowicz. Trends in NO_x abatement : A review, *Sci. Total Environ.* 2010, **408**, 3976-3989.
- [4] V. I. Pârvulescu, P. Grange, and B. Delmon. Catalytic removal of NO, *Catal. Today* 1998, **46**, 233-316.
- [5] L. S. Rothman, I. E. Gordon, A. Barbe, D. C. Benner, P. F. Bernath, M. Birk, V. Boudon, L. R. Brown, A. Campargue, J. P. Champion, K. Chance, R. R. Gamache, A. Goldman, D. Jacquemart, I. Kleiner, N. Lacome, W. Lafferty, O. V. Naumenko, A. V. Nikitin, J. Orphal, V. I. Perevalov, A. Perrin, A. Predoi-Cross, C. P. Rinsland, M. Rotger, M. Simeckova, M. A. H. Smith, K. Sung, S. A. Tashkun, J. Tennyson, R. A. Toth, A. C. Vandaele, and J. V. Auwera. The HITRAN 2008 molecular spectroscopic database, *J. Quant. Spectrosc. Radiat. Transfer* 2009, **96**, 139-204.
- [6] X. Cui, C. Lengignon, T. Wu, W. Zhao, G. Wysocki, E. Fertein, C. Coeur , A. Cassez, L. Crois é W. Chen, Y. Wang, W. Zhang, X. Gao, W. Liu , Y. Zhang, and F. Dong. Photonic sensing of the atmosphere by absorption spectroscopy, *J. Quant. Spectrosc. Radiat. Transfer* 2012, **113**, 1300-1316.
- [7] P. Werle. Tunable diode laser absorption spectroscopy : Recent findings and novel approaches, *Infrared Phys. Technol.* 1996, **37**, 59-66.
- [8] P. Werle, R. Mücke, and F. Slemr. The limits of signal averaging in atmospheric trace-gas monitoring by tunable diode-laser absorption spectroscopy (TDLAS), *Appl. Phys. B* 1993, **57**, 131-139.
- [9] B. H. Armstrong. Spectrum line profiles : The Voigt function, *J. Quant. Spectrosc. Radiat. Transfer* 1967, **7**, 61-88.
- [10] G. Blanquet, J. Walrand, and J. P. Bouanich. Diode-laser measurements of O₂-broadening coefficients in the ν_3 band of CH₃³⁵Cl, *J. Mol. Spectrosc.* 1993, **159**, 137-143.

- [11] J. J. Olivero and R. L. Longbothum. Empirical fits to the Voigt line width : A brief review, *J. Quant. Spectrosc. Radiat. Transfer* 1977, **17**, 233-236.
- [12] F. Shen, J. Akil, G. Wang, C. Poupin, R. Cousin, S. Siffert, E. Fertein, T. Ba, and W. Chen. Real-time monitoring of N₂O production in a catalytic reaction process using mid-infrared quantum cascade laser, *J. Quant. Spectrosc. Radiat. Transfer* 2018, **221**, 1-7.

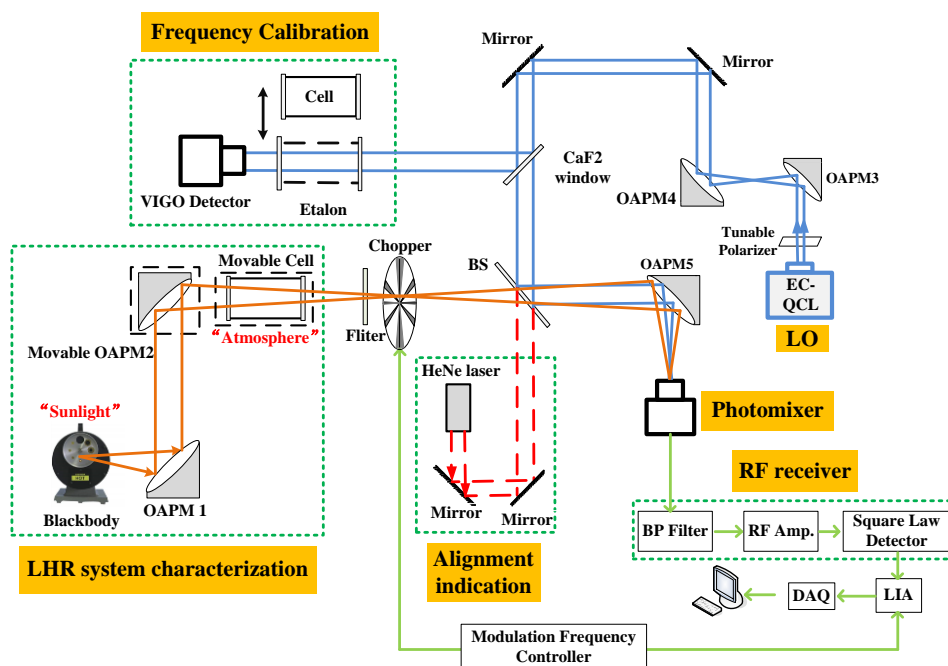
Chapter 4 Development of a proof of concept mid-IR LHR

Objective

In this Chapter, the development of a proof of concept (PoC) mid-IR LHR is presented. The developed LHR was tested on the QualAir platform of the universit   Pierre et Marie Curie (UPMC), in collaboration with the « Laboratoire d'  tudes du Rayonnement et de la Mati  re en Astrophysique et Atmosph  res (LERMA) » of the UPMC (Dr. Yao TE). Ground-based measurements of tropospheric CH₄ in the atmospheric column were performed.

4.1 A PoC LHR operating at 8   m

The developed PoC LHR is schematically shown in Fig. 4.1. A typical LHR receiver includes a sunlight collection system associated with a sun-tracker, a local oscillator, a photomixer, a RF receiver, a signal modulation and demodulation module, as well as a frequency metrology module (in our case direct absorption of the target molecule in a 12.5-cm long single-pass reference cell was used). To characterize and optimize the performance of the developed PoC LHR receiver, a stable blackbody source was used as sunlight. Heterodyne measurements of CH₄ absorption spectra were performed in a 12.5-cm single-pass cell in laboratory.



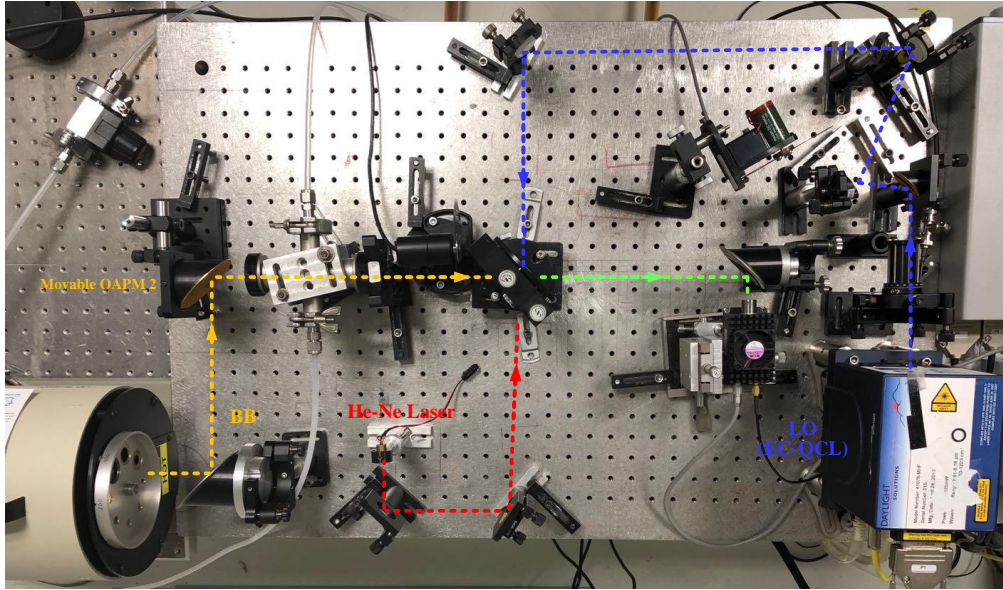


Figure 4.1 *upper*: schematic of the developed LHR receiver. BS: Beam splitter; OAPM: off axis parabolic mirror; photomixer: VIGO detector (Model PVI-4TE-10.6, VIGO System S.A.); BP Filter: band-pass filter (27-33MHz, Model 15542, Mini-Circuits®); LIA: lock-in amplifier; *lower*: picture of the developed 8- μm mid-IR LHR in the present work. Orange dot line : blackbody beam path; red dot line : He-Ne laser beam path; blue dot line : LO (EC-QCL) beam path; green dot line : combined LO-BB beams to photomixer.

Radiation from a blackbody (BB, MODELS 67030, Newport Inc.) is collected and collimated with off-axis parabolic mirror (OAPM) 1 ($f_1 = 120$ mm) and OAPM 2 ($f_2 = 75$ mm). The BB beam is filtered by an optical filter (in Germanium in order to limit the bandwidth of the incident radiation and let only the transmission of the radiation at wavelengths longer than 7 μm and shorter than 12 in our case to minimize detected source shot noise [1]). Amplitude modulation of the injected BB beam is made at 1 kHz using a chopper located at the real focal point of OAPM2. It is then directed to a 5%R / 95%T beam splitter (in CaF_2). The BB beam will be superimposed with the LO beam from the EC-QCL (TLS-41000-MHF, Daylight solutions Inc.) which is size-expanded by two OAPMs ($f_3 = 12.7$ mm and $f_4 = 38.1$ mm), intensity-controlled and polarization-adjusted using a wideband IR polarizer (2 μm -12 μm , PGC-5, Innpho. Inc.). The combined beams are focused by OAPM 5 ($f_5 = 12.7$ mm) onto a VIGO photomixer (PVI-4TE-10.6, VIGO System S.A.).

The beat note signal at $|\omega - \omega_L|$ in the radio frequency (RF) domain, generated from the photomixer, enters the RF receiver through a 27-33 MHz band-pass filter (Model 15542, Mini-Circuits®) followed by 2-stage low noise amplifiers (Model ZFL-500LN+, Mini-Circuits®) with a gain of 24 dB each. After that, the amplified beat signal is connected to a square-law Schottky diode (Model 8472B, Keysight Inc.) for power measurement of the RF

signal that is proportional to the square of the input beat signal amplitude. The output signal from the square law detector is demodulated with a lock-in amplifier (LIA, Model 5110, AMETEK Inc.). A National Instruments data acquisition card (PCI 6251, NI Inc.) is used to digitalize the output signal from the LIA via a LabVIEW program. The data is then transferred to a laptop for further data processing.

4.2 LHR performance characterization

4.2.1 Beat signal generation

Beat signal was generated by mixing the blackbody (67030, Newport Inc.) radiation and the EC-QCL (LO) light (the frequency was set at a non-absorption position to avoid any air absorption within the optical path). Time series measurements of the RF signal from the lock-in amplifier were carried out. During the experimental measurements, the effective LO power-induced amplitude measured with the photomixer was 2.5 V. Time constant of the lock-in amplifier was set at 1 s and using LP filters (12 dB/oct).

4.2.1.1 SNR of the beating signal

SNR of the generated beat signal was experimentally determined to investigate the quality of the generated beat signal. Based on the measurement of a beat note amplitude of 79.82 μV and a noise level (1 standard deviation) of 0.67 μV in the beat note (Fig. 4.2), a SNR of ~ 119 was deduced for the generated beat signal.

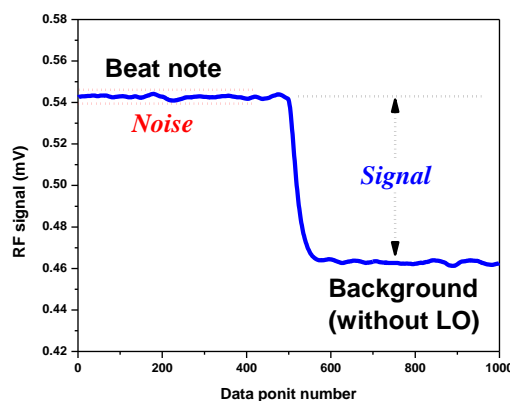


Figure 4.2 Beat note signal measured at the output of the LIA.

Blackbody temperature was set at $T_{\text{BB}} = 1000^\circ\text{C}$. Throughout the optical system up to the photomixer, overall optical coupling efficiency (κ) of the blackbody radiation in the free-space LHR receiver is 0.82, and it is mainly resulted from a silver-plated OAPM (assumed

reflectance ~ 0.97), two gold-plated OPAMs (assumed reflectance ~ 0.98), an optical filter (transmission ~ 0.975), a beam splitter (transmission ~ 0.95) and a BaF₂ wedged window in front of the photomixer (transmission ~ 0.95). The quantum efficiency of the photomixer η is 0.5 at 8 μm (provided by the manufacturer). The LHR double side bandwidth is 12 MHz and the time constant of the LIA is 1 s. Under these conditions, at fixed LO frequency (1242.3 cm^{-1} or 3.73×10^{13} Hz), the calculated ideal SNR (c.f. Eq. 1.57 in Chapter 1.5) is :

$$SNR_{\text{ideal}} = \frac{\eta \kappa \sqrt{B \tau}}{\exp\left(\frac{h\nu}{kT}\right) - 1} \approx 356 \quad (4.1)$$

This value is different from the experimentally deduced value of ~ 119 . The reason for this kind of difference will be discussed in Chapter 5.1.2.1.

4.2.1.2 Beating level vs. the LO power

Beat signal level as a function of the LO (EC-QCL) power was experimentally investigated (note : different experimental conditions from Section 4.2.1.1). The EC-QCL power intensities were monitored at the output of the photomixer and the beating levels were deduced from the difference of the LIA outputs with and without the injection of LO light. Beat signal amplitude versus LO signal level (in [mV]) is plotted in Fig. 4.3. As can be seen, the beat note increases linearly with the LO power, as predicted by Eq. (1.12) in Chapter 1.2.3. Heterodyning conversion efficiency can be deduced from the slope of the linear fit : P_{HET} (in mV) $\approx 0.09 * P_{\text{LO}}$ (in [V]), i.e. a heterodyning conversion efficiency of $\sim 10^{-4}$.

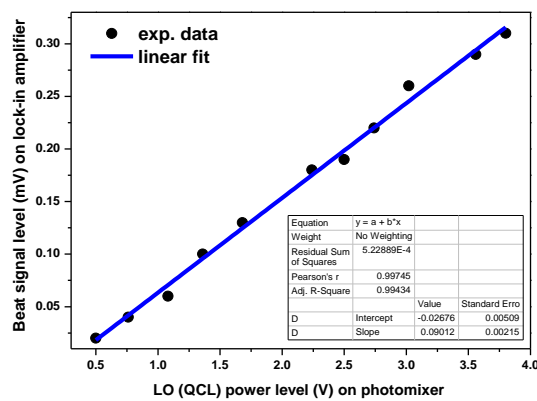


Figure 4.3 Beat note amplitude vs. LO power.

4.2.2 Laser heterodyne spectrum of CH₄

4.2.2.1 CH₄ absorption line selection for sensitive and selective heterodyne measurement

Spectral interference between atmospheric species, in particular with ubiquitous water vapor (H₂O) and carbon dioxide (CO₂) in the atmosphere, is a serious issue in a complex environment. Selection of suitable spectral lines for field test should be carefully addressed. Fig. 4.4 (a) shows an atmospheric absorption spectrum recorded with a high-resolution Fourier transform spectrometer (Bruker IFS 125HR) on the QualAir platform of the Université Pierre et Marie Curie (UPMC), accompanied with a HITRAN database-based [2] simulation spectrum of 5-km long absorption on the ground at atmospheric pressure. The following molecular species were taken into account : 0.5% H₂O, 2 ppm CH₄, 450 ppm CO₂ and 320 ppb N₂O (Fig. 4.4 (b)).

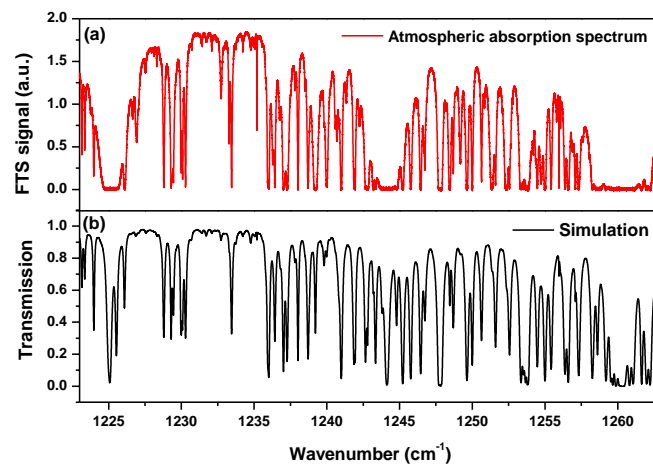


Figure 4.4 (a) Atmospheric absorption spectrum recorded with a Bruker IFS 125; (b) Simulation spectrum of multi-GHG using 0.5% H₂O, 2 ppm CH₄, 450 ppm CO₂ and 320 ppb N₂O in the range of 1223-1263 cm⁻¹.

Figs. 4.5 (a) and 4.6 (a) show atmospheric absorption spectra in the frequency range of 1241.3-1242.5 cm⁻¹ and 1261.2-1262.8 cm⁻¹, respectively; accompanied with HITRAN database [2] simulation spectra of multi-GHG (0.5% H₂O, 2 ppm CH₄, 450 ppm CO₂ and 320 ppb N₂O) in a 5-km long direct absorption scheme at atmospheric pressure (Figs. 4.5 (b) *black* and 4.6 (b) *black*). Figs. 4.5 (b) and 4.6 (b) simultaneously provide individual spectra of 0.5% H₂O (*blue*), 2 ppm CH₄ (*orange*), 450 ppm CO₂ (*pink*) and 320 ppb N₂O (*green*) for the HITRAN database [2] simulation.

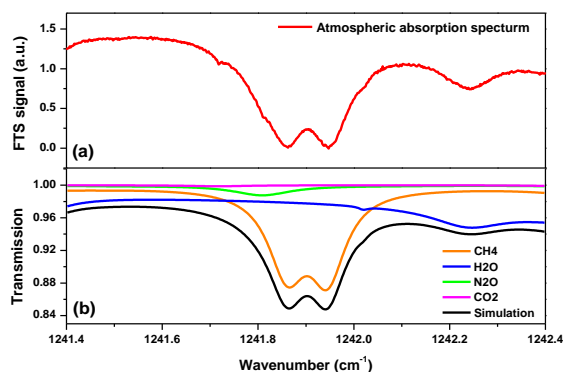


Figure 4.5 (a) Atmospheric absorption spectrum; (b) Simulation spectrum of multi-GHG using 0.5% H₂O, 2 ppm CH₄, 450 ppm CO₂ and 320 ppb N₂O (*black*); Individually simulated absorption spectra of 0.5% H₂O (*blue*), 2 ppm CH₄ (*orange*), 450 ppm CO₂ (*in pink*) and 320 ppb N₂O (*green*) in the range of 1241.3-1242.5 cm⁻¹ (Note : the absorption peak located at 1242.24 cm⁻¹ is H₂O).

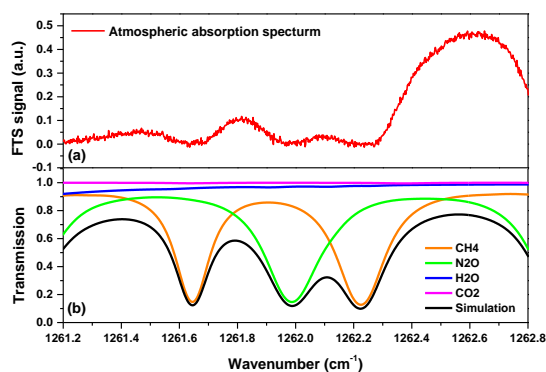


Figure 4.6 (a) Atmospheric absorption spectrum; (b) Simulation spectrum of multi-GHG using 0.5% H₂O, 2 ppm CH₄, 450 ppm CO₂ and 320 ppb N₂O (*black*); Individual Simulation spectra of 0.5% H₂O (*blue*), 2 ppm CH₄ (*orange*), 450 ppm CO₂ (*pink*) and 320 ppb N₂O (*green*) in the range of 1261.2-1262.8 cm⁻¹.

Based on the comparison and analysis, the CH₄ absorption lines (shown in Table 4.1) were selected in the present work for heterodyne measurement of atmospheric CH₄ absorption.

Table 4.1 Selected CH₄ and N₂O absorption lines.

Mol.	HITRAN		FTS*
	Wavenumber (cm ⁻¹)	Line intensity (cm/molecule)	Wavenumber (cm ⁻¹)
CH ₄	1241.8632	6.590E-21	1241.8626
CH ₄	1241.9489	6.596E-21	1241.9474
CH ₄	1261.6450	1.834E-20	1261.6370
N ₂ O	1261.9871	1.044E-19	1261.9854
CH ₄	1262.2249	2.748E-20	1262.2321

* FTS frequencies were obtained from the atmospheric absorption spectrum recorded with a FTS (Bruker IFS 125HR) on the QualAir platform of the UPMC (TCCON-Paris station).

4.2.2.2 Laser heterodyne spectrum of CH₄ absorption at 8 μm

In order to validate the spectroscopic performance of the developed LHR receiver, laser heterodyne spectrum and direct absorption spectrum of CH₄ at 8 μm were simultaneously measured and compared.

In this work, laser heterodyne spectrum of CH₄ absorption at 1233.46 cm⁻¹ was recorded with the experimental conditions as follows :

- temperature of the BB : 1000 °C,
- LO center frequency : 1233.25 cm⁻¹,
- scanning frequency : 100 mHz,
- scanning voltage and offset of a sine-wave signal : 3.0 V and 1.6 V, respectively,
- electronic filter bandwidth : 6 MHz (pass-band : 27-33 MHz),
- sensitivity and time constant of the LIA : 100 mV and 100 ms, respectively.

Radiation from the blackbody was collected and collimated with OAPM 1. It was then focused and directed by OAPM 2 towards a 12.5-cm long single-pass cell filled with CH₄ mixture in air at atmospheric pressure. The beam emerging from the cell was amplitude modulated at 1 kHz using the chopper. The beam filtered by an optical filter was directed to a beam splitter on which it was superimposed with the LO beam from the EC-QCL. The combined beams were focused by OAPM 5 onto the VIGO photomixer.

One part of the EC-QCL radiation separated by a beam splitter (CaF₂ window) was injected into a 12.5-cm single-pass cell filled with the CH₄ mixture in air at atmospheric pressure. The direct absorption spectrum of CH₄ in the single-pass cell was used to evaluate the laser heterodyne spectrum of CH₄ absorption.

A PZT driven by a sine-wave signal was used to scan the LO (EC-QCL) frequency, direct CH₄ absorption spectrum of the LO in the single-pass cell (Fig. 4.7 *upper*) and its heterodyne absorption spectrum of the incident BB radiation (Fig. 4.7, *lower*) were recorded simultaneously. Heterodyne and direct CH₄ absorption spectra were both fitted to a Lorentz profile (Fig. 4.7 *red*) with a fixed center absorption frequency at 1233.45545 cm⁻¹, respectively. The FWHM (Full Width at Half Maximum) of the Lorentz line width of ~0.1065 cm⁻¹) for the heterodyne CH₄ absorption spectrum (Fig. 4.7 *lower*) is well consistent with that of ~0.1068 cm⁻¹ for the direct CH₄ absorption spectrum (Fig. 4.7 *upper*). The difference in absorption depth was resulted from strong background signal of LHR system. This work demonstrates the functionality of the PoC LHR.

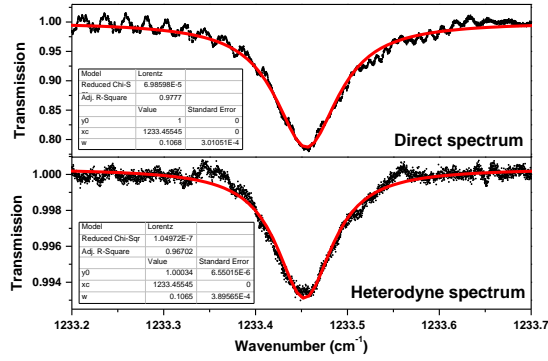


Figure 4.7 *upper*: direct absorption used as spectrum reference (*black*) fitted with a Lorentz profile (*red*); *lower*: heterodyne spectrum of CH₄ absorption near 8 μm (*black*) fitted with a Lorentz profile (*red*).

4.2.2.3 Frequency scanning speed vs. time constant of the LIA

The time constant (τ) in the LIA is a very critical parameter that impacts on noise suppression and absorption line-shape of the measured LHR spectrum. Longer time constant τ can significantly reduce the noise, but it also results in a shift of the spectral line center and distorts the line-shape [3]. In order to minimize such undesired effects, the time ΔT_{scan} for scanning through the halfwidth Δv_{HWHM} of the absorption line should be at least equal to 14 times of the time constant τ of the LIA (c.f. Chapter 2.1.6).

Experimental investigation on BB-based heterodyne spectra using different τ and ν_{sc} combination was carried out. Heterodyne spectra of CH₄ were recorded using four combinations of different τ and ν_{sc} (Table 4.2). The results are shown in Figs. 4.8-4.11(*black*).

Table 4.2 Used time constants at a given scanning speed of the LO frequency ν_{sc} . (Note : the spectral half width Δv_{HWHM} of the used CH₄ line around 1233.46 cm⁻¹ is 0.0538 cm⁻¹ [2] at ambient pressure.)

Scanning frequency (mHz)	20	50	100	250
Scanning period T (s)	25	10	5	2
Scanning range Δv_{scan} (cm ⁻¹)	0.787	0.787	0.787	0.787
halfwidth Δv_{HWHM} (cm ⁻¹)	0.0538	0.0538	0.0538	0.0538
Scanning speed ν_{sc} (cm ⁻¹ /s) = $\Delta v_{\text{scan}} / T$	0.03148	0.0787	0.1574	0.3935
Scanning time ΔT_{scan} (ms) = $\Delta v_{\text{HWHM}} / \nu_{\text{sc}}$	1709	684	342	137
τ (ms)	100	30	10	1
	300	100	30	10
	1000	300	100	30
	-	1000	300	-

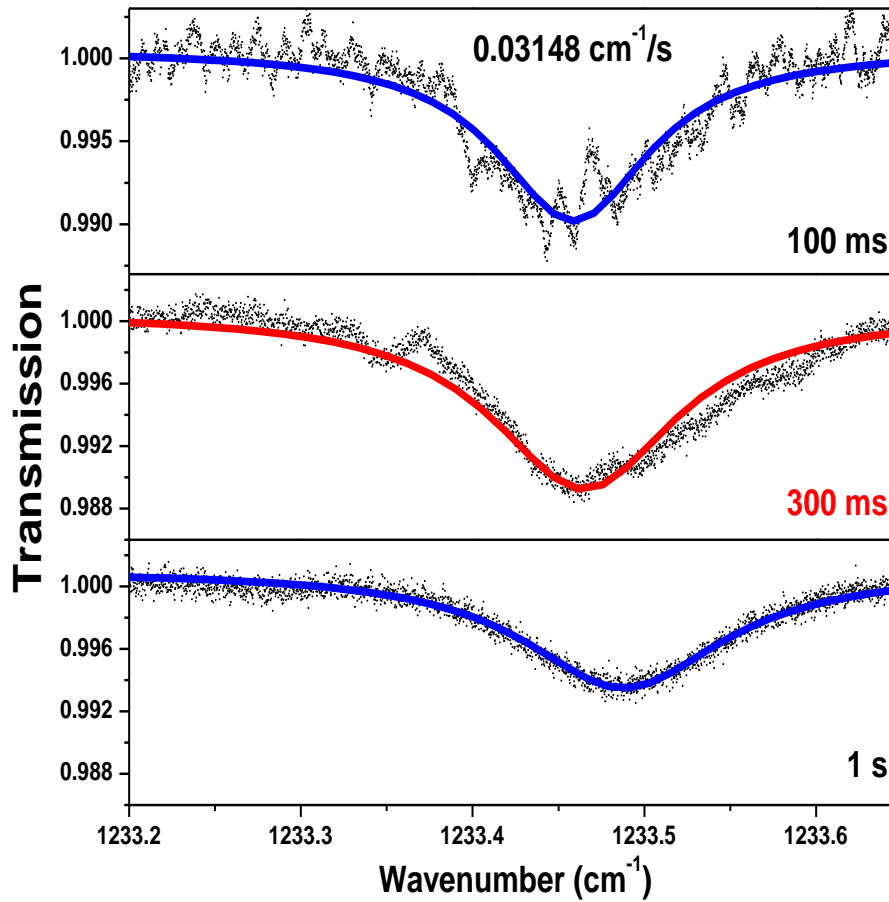


Figure 4.8 BB-based heterodyne spectra of CH₄ absorption at a scanning speed ν_{sc} of 0.03148 cm⁻¹/s (a scanning time ΔT_{scan} of 1709 ms) combined with different time constants, respectively.

Table 4.3 Analysis of BB-based heterodyne spectra of CH₄ absorption at the scanning speed of the LO frequency (ν_{sc}) of 0.03148 cm⁻¹/s (the scanning time (ΔT_{scan}) of 1709 ms) with different time constants (τ) (Fig. 4.8) (1 σ : Standard deviation).

ν_{sc} (cm ⁻¹ /s)	ΔT_{scan} (ms)	τ (ms)	SNR	$\Delta\nu_b$ (cm ⁻¹)	Absorption depth	$\delta\nu$ (cm ⁻¹)	Fit residual (1 σ)
0.03148	1709	100	5	0.0545	0.0126	0.0032	0.0026
		300	8	0.0656	0.0114	0.0095	0.0015
		1000	8	0.0711	0.0062	0.0325	0.0008

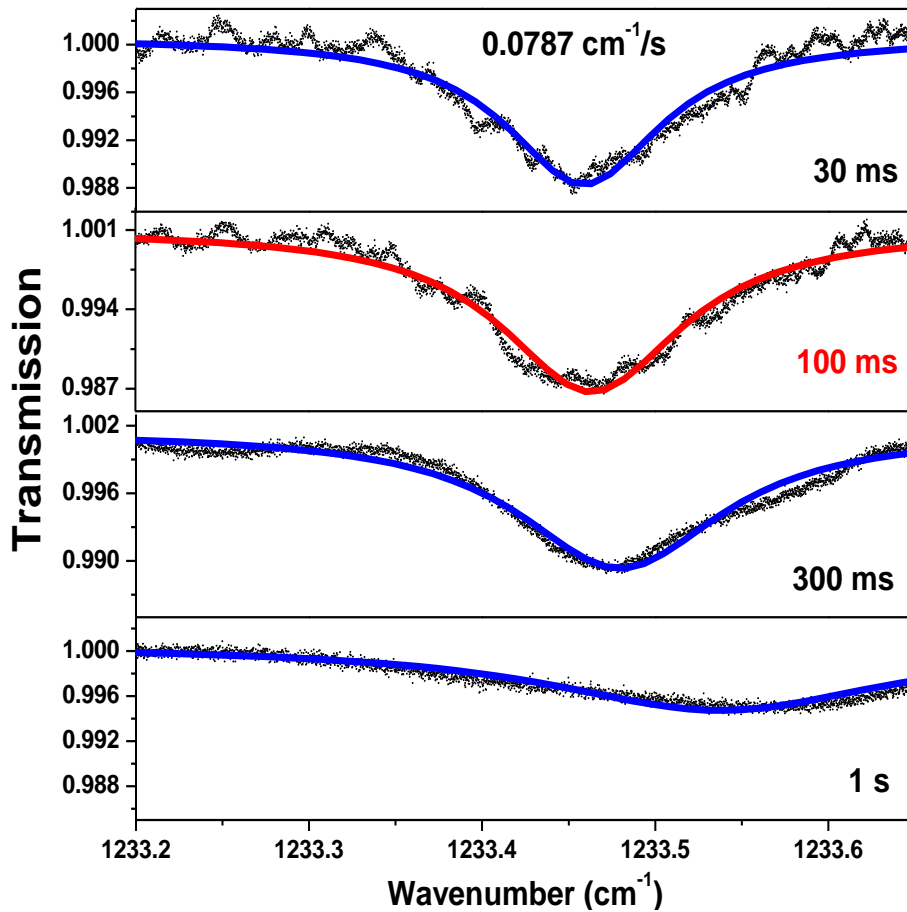


Figure 4.9 BB-based heterodyne spectra of CH₄ absorption at a scanning speed ν_{sc} of 0.0787 cm⁻¹/s (a scanning time ΔT_{scan} of 684 ms) combined with different time constants, respectively.

Table 4.4 Analysis of BB-based heterodyne spectra of CH₄ absorption at the scanning speed of the LO frequency (ν_{sc}) of 0.0787 cm⁻¹/s (the scanning time (ΔT_{scan}) of 684 ms) with different time constants (τ) (Fig. 4.9) (1 σ : Standard deviation).

ν_{sc} (cm ⁻¹ /s)	ΔT_{scan} (ms)	τ (ms)	SNR	$\Delta\nu_b$ (cm ⁻¹)	Absorption depth	$\delta\nu$ (cm ⁻¹)	Fit residual (1 σ)
0.0787	684	30	5	0.0548	0.01258	0.0031	0.00230
		100	6	0.0640	0.01244	0.0081	0.00210
		300	6	0.0722	0.01154	0.0243	0.00180
		1000	6	0.1222	0.00570	0.0821	0.00089

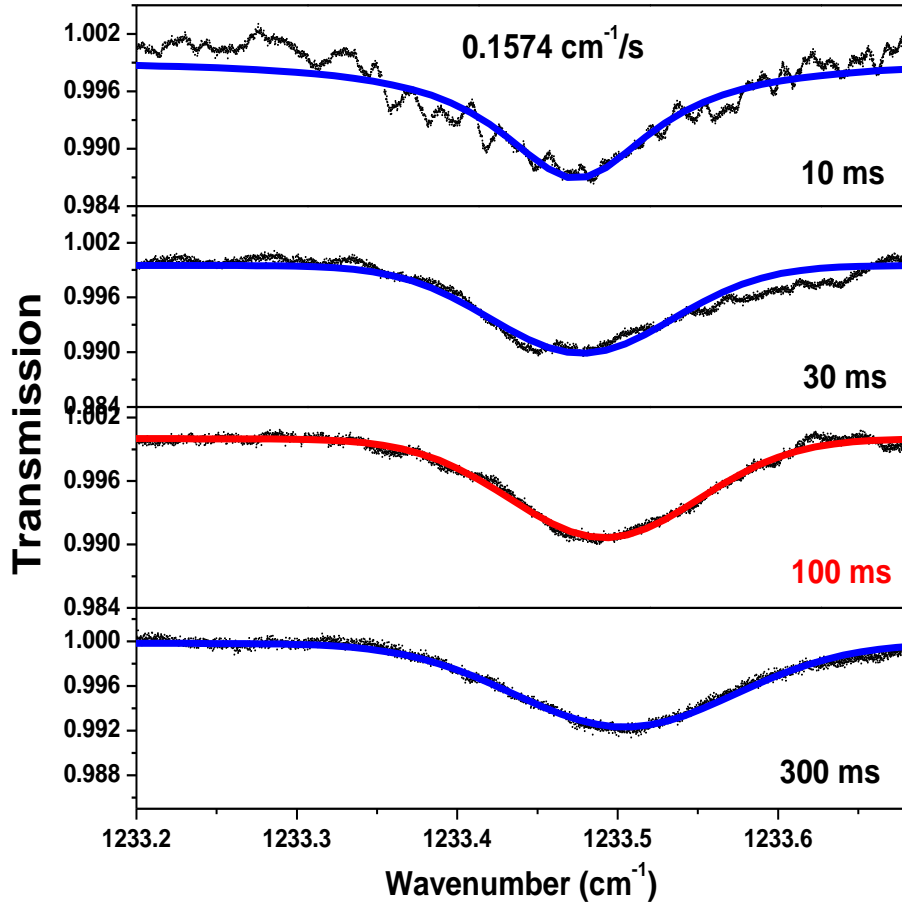


Figure 4.10 BB-based heterodyne spectra of CH₄ absorption at a scanning speed ν_{sc} of 0.1574 cm⁻¹/s (a scanning time ΔT_{scan} of 342 ms) combined with different time constants, respectively.

Table 4.5 Analysis of BB-based heterodyne spectra of CH₄ absorption at the scanning speed of the LO frequency (ν_{sc}) of 0.1574 cm⁻¹/s (the scanning time (ΔT_{scan}) of 342 ms) with different time constants (τ) (Fig. 4.10) (1 σ : Standard deviation).

ν_{sc} (cm ⁻¹ /s)	ΔT_{scan} (ms)	τ (ms)	SNR	$\Delta\nu_b$ (cm ⁻¹)	Absorption depth	$\delta\nu$ (cm ⁻¹)	Fit residual (1 σ)
0.1574	342	10	5	0.0550	0.01251	0.0016	0.00230
		30	6	0.0627	0.01204	0.0048	0.00209
		100	7	0.0672	0.01101	0.0181	0.00156
		300	7	0.0812	0.00824	0.0490	0.00115

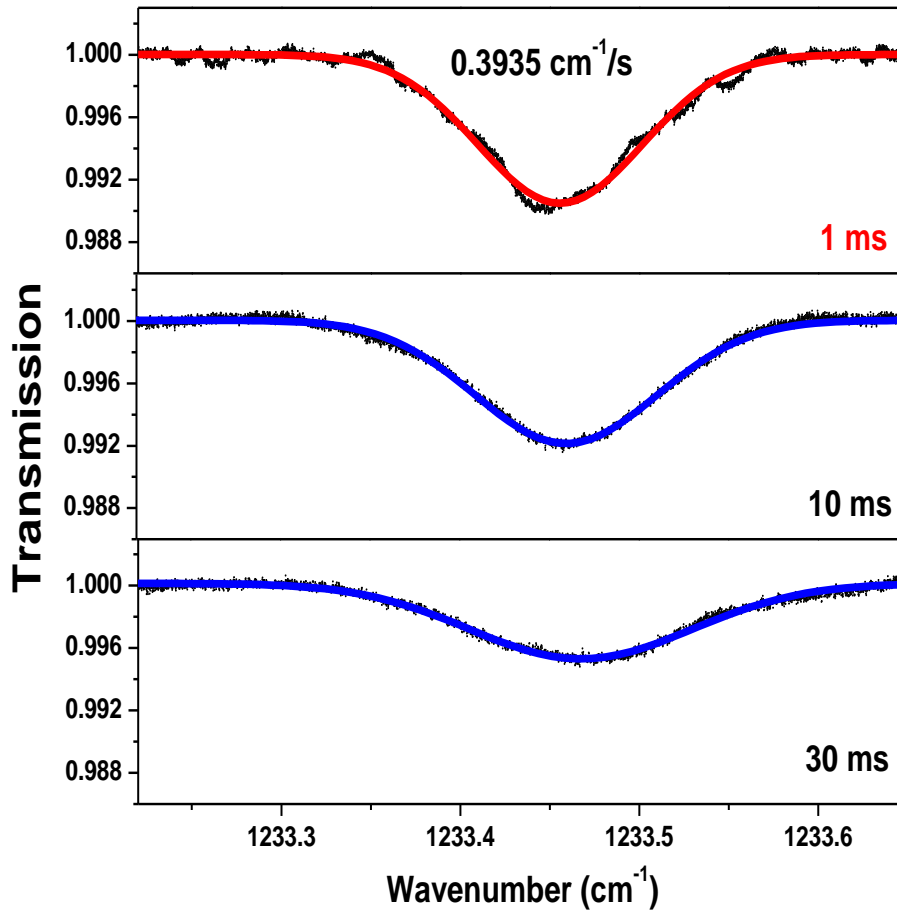


Figure 4.11 BB-based heterodyne spectra of CH₄ absorption at a scanning speed ν_{sc} of 0.3935 cm⁻¹/s (a scanning time ΔT_{scan} of 137 ms) combined with different time constants, respectively.

Table 4.6 Analysis of BB-based heterodyne spectra of CH₄ absorption at the scanning speed of the LO frequency (ν_{sc}) of 0.3935 cm⁻¹/s (the scanning time (ΔT_{scan}) of 137 ms) with different time constants (τ) (Fig. 4.11) (1 σ : Standard deviation).

ν_{sc} (cm ⁻¹ /s)	ΔT_{scan} (ms)	τ (ms)	SNR	$\Delta\nu_b$ (cm ⁻¹)	Absorption depth	$\delta\nu$ (cm ⁻¹)	Fit residual (1 σ)
0.3935	137	1	7	0.0541	0.01261	0.0004	0.00174
		10	9	0.0599	0.01181	0.0041	0.00129
		30	8	0.0733	0.00736	0.0120	0.00096

Based on the analysis of the heterodyne absorption spectra shown in Figs. 4.8-4.11 (black), SNR, line width broadening ($\Delta\nu_b$), absorption depth, line shift ($\delta\nu$), and noise level (1 σ) of these spectra were analyzed from the Lorentz profile fits (Figs. 4.8-4.11 red and blue) and summarized in Table 4.3-4.6, the optimal time constants (τ) at given scanning speeds of

LO frequency (ν_{sc}) and scanning times (ΔT_{scan}) were obtained for the current work, as shown in Table 4.3-4.6 in **bold** and Fig.4.8-4.11 in *red*.

As can be seen, selection of the LIA time constant should be well matched to the scanning speed of the LO frequency as well as the scanning time. When the time constant is too small, the noise will increase. While longer (than the optimal one) time constant would result in reduced absorption depth, in shift in absorption center frequency and in distortion of absorption line-shape.

Comparing above four optimal combinations for heterodyne detection, summarized in Table 4.7, the combination of the scanning speed of the LO frequency of $0.3935 \text{ cm}^{-1}/\text{s}$ (the scanning time of 137 ms) and the LIA time constant of 1 ms has a relatively low noise level, highest absorption depth, no significant shift in absorption center frequency and no distortion of absorption line shape (Table 4.7 in **bold**).

Table 4.7 Analysis of BB-based heterodyne spectra of CH_4 absorption with optimal τ at given ν_{sc} and ΔT_{scan} .

ν_{sc} (cm^{-1}/s)	ΔT_{scan} (ms)	τ (ms)	SNR	$\Delta \nu_b$ (cm^{-1})	Absorption depth	$\delta \nu$ (cm^{-1})	Fit residual (1σ)
0.03148	1709	300	8	0.0656	0.01143	0.0095	0.00148
0.0787	684	100	6	0.0640	0.01244	0.0081	0.00210
0.1574	342	100	7	0.0672	0.01101	0.0181	0.00156
0.3935	137	1	7	0.0541	0.01261	0.0004	0.00174

In principle, the relationship between the scanning time (ΔT_{scan}) and the LIA time constant (τ) should be (c.f. Chapter 2.1.6) :

$$\Delta T_{scan} = \frac{\Delta \nu_{HWHM}}{\nu_{sc}} \geq 14 \cdot \tau \quad (4.2)$$

According to ΔT_{scan} and τ in Table 4.7, the combination of the scanning time of 137 ms and the time constant of 1 ms meets well Eq. (4.2) which can efficiently reduce the noise without causing obvious shift and distortion of the line-shape, and is consistent with our spectral analysis as discussed above. This combination was therefore selected for our further LHR measurements.

4.3 Field measurement in Paris

The developed PoC LHR was field tested on the QualAir platform of the UPMC, in collaboration with the « Laboratoire d'Études du Rayonnement et de la Matière en Astrophysique et Atmosphères (LERMA) » of the UPMC in Paris. (Dr. Yao TE).

The Paris' instrument is part of the TCCON (TCCON-Paris station). The TCCON is a network of ground-based Fourier transform spectrometers recording direct atmospheric absorption spectra in the infrared spectral region. From these spectra, accurate and precise column-averaged abundances of CO₂, CH₄, N₂O, HF, CO, H₂O, and HDO are retrieved (<http://www.tccon.caltech.edu/>). The QualAir platform Fourier transform spectrometer (Bruker's IFS 125HR) with a spectral resolution of 0.02 cm⁻¹ is adapted for ground-based remote sensing of molecular species in the atmospheric column. Connected to a sun-tracker on the roof terrace (Fig. 4.12 *left*), the QualAir FTS (Fig. 4.12 *right*) operates in the solar absorption configuration and enables the detection of a large number of atmospheric pollutants.

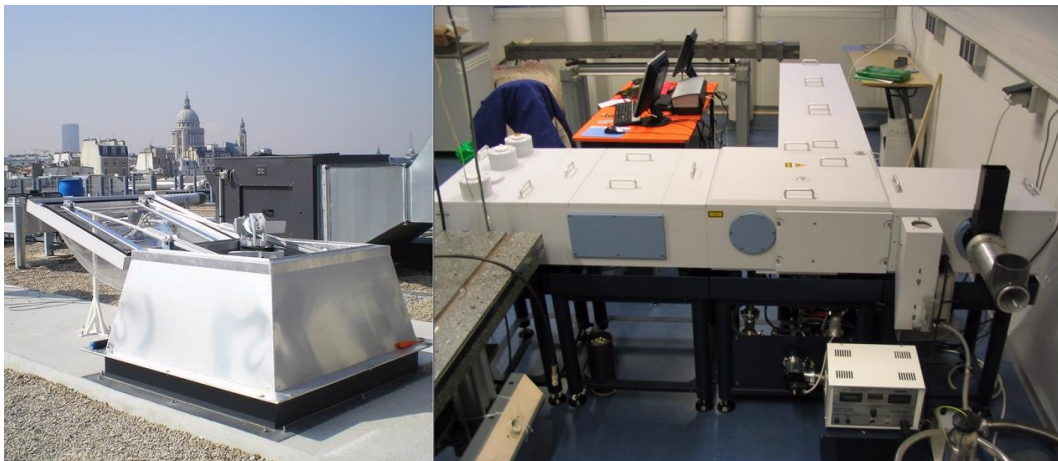


Figure 4.12 *left*: external heliostat (sun-tracker) installed on the roof terrace; *right*: Bruker IFS 125HR located in the lower-level experimental room (TCCON-Paris station).

4.3.1 LHR involving a telescope system for free-space coupling of sunlight

In order to couple the sunlight, collected by the heliostat on the QualAir platform, to our LHR, a Thorlabs 60 mm cage assembly system was utilized for a free-space coupling telescope system. Cage assembly system using four rigid steel rods on which optical components can be mounted along a common optical axis, provides a convenient way to construct stable opto-mechanical systems with an established line of precision-machined building blocks designed

for high flexibility and accurate alignment.

The used cage system for sunlight coupling consists of a mirror mounted in a rotating cube to reflect the sunlight from the heliostat to our LHR, a diaphragm used to control the sunlight beam size, and two lenses (in CaF_2 , $f_1 = 150 \text{ mm}$ and $f_2 = 75 \text{ mm}$) used for $2\times$ beam contraction, as shown in Fig. 4.13.

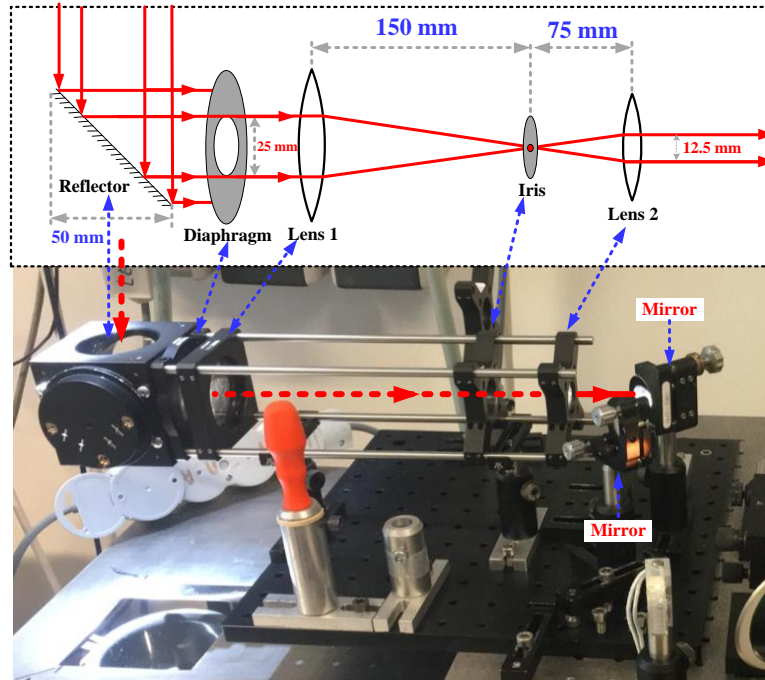


Figure 4.13 *upper*: schematic of a telescope system for free-space coupling of sunlight; *lower*: photo of the telescope system.

The experimental setup deployed on the QualAir platform is schematically shown in Figs. 4.14 and 4.15. Solar radiation is captured by an external heliostat installed on the roof terrace and directed down towards the low-level laboratory. The sunlight is first reflected, collimated and shaped by the cage system. The shaped sunlight beam is filtered with an optical filter (for removing the UV and the visible radiations and limiting the bandwidth of the incident radiation in the infrared region) and amplitude modulated with a chopper at 1 kHz. It is then directed towards a beam splitter on which it is superimposed with the LO beam from the EC-QCL. The LO laser beam size is firstly expanded by OAPM 3-OAPM 4, intensity-controlled and polarization adjusted using a wideband IR polarizer. The combined beams are focused with OAPM 5 onto the VIGO photomixer. The LO power reflected by a beam splitter (CaF_2 window) is used for frequency metrology, through direct absorption of CH_4 in a single-pass cell at atmospheric pressure, or through a 12.5-cm long home-made etalon in Ge to record etalon fringes for relative frequency calibration.

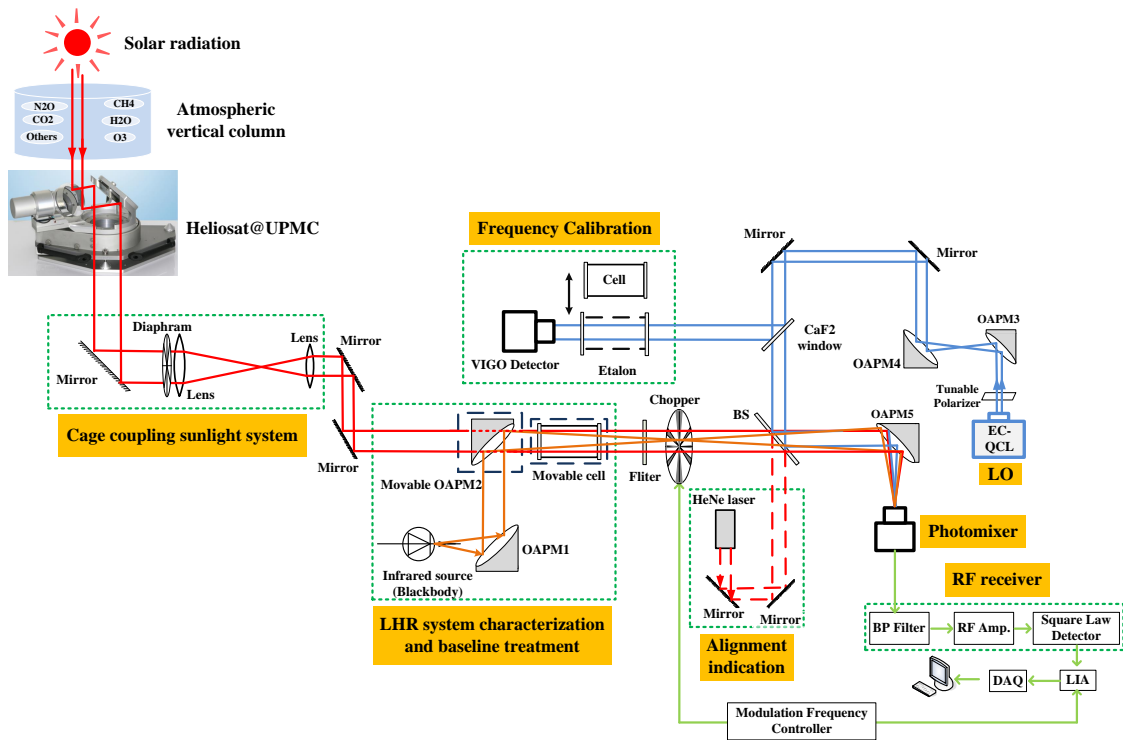


Figure 4.14 Schematic of the LHR deployed for the field test on the QualAir platform at the UPMC.

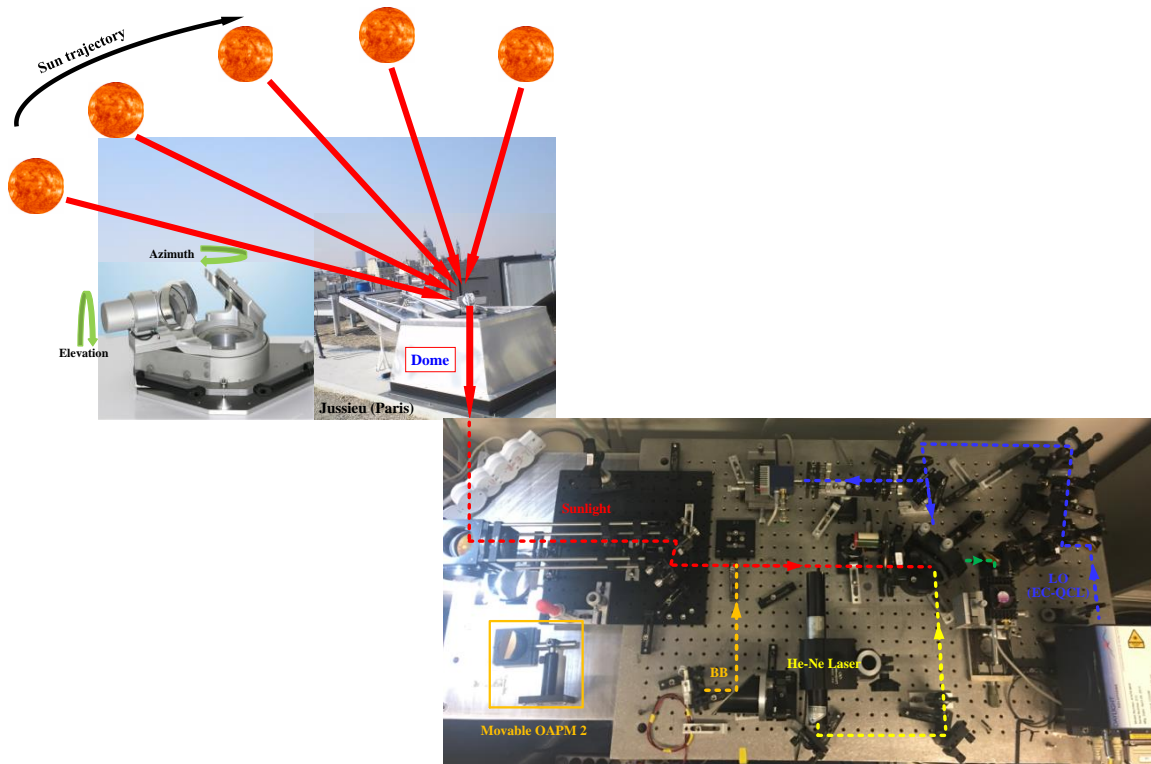


Figure 4.15 upper: sun-tracker installed on the roof terrace on the QualAir platform; lower: a free-space telescope coupling system used for sunlight coupling to the LHR in a field test at the UPMC. Red dot line : sunlight beam path; Orange dot line : blackbody beam path; Yellow dot line : He-Ne laser beam path; Blue dot line : EC-QCL beam path; Green dot line : combined LO-BB beams to the photomixer.

4.3.2 Preliminary field test results of the developed PoC LHR

4.3.2.1 LHR baseline treatment

To retrieve the atmospheric vertical column, baseline treatment is a key issue which needs to be seriously considered. Traditional baseline treatment in applied spectroscopy using an absorption cell/cavity is to vacuum the cell and then fill the cell with nitrogen or zero air in the same experimental conditions to measure target molecule-free baseline. This method is, however, no longer applicable for open-path remote sensing like LHR monitoring. According to the formula ($P_{\text{HET}} \propto P_{\text{S}} \times P_{\text{L}}$), the heterodyne signal intensity (P_{HET}) is proportional to the product of the sunlight intensity (P_{S}) and the LO laser power (P_{L}). Since the frequency scanning range of the LO EC-QCL is very small ($\sim 1 \text{ cm}^{-1}$), the sunlight power can be considered as a constant. The baseline feature of the LHR spectrum can be reasonably considered as determined by variation in the LO laser power during frequency scan.

In the present work, frequency scan of the used EC-QCL is realized by applying a sine-wave signal to a PZT element that scans the laser external cavity. Compared to LHR working with a DFB laser as a LO whose frequency is scanned using a sawtooth-wave signal, the baseline feature in our case is more complex. In addition, structured baseline resulting from dysfunction of our used LO EC-QCL is inevitable at some frequencies of interest. Therefore it is unable to describe the baseline with a standard curve fitting. In this study, blackbody radiation was used to replace sunlight which allowed us to record the baseline (rather than LO laser power variation curve) of the heterodyne spectrum.

Sunlight-coupled heterodyne spectral signal was recorded (Fig. 4.16 (b)), and under the same experimental conditions (LO power), blackbody-coupled heterodyne spectral signal (baseline) was recorded (Fig. 4.16 (c)). As can be seen, both of these spectra have similar variation features and both are similar to the LO variation baseline (Fig. 4.16 (a)) which shows that the LHR spectral baseline is mainly determined by the LO power variation when scanning the LO frequency. Fig. 4.16 (a) shows also that the used LO power variation is not a regular sine-wave signal applied to the PZT.

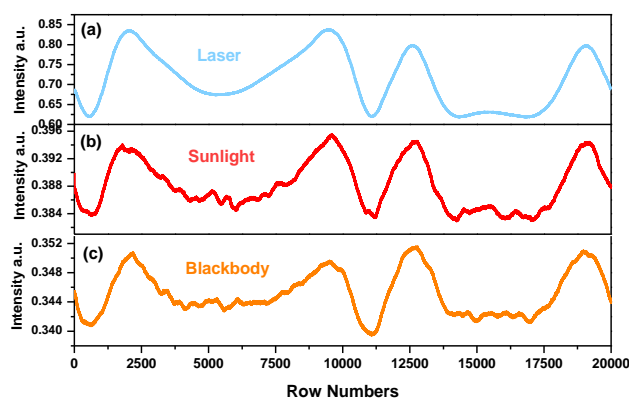


Figure 4.16 (a) Local oscillator signal; (b) Sunlight-coupled heterodyne signal; (c) Blackbody-coupled heterodyne signal.

The BB-coupled heterodyne baseline was thus used to simulate the baseline of the sunlight-coupled heterodyne spectrum. Heterodyne signals from sunlight and from blackbody radiation were normalized to obtain baseline-corrected LHR spectra in the atmospheric column.

In this study, LHR receiver parameters were set as follows : LO center frequency at 1231.00 cm^{-1} , scanning frequency : 250 mHz, scanning voltage : 3.0 V, scanning voltage offset : 1.6 V, electronic filter bandwidth : 6 MHz (27-33 MHz), and sensitivity and time constant of the LIA are 100 mV and 1 ms, respectively.

4.3.2.2 Heterodyne measurement of atmospheric CH_4 absorption spectrum

Atmospheric CH_4 absorption signal was field extracted using the developed LHR. In this study, LHR receiver parameters were set as follows : LO (EC-QCL) was scanned using PZT scan mode around 1242.00 cm^{-1} with a scanning frequency of 250 mHz. The scanning voltage is 3.0 V with an offset of 1.6 V. Electronic filter bandwidth is 6 MHz (27-33 MHz), and sensitivity and time constant of the LIA are 100 mV and 1 ms, respectively.

In Fig.4.17 (a), red curve shows an atmospheric CH_4 absorption spectrum measured with the LHR coupled to sunlight, while the black curve shows the LHR baseline when the blackbody radiation was coupled into the LHR. Due to the difference in light intensity between sunlight and blackbody radiation, the spectra recorded in Fig.4.17 (a) were normalized by data post-processing, the corresponding normalized spectra are shown in Fig.4.17 (b). Fig.4.17 (c) shows the atmospheric CH_4 absorption signal after normalization.

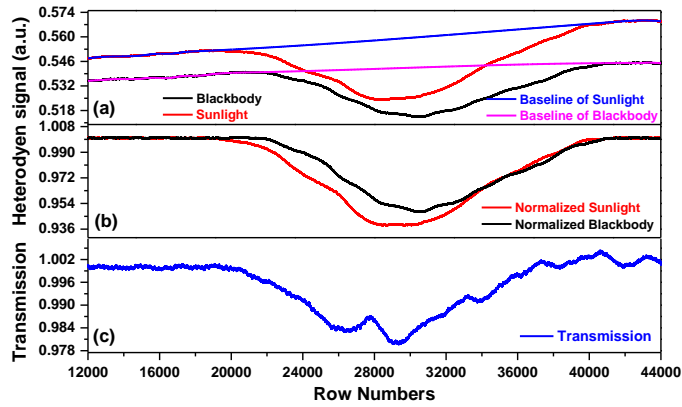


Figure 4.17 (a) LHR CH₄ absorption signal (*red*) associated with a polynomial-fitted baseline of sunlight (*blue*) and BB-based LHR baseline (*black*) associated with a polynomial-fitted baseline of blackbody (*pink*); (b) Normalized LHR atmospheric CH₄ absorption signal (*red*) obtained by dividing the absorption signal ((a), *red*) by the polynomial-fitted baseline ((a), *blue*) and LHR baseline (*black*) obtained by dividing the BB-based LHR baseline ((a), *black*) by the polynomial-fitted baseline ((a), *pink*); (c) Post-processed LHR atmospheric CH₄ transmission signal (*blue*) obtained by dividing the normalized LHR spectrum ((b), *red*) by the normalized BB baseline ((b), *black*).

In order to confirm this CH₄ LHR spectrum, under the same experiment conditions, the LO center frequency was tuned to a nearby non-absorbing frequency at 1231.45 cm⁻¹, the experimental process was repeated. The results are shown in Fig.4.18. In Fig.4.18 (a), the red curve shows the original heterodyne signal measured with sunlight, the black curve shows the original LHR baseline with blackbody radiation coupled into the LHR. In Fig.4.18 (b), the red and the black curves show their corresponding normalized heterodyne signal, respectively. The blue curve in Fig.4.18 (c) shows the result of normalization by dividing the normalized heterodyne signal by the normalized baseline. As can be seen, no absorption feature was observed, which confirms the absorption feature (*blue*) in Fig.4.17 resulting from atmospheric CH₄ absorption.

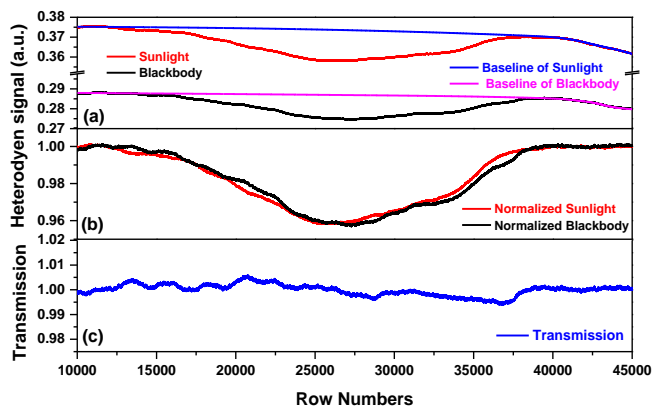


Figure 4.18 (a) Recorded LHR signal (*red*) and baseline (*black*); (b) Normalized LHR signal (*red*) and baseline (*black*); (c) Normalized signal (*blue*) by dividing the red curve by the black one, both shown in (b).

Experimentally extracted atmospheric LHR spectrum of CH₄ was compared with a spectrum from a high-resolution Bruker IFS 125HR Fourier transform spectrometer and from an atmospheric transmission model. The three spectra are plotted in Fig. 4.19.

Due to the structured baseline resulting from the LO, atmospheric LHR spectrum of CH₄ (Fig. 4.19 (b)) has to be extracted from a BB-based baseline. In addition, the background signal of LHR system (when there is no LO injection) was not corrected. The absorption depth is inconsistent with the corresponding atmospheric FTS spectrum (Fig. 4.19 (a)) and the atmospheric transmission modelling CH₄ spectrum (Fig. 4.19 (c)). Nevertheless, the overall spectral line-shape is consistent with the corresponding reference spectra.

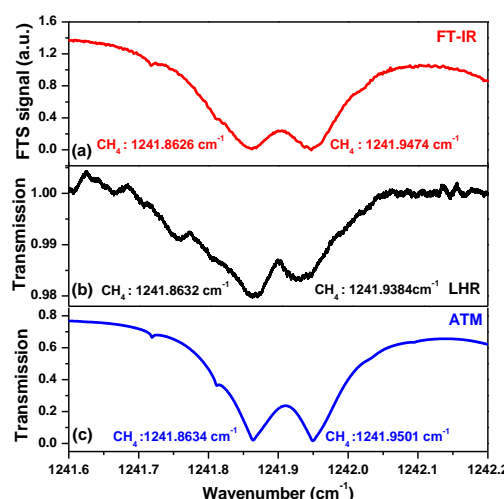


Figure 4.19 Atmospheric absorption spectrum of CH₄ recorded with a Bruker IFS 125HR FTS in Paris (a), with our LHR (b), and from an atmospheric transmission model (c).

Conclusion

In this chapter, a PoC mid-IR LHR was developed and its performance was evaluated and optimized with the help of a high temperature IR blackbody used as sunlight with stable intensity. BB-based heterodyne spectra of CH₄ in a single cell at ~8 μm were used for characterization of the developed LHR. The developed LHR was then deployed for field tests on the QualAir platform at the UPMC. Ground-based measurement of tropospheric CH₄ in the atmospheric column was obtained. Though suffered from the structured baseline resulting from the dysfunction of the used LO EC-QCL, extracted LHR spectrum of CH₄ was confirmed by the nearby non-absorption LHR measurement and by comparison with the FTR spectrum measured by a Bruker IFS 125HR FTS and with an atmospheric transmission modelling spectrum.

In the following work, great efforts were devoted to make the mid-IR LHR transportable and compact for in situ measurement, and to move the LO frequency to another molecular line to avoid the laser structured baseline as much as possible.

References

- [1] T. Kostiuk and M. J. Mumma. Remote sensing by IR heterodyne spectroscopy, *Appl. Opt.* 1983, **22**, 2644-2654.
- [2] L. S. Rothman, I. E. Gordon, A. Barbe, D. C. Benner, P. F. Bernath, M. Birk, V. Boudon, L. R. Brown, A. Campargue, J. P. Champion, K. Chance, R. R. Gamache, A. Goldman, D. Jacquemart, I. Kleiner, N. Lacome, W. Lafferty, O. V. Naumenko, A. V. Nikitin, J. Orphal, V. I. Perevalov, A. Perrin, A. Predoi-Cross, C. P. Rinsland, M. Rotger, M. Simeckova, M. A. H. Smith, K. Sung, S. A. Tashkun, J. Tennyson, R. A. Toth, A. C. Vandaele, and J. Vander Auwera. The HITRAN 2008 molecular spectroscopic database, *J. Quant. Spectrosc. Rad. Transfer* 2005, **96**, 139-204.
- [3] S. Brodersen. Noise filter effects in recording spectroscopes, *J. Opt. Soc. Am.* 1953, **43**, 1216-1220.

Chapter 5 Development of a transportable mid-IR LHR prototype

Objective

In Chapter 4, a PoC mid-IR LHR was developed and validated via ground-based measurements of CH₄ through an external sun-tracker installed on the roof terrace of the QualAir platform (48°50'47"N/2°21'21"E, 60 m above sea level) of the Université Pierre et Marie Curie (UPMC). In this Chapter, development of a fully transportable mid-IR LHR prototype is described. We explored a mid-IR fiber to couple the sunlight to the heterodyne receiver, which makes our LHR, equipped with an EKO sun-tracker, fully transportable. The developed LHR instrument was tested and validated via ground-based field measurements of tropospheric CH₄ and N₂O in the atmospheric column on the roof terrace of the IRENE (Innovation Recherche en Environnement) platform in Dunkerque (51.05°N/2.34°E).

5.1 LHR prototype involving a mid-IR fiber to couple blackbody radiation

5.1.1 Instrumental description

In order to test and characterize the performance of the newly commercially available mid-IR fiber used for LHR application, a LHR setup using fiber coupling of blackbody radiation was realized (Figs 5.1 and 5.2).

Radiation from the blackbody (Model 67030, Newport Inc.) is collected and collimated with a CaF₂ lens ($f_1 = 40$ mm, dia. = 25.4 mm) and then coupled to an 860- μ m-core polycrystalline fiber through a second CaF₂ lens ($f_2 = 20$ mm, dia. = 12.7 mm). The blackbody radiation emerging from the fiber is then collimated and filtered using a lens3 ($f_3 = 50$ mm, dia. = 12.7 mm) in Germanium with AR coating for 3-12 μ m region in order to filter out radiation out of the spectral region of interest to minimize shot noise resulting from the BB source [1]). The BB beam is amplitude modulated at 1 kHz using a mechanical chopper (Model MC2000B, Thorlabs, Inc.) and is then directed to a 5% (R) - 95% (T) beam splitter (BS, in CaF₂). The BB beam is superimposed with the LO beam from the EC-QCL. The LO light is size-expanded by a factor of 3 through two OAPMs (OAPM4: $f_4 = 12.7$ mm and OAPM5: $f_5 = 38.1$ mm). It is intensity-controlled and polarization-adjusted using a wideband IR polarizer (2-12 μ m). The combined BB and LO beams are then focused by an OAPM6 ($f_6 = 38.1$ mm) onto a VIGO photomixer (PVI-4TE-10.6, VIGO System S.A.). The

RF beat note signal from the photomixer enters the same RF receiver involved in the PoC mid-IR LHR (c.f. Chapter 4) except for the RF filter having a pass-band of 27.5-270 MHz instead of 27-33 MHz (c.f. 5.1.2.2.II).

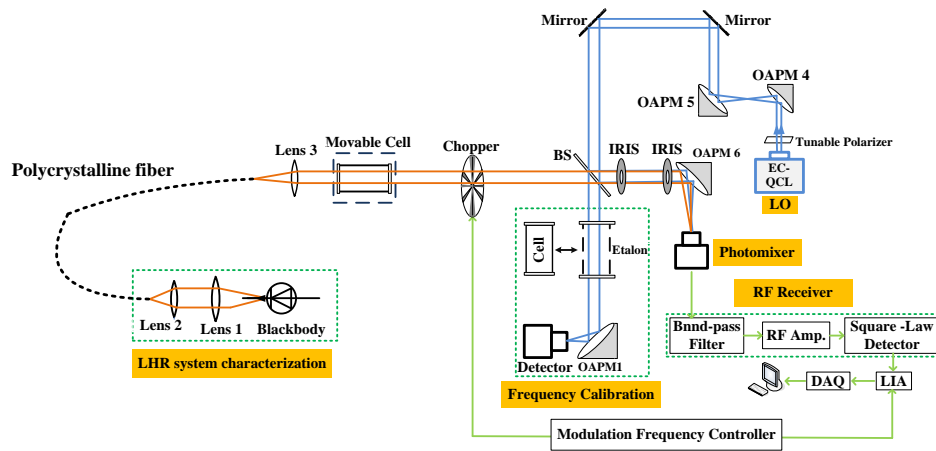


Figure 5.1 Schematic of a mid-IR LHR prototype using a fiber to couple blackbody radiation.

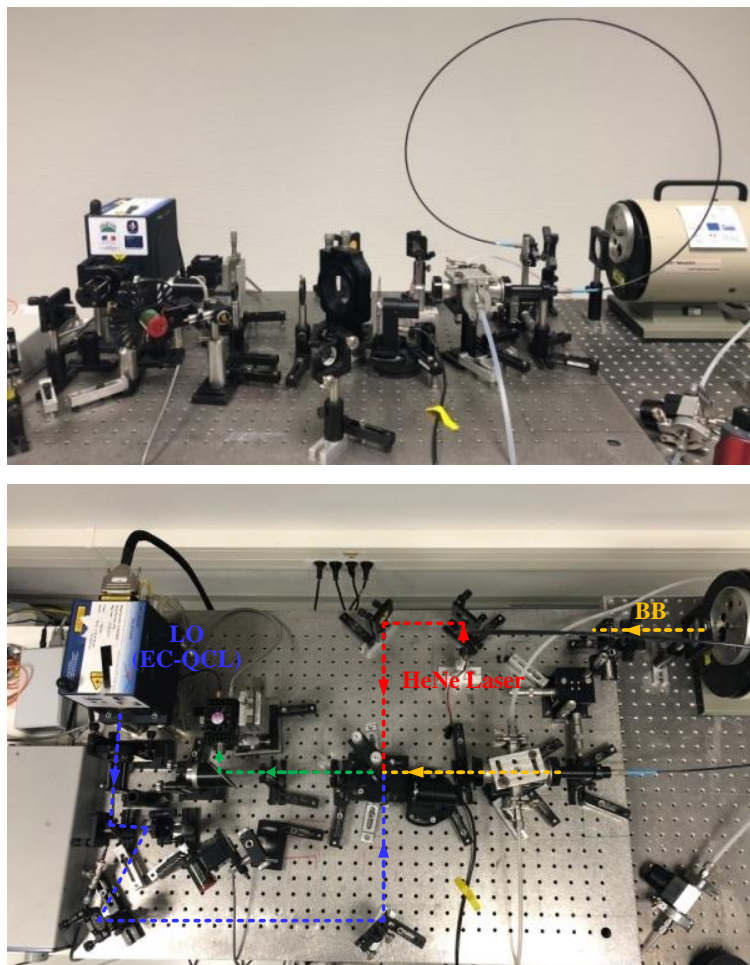


Figure 5.2 LHR prototype involving a mid-IR fiber to couple blackbody radiation (*upper*: front view; *lower*: top view). Orange dot line : blackbody beam path; red dot line : He-Ne laser beam path; blue dot line : LO (EC-QCL) beam path; green dot line : combined LO-BB beams to photomixer.

5.1.2 Performance characterization of the LHR prototype

5.1.2.1 SNR of the beating signal

I. SNR of the LHR using fiber coupling system

In order to characterize the LHR performance using a fiber coupling system for sunlight collection, investigation in terms of SNR of the LHR signal was performed using a calibrated blackbody source. In this study, the blackbody's temperature was set to 1000 °C. Time series measurements of the RF signal from the LIA with and without LO radiation injection were carried out. The effective LO and BB powers were measured at the output of the photomixer and displayed on oscilloscope (in [V]). These light powers are expressed in this work in terms of photocurrent, in [μA], induced by the incident light power, which is obtained by dividing the light power in [V] by the photomixer transimpedance of 6000 V/A.

LO and BB power-induced photocurrents, were 610 μA and 117 μA , respectively. Based on the measurement (Fig. 5.3) of a beat note amplitude of 150.18 μV and a noise level (1σ) of 0.36 μV in the beat note, a SNR of ~ 419 was deduced.

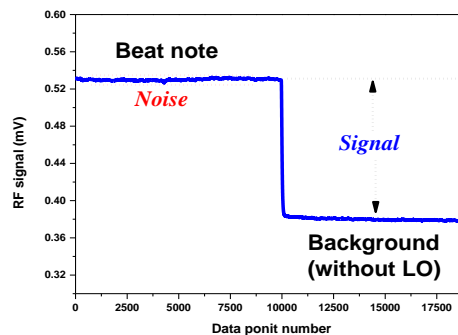


Figure 5.3 SNR measurement of the beat note at the output of the LIA. The mixed LO and BB power measured at the output of the photomixer were 3.66 V and 0.70 V, respectively. A filter with a pass-band of 27.5-270 MHz was used. A time constant of 1 s combined with LP filters (12 dB/oct) was used for the LIA.

The theoretical shot-noise-limited SNR of the LHR can be expressed by Eq. (5.1) [2] (c.f. Eq. 1.57 in Chapter 1.5). This equation can be used to assess the experimental LHR performance when referenced to the ideal shot-noise-limit. In other words, it corresponds to the expected performance of an ideal LHR in which shot noise is the sole noise [3] :

$$SNR = \eta_{het} \cdot \frac{\eta \cdot P_s \cdot \sqrt{B\tau}}{h \cdot \nu \cdot B} = \eta_{het} \cdot \frac{\eta \cdot \kappa \cdot \sqrt{B \cdot \tau}}{\exp\left(\frac{h \cdot \nu}{k \cdot T}\right) - 1} \quad (5.1)$$

where the overall optical coupling efficiency κ is defined as the fraction of the incoming signal radiation transmitted through all the optical components to the photomixer [3]. For the

blackbody, this accounts for two CaF₂ lenses (transmission ~0.92 each), the polycrystalline IR-fiber (transmission ~0.54), the Germanium lens (transmission ~0.99), the beam splitter (transmission ~0.95), the silver-plated OAPM (assumed reflectance ~0.97) and the BaF₂ wedged window in front of the photomixer (transmission ~0.95) which results in an overall coupling efficiency of 0.396. The heterodyne efficiency η_{het} of photomixing of the sunlight beam and the LO beam is considered to be 1 in the ideal case (c.f. Chapter 1.3), the quantum efficiency η of the photomixer provided by the manufacturer at this wavelength is 0.5. Under these conditions, given a LHR double side bandwidth of 485 MHz (for a RF pass band of 27.5-270 MHz) and 1 s time constant of the LIA at a LO frequency (1242.3 cm⁻¹ or 3.73×10¹³ Hz), a shot-noise-limited SNR of about 1430 was obtained. The theoretical shot-noise-limited SNR is 3.4 higher than the measured SNR at a photocurrent of 610 μA , or a factor ρ of 0.29 in theoretical SNR is observed. The factor of 0.29 (=419/1430) may come from the unexpected performance of the developed LHR.

Please note that in the following experiment description, the LO and BB power will both be expressed as photocurrent (in [μA]).

I.1 Noise sources in LHR system

In order to understand the difference between the measured and the calculated ideal SNRs, the noises in various parts of the LHR system were investigated with the help of a signal analyzer (N9000B, CXA X-Series, Keysight, Inc.). In this study, the parameters of the signal analyzer were set as Table 5.1.

Table 5.1 Parameter setting on the Signal Analyzer.

RBW	VBW	Frequency scan range	Average count
100 kHz	51 Hz	1 kHz-500 MHz	1

where the RBW (Resolution BandWidth) is the frequency span of the final filter applied to the input signal in the signal analyzer. Smaller RBW provides finer frequency resolution. The VBW filtering is a time-domain low-pass filter, mathematically equivalent to the mean or average. The main effect of the VBW filter is to smooth the signal and decrease noise. The VBW (Video BandWidth) affects therefore the displayed signal quality.

In this study, the total noise density N_{total} ($nV/\sqrt{\text{Hz}}$) of the LHR system can be expressed by (c.f. Chapter 1.4) :

$$N_{\text{total}} = \sqrt{N_{\text{Det}}^2 + N_{\text{LIN}}^2 + N_{\text{SIN}}^2} \quad (5.2)$$

$$N_{\text{LIN}}^2 = N_{\text{LSN}}^2 + N_{\text{LEN}}^2 \quad (5.3)$$

and
$$N_{\text{SIN}}^2 = N_{\text{SSN}}^2 + N_{\text{SEN}}^2 \quad (5.4)$$

where N_{Det} , N_{LIN} and N_{SIN} are the noise from the detection chain, the laser-induced noise and signal-induced noise, respectively. The laser-induced noise includes laser-induced shot noise N_{LSN} and laser excess noise N_{LEN} , respectively. While the signal-induced noise includes signal-induced shot noise N_{SSN} and signal excess noise N_{SEN} .

The contribution of each type of noises in the above expressions is discussed below in detail.

(1) Noise from the detection chain (N_{Det})

As mentioned in Chapter 1.4.1, noise from the detection chain N_{Det} includes the background noise, the Johnson noise resulted from the amplifier associated to the photodetector, and the dark noise. It can be measured when there is no light incident on the detector.

In order to identify noise sources, signals at the RF output of the photomixer were measured with the signal analyzer under different conditions :

(A) input of the signal analyzer directly connected to a resistance of 50Ω (Fig. 5.4, (1) *blue curve*) for the measurement of the background noise N_{SA} of the signal analyzer.

(B) with only detector output connected to the signal analyzer (Fig. 5.4, (2) *red curve*), representing the sum of the signal analyzer's background noise N_{SA} and the detection chain noise N_{Det} .

(C) with the presence of the LO but without BB radiation injection (Fig. 5.4, (3) *green curve*), representing the sum of the signal analyzer's background noise N_{SA} , the detection chain noise N_{Det} and the laser-induced noise N_{LIN} .

(D) with the presence of both LO and BB radiations (Fig. 5.4, (4) *black curve*), representing the sum of heterodyne signal, the signal analyzer's background noise N_{SA} , the detection chain noise N_{Det} , the laser-induced noise N_{LIN} and the BB source-induced noise N_{SIN} .

Comparing the RF output (after the associated amplifier to the photodetector) of the photomixer with both LO and BB radiation injections (Fig. 5.4, (4) *black curve*) to that of the photomixer with only LO injection (Fig. 5.4, (3) *green curve*), two signals were almost overlapped, which indicates that there was almost no additional noise contribution from the BB radiation, i.e. signal-induced noise N_{SIN} can be neglected at this stage analysis.

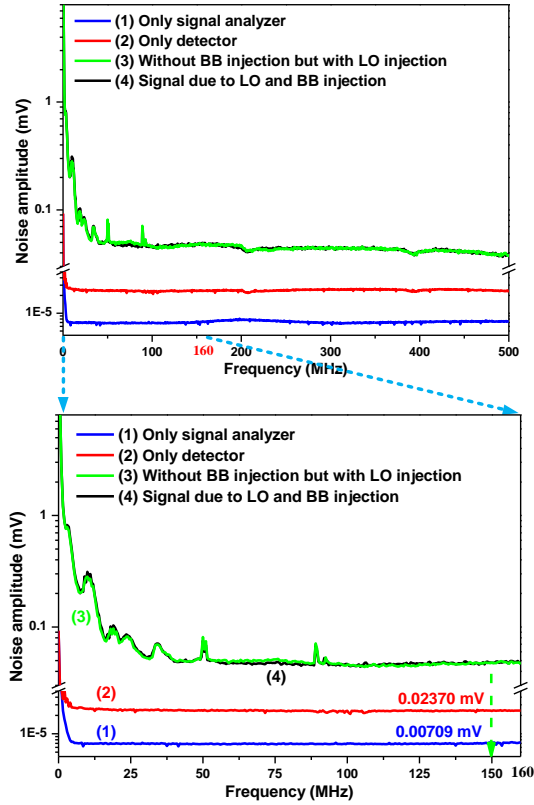


Figure 5.4 *upper*: noise amplitude spectra of the heterodyne system in the bandwidth of 1kHz-500 MHz; *lower*: zoom of the upper figure in the bandwidth of 1kHz-160 MHz.

Therefore, the total noise density N_{total} (Eq. (5.2)) of the LHR system becomes :

$$N_{\text{total}} = \sqrt{N_{\text{Det}}^2 + N_{\text{LIN}}^2} \quad (5.5)$$

As can be seen in Fig. 5.4 *upper*, the LHR system noise (measured at the RF output of the photomixer) was mainly distributed in the range of 1 kHz-100 MHz, which is enlarged in Fig. 5.4 *lower*. It is seen that the noise is mainly composed of 1/f and white noises. In the low frequency range, the noise is dominated by 1/f, and then the noise distribution tends to be flat. Therefore, the pass-band should be selected in the higher frequency range where 1/f is significantly reduced. In order to study the characteristics of white noise in the high frequency range, the detection chain noise N_{Det} was analyzed at 150 MHz where the noise is dominated by white noise.

Given the readings from the signal analyzer at 150 MHz : 0.00709 mV for the noise amplitude of the signal analyzer's background noise (Fig. 5.4, (1) *blue curve*), and 0.02370 mV for the noise amplitude (Fig. 5.4, (2) *red curve*) resulting from the signal analyzer background noise and the detection chain noise, the detection chain noise amplitude can be deduced from Eq. (5.6) :

$$\sqrt{0.02370^2 - 0.00709^2} = 0.02261 \text{ (in [mV])} \quad (5.6)$$

This was the integrated detection chain noise level within the set RBW of 100 kHz, the corresponding detection chain noise density N_{Det} was thus :

$$N_{Det} = 0.02261 \text{ mV} / \sqrt{10^5 \text{ Hz}} = 71.5 \text{ nV} / \sqrt{\text{Hz}} \quad (5.7)$$

Comparing the signal levels with LO injection (Fig. 5.4, (3) *green curve*) and without LO injection (Fig. 5.4, (4) *black curve*), the increase in the noise level was observed which indicates primarily an influence of the LO injection, which includes laser-induced shot noise and laser excess noise and both resulted from the used EC-QCL LO.

Fig. 5.5 *left* shows noise levels at the RF output of the photomixer in the bandwidth of 1kHz-500 MHz with two different LO power-induced photocurrents (*black curve*: 587 μA , (*red curve*: 410 μA), respectively. The LO power was adjusted through a polarizer in front of the LO laser. As can be seen in Fig. 5.5 (*right*), which is the enlarged scale of Fig. 5.5 (*left*), higher LO photocurrent will contribute more laser-induced shot noise N_{LSN} and laser excess noise N_{LEN} .

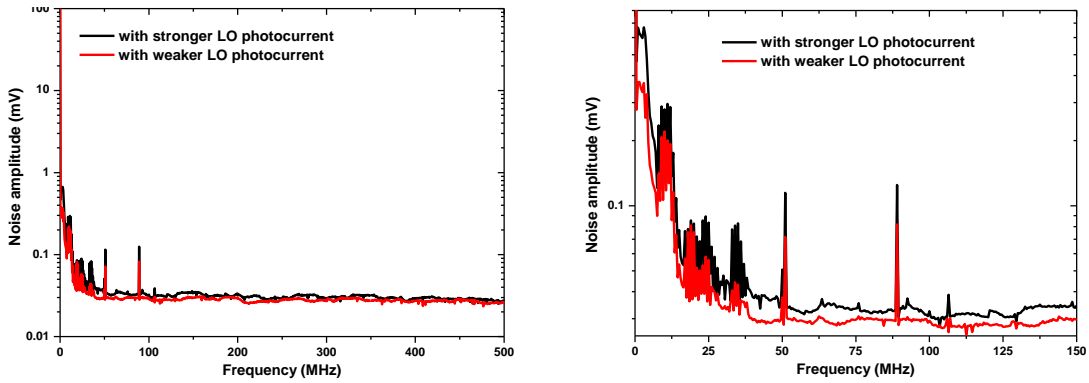


Figure 5.5 *left*: noise amplitude spectra of the RF output of the photomixer in the bandwidth of 1kHz-500 MHz with different LO photocurrents; *right*: enlarged scale in the bandwidth of 1kHz-150 MHz.

Next, laser-induced noise N_{LIN} including laser-induced shot noise N_{LSN} and laser excess noise N_{LEN} is analyzed.

(2) Laser-induced noise (N_{LIN})

In order to quantitatively analyze contributions of laser-induced shot noise N_{LSN} and laser excess noise N_{LEN} , detailed study was carried out. The LO power injected into the photomixer was adjusted through a polarizer in front of the LO laser and the LO power-induced photocurrent was used as indicator of the LO power injected in the photomixer.

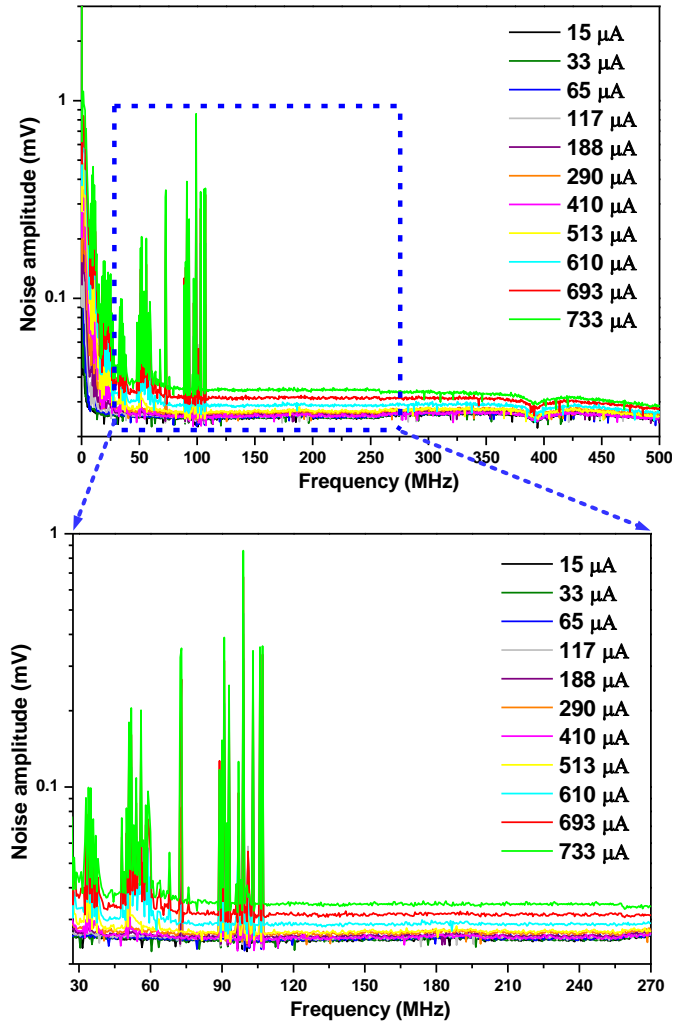


Figure 5.6 *upper*: noise density spectra from the RF output of the photomixer at different LO power-induced photocurrents measured with a signal analyzer; *lower*: zoom of the upper figure in the pass-band of 27.5-270 MHz.

Noise from the RF output of the photomixer within its pass-band of 1kHz-500 MHz was analyzed using the signal analyzer, as shown in Fig. 5.6 *upper*, at different LO photocurrents (note : here the signal analyzer background noise has all been subtracted).

The system total noise density N_{total} in $[nV/\sqrt{Hz}]$ (Fig. 5.7, (2) *black square*) was calculated by dividing the mean of all total noise amplitudes (including detection chain noise N_{Det} and laser-induced noise N_{LIN}) measured in the pass-band of 27.5-270 MHz (i.e. the pass-band of the used RF filter) (Fig. 5.6 *lower*) by the square root of the RBW (100 kHz). Given the detection chain noise density of $71.5nV/\sqrt{Hz}$ (Fig. 5.7, (1) *red line*) determined above (Eq. (5.7)), the laser-induced noise N_{LIN} (Fig. 5.7, (3) *blue triangle*) was calculated by subtracting the detection chain noise N_{Det} (Fig. 5.7, (1) *red line*) from the system total noise density N_{total} (Fig. 5.7, (2) *black square*) based on Eq. (5.5).

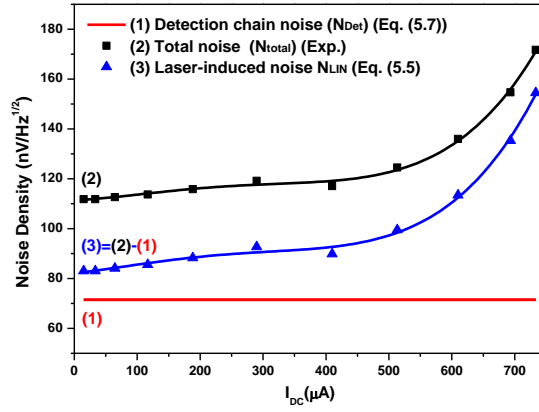


Figure 5.7 Plots of : (1) detection chain noise density N_{Det} (red line), (2) measured system total noise density N_{total} (black square), deduced from dividing the total noise amplitude measured at 150 MHz (Fig. 5.6 lower) by the square root of the RBW (100 kHz), and (3) the laser-induced noise N_{LIN} (blue triangle) deduced by subtracting the detection chain noise N_{Det} ((1) red line) from the total noise N_{total} ((2) black square), vs. LO photocurrents.

Based on the laser-induced noise N_{LIN} deduced as shown in Fig. 5.7, laser-induced shot noise and laser excess noise are studied in detail.

(2.1) Laser-induced shot noise (N_{LSN})

Voltage V_{SN} and current I_{SN} of the laser-induced shot noise can be calculated with Eqs. (5.8) and (5.9), respectively [4] :

$$V_{SN}(V) = R_{ii} \cdot I_{SN}(A) \quad (5.8)$$

$$I_{SN}(A) = \sqrt{2 \cdot e \cdot I_{DC}(\mu A) \cdot 10^{-6} \cdot B} \quad (5.9)$$

and
$$I_{DC}(\mu A) = V_{DC}(V) \cdot 10^6 / R_{ii} \quad (5.10)$$

where $R_{ii} = 6000$ V/A is the transimpedance of the photomixer, $e = 1.602 \times 10^{-19}$ C is the electric charge, $B = 5 \times 10^8$ Hz is the bandwidth of the photomixer over which the noise is considered, I_{DC} is the DC LO photocurrent induced by the LO laser power in the photomixer, V_{DC} is the DC LO voltage induced by LO laser power monitored at the output of the photomixer and 10^6 represents the unit conversion from V to μV .

From Eqs. (5.8) (5.9) and (5.10), the laser-induced shot noise density N_{LSN} (in $[nV / \sqrt{Hz}]$) can be expressed as [5] :

$$N_{LSN}(nV / \sqrt{Hz}) = V_{SN}(V) \cdot 10^9 / \sqrt{B} = \sqrt{2 \cdot e \cdot I_{DC}(\mu A) \cdot 10^{-6} \cdot R_{ii}^2} \cdot 10^9 = 3.396 \cdot \sqrt{I_{DC}(\mu A)} \quad (5.11)$$

where 10^9 represents the unit conversion from V to nV and 10^{-6} represents the unit conversion from μA to A.

The calculated laser-induced shot noise N_{LSN} is plotted in Fig. 5.8 (curve (4)). The total laser-induced noise, determined and shown in Fig. 5.7 is plotted again in Fig. 5.8 (curve (3)).

(2.2) Laser excess noise (N_{LEN})

The laser excess noise N_{LEN} (Fig. 5.8, (5) *green star*) can then be calculated (Eq. (5.3)) by subtracting the laser-induced shot noise N_{LSN} (Fig. 5.8, (4) *black circle*), determined using Eq. (5.11), from the laser-induced noise N_{LIN} (Fig. 5.8, (3) *blue triangle*).

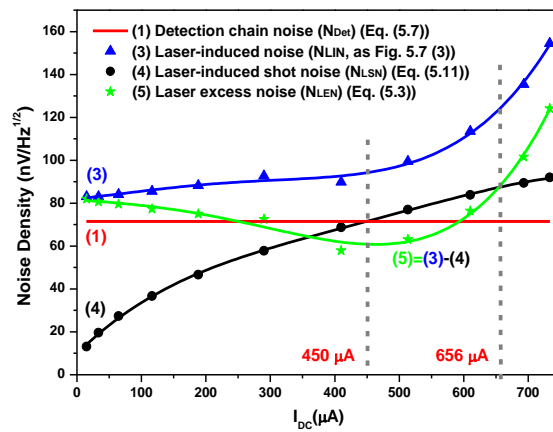


Figure 5.8 Densities of laser-induced noise N_{LIN} ((3) *blue triangle*), laser-induced shot noise N_{LSN} ((4) *black circle*), laser excess noise N_{LEN} ((5) *green star*), and detection chain noise N_{Det} ((1) *red line*) vs. photocurrent of the LO laser, respectively.

As can be seen from Fig. 5.8, at LO photocurrents $I_{DC} < 450 \mu A$ the detection chain noise N_{Det} ((1) *red line*) is larger than the laser-induced shot noise N_{LSN} ((4) *black circle*), only in the range of $450 \mu A < I_{DC} < 656 \mu A$ the laser excess noise N_{LEN} ((5) *green star*) and the detection chain noise N_{Det} ((1) *red line*) are both smaller than the laser-induced shot noise N_{LSN} ((4) *black circle*), and the LHR system operates in shot-noise dominated regime (with shot-noise limited high sensitivity performance). The higher LO photocurrent limit could not be verified, because the saturation of detector preamplifier for optical powers above $733 \mu A$ was observed.

I.2 Theoretical SNR vs. measured SNR

Based on the above analysis of the system noises, compared to the measured SNR (~419) with the theoretical SNR (~1430), the factor of 0.29 (=419/1430) is analyzed as follows :

(1) At a LO power-induced photocurrent of $610 \mu A$, at which SNR=419 was determined, the laser excess noise N_{LEN} (Fig. 5.8, (5) *green star*) and the detection chain noise N_{Det} (Fig.

5.8, (1) *red line*) were 0.9 times and 0.9 times the laser-induced shot noise N_{LSN} (Fig. 5.8, (4) *black circle*), respectively. The total noise of the LHR system N_{total} exceeds thus the laser-induced shot noise N_{LSN} by (using Eqs. (5.2) (5.3) and (5.4)) :

$$N_{total} = \sqrt{N_{Det}^2 + N_{LSN}^2 + N_{LEN}^2} = \sqrt{(0.9 \cdot N_{LSN})^2 + N_{LSN}^2 + (0.9 \cdot N_{LSN})^2} = 1.62 \cdot N_{LSN} \quad (5.12)$$

The system total noise N_{total} is 1.62 times laser-induced shot noise N_{LSN} , a correction factor ρ_1 of 0.62 (=1/1.62) is obtained for the theoretically calculated SNR under ideal shot-noise condition.

(2) The overall optical coupling efficiency κ of 0.40 for the blackbody radiation, based on the transmission of each optical component given by the manufacturer, would be overestimated. The measured overall optical coupling efficiency was about 0.27, and this difference between 0.27 and 0.40 in κ may be due to the long-time exposure of these optical components to a humid and salty environment at the seaside. An additional correction factor ρ_2 of 0.68 (=0.27/0.40) was obtained.

(3) The heterodyne efficiency η_{het} of 1 for the ideal case (c.f. Chapter 1.3) would be overestimated. The difference in shaped beam sizes of sunlight (12.5 mm) and LO light (7.5 mm) caused a heterodyne efficiency of ~ 0.8 (c.f. Fig. 1.12). As well the photomixer has a small photo-sensitive area of $0.5 \times 0.5 \text{ mm}^2$, even a small mismatch angle would result in a heterodyne efficiency of ~ 0.9 (c.f. Fig. 1.14 *left*). An additional correction factor ρ_3 of 0.72 (= 0.8×0.9) was achieved.

Based on the above analysis, a total correction factor ρ_{exp} for the theoretical SNR, resulted from the above reasons, is :

$$\rho_{exp} = \rho_1 \times \rho_2 \times \rho_3 = 0.30 \quad (5.13)$$

This value is comparable to the factor ρ of 0.29.

We dealt with the noise sources in Section I.1 and then the analysis for understanding the difference between the theoretical SNR and the experimentally measured SNR in section I.2. In next section, the heterodyne signal and SNR of the LHR as function of LO power (in terms of photocurrent) will be discussed.

I.3 Heterodyne signal and SNR of the LHR vs. LO photocurrent

Based on the study performed on the noises as function of LO power-induced photocurrent, we now investigate the heterodyne signal and the corresponding SNR as the function of the

LO photocurrent. The LO power was varied by adjusting a polarizer in front of the LO output, both the mean heterodyne signal and its standard deviation were measured from which, the corresponding SNR was derived. The results are shown in Fig. 5.9.

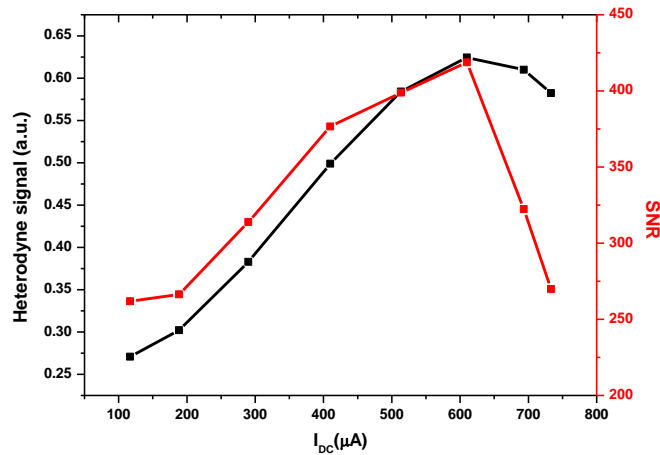


Figure 5.9 Evolution of heterodyne signal (*black square*) and SNR (*red square*) as a function of LO photocurrent.

Fig. 5.9 clearly shows that the amplitude of the heterodyne signal increases almost linearly at low LO photocurrent (*black square*), which is consistent with $P_{\text{HET}} \propto P_S \times P_L$, before reaching a rollover point at an LO photocurrent of $\sim 610 \mu\text{A}$. The SNR increases with the LO power and reaches a maximum when LO photocurrent is equal to $610 \mu\text{A}$ too. Above $610 \mu\text{A}$, the heterodyne signal became smaller and the noise on the heterodyne signal rapidly increased (c.f. Figs. 5.7 and 5.8), that is, the SNR significantly decreased. The data shows that the maximum SNR of the LHR can be obtained with an optimum LO photocurrent. The optimum LO photocurrent is highly dependent on detector (used as photomixer) technology and characteristics [3]. For each type of detector the optimum LO photocurrent must be determined because saturation effects, detection chain noise and detector response homogeneity will affect the performance.

Therefore, the LO power should be precisely adjusted in order to significantly reduce the noise on heterodyne signal to achieve high SNR while without any device saturation.

Section I mainly analyzed the noise sources and SNR of the LHR system using fiber for sunlight coupling to the LHR receiver. The following section will compare the performance, in terms of SNR, of LHRs using free-space coupling and using fiber coupling for BB source collection.

II. SNR comparison between LHRs using free-space coupling and fiber coupling for sunlight collection

In the LHR using free-space coupling system, an experimental SNR of ~ 119 (with an injected BB power-induced photocurrent of $207 \mu\text{A}$, an LO power-induced photocurrent of $417 \mu\text{A}$, a LIA time constant of 1 s and a pass-band of $27\text{-}33 \text{ MHz}$) was obtained, in comparison with a calculated ideal SNR of ~ 356 , as discussed in Chapter 4.

The experimental SNR of the LHR using fiber coupling was ~ 419 (with an injected BB power-induced photocurrent of $117 \mu\text{A}$, an LO power-induced photocurrent of $610 \mu\text{A}$, a LIA time constant of 1 s and a pass-band of $27.5\text{-}270 \text{ MHz}$) and it was about 3.52 times higher than that obtained in the free-space coupling configuration (~ 119). This difference is analyzed as follows.

(1) As SNR is proportional to the LHR double-sideband bandwidth (B) (c.f. Eq. (5.1)), the difference in SNR between these two optical coupling systems is mainly attributed to the difference in the bandwidths of the used RF filters in two system, a factor α_1 of ~ 6.36 ($= \sqrt{485/12}$ where $B_{\text{fiber}}=485 \text{ MHz}=2 \times (270-27.5) \text{ MHz}$ for the fiber coupling system against $B_{\text{free-space}}=12 \text{ MHz}=2 \times (33-27) \text{ MHz}$ for the free-space coupling system) in favor of the fiber coupling LHR.

(2) As SNR is proportional to BB photocurrent (c.f. Eq. (5.1)), the difference in SNR is related to the difference in the BB photocurrent, a factor α_2 of ~ 0.57 ($= 117/207$ the BB photocurrent ratio between two LHR systems).

The total difference in the SNRs due to above two reasons is :

$$\alpha_1 \times \alpha_2 = 6.36 \times 0.57 = 3.63 \quad (5.14)$$

which is comparable to the factor of 3.52.

Summarizing Section 5.1.1, the noise sources, heterodyne signal and SNR of the LHR prototype are analyzed, the optimum operating LO photocurrent ($\sim 610 \mu\text{A}$) is experimentally obtained. Spectroscopic performance of the LHR system will be evaluated in the following section under the optimal LO photocurrent.

5.1.2.2 Spectroscopic performance

The capacity of the mid-IR optical fiber used to couple broadband source (BB or sunlight) was evaluated in this section. To that end, the same blackbody source as used in Chapter 4 was coupled to a direct absorption cell through the optical fiber. The common parameters were set as follows :

(1) temperature of the blackbody : 1000 °C;

(2) LO center frequency was scanned with a PZT driven by a sine-wave of 3.0 V with an offset of 1.6 V.

I. BB-laser heterodyne spectrum of CH₄ absorption at 8 μm

Two very adjacent absorption lines of CH₄ were chosen (centered at 1241.8632 cm⁻¹ and 1241.9489 cm⁻¹ with a line intensity of 6.590E-21 cm/molecule and 6.596E-21 cm/molecule, respectively [6]). Heterodyne spectrum of these CH₄ lines were recorded and compared with its direct laser absorption spectrum. The experimental parameters were set as follows :

(1) LO center frequency : 1242.00 cm⁻¹;

(2) frequency scanning rate : 500 mHz;

(3) electronic filter pass-band : 27.5-270 MHz;

(4) LIA sensitivity and time constant : 10 mV and 10 ms, respectively.

In order to record direct absorption spectrum of CH₄, one part of the EC-QCL radiation separated by a beam splitter was injected into a 12.5-cm long single-pass cell filled with a mixture of CH₄ in air at 260 mbar.

Using a PZT, driven by a sine-wave signal, to scan the external cavity of the LO laser and hence the laser frequency, direct laser absorption signal of CH₄ (Fig. 5.10 *left, black*), background (Fig. 5.10 *left, red*) and the corresponding direct absorption spectrum (Fig. 5.10 *left, blue*) in a single-pass cell were recorded. The BB-based laser heterodyne absorption signal of CH₄ (Fig. 5.10 *right, black*), background (Fig. 5.10 *right, red*) and the corresponding heterodyne absorption spectrum (Fig. 5.10 *right, blue*) in another single-pass cell were measured as well. Heterodyne (Fig. 5.10 *right, blue*) and direct (Fig. 5.10 *left, blue*) CH₄ absorption spectra were both fitted to a Voigt profile (Fig. 5.10 *left and right, green*).

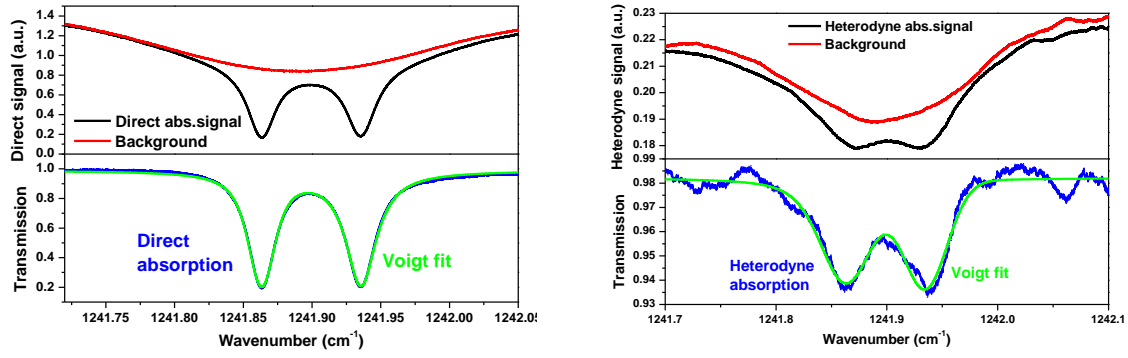


Figure 5.10 *left*: background (red) and direct absorption signal of CH₄ at 260 mbar (black); direct absorption spectrum (blue) fitted with a Voigt profile (green); *right*: background (red) and heterodyne absorption signal of CH₄ at 260 mbar (black); heterodyne spectrum of CH₄ absorption (blue) fitted with a Voigt profile (green).

It is seen that two adjacent CH₄ absorption lines of the LHR spectrum (Fig. 5.10 *right*) were resolved and in good agreement with the CH₄ direct absorption spectrum (Fig. 5.10 *left*). As can be observed in the spectral comparison, the heterodyne spectrum with a fitted Voigt linewidth (FWHM) of 0.0457 cm⁻¹ (Fig. 5.10 *right*, green) is significantly broader than the direct absorption spectrum with a experimentally fitted Voigt linewidth of 0.0239 cm⁻¹ (Fig. 5.10 *left*, green).

The theoretical Voigt line width (Δv_V , FWHM) can be approximately expressed as follow (c.f. Chapter 3.2.5) [7] :

$$\Delta v_V = 0.5346\Delta v_L + \sqrt{0.2166\Delta v_L^2 + (\Delta v_G^2 + \Delta v_{INS}^2)} \quad (5.15)$$

where the Lorentz linewidth Δv_L is 0.0221 cm⁻¹ [6] at 260 mbar, the instrument function of the LHR system Δv_{INS} is 0.0162 cm⁻¹ mainly determined by the doubled RF filter bandwidth of 485 MHz (for the pass-band of 27.5-270 MHz), the Δv_{INS} for the direct absorption spectrum measurement is determined by the laser emission linewidth of 9.2 MHz (or 0.00031 cm⁻¹), and the Gaussian linewidth Δv_G of 0.00383 cm⁻¹ is calculated from Eq. (3.7) [8] with v_0 of 1241.8632 cm⁻¹, T of 300 K, and M of 16 g/mole.

With above parameters, the theoretical Voigt linewidths of the LHR and direct absorption spectra of 0.0314 cm⁻¹ and 0.0228 cm⁻¹ are calculated using Eq. (5.15), respectively. As can be seen, the significant broadening characteristic in heterodyne spectrum is due to the wider instrument function.

Table 5.2 Comparisons between theoretical Voigt linewidths and measured Voigt linewidths of the LHR and the direct absorption spectra.

	LHR	Direct
Theoretical Voigt linewidth (cm ⁻¹)	0.0314	0.0228
Measured Voigt linewidth (cm ⁻¹)	0.0457	0.0239

Table 5.2 shows comparisons of theoretical Voigt linewidths to the measured Voigt linewidths of the LHR and the direct absorption spectra. It is seen that the measured Voigt linewidth of the direct absorption spectrum was comparable to the theoretical value, while the measured Voigt linewidth of LHR spectrum was obviously wider than the theoretical value. The broadening reasons are addressed as follows :

(1) The used LIA time constant of 10 ms was not adapted to the scanning time of $\Delta T_{scan}=14$ ms needed to scan across the halfwidth of the absorption line (i.e. the used time constant cannot meet $\Delta T_{scan} \geq 14 \cdot \tau$), that would broaden the heterodyne spectral line width (c.f. 5.1.2.2 (III)), in this case the scanning speed of LO frequency ν_{sc} is 0.787 cm⁻¹/s and the $\Delta\nu_{HWHM}$ is 0.0111 cm⁻¹).

(2) A uncertainty of ~15% in the pressure measurement resulting from the single-cell leakage would cause a broadening of 0.0033 cm⁻¹ (corresponding to a $\Delta P=39$ mbar where the pressure-broadening coefficient γ is 0.0861 cm⁻¹atm⁻¹ [6]).

This work demonstrated that the 860- μ m-core polycrystalline fiber is suitable for application of coupling mid-IR BB radiation to LHR. According to the analysis of the broadening effects, the impact of LHR instrument function (such as RF filter pass-band, LIA time constant with respect to the scanning speed of LO frequency, etc.) on LHR spectrum will be studied in the following sections.

II. Impact of RF pass-band on LHR spectrum

To investigate the impact of the RF filter pass-band on the LHR spectral signal, heterodyne absorption spectra of CH₄ in a single-pass cell were experimentally extracted and analysed with different pass-bands of RF filters. The experimental parameters were the same as those set above, except for :

- (1) LO center frequency : 1255.00 cm⁻¹;
- (2) frequency scanning rate : 500 mHz;

- (3) pressure of the CH₄ mixture in air in the single-pass cell : 280 mbar;
- (4) LIA sensitivity and time constant : 5 mV and 10 ms, respectively.

LHR noise has been investigated at first. Fig. 5.11 shows a noise amplitude spectrum of LHR signal from the RF output of the photomixer recorded using a signal analyzer (with a RBW of 100 kHz). As can be seen, there are strong 1/f noises in the low frequency range which has to be filtered out.

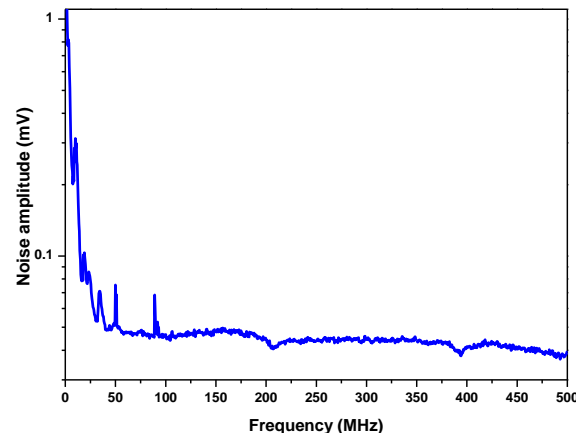


Figure 5.11 Noise amplitude spectrum from the RF output of the photomixer in the 1kHz-500 MHz range.

The noise densities within different pass-bands of the RF filters available in the present work were estimated by dividing the integral noise over each pass-band by both the bandwidth and the square root of the RBW (100 kHz) (Table 5.3). As shown in Table 5.3, the noise density of the RF filter with a pass-band of 27.5-270 MHz was lowest and the corresponding SNR was highest because of its wider filter bandwidth (at the cost of lower spectral resolution).

Table 5.3 Noise density with different RF filter pass-bands.

Pass-band (MHz)	DC-270	DC-520	DC-720	27-33	27.5-270
Noise density ($\mu V / \sqrt{Hz}$)	0.396	0.239	0.239	0.180	0.149

LHR CH₄ absorption spectra were then recorded with these five available RF filters, as shown in Fig. 5.12. The LHR CH₄ absorption spectra measured with AC-coupling band-pass RF filters (Fig. 5.12 left), which can significantly filter out low frequency noises, have higher SNR and better spectral line-shape, while the spectra measured with DC-coupling low-pass RF filters (Fig. 5.12 right) are noisy resulted from high 1/f noise.

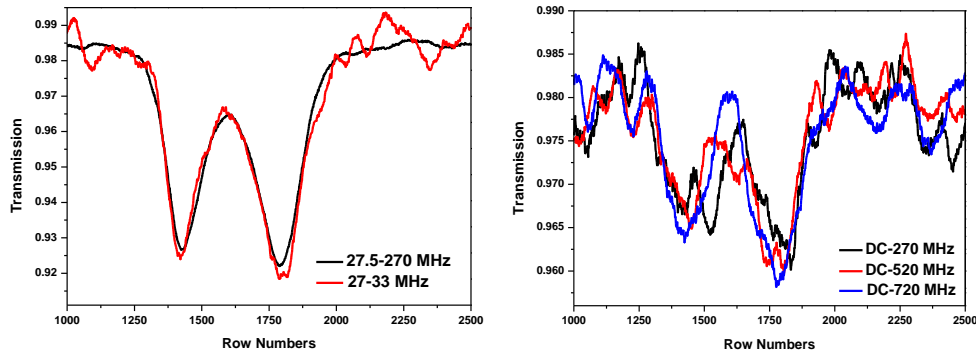


Fig. 5.12 Heterodyne spectra of CH₄ extracted with different RF filter pass-bands.

It's seen that the noise level of the spectrum measured with the RF filter with a pass-band of 27.5-270 MHz (Fig. 5.12 left in *black*) is lower than that measured with a pass-band of 27-33 MHz (Fig. 5.12 left in *red*). Moreover, there is no obvious difference in spectral line widths between two LHR CH₄ absorption spectra. The reason is that the theoretical spectral line width (FWHM) of CH₄ absorption around 1255.00 cm⁻¹ at 280 mbar is 0.034 cm⁻¹ (1020 MHz [9]) that is wider than the doubled RF filter bandwidths (12 MHz and 485 MHz) and therefore there is no any obvious effect of the RF filter bandwidths on the measured line widths.

Based on such analysis, the RF filter with a pass-band of 27.5-270 MHz was selected for the current LHR system.

III. LHR spectral line-shape vs. scanning speed of LO frequency

As discussed in Chapter 2.1.6 and Chapter 4.2.2.3, in order to obtain high-precision heterodyne spectrum (with minimized line shape shift and distortion), the scanning time ΔT_{scan} across the halfwidth of the absorption line Δv_{HWHM} (in [cm⁻¹]), which is also dependent on the scanning speed of the LO frequency v_{sc} (in [cm⁻¹/s]), should be appropriately adapted to a LIA time constant τ such that $\Delta T_{scan} = \Delta v_{HWHM} / v_{sc} \geq 14 \cdot \tau$. Experimental investigation on BB-based heterodyne spectra using different scanning speeds with a selected LIA time constant of 1 ms were carried out.

In this study, the experimental parameters were the same as those set above, except for :

- (1) LO center frequency : 1242.00 cm⁻¹;
- (2) RF filter pass-band : 27.5-270 MHz;
- (3) pressure of the CH₄ mixture in air in the single-pass cell : 280 mbar;
- (4) LIA sensitivity : 2 mV (Model SR830, Stanford Research Inc.).

LHR CH₄ absorption spectra recorded by scanning the LO frequency at different speeds (see Table 5.4) using the same LIA time constant of 1 ms are plotted in Fig. 5.13. As can be seen, selection of the scanning speed of the LO frequency should be well matched to the applied LIA time constant. Comparing these four heterodyne absorption spectra of CH₄, SNR, linewidth broadening $\Delta\nu_b$ (FWHM), line shift $\delta\nu$, and noise level (1σ) of these heterodyne absorption spectra were analyzed based on Voigt profile fit (Fig. 5.13, *blue*) and summarized in Table 5.4. It is seen that the combination of 1 ms time constant and the 0.3935 cm⁻¹/s scanning speed (with a scanning time of 36 ms), the heterodyne spectrum has a lower noise level and a smaller line shift while keeping high spectral resolution (Fig. 5.13 (b) and Table 5.4 in **bold**).

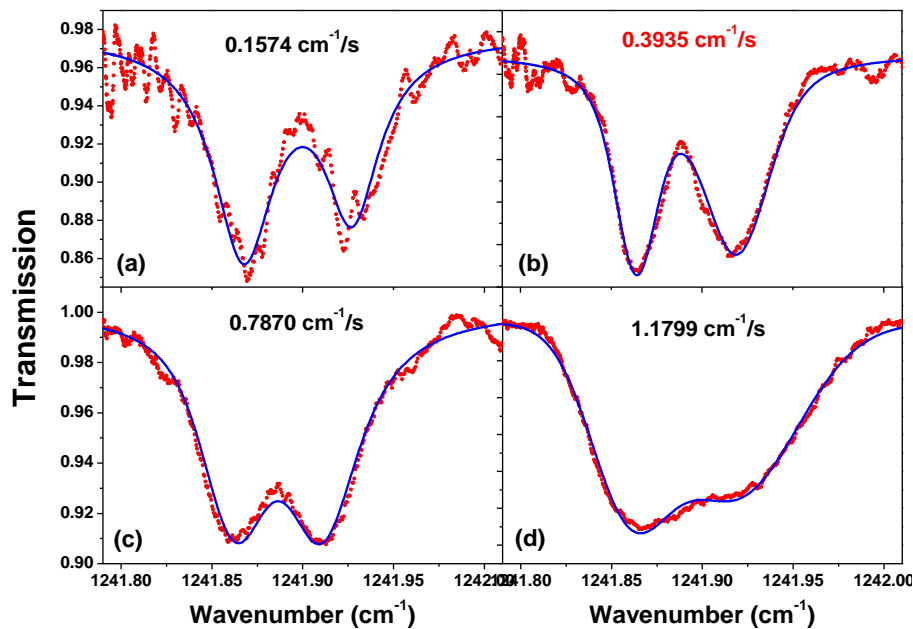


Figure 5.13 Heterodyne absorption spectra of CH₄ (*red*), fitted with Voigt profiles (*blue*).

Table 5.4 Analysis of BB-based heterodyne spectra (Fig. 5.13) of CH₄ absorption with the used time constants (τ) of 1 ms at different scanning speeds of the LO frequency (ν_{sc}). (Note : the halfwidth of the used CH₄ line $\Delta\nu_{HWHM}$ at 280 mbar is 0.014 cm⁻¹ [6].)

τ (ms)	ν_{sc} (cm ⁻¹ /s)	ΔT_{scan} (ms)	SNR	$\Delta\nu_b$ (cm ⁻¹)	Absorption depth	$\delta\nu$ (cm ⁻¹)	Fit residual (1σ)
1	0.1574	89	13	0.038	0.1142	1.6E-4	0.0091
	0.3935	36	24	0.042	0.1037	4.0E-4	0.0043
	0.7870	18	30	0.048	0.0975	8.2E-4	0.0032
	1.1799	12	43	0.079	0.0909	1.2E-3	0.0021

1 σ : Standard Deviation (SD)

Meanwhile, it is generally considered that the scanning speed of the LO frequency ν_{sc} set to a slower value, which meets well $\Delta T_{scan} = \Delta \nu_{HWHM} / \nu_{sc} \geq 14 \cdot \tau$, can limit the distortion of the line shape.

As can be seen from Table 5.4, at a LO frequency scanning speed of $0.1574 \text{ cm}^{-1}/\text{s}$, the scanning time of 89 ms was far more than 14 times the applied LIA time constant of 1 ms. In this case, the measured line shift was smallest, the absorption depth was deepest, the linewidth $\Delta \nu_b$ (Table 5.4) was narrowest and close to the theoretical value of $\sim 0.036 \text{ cm}^{-1}$ calculated from Eq. 5.15 using $\Delta \nu_L$ of 0.028 cm^{-1} , $\Delta \nu_{INS}$ of 0.0162 cm^{-1} and $\Delta \nu_G$ of 0.0038 cm^{-1} (c.f. 5.1.2.2 (I)). However, the noise ($1 \sigma : 0.0091$) was highest and SNR (~ 12) was lowest (Table 5.4). A trade-off has to be made. Therefore at the LIA time constant of 1 ms, the scanning speed of the LO frequency of $0.3935 \text{ cm}^{-1}/\text{s}$ (the scanning time of 36 ms), with which the noise ($1 \sigma : 0.0043$) was relatively low, the SNR of system (~ 24) was relatively high, the line shift ($\sim 0.0004 \text{ cm}^{-1}$) was relatively small and the achievable spectral resolution (spectral line width of $\sim 0.042 \text{ cm}^{-1}$) was relatively high, was thus selected for the LHR prototype measurement.

5.2 LHR prototype involving a mid-IR fiber to couple sunlight radiation

5.2.1 Instrumental description

The developed LHR prototype using a mid-IR polycrystalline fiber to couple sunlight to the LHR receiver is schematically shown in Fig. 5.14 and Fig. 5.15. The LHR prototype uses an EKO sun-tracker to real-time follow the Sun's movement. Collection of the sunlight in the atmospheric column into a mid-IR fiber is achieved through a lens associated with an optical filter in Germanium. The collection optics is installed on the instrument mount of the sun-tracker. The Ge-filter in front of the fiber is used to protect the fiber input terminal from damage caused by the direct exposure to the intense ultraviolet and visible part of the sunlight, and to limit the optical bandwidth of the incident radiation and let only the transmission of the solar radiation at wavelengths longer than $7 \mu\text{m}$ in our case to minimize shot noise resulting from the solar radiation [1].

The emerging sunlight from the fiber is collimated with a lens3 (in Germanium, AR coating ($3\text{-}12 \mu\text{m}$)) and injected into free-space. The sunlight is then amplitude modulated at a rate of about 1 kHz and directed to a beam splitter. The sunlight beam of 12.5 mm in diameter is superimposed on the beam splitter with a LO beam of 7.5 mm from the EC-QCL

determination, or to a 12.5 cm long home-made Ge-etalon ($\text{FSR} = 0.0333 \text{ cm}^{-1}$) for relative frequency calibration when the LO frequency is tuned.

5.2.2 Heterodyne measurement of atmospheric CH_4 and N_2O absorption spectrum

The developed LHR prototype was deployed on the roof of the ULCO-IRENE platform in Dunkerque ($51.05^\circ\text{N}/2.34^\circ\text{E}$) for ground-based remote sensing of trace gases in the atmospheric column.

When checking the system noise at the RF output port of the photomixer with the signal analyzer, it was found that the system noise was enhanced within 110 MHz, and became especially significant around 100 MHz, as shown in Fig. 5.16. This enhanced system noise may be resulted from the instability of the external cavity of the laser due to frequent field deployments.

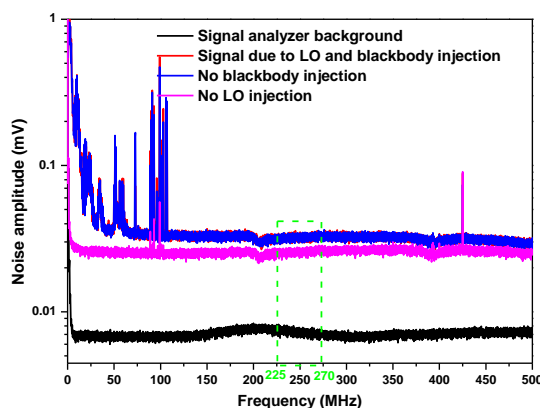


Figure 5.16 Noise amplitude spectra of the RF output from the photomixer within the bandwidth of 1kHz-500 MHz.

Therefore the previously optimized RF filter pass-band of 27.5-270 MHz was no longer adapted, a new RF filter with a pass-band of 225-270 MHz was selected to remove this excess noise. The LHR operational parameters were set as follows :

- (1) LO center frequency : 1262.00 cm^{-1} , scanned at a frequency of 250 mHz with a scanning voltage of 3.8 V and an offset of 2.0 V;
- (2) LIA sensitivity and time constant : 10 mV and 1 ms, respectively;
- (3) acquisition time per spectrum : 60 s;
- (4) averaging number of spectra : 15.

The LO frequency was scanned around 1262.00 cm^{-1} using PZT scan mode, atmospheric CH_4 and N_2O absorption spectrum was measured in the atmospheric column. Fig. 5.17 shows

a heterodyne absorption spectrum of atmospheric CH₄ and N₂O around 1262.00 cm⁻¹ (*left*). Fig. 5.17 also shows simulation spectra (*right*) for spectral identification.

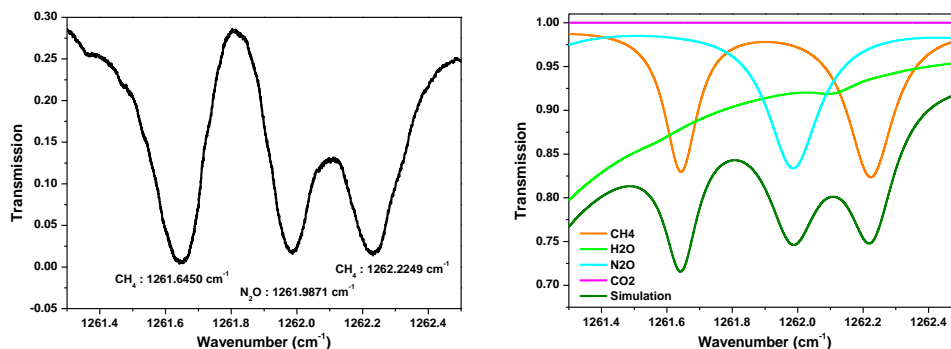


Figure 5.17 *left*: LHR spectrum of CH₄ and N₂O absorptions in the atmospheric column (Sun position: 16.69° Zenith / 156.47° Azimuth, 24 m above sea level, 18 Nov. 2018); *right*: simulation spectrum of multi-GHG (*olive*) using 0.5% H₂O (*green*), 2 ppm CH₄ (*orange*), 450 ppm CO₂ (*pink*) and 320 ppb N₂O (*cyan*) in the range of 1261.2-1262.8 cm⁻¹, accompanied with individual simulation spectra of all species mentioned above.

Fig. 5.18 shows a comparison of our experimentally extracted LHR spectrum (*black*) with a FT-IR spectrum (*red*) measured using a high-resolution Bruker IFS 125HR Fourier transform spectrometer on the QualAir platform of the UPMC (48°50'47"N/2°21'21"E, 60 m above sea level), as well as with a spectrum from an atmospheric transmission model (*blue*).

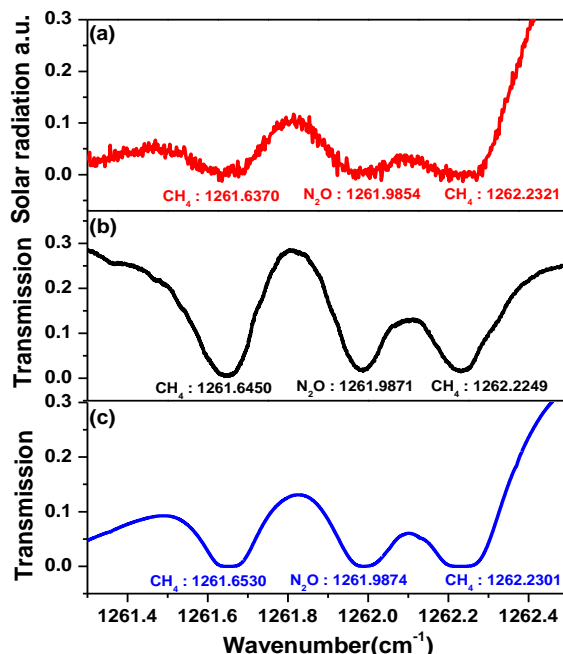


Figure 5.18 (a) Atmospheric absorption spectrum of CH₄ and N₂O from 1261.3 to 1262.3 cm⁻¹ recorded using a Bruker IFS 125HR FTS on the TCCON observation site in Paris; (b) the corresponding laser heterodyne spectrum of CH₄ and N₂O absorptions in the atmospheric column; (c) the atmospheric transmission modelling spectrum.

As can be seen in Fig. 5.18, the absorption line positions of CH₄ and N₂O from the LHR spectrum were in good agreement with those of the FT-IR spectrum as well as with an atmospheric transmission modeling. As water vapor was interfering with the LHR spectrum of CH₄-N₂O (shown in Fig. 5.17), and the water vapor distribution changes with time and space [9-11], the line-shape of the LHR spectrum was slightly different from the FT-IR spectrum and the atmospheric transmission modelling spectrum, made at different locations and different time under different atmospheric conditions. The overall spectral line-shapes of all three spectra were consistent.

Comparing to the FT-IR spectrometer used for ground-based remote measurements of trace gases in the atmospheric column, LHR is advantageous in terms of room temperature operation, a compact size, portability, higher spectral resolution, and smaller FoV, as summarized in Table 5.5.

Table 5.5 Comparisons between LHR and FTS

	Spectral resolution	FoV	Operation temperature	Instrument size / weight
LHR	0.003 cm ⁻¹	~0.4 mrad	Room temperature	~0.6 × 1.5 m ² / ~30 kg
FTS	0.02 cm ⁻¹	~2.39 mrad	Liquid nitrogen-cooled detector	~2 × 4 m ² / ~700 kg

Conclusion

In this chapter, a full transportable LHR prototype involving a mid-IR fiber to collect sunlight through an EKO sun-tracker was developed. Evaluation and optimization of the developed LHR prototype with the help of a stable high temperature blackbody radiation to simulate the sunlight was performed. The developed LHR instrument was then tested and validated via ground-based field measurements of tropospheric CH₄ and N₂O in the atmospheric column on the roof of the IRENE platform of the ULCO in Dunkerque (51.05°N/2.34°E). The extracted spectrum by the LHR was in a good agreement with the FT-IR spectrum measured using a Bruker IFS 125HR FTS and with an atmospheric transmission modelling spectrum, which demonstrated that the developed portable LHR prototype could be used for ground-based atmospheric sounding measurements of GHGs in the atmospheric column.

In the future work, vertical profiles of GHGs in the atmospheric column will be retrieved from the ground-based measured LHR spectrum using a retrieval algorithm, given a decent

knowledge of additional atmospheric parameters, like solar angle, atmospheric temperature, atmospheric pressure, composition of the atmosphere, and refractive index [12].

References

- [1] A. Rodin, A. Klimchuk, A. Nadezhdinskiy, D. Churbanov, and M. Spiridonov. High resolution heterodyne spectroscopy of atmospheric methane NIR absorption, *Opt. Express* 2014, **22**, 13825-13834.
- [2] D. Weidmann and D. Courtois. Infrared 7.6 μm lead-salt diode laser heterodyne radiometry of water vapor in a CH_4 -air premixed flat flame, *Appl. Opt.* 2003, **42**, 1115-1121.
- [3] A. Hoffmann, N. A. Macleod, M. Huebner, and D. Weidmann. Thermal infrared laser heterodyne spectroradiometry for solar occultation atmospheric CO_2 measurements, *Atmos. Meas. Tech.* 2016, **9**, 5975-5996.
- [4] P. Horowitz and W. Hill. *The Art of Electronics*, 2nd edition. Cambridge (UK) : Cambridge University Press, 1989, 431-432.
- [5] A. Klimchuk, A. Nadezhdinskii, Ya. Ponurovskii, Yu. Shapovalov, and A. Rodin. On the possibility of designing a high-resolution heterodyne spectrometer for near-IR range on the basis of a tunable diode laser, *Quantum Electron.* 2012, **42**, 244-249.
- [6] L. S. Rothman, I. E. Gordon, A. Barbe, D. C. Benner, P. F. Bernath, M. Birk, V. Boudon, L. R. Brown, A. Campargue, J. P. Champion, K. Chance, R. R. Gamache, A. Goldman, D. Jacquemart, I. Kleiner, N. Lacome, W. Lafferty, O. V. Naumenko, A. V. Nikitin, J. Orphal, V. I. Perevalov, A. Perrin, A. Predoi-Cross, C. P. Rinsland, M. Rotger, M. Simeckova, M. A. H. Smith, K. Sung, S. A. Tashkun, J. Tennyson, R. A. Toth, A. C. Vandaele, and J. V. Auwera. The HITRAN 2008 molecular spectroscopic database, *J. Quant. Spec. Rad. Transfer* 2005, **96**, 139-204.
- [7] J. J. Olivero and R. L. Longbothum, Empirical fits to the Voigt line width : A brief review, *J. Quant. Spectrosc. Radiat. Transfer* 1977, **17**, 233-236.
- [8] B. H. Armstrong. Spectrum line profiles : The Voigt function, *J. Quant. Spectrosc. Radiat. Transfer* 1967, **7**, 61-88.
- [9] IPCC, *Climate Change 2007 : The Physical Science Basis. Contribution of Working Group I to the Fourth Assessment Report of the Intergovernmental Panel on Climate Change* (Cambridge University Press, Cambridge, 2007).
- [10] N. Kämpfer. *Monitoring atmospheric water vapour*, Springer, 2013.
- [11] I. M. Held and B. J. Soden. Water vapor feedback and global warming, *Annu. Rev. Energ. Environ.* 2000, **25**, 441-475.
- [12] E. L. Wilson, M. L. McLinden, and J. H. Miller. Miniaturized laser heterodyne radiometer for measurements of CO_2 in the atmospheric column, *Appl. Phys. B* 2014, **114**, 385-393.

Summary and perspectives

LHR is advantageous in terms of high spectral resolution, high sensitivity and high vertical resolution in conjunction with a compact instrumental size deployable for field remote sensing of vertical concentration profiles of key trace gases in the atmospheric column.

In this PhD thesis, my work has focused on the development of a fully transportable mid-IR LHR instrument for ground-based remote sensing of CH_4 and N_2O in the atmospheric column.

First, the performance of the EC-QCL being used as the LO in our LHR was evaluated via the N_2O measurement produced in a chemical catalysis process by direct absorption spectroscopy in a multi-pass cell. The evaluation, performed from the aspects of laser emission line width, single-mode wavelength tunability, stabilization of the LO source and wavelength-dependent baseline, illustrated that the EC-QCL is suitable for being the LO in our LHR.

Second, in order to test our design of a fully transportable mid-IR LHR instrument and characterize its performance, a PoC mid-IR LHR receiver involving a free-space telescope system for sunlight coupling was developed. The developed LHR receiver was field tested on the QualAir platform of the UPMC with the help of the heliostat of the TCCON-Paris station. LHR absorption spectrum of CH_4 in the atmospheric column was extracted from the solar radiation using the developed ground-based LHR receiver and in good agreement with the spectrum measured by the TCCON-Paris station.

Finally, based on the developed ground-based LHR receiver, a full transportable mid-IR LHR prototype was developed. A mid-IR fiber combined with an EKO sun-tracker was exploited to collect sunlight for heterodyne detection, which renders the LHR fully transportable. The developed LHR prototype was field deployed on the roof of the IRENE platform of the ULCO in Dunkerque. The extracted LHR spectrum of CH_4 and N_2O in the atmospheric column was in a good agreement with the TCCON FT-IR spectrum of CH_4 and N_2O , as well as in good agreement with the atmospheric transmission modelling spectrum. This field measurement validates that the developed fully transportable mid-IR LHR instrument could be used for ground-based measurements of key trace gases in the atmospheric column. In addition, it also has high potential for applications on spacecraft or on airborne platform.

Compared to other currently existed LHR instruments, the developed LHR is advantageous due to the following two characteristics :

(1) fully transportable in the mid-IR : a mid-IR polycrystalline fiber with high flexibility and high transmission at 8 μm was firstly applied to couple the sunlight to the LHR receiver which makes LHR system fully transportable.

(2) very compact in the mid-IR : a commercially available and mature EC-QCL from Daylight Inc. was firstly used as the LO. It operates at room temperature and has high output optical power and narrow emission line width.

Ground-based measurement of vertical concentration profiles of trace gases with high spectral resolution, high sensitivity and high vertical resolution is a key challenge in atmospheric science and climate change research. For the developments on going, the following considerations are taken into account :

(1) In order to well match the theoretical atmospheric absorption spectrum, LHR baseline and LHR background signal should be subtracted, and variation in solar power should be corrected.

(2) The tracking accuracy of the sun-tracker is 0.01° which may result in a minor oscillation that can be seen in the LHR baseline when scanning the LO frequency. To calibrate this oscillation, a beam splitter in combination with a mid-IR photodetector should be introduced as a reference channel performing simultaneous monitoring of the solar radiation. This channel is sensitive to the accuracy of the sun-tracker as well as drops in the signal due to cloud covering.

(3) To satisfy the demands for the measurements of vertical concentration profiles of the key atmospheric trace gases, it is quite necessary to make a profound research about the retrieval algorithm in collaboration with Moscow Institute of Physics and Technology (MIPT) who has well developed a retrieval algorithm.

(4) Unlike the near-IR, in the mid-IR, there is no commercially available fiber collimating optics, coupling sunlight into the mid-IR fiber with a spatially separated optics is thus a big challenge which needs a very professional and precise alignment. Furthermore following the movement of the Sun, the fiber should be long enough and also can be bended, which increases the power loss. Therefore all integrated fiber coupling system having a potential to highly increase the heterodyne efficiency is a good choice for compensating for above losses (c.f. Appendix 1).

(5) In the next 5 or 10 years, we propose to develop a next generation laser heterodyne radiometer (NexLHR) based on the nowadays modern photonic integrated circuits (ICs)

technology. The objective is to realize a “on-chip” LHR receiver. It will make the NexLHR cost-effective, energy efficient, autonomous and ultra-portable. It will be most suitable for field deployment for the measurements of atmospheric vertical profiles of key atmospheric species through in situ ground-based measurements, aircraft and satellite observations, as well as for integration into currently operational worldwide observation networks. Meanwhile, the proposed infrared LHR instrument presents high potential for technology transfer and commercialization.

Résumé

La mesure des profils de concentration verticale des gaz traces dans l'atmosphère est d'une grande importance pour comprendre la physique, la chimie, la dynamique et le budget de rayonnement de l'atmosphère ainsi que pour valider les résultats des modèles chimiques et des satellites observations.

RHL offre des avantages combinés significatifs pour la télédétection passive des profils de concentration verticale des gaz traces atmosphériques : (1) pureté spectrale élevée de la ligne d'émission laser (~10 MHz), résultant en une puissance de résolution : 10^5 - 10^7 , ce qui rend la résolution spectrale du RHL non limitée en fonction de l'appareil et est déterminée par les filtres électroniques sélectionnés. Généralement, une résolution spectrale applicable plus élevée (10^{-3} cm^{-1}) permettrait d'atteindre ; (1) une résolution verticale élevée dans le profil de concentration verticale ; (2) une sensibilité plus élevée (dans un facteur de 2-3 de la limite quantique), ce qui permet une limite de détection plus faible des espèces de gaz avec une grande précision; (3) une résolution verticale plus élevée due à une très petite FoV cohérente, ce qui rend RHL ont une couverture géographique ultrafine avec moins d'interférences nuageuses; (4) une dimension instrumentale compacte rendant RHL facile pour le déploiement sur le terrain.

RHL est une sorte de radiomètre basé sur un récepteur hétérodine qui traite du rayonnement solaire d'entrée comme source spectrale recueillie à partir d'un télescope en le mélangeant avec le rayonnement d'un laser utilisé comme oscillateur local (OL) sur un photodétecteur utilisé comme photomixteur. L'amplitude du signal de battement résultant du photomixteur varie en fonction de la caractéristique d'absorption des gaz traces atmosphériques. En scannant la fréquence OL à travers cette caractéristique, le spectre d'absorption atmosphérique peut être obtenu. Les profils de concentration verticale des gaz traces atmosphériques cibles peuvent être récupérés en se basant sur les spectres d'absorption mesurés par RHL dans la colonne atmosphérique à l'aide d'un algorithme de récupération approprié

L'objectif de cette thèse consiste à développer un instrument RHL entièrement transportable pour la télédétection au sol, dans le domaine de l'infrarouge moyen (mi-IR), de gaz à l'état de traces présents dans la colonne atmosphérique.

Afin de tester notre appareil et de caractériser ses performances, un récepteur RHL mi-IR a été émis au point comme Preuve de Concept (PdC). Il a été validé sur la plate-forme QualAir

de l'Université Pierre et Marie Curie (UPMC) associé à un héliostat de la station TCCON-Paris. Ainsi, le spectre d'absorption du CH₄ présent dans la colonne atmosphérique a été extrait du rayonnement solaire à l'aide de notre récepteur RHL. Il est en bon accord avec le spectre mesuré par la station TCCON-Paris.

Après cette validation d'essai sur le terrain, un instrument LHR mi-IR (~8 μm) entièrement transportable a été développé. Une fibre IR nouvellement disponible dans le commerce est exploitée pour coupler la lumière du soleil au récepteur RHL, équipé d'un EKO sun-tracker, ce qui rend le RHL mid-IR très transportable et stable. Le prototype RHL développé est déployé sur le toit de la plate-forme IRENE de l'Université du Littoral Côte d'Opale (ULCO) à Dunkerque pour la télédétection sur le terrain de CH₄ et N₂O dans la colonne atmosphérique. Le spectre LHR de CH₄ et N₂O dans la colonne atmosphérique est en bon accord avec le spectre FT-IR de CH₄ et N₂O et la modélisation de la transmission atmosphérique.

L'instrument LHR mi-IR entièrement transportable mis au point dans le cadre de cette thèse possède un fort potentiel d'utilisation dans la mesure des profils verticaux de concentration d'espèces clés atmosphériques. Il peut potentiellement être positionné sur des engins spatiaux, sur des plates-formes aéroportées ou au sol.

i. Évaluation de la performance de l'oscillateur local utilisé

Dans un premier temps, la performance d'un EC-QCL qui sera utilisé comme OL dans notre système RHL mid-IR, en termes de largeur de ligne d'émission laser, de réglage de longueur d'onde en mode unique, de stabilisation de la source OL et de ligne de base dépendante de la longueur d'onde, a été évaluée par la surveillance en temps réel de N₂O produit dans un processus de catalyse chimique. Ce travail a été réalisé en collaboration avec l'UCEIV de l'ULCO. (Note : Dans cette partie, pour les figures, les tableaux et les formules, veuillez vous référer au Chapitre 3.)

i.1. Surveillance N₂O par spectroscopie optique d'absorption de longue trajectoire

La configuration expérimentale est montrée dans la Fig. 3.1. Une onde continue EC-QCL, est utilisée comme OL dans notre expérience mi-RHL, est couplée à une cellule multi-pass hermanni-Herriot modifiée. La fréquence EC-QCL est numérisée sur une ligne d'absorption N₂O appropriée pour déterminer son absorption intégrée dépendante de la concentration en adaptant le spectre d'absorption expérimental à un modèle de profil Voigt. Le réglage de

fréquence fine de l'EC-QCL est réalisé en appliquant un signal de 50 Hz sinusoïdes (avec une amplitude de $3,0 V_{PP}$ et un décalage de $1,6 V_{DC}$) à partir d'un générateur de fonction à l'élément PZT de la cavité externe de l'EC-QCL. Comme le montre la Fig. 3.1 (à gauche), 10 % de faisceau laser réfléchi est envoyé à un étalon Fabry-Perot pour l'étalonnage de la fréquence laser, et 90 % du faisceau laser transmis est dirigé vers la cellule multi-pass pour sonder l'absorption de long chemin optique de N_2O .

La cellule multi-pass modifiée de 3,2 L utilisée est formée de deux miroirs de réflectivité élevés (séparés par 55 cm). La lumière laser entre et sort de la cellule multi-pass à travers un trou commun équipé d'une fenêtre d'accouplement coincée à l'avant de la cellule. Dans le présent travail, 90 parcours ont été faites entre les miroirs, ce qui a donné une longueur optique efficace de 50 m. Le faisceau laser sortant de la cellule multi-pass est concentré dans un détecteur thermoélectrique de photovoltaïque infrarouge refroidi. Une carte d'acquisition de données de National Instruments, contrôlée par un programme LabVIEW, est utilisée pour l'échantillonnage et l'acquisition de données. Les données enregistrées sont numérisées et transférées sur un ordinateur portable pour un traitement ultérieur des données afin de récupérer la concentration N_2O .

i.2. Évaluation de la largeur de la ligne laser

La largeur de la ligne de l'émission EC-QCL utilisée comme OL joue un rôle clé dans la résolution spectrale du RHL. Ce paramètre a été évalué dans le travail actuel en utilisant la méthode spectroscopique.

Une largeur de ligne de laser (FWHM) de 9.2 MHz a été déduite expérimentalement qui correspond à une puissance de résolution de laser d'environ 10^7 . Ce résultat démontre que l'EC-QCL est très approprié pour une utilisation comme OL dans le système RHL en cours de développement et il pourrait assurer l'exigence de résolution spectrale élevée (la largeur de la ligne laser-bande de filtre électronique classique allant de 10 MHz à quelques dizaines de MHz).

i.3. Précision de mesure et LoD

La stabilité d'un instrument d'analyse est un paramètre important qui affecte la sensibilité de détection et la précision de mesure. La moyenne des signaux est généralement utilisée pour améliorer la sensibilité à la détection et la précision de la mesure. Cependant, en raison de l'instabilité de l'instrument (tels que les changements dans l'intensité lumineuse, les décalages

de longueur d'onde laser et les dérives sonores sombres de détecteur, les dérives de température, les franges mobiles, les changements dans les spectres de fond, etc.), n'importe quel système réel n'est stable que pour un temps limité donc qu'un temps moyen optimal devrait être précisé par une analyse de variance Allan afin de déterminer le maximum. moyenne, c-à-d., la meilleure précision de mesure.

Mesures de la série chronologique de spectre d'absorption 1 ppmv N₂O ont été effectuées pour l'analyse de variance d'Allan afin de déterminer le temps moyen optimal. 9000 spectres consécutifs d'absorption directe de N₂O ont été enregistrés expérimentalement, avec un temps d'acquisition de 0,2 s par spectre. La Fig. 3.6 présente une déviation d'Allan en fonction du temps moyen basé sur les mesures de la série chronologique des spectres d'absorption N₂O. La pente en décomposition (ligne pointillée rouge) montre la réduction efficace du bruit blanc en signalant en moyenne dans un délai moyen maximal (temps de stabilité du système) d'environ 236 s, ce qui est principalement limité par la température et la stabilité actuelle du contrôleur QCL. La précision de mesure correspondante est de 5,2 ppbv, ce qui conduit à une incertitude relative dans la précision de mesure de 0,5%. Après 236 s, l'écart Allan augmente (ligne pointillée bleue), c-à-d., les instabilités du système instrumental contrebalancent néanmoins la réduction de bruit donnée par la moyenne de temps.

Il est important de noter que ce max. du temps de stabilisation de 236 s prouve également que le temps de stabilité de l'EC-QCL utilisé est au moins aussi bon que 236 s, ce qui est très approprié pour l'acquisition de spectres RHL (~ minute par spectre).

i.4. Conclusion

La performance d'un EC-QCL, qui sera utilisé comme OL dans le système RHL, a été évaluée en termes de largeur de ligne d'émission laser, de réglage de longueur d'onde en mode unique, de stabilisation de la source OL et de ligne de base dépendante de la longueur d'onde. En se basant sur l'analyse des spectres d'absorption N₂O mesurés, la largeur de la ligne d'émission EC-QCL de 9,2 MHz a été réduite. Un temps de fonctionnement stable de la OL aussi bon que 236 s a été estimé à l'aide de l'analyse de variance d'Allan, il est adéquat pour la mesure RHL du spectre d'absorption moléculaire. L'EC-QCL est en réglage continu mode-hop sans interruption avec une ligne de base lisse. En fait, dans un instrument RHL, la ligne de base spectrale est principalement déterminée par la variation de puissance du laser (OL) lors de la numérisation de la longueur d'onde laser par le biais de la caractéristique d'absorption moléculaire cible. Il est donc fortement souhaitable d'avoir une ligne de base

spectrale induite par la puissance laser aussi lisse que possible afin d'obtenir une récupération de haute qualité du spectre RHL atmosphérique.

ii. Développement d'une preuve de concept mid-IR RHL

Deuxièmement, afin de tester notre conception d'un instrument RHL à mid-IR entièrement transportable et de caractériser ses performances, un récepteur RHL de mid-IR PdC impliquant un système de télescope spatial libre pour le couplage de la lumière du soleil a été développé

Le récepteur RHL développé a été testé sur la plate-forme QualAir de l'UPMC avec l'aide de l'héliostat de la station TCCON-Paris. Le spectre d'absorption RHL de CH₄ dans la colonne atmosphérique a été extrait du rayonnement solaire à l'aide du récepteur RHL au sol développé et en bon conformité avec le spectre mesuré par la station TCCON-Paris. (Note : Dans cette partie, pour les figures, les tableaux et les formules, veuillez vous référer au Chapitre 4.)

ii.1. Un RHL PdC fonctionnant à 8 μm

Le RHL PdC développé est schématiquement présenté dans la Fig. 4.1. Un récepteur RHL typique comprend un système de collecte de lumière du soleil associé à un traceur solaire, un oscillateur local, un photomixeur, un récepteur RF, un module de démodulation et de modulation du signal, ainsi qu'un module de métrologie de fréquence (dans notre cas, l'absorption directe de la molécule cible dans une cellule de référence à passage unique de 12,5 cm de long a été utilisé). Pour caractériser et optimiser les performances du récepteur PdC RHL développé une source stable de corps noir a été utilisé comme lumière du soleil. Des mesures d'hérodynne des spectres d'absorption de CH₄ ont été exécutées dans une cellule de 12,5 cm à passage unique en laboratoire.

Le rayonnement d'un corps noir est collecté et collimaté avec le miroir parabolique hors axe (OAPM) 1 et OAPM2. Le faisceau BB est filtré par un filtre optique (en Ge). La modulation d'amplitude du faisceau BB injecté est faite à 1 kHz à l'aide d'un couplet situé au point focal réel de OAPM2. Il est ensuite dirigé vers un séparateur de faisceau. Le faisceau BB sera superposé avec le faisceau OL de l'EC-QCL qui est élargi par deux OAPM, contrôlé par l'intensité et la polarisation ajustée à l'aide d'un polariseur IR à large bande. Les faisceaux combinés sont concentrés par OAPM5 sur un photomixeur VIGO. Le signal de la note de battement à $|\omega - \omega_L|$ dans le domaine RF, généré à partir du photomixeur, entre dans le

récepteur RF par un filtre de 27-33 MHz passe-bande suivi par des amplificateurs à faible bruit à 2 étapes avec un gain de 24 dB chacun. Après cela, le signal de battement amplifié est relié à une diode Schottky de loi carrée pour la mesure de puissance du signal RF qui est proportionnelle au carré de l'amplitude de signal de battement d'entrée. Le signal de sortie du détecteur de droit carré est démodulé. Une carte d'acquisition de données de National Instruments est utilisée pour numériser le signal de sortie de la LIA via un programme LabVIEW. Les données sont ensuite transférées sur un ordinateur portable pour un traitement ultérieur.

ii.2. Spectre d'hétérodiode laser de l'absorption de CH₄ à 8 μm

Afin de valider les performances spectroscopiques du récepteur RHL développé, le spectre d'hétérodiode laser et le spectre d'absorption directe de CH₄ à 8 μm ont été simultanément mesurés et comparés. Dans ce travail, le spectre d'hétérodiode laser de l'absorption de CH₄ à 1233.46 cm⁻¹ a été enregistré avec la fréquence de balayage de 100 mHz et une LIA constante de temps de 100 ms.

Le rayonnement du corps noir a été collecté et collimaté avec OAPM1. Il a ensuite été concentré et dirigé par OAPM2 vers une cellule de passage unique de 12,5 cm de long, remplie de mélange CH₄ dans l'air à la pression atmosphérique. Le faisceau émergent de la cellule a été l'amplitude modulée à 1 kHz à l'aide de l'couperet. Le faisceau filtré par un filtre optique a été dirigé vers un séparateur de faisceau sur lequel il a été superposé avec le faisceau OL de l'EC-QCL. Les faisceaux combinés ont été concentrés par OAPM5 sur le photomixeur VIGO.

Une partie du rayonnement EC-QCL séparé par un séparateur de faisceau a été injecté dans une cellule à passage unique de 12,5 cm remplie du mélange CH₄ dans l'air à la pression atmosphérique. Le spectre d'absorption directe de CH₄ dans la cellule à passage unique a été utilisé pour évaluer le spectre d'hétérodiode laser de l'absorption du CH₄.

Un PZT entraîné par un signal d'onde sinusoïdale a été utilisé pour numériser la longueur d'onde OL (EC-QCL), le spectre d'absorption direct du CH₄ de la OL dans la cellule à une seule passe (Fig. 4.7 supérieur) et son spectre d'absorption hétérodiode du rayonnement BB incident (Fig. 4.7, inférieur) ont été enregistrés simultanément. Les spectres d'absorption de l'hétérodiode et du CH₄ direct ont tous deux été respectivement ajustés sur un profil Lorentz (Fig. 4.7 rouge) avec une fréquence d'absorption centrale fixe à 1233,45545 cm⁻¹, respectivement. La largeur de la ligne Lorentz de 0,1065 cm⁻¹ pour le spectre d'absorption de

l'hétérodiène CH₄ (Fig. 4,7 inférieur) est bien compatible avec celle de 0,1068 cm⁻¹ pour le spectre d'absorption direct du CH₄ (Fig. 4,7 supérieur). Ce travail démontre la fonctionnalité du PdC RHL.

ii.3. Vitesse de balayage de fréquence par rapport à la constante de temps de la LIA

La constante de temps (τ) de la LIA est un paramètre très critique qui a un impact sur la suppression du bruit et la forme de la ligne d'absorption du spectre RHL mesuré. Une constante de temps τ plus longue peut réduire considérablement le bruit, mais elle entraîne également un déplacement du centre spectral de ligne et déforme la forme de ligne. Afin de minimiser ces effets indésirables, le temps ΔT_{scan} de numérisation de la demi-largeur Δv_{HWHM} de la ligne d'absorption doit être au moins égal à 14 fois de la constante temporelle de la LIA (c.f. Chapitre 2.1.6).

Une étude expérimentale sur les spectres d'hétérodiène à base de BB à l'aide de différentes combinaisons de τ et de v_{sc} a été effectuée. Les spectres d'hétérodiène de CH₄ ont été enregistrés à l'aide de quatre combinaisons de différents τ et de v_{sc} (tableau 4.2). Les résultats sont présentés dans Figs. 4.8-4.11 (noir). Sur la base de l'analyse des spectres d'absorption hétérodiène montrés dans Figs. 4.8-4.11 (noir), SNR, élargissement de la largeur de la ligne (Δv_b), profondeur d'absorption, décalage de ligne (δv) et niveau de bruit (1σ) de ces spectres ont été analysés à partir des ajustements de profil Lorentz (Figs. 4.8-4.11 rouge et bleu) et résumés dans le tableau 4.3-4.6, les constantes de temps optimales (τ) à des vitesses de balayage données de la fréquence OL (v_{sc}) et des temps de numérisation (ΔT_{scan}) ont été obtenues pour les travaux en cours, comme le montre le tableau 4.3-4.6 en gras et Fig.4.8-4.11 en rouge.

Comme nous le constatons, la sélection de la constante de temps LIA doit être bien adaptée à la vitesse de numérisation de la fréquence OL ainsi que le temps de numérisation. Lorsque la constante de temps est trop petite, le bruit augmentera. Tandis que quand elle est, plus longue (que la constante optimale), la constante de temps se traduirait par une réduction de la profondeur d'absorption, dans le décalage de la fréquence du centre d'absorption et dans la distorsion de la forme de la ligne d'absorption.

En comparant au-dessus de quatre combinaisons optimales pour la détection de l'hétérodiène, résumés dans le tableau 4.7, la combinaison de la vitesse de balayage de la fréquence OL de 0,3935 cm⁻¹/s (le temps de balayage de 137 ms) et de la constante de temps LIA de 1 ms a un niveau de bruit relativement faible, une profondeur d'absorption la plus

développée, aucun changement significatif de la fréquence du centre d'absorption et aucune distorsion de la forme de la ligne d'absorption (tableau 4.7 en gras).

En principe, la relation entre le temps de numérisation (ΔT_{scan}) doit être égale ou supérieure à 14 fois la constante de temps de la LIA (τ) (c.f. Chapitre 2.1.6).

Selon ΔT_{scan} et τ dans le tableau 4.7, la combinaison du temps de balayage de 137 ms et de la constante de temps de 1 ms s'accorde bien Éq. (4).

2) qui peut réduire efficacement le bruit sans causer de changement évident et de distorsion de la forme de la ligne, et est compatible avec notre l'analyse spectrale comme discuté ci-dessus. Cette combinaison a donc été sélectionnée pour nos autres mesures RHL.

ii.4. Mesure de terrain à Paris

Le PdC RHL développé a été testé sur le terrain sur la plate-forme QualAir de l'UPMC, en collaboration avec le LERMA de l'UPMC à Paris (Dr. Yao TE).

L'instrument parisien fait partie du TCCON (gare De Paris). Le TCCON est un réseau de spectromètres fourier Transform au sol enregistrant des spectres d'absorption atmosphérique directe dans la région spectrale infrarouge. À partir de ces spectres, des abondances précises et cohérentes de CO_2 , CH_4 , N_2O , HF, CO, H_2O et HDO sont récupérées (<http://www.tcon.caltech.edu/>). La plate-forme QualAir Fourier transforme le spectromètre (Bruker's IFS 125HR) avec une résolution spectrale de $0,02 \text{ cm}^{-1}$ adaptée à la télédétection au sol des espèces moléculaires dans la colonne atmosphérique. Connecté à un traceur solaire sur la terrasse sur le toit (Fig. 4.12 à gauche), le QualAir FTS (Fig. 4.12 à droite) fonctionne dans la configuration d'absorption solaire et permet de détecter un grand nombre de polluants atmosphériques.

ii.4.1. RHL impliquant un système de télescope pour le couplage de l'espace libre de la lumière du soleil

Afin de coupler la lumière du soleil, recueillie par l'héliostat sur la plate-forme QualAir, à notre RHL, un système d'assemblage de cages Thorlabs de 60 mm a été utilisé pour un système de télescope de couplage en espace libre. Le système d'assemblage de cage utilisant quatre tiges rigides en acier sur lesquelles les composants optiques peuvent être montés le long d'un axe optique commun, fournit un moyen commode pour construction des systèmes opto-mécaniques stables avec une ligne établie de blocs de construction de précision-machines conçus pour une grande flexibilité et un alignement précis.

Le système de cage utilisé pour l'accouplement de la lumière du soleil se compose d'un miroir monté dans un cube rotatif pour refléter la lumière du soleil de l'héliostat à notre RHL, un diaphragme a été utilisé pour contrôler la taille du faisceau de lumière du soleil, et deux lentilles (en CaF_2 , $f_1 = 150$ mm et $f_2 = 75$ mm) ont été utilisés pour $2 \times$ contraction de faisceau, comme le montre la Fig. 4.13.

La configuration expérimentale déployée sur la plate-forme QualAir est présentée par schéma dans Figs. 4.14 et 4.15. Le rayonnement solaire est capté par un héliostat externe installé sur la terrasse du toit et dirigé vers le laboratoire de bas niveau. La lumière du soleil est d'abord reflétée, collimatée et façonnée par le système de cage. Ce dernier est filtré par un filtre optique (pour enlever les rayons UV et les rayonnements visibles et limiter la bande passante du rayonnement incident dans la région infrarouge) et l'amplitude modulée avec un couperet à 1 kHz. Il est ensuite dirigé vers un séparateur de faisceau sur lequel il est superposé avec le faisceau OL de l'EC-QCL. La taille du faisceau laser OL est d'abord augmentée par OAPM3-OAPM4, avec une intensité contrôlable et une polarisation ajustée à l'aide d'un polariseur IR à large bande. Les faisceaux combinés sont concentrés avec OAPM5 sur le mixer VIGO. La puissance OL réfléchiée par un séparateur de faisceau (fenêtre CaF_2) est utilisée pour la métrologie de fréquence, par l'absorption directe de CH_4 dans une cellule de passage unique à la pression atmosphérique, ou par un étalon fait maison de 12,5 cm de long dans Ge pour enregistrer des franges étalon pour une fréquence relative étalonnage.

ii.4.2. Prédicteurs des essais sur le terrain du RHL PdC développé

Le signal d'absorption atmosphérique du CH_4 a été extrait sur le champ à l'aide du RHL développé. Dans cette étude, les paramètres du récepteur RHL ont été fixés comme suit : OL (EC-QCL) a été énuméré à l'aide du mode de balayage PZT autour de $1242,00 \text{ cm}^{-1}$ avec une fréquence de balayage de 250 mHz. La tension de balayage est de 3,0 V avec un décalage de 1,6 V. Bande passante de filtre électronique et LIA constante de temps sont 6 MHz et 1 ms, respectivement.

Le spectre RHL atmosphérique extrait expérimentalement de CH_4 a été comparé à un spectre d'un Bruker IFS 125HR FTS à haute résolution et à un modèle de transmission atmosphérique. Les trois spectres sont tracés dans la Fig. 4.19. Bien qu'en raison de la ligne de base structurée résultant du OL, le spectre RHL atmosphérique du CH_4 (Fig. 4.19 (b)) doit être extrait d'une ligne de base basée sur BB, la forme spectrale globale de ligne est compatible avec le spectre atmosphérique correspondant de FTS (Fig. 4.19 (a)) et la

modélisation de la transmission atmosphérique du spectre CH₄ (Fig. 4.19 (c)).

ii.5. Conclusion

Un RHL de mid-IR de PdC a été développé et sa performance a été évaluée et optimisée à l'aide d'un corps noir d'IR à haute température utilisé comme lumière du soleil avec l'intensité stable. Des spectres d'hétérodième bb-basés de CH₄ dans une seule cellule à ~8 μm ont été employés pour la caractérisation du RHL développé. Le RHL développé a ensuite été déployé pour des essais sur le terrain sur la plate-forme QualAir à l'UPMC. La mesure au sol du CH₄ troposphérique dans la colonne atmosphérique a été obtenue. Bien qu'il ait subi à la ligne de base structurée résultant du dysfonctionnement du OL EC-QCL utilisé, le spectre RHL extrait de CH₄ a été confirmé par la mesure de non-absorption RHL d'à proximité et par une comparaison avec le spectre FTR mesuré par un Bruker IFS 125HR FTS et avec un spectre de modélisation de la transmission atmosphérique.

Dans les travaux suivants, de grands efforts ont été consacrés pour rendre le RHL mid-IR transportable et compact pour la mesure in situ, et de déplacer la longueur d'onde OL à une autre ligne moléculaire pour éviter la ligne de base structurée au laser autant que possible.

iii. Développement d'un prototype RHL moyen-IR transportable

Enfin, sur la base du récepteur RHL au sol développé, un prototype complet de RHL mid-IR transportable a été développé. Nous avons exploré une fibre mid-IR pour coupler la lumière du soleil au récepteur hétérodième, ce qui rend notre RHL, équipé d'un EKO sun-tracker, entièrement transportable. L'instrument RHL développé a été testé et validé au moyen de mesures au sol sur le terrain du CH₄ et du N₂O troposphériques dans la colonne atmosphérique sur la terrasse du toit de la plate-forme IRENE à Dunkerque (51.05°N/2.34°E). (Note : Dans cette partie, pour les figures, les tableaux et les formules, veuillez vous référer au Chapitre 5.)

iii.1. Prototype RHL impliquant une fibre mid-IR pour coupler le rayonnement du corps noir

iii.1.1. Description instrumentale

Afin de tester et de caractériser les performances de la fibre mid-IR nouvellement disponible dans le commerce utilisée pour l'application RHL, une configuration RHL utilisant le couplage de fibres de rayonnement du corps noir a été établie (Figs 5.1 et 5.2).

Le rayonnement du corps noir est collecté et collimaté avec une lentille CaF₂, puis couplé à une fibre polycrystalline de 860 µm-noyau à travers une deuxième lentille CaF₂. Le rayonnement du corps noir émergent de la fibre est ensuite collimaté et filtré à l'aide d'une lens³ dans Germanium avec revêtement AR pour 3-12 µm région. L'amplitude du faisceau BB est amplitude modulée à 1 kHz à l'aide d'un couperet mécanique et est ensuite dirigé vers un séparateur de faisceaux. Le faisceau BB est superposé avec le faisceau OL de l'EC-QCL. La lumière OL est étendue de taille par un facteur de 3 à deux OAPM, avec une intensité contrôlable et une polarisation ajustée à l'aide d'un polariseur IR à large bande. Les faisceaux combinés BB et OL sont ensuite concentrés par un OAPM₆ (f₆ à 38,1 mm) sur un photomixeur VIGO. Le signal de note de battement RF du photomixer introduit le même récepteur RF impliqué dans le PdC mid-IR RHL (c.f. Chapitre 4) à l'exception du filtre RF ayant une bande de passage de 27,5-270 MHz au lieu de 27-33 MHz.

iii.1.2. Caractérisation des performances du prototype RHL

iii.1.2.1. RSB du signal de battement

Afin de caractériser la performance RHL à l'aide d'un système de couplage de fibres pour la collecte de la lumière du soleil, l'enquête en termes de RSB du signal RHL a été effectuée à l'aide d'une source de corps noir calibré. Dans cette étude, la température du corps noir a été fixée à 1000 °C. Des mesures de série de temps du signal RF du LIA avec et sans injection de rayonnement de OL ont été effectuées. Les puissances efficaces de OL et de BB ont été mesurées à la sortie du photomixer et affichées sur l'oscilloscope (en [V]). Ces puissances de lumière sont exprimés dans ce travail en termes de photocourant, en [µA], induit par la puissance lumineuse incidente, qui est obtenue en divisant la puissance de lumière en [V] par la transimpédance photomixeur de 6000 V/A.

Les photocourants induits par l'énergie OL et BB étaient respectivement de 610 et 117 µA. D'après la mesure (Fig. 5.3) d'une amplitude de note de battement de 150,18 µV et d'un niveau de bruit (1 σ) de 0.36 µV dans la note de battement, un RSB de ~419 a été déduit.

Le RSB théorique limité au bruit de tir du RHL peut être exprimé par l'équation. (5.1), où l'efficacité globale de couplage optique κ est d'environ 0,396. L'efficacité hétérodynique η_{het} du photomixage du faisceau de lumière du soleil et du faisceau OL est considéré comme 1 dans le cas idéal (c.f. Chapitre 1.3), l'efficacité quantique η du photomixteur fourni par le fabricant à cette longueur d'onde est de 0,5. Dans ces conditions, avec une bande passante double RHL de 485 MHz (pour une bande de passage RF de 27,5-270 MHz) et une constante de temps de

1 s de la LIA à une fréquence OL ($1242,3 \text{ cm}^{-1}$ ou $3.73 \times 10^{13} \text{ Hz}$), un RSB limité par le bruit de tir d'environ 1430 a été obtenu. Le RSB théorique limité par le bruit de tir est 3,4 plus élevé que le RSB mesuré à un photocourant de $610 \mu\text{A}$, où un facteur ρ de 0,29 dans le RSB théorique est observé. Le facteur de 0,29 ($=419/1430$) peut provenir de la performance inattendue du RHL développé.

A noter que dans la description de l'expérience suivante, la puissance OL et BB sera exprimée en photocourant (en $[\mu\text{A}]$).

iii.1.2.2. Sources de bruit dans le système RHL

Afin de comprendre la différence entre les RSB idéaux mesurés et calculés, les bruits dans diverses parties du système RHL ont été étudiés à l'aide d'un analyseur de signaux. Dans cette étude, les paramètres de l'analyseur de signaux ont été fixés comme le montre le tableau 5.1.

Dans cette étude, la densité sonore totale N_{total} ($nV/\sqrt{\text{Hz}}$) du système RHL peut être exprimé par Éqs. (5.2)-(5.4) (c.f. Chapitre 1.4), où N_{Det} , N_{LIN} et N_{SIN} sont respectivement : le bruit de la chaîne de détection, le bruit induit par laser et le bruit induit par le signal. Le bruit induit par laser inclut le bruit de tir induit par laser N_{LSN} et le bruit excessif de laser N_{LEN} , respectivement. Tandis que le bruit induit par le signal inclut le bruit de tir induit par le signal N_{SSN} et le bruit excessif de signal N_{SEN} .

La contribution de chaque type de bruits dans les expressions ci-dessus est discutée ci-dessous en détail.

(1) Bruit de la chaîne de détection (N_{Det})

Comme mentionné dans le chapitre 1.4.1, le bruit de la chaîne de détection N_{Det} comprend le bruit de fond, le bruit Johnson résultant de l'amplificateur associé au photodétecteur, et le bruit sombre. Il peut être mesuré lorsqu'il n'y a pas d'incident léger sur le détecteur.

Afin d'identifier les sources de bruit, les signaux à la sortie RF du photomixteur ont été mesurés avec l'analyseur de signaux dans des conditions différents :

(A) entrée de l'analyseur de signal directement relié à une résistance de 50Ω (Fig. 5.4, (1) courbe bleue) pour la mesure du bruit de fond N_{SA} de l'analyseur de signal.

(B) avec seulement sortie de détecteur connectée à l'analyseur de signal (Fig. 5.4, (2) courbe rouge), représentant la somme du bruit de fond de l'analyseur de signal N_{SA} et du bruit de chaîne de détection N_{Det} .

(C) avec la présence du OL mais sans injection de rayonnement BB (Fig. 5.4, (3) courbe verte), représentant la somme du bruit de fond de l'analyseur de signal N_{SA} , le bruit de chaîne de détection N_{Det} et le bruit induit par laser N_{LIN} .

(D) avec la présence de rayonnements OL et BB (Fig. 5.4, (4) courbe noire), représentant la somme du signal d'hétérodié, le bruit de fond de l'analyseur de signal N_{SA} , le bruit de chaîne de détection N_{Det} , le bruit induit par laser N_{LIN} et le bruit induit par la source BB N_{SIN} .

En comparant la sortie RF (après l'amplificateur associé au photodétecteur) du photomixeur avec des injections de rayonnement OL et BB (Fig. 5.4, (4) courbe noire) à celle du photomixeur avec seulement injection OL (Fig. 5.4, (3) courbe verte), deux signaux s'étaient presque chevauchés, ce qui indique qu'il n'y a presque pas eu de contribution sonore supplémentaire du rayonnement BB, c'est-à-dire que le N_{SIN} , qui induit par le signal, peut être négligé à ce stade d'analyse.

Par conséquent, la densité sonore totale N_{total} (Éq. (5.2)) du système RHL devient Éq. (5.5). Comme on peut le voir dans la Fig. 5.4 (en haut), le bruit du système RHL (mesuré à la sortie RF du photomixeur) a été principalement distribué dans la gamme de 1 kHz-100 MHz, qui est agrandi dans Fig. 5.4 plus bas. On voit que le bruit est principalement composé de $1/f$ et de bruits blancs. Dans la plage de basse fréquence, le bruit est dominé par $1/f$, puis la distribution du bruit tend à être plate. Par conséquent, la bande passante doit être sélectionnée dans la plage de fréquence où $1/f$ est considérablement réduite. Afin d'étudier les caractéristiques du bruit blanc dans la plage de haute fréquence, le bruit de chaîne de détection N_{Det} a été analysé à 150 MHz où le bruit est dominé par le bruit blanc.

Compte tenu des lectures de l'analyseur de signaux à 150 MHz : 0,00709 mV pour l'amplitude sonore du bruit de fond de l'analyseur de signaux (Fig. 5.4, (1) courbe bleue), et 0,02370 mV pour l'amplitude sonore (Fig. 5.4, (2) courbe rouge) résultant de l'analyseur de signaux bruit de fond et le bruit de la chaîne de détection, l'amplitude du bruit de la chaîne de détection peut être déduite de l'Éq. (5.6). Il s'agissait du niveau de bruit de la chaîne de détection intégré dans le set RBW de 100 kHz, la densité sonore correspondante de la chaîne de détection N_{Det} a été ainsi calculée pour être $71.5nV/\sqrt{Hz}$ (c.f. Éq. (5.7)).

En comparant les niveaux de signal avec l'injection OL (Fig. 5.4, (3) courbe verte) et sans injection OL (Fig. 5.4, (4) courbe noire), l'augmentation du niveau de bruit a été observée qui indique principalement une influence de l'injection OL, comprenant le bruit de tir induit par le laser et le bruit excessif de laser et les deux résultant de l'utilisation de L'EC-QCL OL.

Ensuite, le bruit induit par laser N_{LIN} , y compris le bruit de tir induit par laser N_{LSN} et le bruit excédentaire laser N_{LEN} est analysé

(2) Bruit induit par le laser (N_{LIN})

Une étude détaillée a été effectuée afin d'analyser quantitativement les contributions du bruit de tir induit par laser N_{LSN} et du bruit excessif de laser N_{LEN} .

La puissance OL injectée dans le photomixeur a été ajustée par un polariseur devant le laser OL et le photocourant induit par la puissance OL a été utilisé comme indicateur de la puissance OL injectée dans le photomixer.

Le bruit de la sortie RF du photomixeur dans sa bande de passage de 1kHz-500 MHz a été analysé à l'aide de l'analyseur de signaux, comme le montre la Fig. 5.6 (en haut), à différents photocourants OL (note : ici, le bruit de fond de l'analyseur de signaux a tous été soustrait).

La densité sonore totale du système N_{total} dans $[nV/\sqrt{Hz}]$ (Fig. 5.7, (2) black square) a été calculée en divisant la moyenne de toutes les amplitudes totales de bruit (y compris le bruit de chaîne de détection N_{Det} et le bruit induit par laser N_{LIN}), mesuré dans la bande de passage de 27.5-270 MHz (c.-à-d. la bande passante du filtre RF utilisé) (Fig. 5.6 en bas) par la racine carrée du RBW (100 kHz). Compte tenu de la densité sonore de la chaîne de détection de (Fig. 5.7, (1) ligne rouge) déterminée ci-dessus (Éq. (5.7)), le bruit induit par le laser N_{LIN} (Fig. 5.7, (3) triangle bleu) a été calculé en soustrayant le bruit de la chaîne de détection N_{Det} (Fig. 5.7, (1) ligne rouge) du total du système densité sonore N_{total} (Fig. 5.7, (2) carré noir) basé sur Éq. (5.5).

Basé sur le bruit induit par laser N_{LIN} déduit comme indiqué dans la Fig. 5.7, le bruit de tir laser-induit et le bruit excessif de laser sont étudiés en détail.

(2.1) Bruit de tir par le laser induit (N_{LSN})

La tension V_{SN} et le courant I_{SN} du bruit de tir induit par le laser peuvent être calculés avec des Éqs. (5.8)- (5.10), respectivement, où R_i 6000 V/A est la transimpédance du photomixer, $e = 1.602 \times 10^{-19}$ C est la charge électrique, $B = 5 \times 10^8$ Hz est la bande passante du photomixeur sur lequel le bruit est considéré, I_{DC} est le photocourant DC OL induit par la puissance laser OL dans le photomixer, V_{DC} est la tension DC OL induite par la puissance laser OL surveillée à la sortie du photomixeur et 10^6 représente la conversion de l'unité de V à μV .

De Éqs. (5.8) - (5.10), la densité de bruit de tir induite par laser N_{LSN} (en $[nV/\sqrt{Hz}]$) peut être exprimée en Éq. (5.11), où 10^9 représente la conversion unitaire de V en nV et 10^{-6} représente la conversion unitaire de μA en A.

La densité de bruit de grenaille induite par laser calculée N_{LSN} est représentée sur la figure 5.8 (courbe (4)). Le bruit total induit par laser, déterminé et représenté sur la figure 5.7, est à nouveau tracé sur la figure 5.8 (courbe (3)).

(2.2) Bruit excessif de laser (N_{LEN})

L'excès de bruit laser N_{LEN} (Fig. 5.8, (5) étoile verte) peut ensuite être calculé (Éq. (5.3)) en soustrayant le bruit de tir induit par laser N_{LSN} (Fig. 5.8, (4) cercle noir), déterminé à l'aide d'Éq. (5.11), à partir du bruit induit par laser N_{LIN} (Fig. 5.8, (3) triangle bleu).

Comme on peut le voir à partir de la fig. 5.8, à OL photocurrents $I_{DC} < 450 \mu A$ le bruit de chaîne de détection N_{Det} ((1) ligne rouge) est plus grand que le bruit de tir induit par laser N_{LSN} ((4) cercle noir), seulement dans la gamme de $450 \mu A < I_{DC} < 656 \mu A$ l'excès de laser le bruit N_{LEN} ((5) étoile verte) et le bruit de chaîne de détection N_{Det} ((1) ligne rouge) sont tous deux plus petits que le bruit de tir induit par le laser N_{LSN} ((4) cercle noir), et le système RHL fonctionne dans le régime dominé par le bruit de tir (avec des performances de sensibilité élevée limitées au bruit de tir). La limite photocourante OL plus élevée n'a pas pu être vérifiée, parce que la saturation du préamplificateur de détecteur pour les puissances optiques au-dessus de $733 \mu A$ a été observée.

iii.1.2.3. RSB théorique vs RSB mesuré

Sur la base de l'analyse ci-dessus des bruits du système, par rapport au RSB mesuré (419) avec le RSB théorique (1430), le facteur de 0,29 ($=419/1430$) est analysé comme suit :

(1) À un photocourant induit par la puissance OL de $610 \mu A$, au cours duquel le RSB-419 a été déterminé, le bruit d'excès du laser N_{LEN} (Fig. 5.8, (5) étoile verte) et le bruit de chaîne de détection N_{Det} (Fig. 5.8, (1) ligne rouge) étaient 0,9 fois et 0,9 fois le bruit de tir induit par laser N_{LSN} (Fig. 5.8, (4) cercle noir), respectivement. Le bruit total du système de RHL N_{total} dépasse ainsi le bruit de tir induit par laser N_{LSN} de 1,62 (en utilisant des Éqs. (5.2)-(5.4)).

Le bruit total du système N_{total} est 1,62 fois le bruit de tir induit par laser N_{LSN} , un facteur de correction ρ_1 de 0,62 ($1/1,62$) est obtenu pour le RSB théoriquement calculé dans un état idéal de bruit de tir.

(2) L'efficacité globale du couplage optique de 0,40 pour le rayonnement du corps noir, basé sur la transmission de chaque composant optique donné par le fabricant, serait surestimé. L'efficacité globale mesurée du couplage optique était d'environ 0,27, et cette différence entre 0,27 et 0,40 peut être due à l'exposition à long terme de ces composants optiques à un environnement humide et salé au bord de la mer. Un facteur de correction supplémentaire de ρ_2 de 0,68 ($0,27/0,40$) a été obtenu.

(3) L'efficacité hétérododyne η_{het} de 1 pour le cas idéal (c.f. chapitre 1.3) serait surestimé. La différence dans la taille des faisceaux en forme de la lumière du soleil (12,5 mm) et de la lumière OL (7,5 mm) a causé une efficacité hétérododyne de $\sim 0,8$ (c.f. Fig. 1.12). De plus, le photomixteur a une petite zone photo-sensible de $0,5 \times 0,5 \text{ mm}^2$, même un petit angle d'inadéquation se traduirait par une efficacité hétérododyne de $\sim 0,9$ (c.f. Fig. 1,14 à gauche). Un facteur de correction supplémentaire de ρ_3 de 0,72 ($0,8 \times 0,9$) a été atteint.

D'après l'analyse ci-dessus, un facteur de correction total, exp pour le RSB théorique, a résulté des raisons ci-dessus, est de $\rho_1 \times \rho_2 \times \rho_3 = 0.30$ qui est comparable au facteur de 0,29.

iii.1.2.4. Signal hétérododyne et RSB du Photocurrent RHL vs OL

En se basant sur l'étude réalisée sur les bruits en fonction du photocourant induit par la puissance OL, nous étudions maintenant le signal hétérododyne et le RSB correspondant comme fonction du photocourant OL. La puissance OL a été modifiée en ajustant un polariseur devant la sortie OL, à la fois le signal moyen d'hétérododyne et son écart standard ont été mesurés à partir de lesquels, le RSB correspondant a été dérivé. Les résultats sont présentés à la Fig. 5.9.

Fig. 5.9 montre clairement que l'amplitude du signal hétérododyne augmente presque linéairement à faible OL photocourant (carré noir), ce qui est compatible avec $P_{\text{HET}} \propto P_s \times P_L$, avant d'atteindre un point de roulement à un photocourant OL de $610 \mu\text{A}$. Le RSB augmente avec la puissance OL et atteint un maximum lorsque OL photocourant est égal à $\sim 610 \mu\text{A}$ trop. Au-dessus de $610 \mu\text{A}$, le signal hétérododyne est devenu plus petit et le bruit sur le signal hétérododyne a rapidement augmenté (c.f. Figs. 5.7 et 5.8), c'est-à-dire que le RSB a considérablement diminué. Les données montrent que le RSB maximum du RHL peut être obtenu avec un photocourant OL optimal. Le photocourant OL optimal dépend fortement de la technologie et des caractéristiques du détecteur (utilisé comme photomixteur). Pour chaque type de détecteur, le photocourant OL optimal doit être déterminé parce que les effets de

saturation, le bruit de la chaîne de détection et l'homogénéité de la réponse du détecteur affecteront les performances.

Par conséquent, la puissance OL doit être ajustée avec précision afin de réduire considérablement le bruit sur le signal hétérodène pour atteindre une RSB élevée sans aucune saturation de l'appareil.

En se basant sur l'analyse ci-dessus, les performances spectroscopiques du système RHL seront évaluées dans la section suivante sous le photocourant OL optimal.

iii.1.2.5. Performance spectroscopique

La capacité de la fibre optique mid-IR utilisée pour coupler la source à large bande (BB ou lumière du soleil) a été évaluée dans cette section. Pour cette raison, la même source de corps noir utilisée dans le chapitre 4 a été couplée à une cellule d'absorption directe à travers la fibre optique. Les paramètres communs ont été fixés comme suit :

- (1) température du corps noir : 1000 °C;
- (2) la fréquence du centre OL a été numérisée avec un PZT entraîné par une onde sinuél de 3,0 V avec un décalage de 1,6 V.

(a) Impact de la bande de passe RF sur le spectre RHL

Pour étudier l'impact de la bande de passage du filtre RF sur le signal spectral RHL, les spectres d'absorption hétérodine du CH₄ dans une cellule à passage unique ont été extraits expérimentalement et analysés avec différentes bandes de transmission de filtres RF. Les paramètres expérimentaux étaient les mêmes que ceux fixés ci-dessus, à l'exception de :

- (1) fréquence centrale OL : 1255,00 cm⁻¹;
- (2) taux de balayage de fréquence : 500 mHz;
- (3) pression du mélange CH₄ dans l'air dans la cellule à une passage unique : 280 mbar;
- (4) LIA constante de temps : 10 ms, respectivement.

Le bruit de RHL a été étudié dans un premier temps. Fig. 5.11 montre un spectre d'amplitude sonore du signal RHL à partir de la sortie RF du photomixteur enregistré à l'aide d'un analyseur de signaux (avec un RBW de 100 kHz). Nous remarquons, il ya des forts bruits 1 / f dans la gamme de basse fréquence qui doit être filtré

Les densités de bruit dans les différentes bandes de passage des filtres RF disponibles dans le présent travail ont été estimées en divisant le bruit intégral sur chaque bande de passage par la bande passante et la racine carrée du RBW (100 kHz) (tableau 5.3). Comme le

montre le tableau 5.3, la densité sonore du filtre RF avec une bande de passage de 27,5 à 270 MHz était la plus faible et la RSB correspondante était la plus élevée en raison de sa bande passante filtrante plus large (au prix d'une résolution spectrale plus faible).

Des spectres d'absorption RHL CH₄ ont ensuite été enregistrés avec ces cinq filtres RF disponibles, comme le montre la Fig. 5.12. Les spectres d'absorption RHL CH₄ mesurés par des filtres RF à col de bande AC (Fig. 5.12 à gauche), qui peuvent filtrer considérablement les bruits de basse fréquence, ont une RSB plus élevée et une meilleure forme spectrale de ligne, tandis que les spectres mesurés avec des filtres RF à faible passage à couplage DC (Fig. 5.12 à droite) sont bruyants résultant d'un son élevé de 1/f.

C'est montré que le niveau de bruit du spectre mesuré avec le filtre RF avec une bande de passage de 27,5-270 MHz (Fig. 5.12 en noir) est inférieur à celui mesuré avec une bande de passage de 27-33 MHz (Fig. 5.12 en rouge). De plus, il n'y a pas de différence évidente dans les largeurs spectrales des lignes entre deux spectres d'absorption CH₄ RHL. La raison en est que la largeur théorique de la ligne spectrale (FWHM) de l'absorption CH₄ autour de 1255,00 cm⁻¹ à 280 mbar est de 0,034 cm⁻¹ (1020 MHz qui est plus large que les bandes passantes de filtre RF doublés (12 MHz et 485 MHz) et donc il n'y a pas d'effet évident des largeurs de bande du filtre RF sur les largeurs de ligne mesurées.

En se basant sur cette analyse, le filtre RF avec une bande de passage de 27,5-270 MHz a été sélectionné pour le système RHL actuel.

(b) RHL spectral line-shape vs vitesse de balayage de la fréquence OL

Comme nous l'avons vu dans les chapitres 2.1.6 et 4.2.2.3, afin d'obtenir un spectre d'hétérothène de haute précision (avec un décalage et une distorsion de la forme de la ligne minimisée), le temps ΔT_{scan} de balayage de l'ensemble de la demi-largeur de la ligne d'absorption $\Delta \nu_{HWHM}$ (en [cm⁻¹]), qui dépend également de la vitesse de balayage de la fréquence OL ν_{sc} (en [cm⁻¹/s]), devrait être adapté de manière appropriée à une constante temporelle de la LIA τ , telle que $\Delta T_{scan} = \Delta \nu_{HWHM} / \nu_{sc} \geq 14 \cdot \tau$. Des recherches expérimentales sur les spectres d'hétérothène à base de BB à l'aide de différentes vitesses de balayage avec une constante de temps LIA sélectionnée de 1 ms ont été effectuées. Dans cette étude, les paramètres expérimentaux étaient les mêmes que ceux fixés ci-dessus, à l'exception de :

- (1) fréquence centrale OL : 1242,00 cm⁻¹;
- (2) pression du mélange CH₄ dans l'air dans la cellule à une seule passe : 280 mbar;

Les spectres d'absorption RHL CH₄ enregistrés en scannant la fréquence OL à différentes vitesses (voir le tableau 5.4) à l'aide de la même constante de temps LIA de 1 ms sont présentés à la Fig. 5.13. Comme nous l'observons, la sélection de la vitesse de numérisation de la fréquence OL doit être bien adaptée à la constante de temps LIA appliqué. En comparant ces quatre spectres d'absorption hétérodyne de CH₄, RSB, élargissement de la largeur de ligne $\Delta\nu_b$ (FWHM), décalage de ligne et niveau de bruit (1σ) de ces spectres d'absorption hétérodyne ont été analysés en fonction de l'ajustement du profil Voigt (Fig. 5.13, bleu) et résumés dans le tableau 5.4. Nous remarquons que la combinaison de 1 ms de la constante de temps et la vitesse de balayage 0,3935 cm⁻¹/s (avec un temps de numérisation de 36 ms), le spectre hétérodyne a un niveau de bruit plus faible et un changement de ligne plus faible tout en gardant une résolution spectrale élevée (Fig. 5.13 (b) et tableau 5.4 en gras).

Pendant ce temps, il est généralement considéré que la vitesse de numérisation de la fréquence OL ν_{sc} est réglée à une valeur plus lente, qui s'accorde bien $\Delta T_{scan} = \Delta\nu_{HWHM} / \nu_{sc} \geq 14 \cdot \tau$, peut limiter la distorsion de la forme de la ligne.

Comme constaté à partir du tableau 5.4, à une vitesse de balayage de fréquence OL de 0.1574 cm⁻¹/s, le temps de numérisation de 89 ms était beaucoup plus de 14 fois la constante de temps LIA appliqué de 1 ms. Dans ce cas, le décalage de ligne mesuré était le plus petit, la profondeur d'absorption était la plus profonde, la largeur de la ligne $\Delta\nu_b$ (tableau 5.4) était la plus étroite et proche de la valeur théorique de ~0,036 cm⁻¹ calculé à partir de Éq. 5.15 à partir de : $\Delta\nu_L$ de 0,028 cm⁻¹, $\Delta\nu_{INS}$ de 0,0162 cm⁻¹ et de 0,0038 cm⁻¹ (c.f. 5.1,2.2) II. Cependant, le bruit (1σ : 0,0091) était le plus élevé et le RSB (~12) était le plus faible (tableau 5.4). Un compromis doit être fait. Par conséquent, à la constante de temps LIA de 1 ms, la vitesse de balayage de la fréquence OL de 0.3935 cm⁻¹/s (le temps de numérisation de 36 ms), avec laquelle le bruit (1σ : 0,0043) était relativement faible, le RNS du système (~24) était relativement élevé, le décalage de ligne (~0,0004 cm⁻¹) était relativement faible et la résolution spectrale réalisable (largeur spectrale de la ligne spectrale de ~0,042 cm⁻¹) était relativement élevée, elle a donc été sélectionnée pour la mesure du prototype RHL.

iii.2. Prototype RHL impliquant une fibre mid-IR pour coupler le rayonnement solaire

iii.2.1. Description instrumentale

Le prototype RHL développé utilisant une fibre polycrystalline mid-IR pour coupler la lumière du soleil au récepteur RHL est schématiquement montré dans les Fig. 5.14 et Fig. 5.15. Le prototype RHL utilise un EKO sun-tracker pour suivre en temps réel le mouvement

du Soleil. La collecte de la lumière du soleil dans la colonne atmosphérique dans une fibre mid-IR est réalisé par une lentille associée à un filtre optique dans Germanium. L'optique de collecte est installé sur la monture d'instrument du sun-tracker. Le filtre Ge en face de la fibre est utilisé pour protéger le terminal d'entrée de fibres contre les dégats causés par l'exposition directe à l'ultraviolet intense et la partie visible de la lumière du soleil, et pour limiter la bande passante optique du rayonnement incident et de laisser seulement la transmission du rayonnement solaire à des longueurs d'onde supérieures à 7 μm .

La lumière du soleil émergente de la fibre est collimatée avec une lentille et injectée dans l'espace libre. L'amplitude de la lumière du soleil est ensuite modulée à une vitesse d'environ 1 kHz et dirigée vers un séparateur de faisceau. Le faisceau solaire de 12,5 mm de diamètre est superposé au séparateur de faisceau avec un faisceau OL de 7,5 mm de l'EC-QCL à l'avance de taille élargie par deux OAPM, en ajustant son intensité à l'aide d'un polariseur IR. Les faisceaux combinés concentrés par un OAPM2 sont injectés dans le photomixteur VIGO pour la détection de l'hétérodié.

Une partie du faisceau OL (puissance OL transmise par le séparateur de faisceau) est dirigée soit vers une cellule de passage unique de 12,5 cm remplie d'un mélange CH_4 dans l'air pour une détermination de fréquence absolue, soit vers un Ge-etalon fait maison de 12,5 cm (FSR à $0,0333 \text{ cm}^{-1}$) pour une calibration de fréquence relative lorsque la fréquence OL est réglée.

iii.2.2. Mesure de l'hétérodié du spectre d'absorption atmosphérique CH_4 et N_2O

Le prototype RHL développé a été déployé sur le toit de la plate-forme ULCO-IRENE à Dunkerque ($51.05 \text{ N}/2.34 \text{ E}$) pour la télédétection au sol des gaz traces dans la colonne atmosphérique.

Lors de la vérification du bruit du système au port de sortie RF du photomixteur avec l'analyseur de signaux, il a été constaté que le bruit du système a été augmenté dans les 110 MHz, et est devenu particulièrement important autour de 100 MHz, comme le montre la Fig. 5.16.

Par conséquent, la bande de filtre RF précédemment optimisée de 27,5-270 MHz n'était plus adaptée, un nouveau filtre RF avec une bande de passage de 225-270 MHz a été sélectionné pour éliminer cet excès de bruit. Les paramètres opérationnels du RHL ont été fixés comme suit :

(1) fréquence centrale OL : $1262,00 \text{ cm}^{-1}$, numérisée à une fréquence de 250 MHz avec

une tension de balayage de 3,8 V et un décalage de 2,0 V;

(2) LIA constante de temps : 1 ms;

(3) temps d'acquisition par spectre : 60 s;

(4) nombre moyen de spectres : 15.

La fréquence OL a été numérisée autour de $1262,00 \text{ cm}^{-1}$ à l'aide du mode de balayage PZT, le spectre atmosphérique d'absorption CH_4 et N_2O a été mesuré dans la colonne atmosphérique. La figure 5.17 montre un spectre d'absorption hétérodine de CH_4 et N_2O atmosphériques autour de $1262,00 \text{ cm}^{-1}$ (à gauche). La figure 5.17 montre également des spectres de simulation (à droite) pour l'identification spectrale.

Fig. 5.18 présente une comparaison de notre spectre RHL extrait expérimentalement (noir) avec un spectre FT-IR (rouge) mesuré à l'aide d'un spectromètre de transformation Bruker 125HR Fourier haute résolution sur la plate-forme QualAir de l'UPMC ($48^\circ 50'47''\text{N}/2^\circ 21'21''\text{E}$, 60 m au-dessus du niveau de la mer), ainsi qu'avec un spectre d'un mode de transmission atmosphérique (bleu).

Comme illustré à la Fig. 5.18, les positions des lignes d'absorption de CH_4 et de N_2O à partir du spectre RHL étaient en bon accord avec celles du spectre FT-IR ainsi qu'avec une modélisation de la transmission atmosphérique. Comme la vapeur d'eau interférait avec le spectre RHL de $\text{CH}_4\text{-N}_2\text{O}$ (indiqué au Fig. 5.17), et que la distribution de vapeur d'eau change avec le temps et l'espace, la forme de la ligne du spectre RHL était légèrement différente du spectre FT-IR et de l'atmosphère spectre de modélisation de transmission, fabriqué à différents endroits et à différents endroits dans des conditions atmosphériques différentes. Les lignes spectrales globales des trois spectres étaient cohérentes.

En comparant le spectromètre FT-IR utilisé pour les mesures à distance au sol des gaz traces dans la colonne atmosphérique, RHL est avantageux en termes de : fonctionnement de la température ambiante, taille compacte, portabilité, résolution spectrale plus élevée, et d'un FoV plus petit, comme résumé dans le tableau 5.5.

iii.3. Conclusion

Un prototype RHL transportable complet impliquant une fibre mid-IR pour recueillir la lumière du soleil à travers un EKO sun-tracker a été développé. L'évaluation et l'optimisation du prototype RHL développé à l'aide d'un rayonnement stable de corps noir à haute température pour simuler la lumière du soleil ont été effectués. L'instrument RHL développé a ensuite été testé et validé au moyen de mesures au sol sur le terrain de CH_4 et N_2O

troposphériques dans la colonne atmosphérique sur le toit de la plate-forme IRENE de l'ULCO à Dunkerque (51.05 N/2.34 E). Le spectre extrait par le RHL était en bon accord avec le spectre FT-IR mesuré à l'aide d'un Bruker IFS 125HR FTS et avec un spectre de modélisation de la transmission atmosphérique, ce qui démontrait que le prototype RHL portable développé pouvait être utilisé pour des mesures de sondage atmosphérique au sol des GHGs dans la colonne atmosphérique.

Dans les futurs travaux, les profils verticaux des GHGs dans la colonne atmosphérique seront récupérés à partir du spectre RHL mesuré au sol à l'aide d'un algorithme de récupération, compte tenu d'une connaissance récente des paramètres atmosphériques supplémentaires, comme l'angle solaire, l'atmosphère la température, la pression atmosphérique, la composition de l'atmosphère et l'indice de réfraction.

Mots-clés : Oscillateur Local (OL); Radiomètre hétérodyne laser (RHL); Télédétection au sol; Laser à cascade quantique à cavité externe (EC-QCL); Infrarouge moyen (IR moyen); Fibre IR polycrystalline.

Appendix

Appendix 1 All fiber-coupled LHR

A compact mid-IR laser heterodyne radiometer involving an all fiber-coupled optical system in principle could significantly improve photomixing efficiency, system stability and flexibility (Fig. 1).

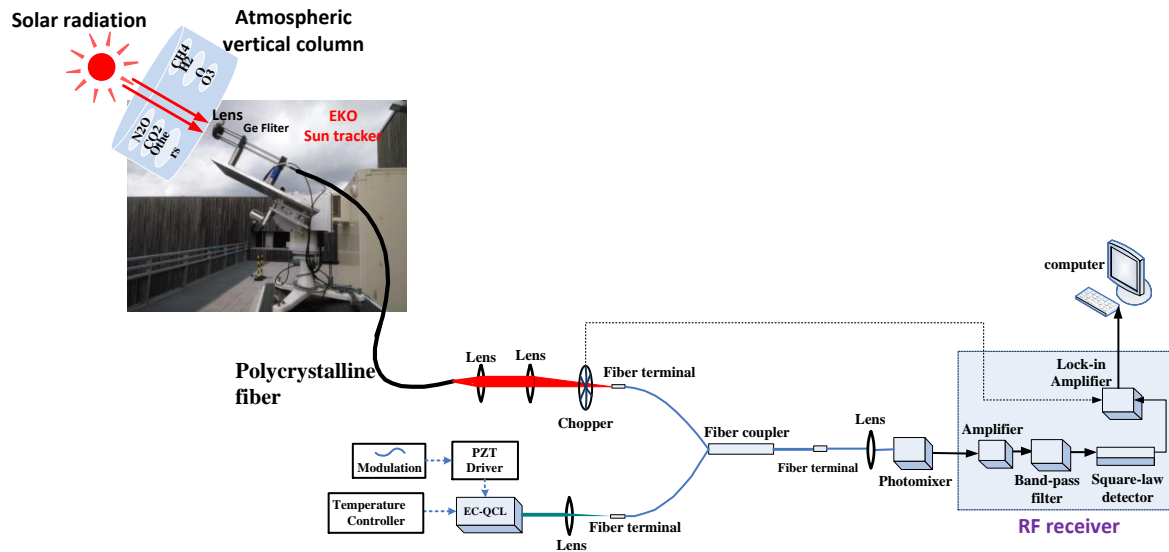


Figure 1 Schematic of an all fiber-coupled mid-IR LHR.

Sunlight is coupled to a polycrystalline fiber via a lens associated with a Ge-filter to block the solar radiation with wavelength short than the near-IR. The outgoing beam from the fiber is coupled to a 320- μm -core single-mode fiber by a collimator. This incoming sunlight is amplitude modulated at a rate of about 1 kHz. Light from the EC-QCL laser (LO) is also coupled to a 320- μm -core single-mode fiber. These two fiber-coupled light beams are superimposed in a larger 1000- μm -core multi-mode fiber and injected into the VIGO photomixer via free-space coupling. Before the design of such all fiber-coupled optical transmission system, the beam coupling loss due to the fiber modes is studied.

(1) Fiber coupling efficiency to the HE_{1m} modes

When a Gaussian beam is on-axis focused into a hollow fiber, only the HE_{1m} modes are excited. The spatial profiles of the HE_{1m} modes in a fiber can be approximated by the zero-order Bessel function, that is :

$$E(r) = E_0 J_0 \left(\mu_{1m} \frac{r}{a} \right) \quad (1)$$

where $0 \leq r < a$. A Gaussian beam with a waist ω_0 can be expressed by :

$$E(r) = E_0 \exp(-r^2/\omega_0^2) \quad (2)$$

The power coupling efficiency of the incident beam to each HE_{1m} mode can be expressed by the overlap integral :

$$\eta_m = \frac{\left[\int_0^a \exp(-r^2/\omega_0^2) J_0 \left(\mu_{1m} \frac{r}{a} \right) r dr \right]^2}{\int_0^\infty \exp(-2r^2/\omega_0^2) r dr \int_0^a J_0^2 \left(\mu_{1m} \frac{r}{a} \right) r dr} \quad (3)$$

This equation describes the amount of light power coupled to the HE_{1m} modes in the fiber for a given light spot size to fiber core size ratio ω_0/a . According to this equation, calculation was performed using MATLAB to obtain theoretical coupling efficiency curves of the first five HE_{1m} modes in 320-, and 1000- μm -core hollow-glass fiber, respectively (Figs. 2 and 3).

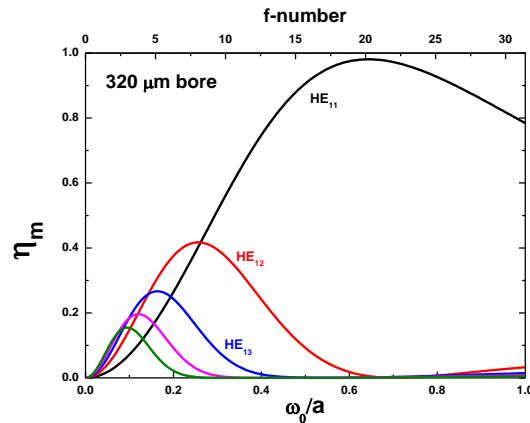


Figure 2 Calculated coupling efficiency curves of the first five HE_{1m} modes in a 320- μm -core hollow-glass fiber.

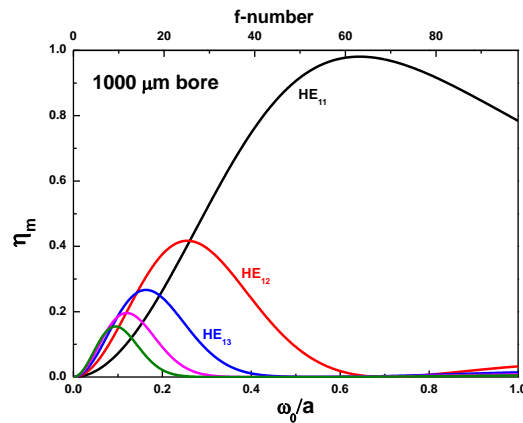


Figure 3 Calculated coupling efficiency curve of the first five HE_{1m} modes in a 1000- μm -core hollow-glass fiber.

As can be seen in Figs. 2 and 3, the highest coupling efficiency were obtained when :

$$\omega_0/a = 0.64 \quad (4)$$

for HE₁₁ mode in a 320-, and 1000- μ m-core hollow-glass fiber, respectively

(2) Attenuation coefficients for the HE_{1m} modes inside the fiber

For a hollow fiber with a single dielectric film, the minimum loss occurs when the films thickness d is given by [1] :

$$d = \frac{\lambda}{2\pi\sqrt{n_d^2 - 1}} \tan^{-1} \left[\frac{n_d}{\sqrt[4]{n_d^2 - 1}} \right] \quad (5)$$

where n_d is the wavelength-dependent refractive index of the dielectric films. The assumption is that there is no absorption in the films. Here :

$$n_d(\lambda) = 1.956 - \frac{0.239}{\lambda} + \frac{1.920}{\lambda^2} - \frac{2.678}{\lambda^3} + \frac{1.233}{\lambda^4} \quad (6)$$

At 8 μ m, $n_d(\lambda) = 1.9512$ which leads to a thickness of $d = 43 \mu$ m.

The attenuation coefficients of the various HE_{nm} fiber modes can be expressed as :

$$\alpha_{nm} = \left(\frac{\mu_{1m}}{2\pi} \right)^2 \frac{\lambda^2}{a^3} \left(\frac{n^2}{n^2 + \kappa^2} \right) \times \left\{ \frac{1}{2} \left[1 + \frac{n_d^2}{\sqrt{n_d^2 - 1}} \right] \right\}, \text{ HE}_{1m} \text{ modes} \quad (7)$$

where n and κ are the real and imaginary parts of the complex index of the metallic guide, μ_{1m} is the m th root of the zero-order Bessel function, λ is the wavelength, and a is the core radius. The μ_{1m} values for the first five HE_{1m} modes are given in Table 1.

Table 1 Values of μ_{1m} for the first five HE_{1m} modes.

μ_{11}	2.40482555769577
μ_{12}	5.52007811028631
μ_{13}	8.65372791291101
μ_{14}	11.7915344390142
μ_{15}	14.9309177084877

Calculation of the attenuation coefficients for the first four HE_{1m} modes in an Ag/AgI hollow-glass fiber is made according to Eq. (9). These four curves show the $1/a^3$, dependence of loss as well as the dramatic increase in loss for the higher order modes (Fig. 4).

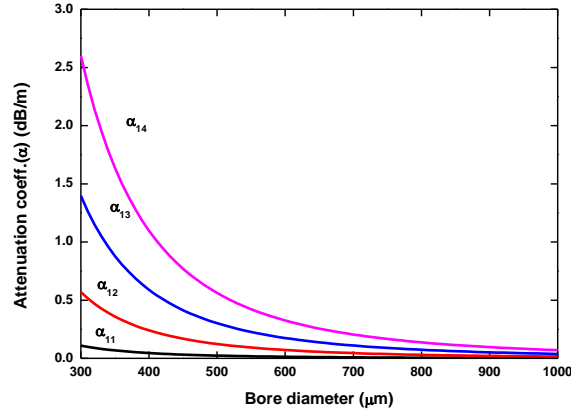


Figure 4 Calculated attenuation coefficients of the first four HE_{1m} modes in an Ag/AgI hollow-glass fiber.

As can be seen in Fig. 4, the HE₁₁ mode will have the smallest attenuation coefficients, i.e. the lowest transmission loss.

(3) Total loss in hollow fibers

To make an estimation on the theoretical transmission losses in a hollow fiber, one needs to take into account both the attenuation and coupling efficiency to each of the modes. Accordingly, the transmission in a length z , P_z , can be expressed as :

$$P_z = \sum_m \eta_m \exp(-2\alpha_m z) \quad (8)$$

where the factor 2 is resulted from squaring the electric field to get the intensity. It is particularly important to sum over all possible modes when calculating a theoretical loss for fiber used under poor launch conditions since it may excite many higher order modes. The theoretical total loss L_z can be expressed as :

$$L_z = -10 \log \sum_m \eta_m \exp(-2\alpha_m z) \quad (9)$$

Fig. 5 shows the coupling conditions necessary to achieve minimal loss through 1-m-long, 320-μm-core and 1000-μm-core hollow fibers. Maximum transmission occurs at a f -number

(f -number = $f/D = \frac{\omega_0 \pi}{2\lambda}$ with D the beam diameter) :

For 320-μm-core hollow fiber : f -number = $f/20$, that is : $\omega_0/a \approx 0.62$;

For 1000-μm-core hollow fiber : f -number = $f/51$, that is : $\omega_0/a \approx 0.52$.

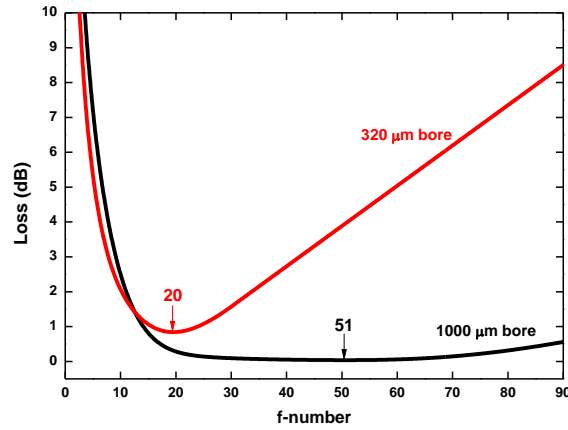


Figure 5 Min-loss coupling conditions for 1-m-long, 320- μm -core and 1000- μm -core hollow fibers.

As indicated by the simulation results, the launch condition for maximum transmission (min-loss) requires a smaller value of ω_0/a than that for optimal coupling to the HE_{11} mode ($\omega_0/a = 0.64$). The difference depends on fiber core size and is more severe for the larger core fibers. As can be seen in Figs. 2 and 3, more power is coupled to the higher order modes at smaller f-numbers ($\omega_0/a < 0.64$) (Fig. 6 (a)), and the focused spot becomes larger than the fiber core diameter ($2a$) at larger f-numbers ($\omega_0/a > 0.64$) (Fig. 6 (c)). In this case, the beam is clipped by the fiber walls.

In a large-bore fiber, attenuation to the higher order modes is not significantly greater than that of the HE_{11} mode (Fig. 4), so the elimination of beam clipping by reducing the input beam spot size does not have an obvious effect on the total loss. In addition, for high-power applications, laser energy cannot hit the fiber walls to avoid any damage. Thus, the possibility of damaging the input can be eliminated by reducing the input beam spot size with the help of the smaller f-number ($\omega_0/a < 0.64$) launch.

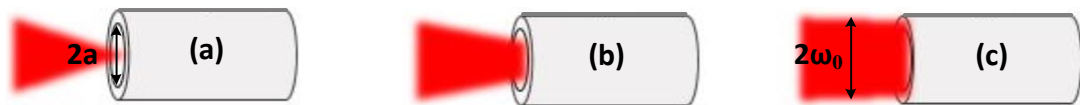


Figure 6 Light coupling with a ratio of light spot size to fiber core size ω_0/a . (a) $\omega_0/a < 0.64$; (b) $\omega_0/a = 0.64$; (c) $\omega_0/a > 0.64$.

(4) Output beam divergence

The divergence of the beam emerging from the hollow fiber depends on the modes propagating in the fiber as well as on the core size. The HE_{1m} modes will couple to free-space modes with a half-angle beam divergence θ given by [2] :

$$\theta \cong \sin \theta_m = \frac{\mu_{1m} \lambda}{2\pi a} \quad (10)$$

Calculations for the beam divergence of the first four HE_{1m} modes as a function of core size are given in Fig. 7. As expected, the lowest order mode gives the smallest beam divergence, as shown in Fig. 7.

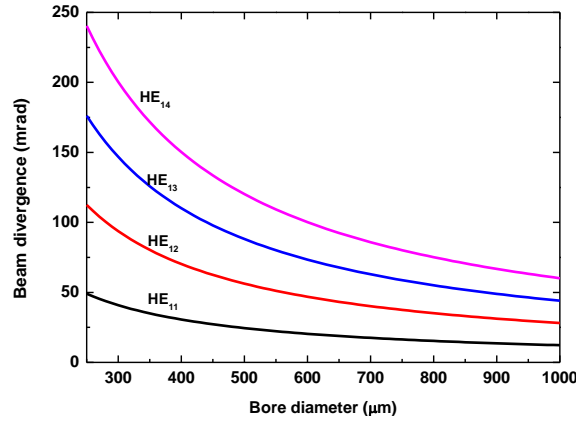


Figure 7 Calculated beam divergence of the first four HE_{1m} modes exciting a hollow fiber.

(5) Fiber-coupled LHR system

A fiber-coupled optical assembly is shown in Fig. 8, two single lenses are used to couple sunlight and laser light into the hollow fibers, respectively, and then a 2 to 1 hollow core fiber coupler is used to realize beams overlapping.

The design work mainly focuses on improving the fiber coupling efficiency issues.

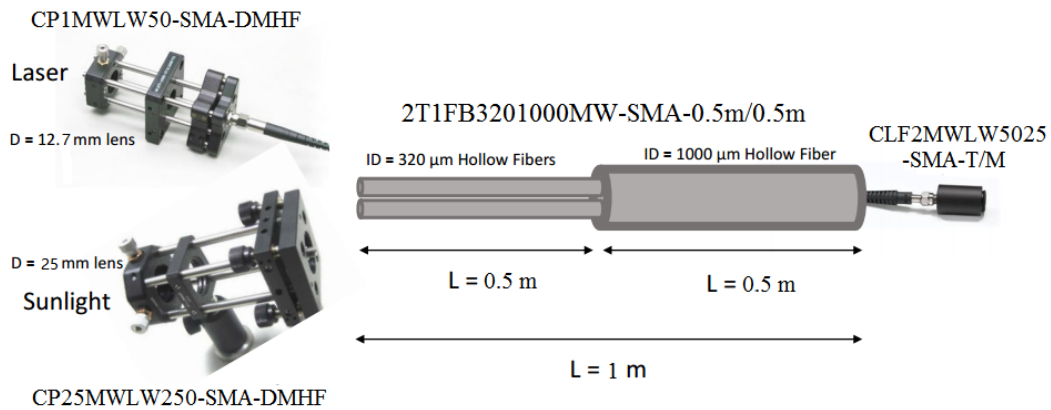


Figure 8 Fiber-coupled LHR assembly.

From above theoretical analysis, the coupling efficiency of a fiber-coupled LHR system depends on the light beam mode coupling to the hollow fibers. The efficiency of light coupling to the fiber is limited by two facts, e.g. the focused spot size and the beam focusing

angle after the light coupling lens. Normally, coupling light into a hollow fiber is relatively simple, given the relatively large core. However, both transmission and beam quality can be adversely affected if the proper focal length optic is not used. In general, the beam should enter straight into the fiber with a relatively gradual focus. The curves drawn in Figs. 2 and 3 show that optimal coupling into the lowest order mode occurs when the ratio of the focused spot size ($2\omega_0$) to the fiber core diameter ($2a$) : $\omega_0/a \approx 0.64$ (where $\omega_0 = \frac{2\lambda}{\pi} \left(\frac{f}{D} \right)$). The beam quality that coupled into the fiber will be highest with the lowest loss. So the calculation for an optimal focus ($f_{opt} = 0.16\pi \times (2a) \times \left(\frac{D}{\lambda} \right)$) assumes an ideal collimated Gaussian input beam, and a non-ideal beam will have a larger focused spot. For this reason, selecting a focal length that is either equal to or less than the optimal focal length is recommended, which can in turn satisfy the smaller f-number ($\omega_0/a < 0.64$) launch condition.

Due to the core size limitation of the 2 to 1 hollow fiber (the maximum option of the core diameter is 1000 μm in our case), so the maximum size of each single fiber core for coupling sunlight/LO is 320 μm .

In our LHR prototype system, the sunlight is collected and collimated with a telescope, the output beam size is specially filtered by a diaphragm, and the final beam size of sunlight is $D=12.5$ mm. Hence, the f_{opt} for coupling the sunlight into the fiber should be equal to or less than 250 mm.

As we know, hollow fibers utilize total internal reflection (TIR) in order to confine and guide light within a solid or liquid structure. Within the fiber, a critical angle of incidence exists such that light will reflect off the core/cladding interface rather than refract into the surrounding medium. To fulfill the TIR conditions in a fiber, the incidence angle of the light launched into a fiber must be as close as possible to the acceptance half-angle θ of the fiber. The numerical aperture (NA) is a dimensionless quantity used by fiber manufacturers to specify the acceptance angle of an optical fiber and is defined as :

$$NA = n \sin \theta = \sin \theta \quad (n = n_{air} = 1) \quad (11)$$

For the 320- μm -core hollow fiber, the acceptance full-angle is 2.29° . Because the focusing angle increases with the decrease of the focal length of the coupling lens, we use Zemax to make a simulation of the coupling lens, the focusing full-angle θ_1 after the coupling lens is about 2.3° when the coupling lens with 250 mm focal length is used, which is

approaching the acceptance angle of the fiber. Therefore, the focal length 250 mm of the coupling lens is selected for coupling sunlight.

For a laser with a TEM₀₀ output mode like our Daylight laser, it is sufficient to take into account only the contribution from the HE₁₁ mode, and to couple as much power as possible to the HE₁₁ mode (at $\omega_0/a \approx 0.64$) into a hollow fiber. Consistent with the fiber core size used for coupling sunlight, the fiber core size used for coupling the laser beam (with $D=2.5$ mm) is also 320 μm . The corresponding focal length f_{opt} of the coupling lens should be equal to and less than 50 mm. when the coupling lens with a 50 mm focal length is used, the result of the simulation shows that the focusing full-angle θ_2 after the coupling lens is about 2.88° , which is a little larger than the acceptance full-angle of the fiber. Considering the focused spot size, the focal length 50 mm is still selected for coupling laser.

Two beams, transmitted by two 320- μm -core hollow fibers, separately, will be coupled into a 1000- μm -core fiber in which they are well overlapped. Finally, the output beam from the 1000- μm -core fiber will be focused into VIGO detector using a dual lens collimating/focusing assembly. The beam focusing full-angle after the dual lens collimating/focusing assembly should be less than the acceptance angle (35°) of the VIGO detector. In order to verify this, the beam focusing full-angle is simulated by Zemax, the result is about 15.3° (as shown in Fig. 9), which is less than 35° .

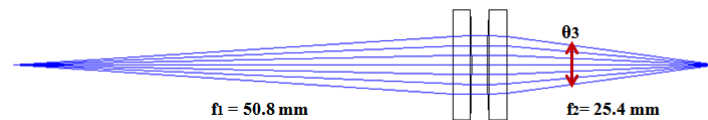


Figure 9 Dual lens collimating/focusing assembly

Finally, the FoV of the fiber-coupled LHR system is calculated based on the Eq. (1.4). The fiber system with a $D=25$ mm diameter lens collecting radiation at $\lambda=8$ μm would provide a FoV of ~ 0.4 mrad (0.023°).

From above analysis, the elements of the fiber-coupled LHR system are as follows :

1. **Coupling sunlight** : Opton-CP25MWLW250-SMA-DMHF (lens in Ge, AR coating (3-12 μm) with a focal length of 250 mm and 25 mm in diameter).
2. **Coupling laser** : Opton-CP1MWLW50-SMA-DMHF (lens in Ge, AR coating (3-12 μm) with a focal length of 50 mm and 12.7 mm in diameter), mounted directly to the Daylight Solution laser head.
3. **Fiber-coupled beam mixing** : OKSI Opton-2T1FB3201000MW-SMA-0.5m/0.5m (2 to 1 hollow core fiber bundle).

4. *Collimating/focusing* : OKSI Opton-CLF2MWLW5025-SMA-T/M (lens in Ge, AR coating (3-12 μm) with a focal length of 25.4 mm and 12.7 mm in diameter).

For this configuration, during the field realization, the problem is that the 2 to 1 fiber cannot be bent on the sun-tracker, and due to the limitation of the sun-tracker, it is not practical to install a coaxial telescope as shown in Fig. 1. Therefore, it is not possible to follow the Sun's movement to collect the solar radiation.

References

- [1] M. Miyagi and S. Kawakami. Design theory of dielectric-coated circular metallic waveguides for infrared transmission, J. Lightwave Technol. 1984, LT-2, 116-126.
- [2] E. Snitzer. Optical dielectric waveguides, In Advances in Quantum Electronics, Columbia University Press, New York, 1961.

Appendix 2 Optimization using Zemax

In computer-aided sequential lens design, rays are traced from one surface to the next in the order in which they are listed. To do this, ZEMAX uses a spreadsheet format called the Lens Data Editor (LDE).

Upon opening ZEMAX, a blank LDE will appear within the main ZEMAX window. The LDE is the primary spreadsheet where the majority of the lens data is entered. Some of the main entries include the following :

- *Surf : Type* : the type of surface (Standard, Even Asphere, Diffraction Grating, etc),
- *Comment* : an optional field for typing in surface specific comments,
- *Radius* : surface radius of curvature (the inverse of curvature) in lens units,
- *Thickness* : the thickness in lens units separating the vertex of the current surface to the vertex of the following surface,
- *Glass* : the material type (glass, air, etc.) which separates the current surface and the next surface listed in the LDE,
- *Semi-Diameter* : the half-size of the surface in lens units.

The Lens Data Editor

Surf	Type	Comment	Radius	Thickness	Glass	Semi-Diameter	Conic
OBJ	Standard		Infinity	Infinity		0.000000	0.000000
STO*	Standard		Infinity	20.000000		12.500000	0.000000
2*	Standard		69.300000	7.000000	CAF2	25.000000	0.000000
3*	Standard		Infinity	282.202272	V	25.000000	0.000000
4*	Standard		64.400000	4.500000	CAF2	12.700000	0.000000
5*	Standard		-64.400000	30.000000		12.700000	0.000000
IMA	Standard		Infinity	-		5.931170	0.000000

Each row within the LDE represents a single surface. In sequential ZEMAX, each optical system begins at the object (OBJ) and ends at the image (IMA). In addition to the object and image planes, one of the surfaces must be defined as the aperture stop (STO).

Data can be entered into the LDE by typing in the required values in the highlighted cell. The cursor keys or the mouse may move the highlighted bar to whichever column is desired.

Once the system settings have been defined, information specific to each surface can be entered into the Lens Data Editor. To reiterate, each row in the LDE represents a single surface. Therefore, two surfaces separated by glass comprise a single element. So, for the purposes of the beam contraction, a total of 7 surfaces are needed :

1. Surface (OBJ) : the location where rays are launched is infinity (Thickness);

2. Surface (STO) : the location of the diaphragm is 20 mm (Thickness) and the semi-diameter (U means the value is set by user) of the diaphragm is 12.5 mm;

3. Surface (2) : the front surface of the first lens where the rays enter this lens. The curvature radius of this surface is 69.3 mm (Radius), the lens thickness is 7 mm (Thickness), the material is CaF₂ (Glass), and the semi-diameter of lens is 25 mm;

4. Surface (3) : the back surface of the first lens where the rays exit the first lens back into air. The curvature radius of this surface is infinity (Radius), the distance between the two lenses is optimized to 282.202272 mm (Thickness (V) : Variable set as the "Solve Type" can be optimized), and the semi-diameter of lens is 25 mm;

5. Surface (4) : the front surface of the second lens where the rays enter this lens. The curvature radius of this surface is 64.4 mm (Radius), the lens thickness is 4.5 mm (Thickness), the material is CaF₂ (Glass), and the semi-diameter of lens is 12.7 mm;

6. Surface (5) : the back surface of the second lens where the rays exit the second lens back into air. The curvature radius of this surface is -64.4 mm (Radius), the distance between the two lenses is optimized to 30 mm (Thickness), and the semi-diameter of lens is 12.7 mm;

7. Surface (IMA) : the location where the ray trace stops. No surfaces can be located after the image surface in the LDE. Note that this surface does not necessarily have to be at an acutal image location.

Because of using stock lenses, the only variable we assign here is the distance between two lenses, that is, the value of the thickness of surface 3 shown in Table.

Appendix 3 Conversion from the measured intensity (in [V]) to the radiation (in [W/m²])

In order to convert the measured intensity (in [V]) to the radiation (in [W/m²]), the following conversion process has been executed :

1. The relationship between the outputs of the detector and the lock-in amplifier

Labview reading from the output of the lock-in amplifier : $V_{lab} = 0.27456$ V;

Oscilloscope reading from the Vigo detector : $V_{det} = 920$ mV;

The relationship between the detector output V_{lab} and lock-in amplifier output V_{det} :

$$V_{det}(V) = 3.3508 \times V_{lab}(V) \quad (1)$$

2. The relationship between the intensity and power

The response characteristics of the Vigo detector from the datasheet :

(1) The voltage responsivity (acc. $\pm 20\%$ at $10.6 \mu\text{m}$) : $R = 2.7E + 4$ V/W;

(2) The active area : $S = 0.5 \text{ mm} \times 0.5 \text{ mm}$.

The relationship between the intensity (in [V]) and the power (in [W]) :

$$\frac{Power(W)}{Intensity(V)} = \frac{1}{R(\frac{V}{W})} = 3.7E - 5(\frac{W}{V}) \quad (2)$$

Here, the intensity is V_{det} , then the power in function of the intensity is obtained by :

$$Power(W) = 3.7E - 5 * Intensity(V_{det}, in[V]) = 1.24E - 4 * V_{lab}(V) \quad (3)$$

3. The conversion between the measured intensity (in [V]) and the radiation (in [W/m²])

$$Radiation = \frac{Power(W)}{Area(m^2)} = \frac{1.24E - 4 * V_{lab}(V)}{0.5E - 3 * 0.5E - 3} = 496 * V_{lab}(V) \quad (4)$$

Appendix 4 Solar emission spectrum

Solar emission spectrum is the distribution of the radiation energy associated with the given wavelengths. More than 99.9% of the energy is concentrated in the wavelength range from 0.2-10.0 μm , and the peak radiation is at 0.48 μm . The energy in the ultraviolet band (<0.40 μm), the visible light band (0.40-0.76 μm) and the infrared band (>0.76 μm) account for about 9%, 44%, and 47% of the total energy, respectively. The solar emission spectrum is a continuous spectrum, but when the visible light below the Sun's surface passes through the layers above the photosphere and chromosphere, some light at particular wavelengths is absorbed by atoms and ions and so it seems missing in the solar emission spectrum that we can see. When there is no light, it appears as black in the solar emission spectrum. These absorption lines are called Fraunhofer lines, and there are more than 2000 Fraunhofer lines of the solar atmosphere when the Sun is viewed from moderate to high resolution [1].

Fig. 1 shows a solar irradiance spectrum in the range of 1223-1263 cm^{-1} computed through a Model by G. Wang [2], and there are no Fraunhofer lines in the range of 1241.4-1242.4 cm^{-1} (Fig. 2 (a)). In the range of 1261.3-1262.5 cm^{-1} (Fig. 2 (b)), there is a very weak Fraunhofer line which can be neglected compared with the atmospheric absorption lines for our research.

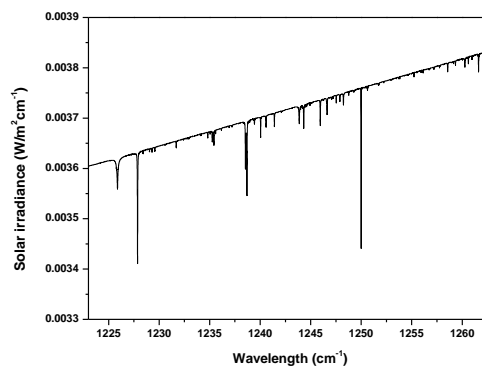


Figure 1 Solar irradiance spectrum in the range of 1223-1263 cm^{-1} computed through a Model by G. Wang [2].

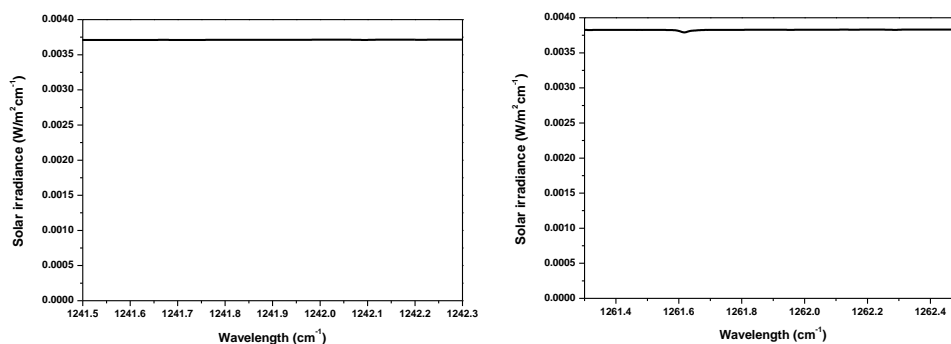


Figure 2 (a) Solar irradiance spectrum in the range of 1241.4-1242.4 cm^{-1} ; (b) Solar irradiance spectrum in the range of 1261.3-1262.5 cm^{-1} computed through a Model by G. Wang [2].

References

- [1] J. Lean and T. N. Woods. Solar spectral irradiance measurements and models, in Evolving Solar Physics and the Climates of Earth and Space, K. Schrijver and G. Siscoe Eds, Cambridge University Press, 2010, 269-298.
- [2] http://rtweb.aer.com/solar_frame.html.

Appendix 5 Article : Real-time monitoring of N₂O production in a catalytic reaction process using mid-infrared quantum cascade laser

Real-time monitoring of N₂O production in a catalytic reaction process using mid-infrared quantum cascade laser

Fengjiao Shen^{a,†}, Joudia Akil^b, Gaoxuan Wang^a, Christophe Poupin^b, Renaud Cousin^b, Stéphane Siffert^b, Eric Fertein^a, Tong-Nguyen Ba^a, Weidong Chen^{a*}

^a *Laboratoire de Physicochimie de l'Atmosphère, Université du Littoral Côte d'Opale Dunkerque, France; fjshen249@gmail.com (F.S.); fertein@univ-littoral.fr (E.F.);*

^b *Unité de Chimie Environnementale et Interactions sur le Vivant, Université du Littoral Côte d'Opale Dunkerque, France*

* *Correspondence: chen@univ-littoral.fr; Tel.: +33-328658264*

† *Current address: 189A, Av. Maurice Schumann, Université du Littoral Côte d'Opale, Dunkerque 59140, France.*

Abstract

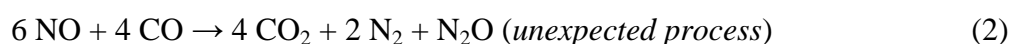
In the context of climate change mitigation, reuse of carbon dioxide (CO₂) represents an alternative with important applications in chemical industry and power generation. Therefore, CO₂ must be purified. Combustion processes lead to high amounts of CO₂ but still with impurities and also accompanied by toxic gases (mainly NO and CO). A catalytic reduction process of NO (to N₂) while oxidizing CO into CO₂ is a promising method to purify the CO₂. However, nitrous oxide (N₂O) with a global warming potential of 300 times greater than CO₂ may be a by-product from this process. It is therefore necessary to optimize the chemical reaction conditions to minimize N₂O production. A room-temperature continuous-wave (CW) external-cavity quantum cascade laser (EC-QCL)-based optical sensor was developed for real-time monitoring N₂O production during the whole catalytic reaction process. A well-isolated N₂O absorption line, located at 1261.0598 cm⁻¹, of the ν_1 fundamental vibrational band was selected for sensitive and selective measurement of N₂O concentration by direct absorption spectroscopy. Using a modified-Herriot multi-pass cell with an effective path-length of 50 m, the limit of detection (1 σ) of 32.3 ppbv was obtained in 12 s with 1.1% relative uncertainty in measurement precision. N₂O productions through the catalytic reduction of NO by CO over Pt/SiO₂ catalyst under different temperatures were investigated. High N₂O production of up to ~ 6.1 ppmv at 190 °C was observed. The optimal reaction conditions for zero N₂O production were found at a temperature higher than 340 °C where 47% of NO was converted to N₂.

Keywords: Catalytic reaction process; NO-CO reaction; Pt/SiO₂ catalyst; Quantum cascade laser; Long-path laser absorption spectroscopy.

1 Introduction

Carbon dioxide (CO₂) is responsible for 55-60% of anthropogenic radiative forcing on global warming. The vast majority of anthropogenic CO₂ emissions come from combustion of fossil fuels (principally coal, oil, and natural gas) [1]. To reduce CO₂ injected into the atmosphere, reuse of CO₂ represents a promising and alternative solution because CO₂ is a valuable industrial gas for chemical industrial applications and power generation [2]. For this purpose, CO₂ should be as pure as possible. Purification of CO₂ can be performed through the following methods: (1) pre-combustion [3], (2) post-combustion [4] and (3) oxyfuel-combustion. Compared to the first two methods, oxyfuel-combustion allows one to obtain a rich CO₂ stream with the highest purity (80%-98%) [5]. In an oxyfuel system, the combustion flow consists of O₂ and CO₂. This Process emits also water (H₂O) vapor, unburned components such as carbon monoxide (CO) generated by incomplete combustion and nitrogen monoxide (NO) due to the oxidation of nitrogen (N₂) included in the fuel. Because NO_x (including NO and NO₂) is considered as one of the main environmental pollutants responsible for production of photochemical smog and acid rain, as well as for ozone layer depletion [6], its production should be minimized.

Purifying CO₂ in an exhaust flow from the oxyfuel-combustion can be realized through the reduction of NO to N₂ by oxidizing CO into CO₂ over catalysts [5]. Products from the chemical process of NO reduction via reaction with CO is, like any chemical reaction, depending upon the reaction conditions (quantity of NO and CO, temperature, pressure, presence of oxygen and water vapor or not), kind of catalyst (active phase, metal dispersion, support type) and synthesis method, etc. The main reactions are given by the following equations [7]:



As shown in Equation (2), in an unexpected process, N₂O may be a by-product from the NO-CO reaction [6]. As N₂O is a very powerful greenhouse gas with a global warming potential of 300 times greater than CO₂, it is therefore necessary to optimize the catalytic reaction conditions to minimize the N₂O production. In the present work, a N₂O sensor based on a continuous-wave external-cavity quantum cascade laser (EC-QCL) has been developed for real-time on-line monitoring of N₂O during the catalytic reduction process of NO by CO.

The analytical techniques currently used to measure N₂O concentration are described as follows:

(1) Gas Chromatograph (GC) which separates different chemical components from a mixture based on the molecular-specific retention times in a separation column, the eluted analyte components from the column may be detected using a thermal conductivity detector (TCD) based on the fact that their thermal conductivities are different from that of the reference carrier gas. However, the retention time for N₂O and CO₂ are almost the same. In case of a huge CO₂ amount in the gas composition, this cross-interference will result in hiding the small N₂O signal [8], which makes GC technique unsuitable for quantifying N₂O in this work.

(2) Mass Spectrometry (MS) in which the gas sample is firstly ionized to electrically charged fragments. By subjecting and accelerating them in an electric or magnetic field, they will be separated according to their mass-to-charge ratio (MCR) [9] which determines the deflection of the moving ion's trajectory inside the electric or magnetic field. They will be detected using an electron multiplier capable of detecting charged particles. The molecular species can thus be identified and quantified via the information on their MCR and the detected ion abundance [10]. As summarized in Table 1, the mass fragments of N₂O are 44, 30, 28, 16 (in [kg/C]) that can be also found in CO₂ (44, 28, 16) and in NO (30 and 16). These interferences will significantly impact N₂O quantification using MS.

Table 1. Mass-to-charge (m/z) ratio of the mass fragments of the main exhaust gases from oxyfuel-combustion.

Fragment	m/z (in [Kg/C])			
N ₂ O	44	30	28	16
NO	30	15	16	
NO ₂	30	46	16	
CO	28	16		
CO ₂	44	28	16	

(3) Tunable diode laser absorption spectroscopy (TDLAS) which identifies and quantifies gaseous species of a mixture based on the Beer-Lambert law. High spectral resolution TDLAS could enable in-situ, real-time, interference-free quantification of target molecular species with high-accuracy and without any sample preparation [11].

In this paper, we report on the development of a N₂O sensor based on a continuous-wave (CW) external-cavity quantum cascade laser (EC-QCL) operating at ~ 8 μm, coupled to a modified-Herriot multi-pass cell. Working at an optimal gas pressure of 120 mbar, a 1σ (SNR = 1) limit of detection of 32.3 ppbv was achieved in 12 s averaging time with a relative uncertainty of 1.1% in measurement precision. Productions of N₂O through catalytic reduction of NO by oxidizing CO into CO₂ over Pt/SiO₂ catalyst under different temperatures were experimentally monitored. N₂O concentration of up to ~ 6.1 ppmv at 190 °C was observed and analyzed. The optimal catalytic reaction condition for zero N₂O production was experimentally determined.

2 Experimental details

2.1 N₂O monitoring by long optical path absorption spectroscopy

The experimental setup is shown in Fig. 1. An EC-QCL (TLS-41000-MHF, Daylight solutions Inc.) was coupled to a modified-Herriot multipass cell. The EC-QCL frequency was scanned across an appropriate N₂O absorption line to determine its concentration-dependent integrated absorbance by fitting the experimental absorption spectrum to a Voigt profile model. The fine frequency tuning of the EC-QCL was realized by applying a 50 Hz sine-

wave (with an amplitude of +3 V_{PP} and an offset of +1.6 V_{DC}) from a function generator to the PZT (Piezoelectric ceramic transducer) element of the external cavity of the EC-QCL. As shown in Fig. 1, a 10% reflected laser beam is sent to a Fabry-Perot etalon for laser frequency calibration, and the 90% transmitted laser beam is directed into the multi-pass cell to perform long optical path absorption.

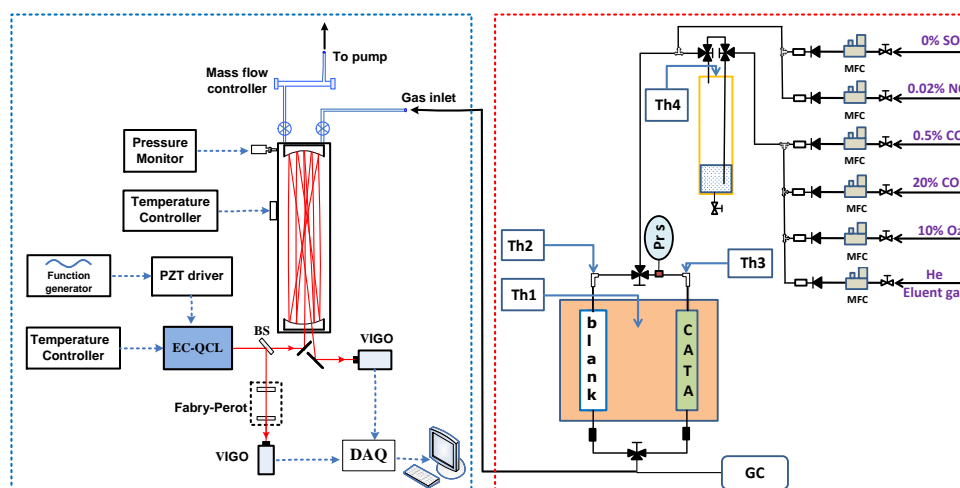


Fig. 1. Experimental setup used for N₂O monitoring. BS : Beam-splitter; GC : Gas chromatograph; MFC 1, 2, 3, 4, 5, 6 : Mass Flow Controllers; Th 1 : Thermocouple oven, Th 2 : Thermocouple blank, Th 3 : Thermocouple reactor, Th 4 : Thermocouple saturator; Prs : Pressure sensor; VIGO : Thermoelectrically cooled infrared photovoltaic detector; DAQ : Data Acquisition card.

The used modified-Herriot multi-pass cell (New Focus, Model 5612) was formed with two high reflectivity mirrors with a volume of 3.2 L. Laser light entered and exited the cell through a common hole equipped with a wedged entrance window at the front of the cell. In the present work, 90 passes were made between the mirrors (the mirror separation is 55 cm) resulting in a fixed effective optical path of 50 m. The exiting laser beam from the cell was focused into a thermoelectrically cooled infrared photovoltaic detector (PVI-4TE-10.6, VIGO System S.A.). A National Instruments data acquisition card (PCI 6251, NI Inc.), controlled using a LabVIEW program was applied for data sampling. The recorded data were transferred to a laptop for further data processing to retrieve N₂O concentration.

2.2 Selection of a N₂O absorption line for sensitive and selective trace gas monitoring

High spectral resolution is required in spectroscopic measurement for discrimination of the target gas absorption from the absorption of other interfering species. Careful selection of appropriate absorption line(s) well isolated from other interference lines was performed. Fig. 2 shows a simulation spectrum of the selected N₂O absorption line (centered at 1261.0598 cm⁻¹ with a line intensity of 9.677E-20 cm/molecule), based on the HITRAN database [12]. The simulation was calculated using 300 ppbv N₂O in a 50 m long absorption cell at 120 mbar. Meanwhile, potential interferences from 450 ppmv CO₂ and 1% H₂O vapor were taken into account in the simulation. As can be seen in Fig. 3, this selected line, well isolated from spectral interferences of CO₂ and H₂O, is a good tradeoff between the required sensitivity and

selectivity for monitoring N_2O by direct absorption spectroscopy in a 50-m long optical path at 120 mbar.

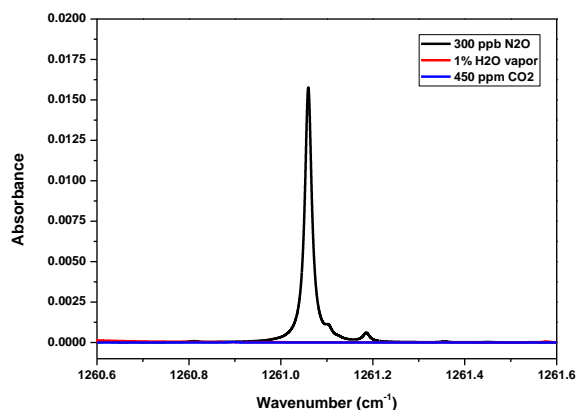


Fig. 2. Simulation of 300 ppbv N_2O absorption spectrum in a multi-pass cell ($L_{\text{eff}}=50$ m) at 120 mbar.

2.3 Frequency metrology and N_2O absorption spectrum retrieval

The N_2O absorption signal was recorded versus the data point number when scanning the EC-QCL frequency around $1261.0598 \text{ cm}^{-1}$ using PZT scan mode. For the conversion of this absorption signal (a) to an absorption spectrum (d) (Fig. 3), interference fringes from a home-made Fabry-Perot etalon with a free spectral range (FSR) of 1 GHz ($\sim 0.0333 \text{ cm}^{-1}$) were recorded (b) and used to determine the relationship between the data point number and the frequency in wave number (c). The absolute frequency was determined with the help of N_2O absorption frequency provided by the HITRAN database [12].

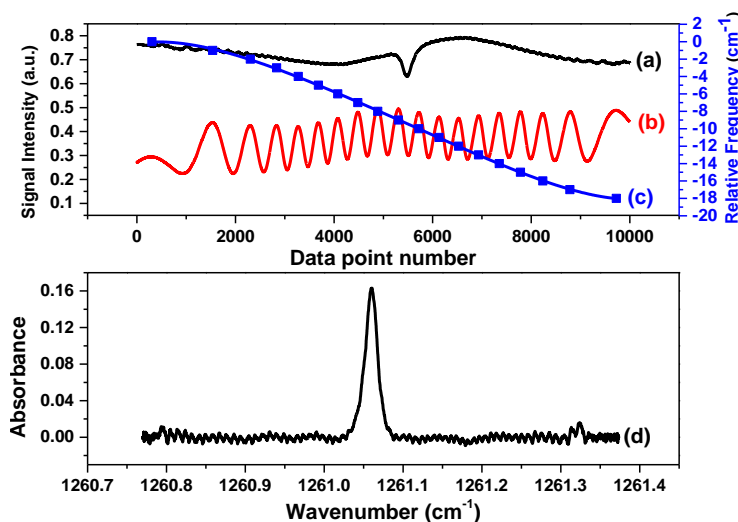


Fig. 3. Absorption signal of 5 ppmv N_2O at 120 mbar (a); the corresponding absorption spectrum (d) obtained by using the relative wavenumber calibration curve (c) which allows one to convert “data point number” into “wave number” by means of the FRS of the used etalon (b).

2.4 N_2O concentration retrieval

N_2O concentration can be determined based on the Beer-Lambert law using known spectral parameters (such as absorption frequency, line intensity, etc.). In the present work, the N_2O concentration was deduced from a calibration curve of concentration vs. integrated

absorbance (absorbance integrated over the scanned spectral range [13]). For this purpose, N₂O samples with different standard concentrations were produced using a high-precision gas dilutor (Model PPA 2000M, Calibrage Inc.).

A N₂O cylinder with a standard concentration of 1000 ppmv ($C_{initial}$) with different flow rate (D_1) was mixed with N₂ gas at a fixed flow rate (D_2) in the gas dilutor. The concentration of the diluted N₂O (C_{final}) was calculated using the following equations :

$$C_{final} = C_{initial} / K \quad (3)$$

$$K = (D_1 + D_2) / D_1 \quad (4)$$

where K is the dilution factor, D_2 is fixed at a constant rate of 2086 ml/min. Different N₂O concentrations were produced at 0.24, 0.51, 0.99, 1.46, 2.01, 2.48, 3.37 and 5.03 ppmv for the calibration in the present work. The relevant settings and the obtained final concentrations are presented in Table 2.

Table 2. Relevant settings and the diluted concentration.

D_1 [ml/min]	K	$C_{initial}$ [ppmv]	C_{final} [ppmv]
0.50	4173.0	1000	0.24
1.06	1968.9	1000	0.51
2.06	1013.6	1000	0.99
3.06	682.7	1000	1.46
4.20	497.7	1000	2.01
5.16	405.3	1000	2.48
7.06	296.5	1000	3.37
10.55	198.7	1000	5.03

The multi-pass cell was initially rinsed with pure nitrogen (N₂) before the N₂O measurement. The N₂O absorption spectra centered at 1261.0598 cm⁻¹ of ambient air and of different concentrations produced by dilution were recorded at 120 mbar, as shown in Fig. 4 (a). The relationship between the integrated absorbance A_I and the corresponding N₂O concentration (Fig. 4 (b)) was obtained from a linear fit :

$$C_{N_2O} = \frac{A_I}{k} \quad (5)$$

where $k = 7.7656E-4$. Based on this calibration formula, the ambient N₂O concentration was determined to be about 325 ± 7 ppbv. The relative uncertainty of about 4% is mainly contributed by the uncertainties in the linear fit ($\Delta k/k < 2\%$) and in the Voigt profile fitting ($\Delta A_I/A_I < 2\%$).

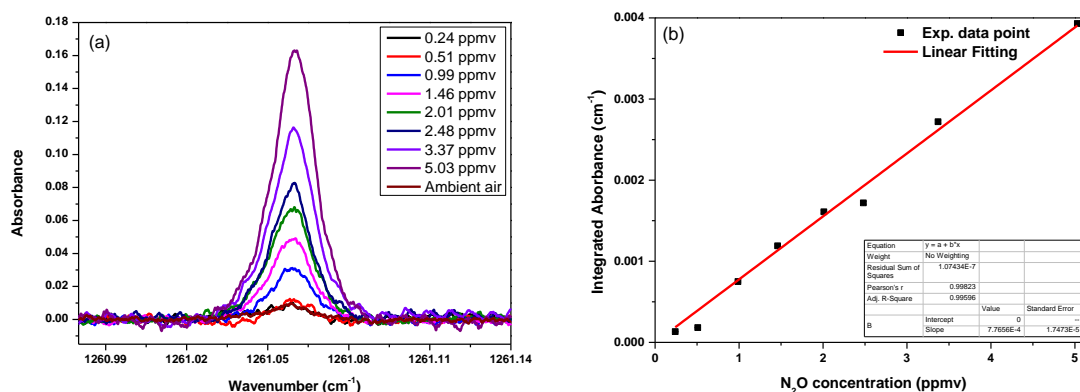


Fig. 4. (a) N₂O absorption spectra at different concentrations at 120 mbar; (b) Plot of the integrated absorbance vs. concentration, associated with a linear fit.

2.5 Measurement precision and limit of detection (LoD)

Analytical instrument stability is an important issue that affects the detection sensitivity and the measurement precision. In general, signal averaging is used to improve the detection sensitivity and the measurement precision. However, due to the instability of the instrument (such as changes in light intensity, laser wavelength shift and detector dark noise drift, etc.), any actual system is only stable for a limited time, i.e. an optimal averaging time should be determined via an Allan variance analysis [14].

In the present work, time series measurements of 1 ppmv N₂O absorption spectra were carried out for the Allan variance analysis to determine the optimal averaging time. 9000 consecutive direct absorption spectra of N₂O were experimentally recorded, with an acquisition time of 0.2 s for each spectrum. Fig. 5 plots an Allan deviation as a function of the averaging time [15] based on the time series measurements of N₂O absorption spectra. The decaying slope (red dashed line) shows the efficient white noise reduction by signal averaging with a maximum averaging time (system stability time) of about 236 s, which is mainly limited by the temperature and current stability of the QCL controller. The corresponding measurement precision is 5.2 ppbv, leading to a relative uncertainty in measurement precision of 0.5%. After 236 s, the Allan deviation increases (blue dashed line), where the system instability plays a major role which surmounts the noise reduction by increasing averaging time.

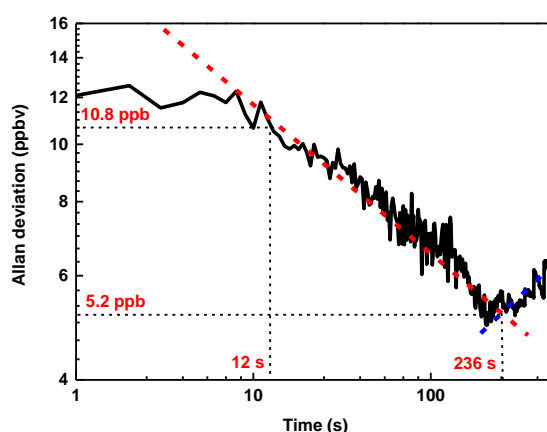


Fig. 5. Allan deviation plot.

In the present work on monitoring a chemical reaction, a measurement precision of 10.8 ppbv (corresponding to a relative precision uncertainty of 1.1%) in 12 s was used to real-time track N₂O production.

Fig.6 shows an experimental absorption spectrum of N₂O in air at a pressure of 120 mbar with 240 averaged spectra in 12 s, the concentration retrieved was 325 ppbv. Based on the signal-to-noise ratio (SNR = 10.1) deduced from the Voigt profile fit to an experimental absorption spectrum of N₂O in air and the fit residual, a 1 σ (SNR = 1) limit of detection was determined to be 32.3 ppbv in 12 s.

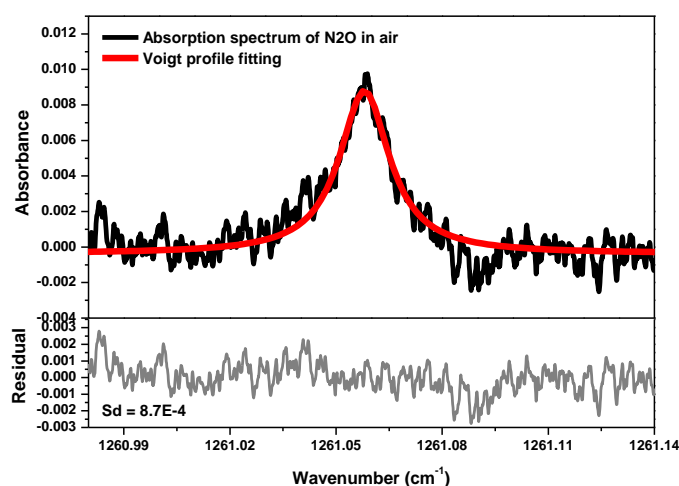


Fig. 6. *Upper panel* : Absorption spectrum of N₂O in air (black curve) @ 120 mbar accompanied with a Voigt profile fit (red curve). *Lower panel*: Fit residual.

3 Results and discussions

Before performing the catalytic reaction of NO with CO, a Pt/SiO₂ catalyst was pre-treated in a flow of He with a flow rate of 40 mL/min at 200 °C for 1.5 hours. The catalyst was sieved in order to retain particles of a diameter between 0.315 and 0.500 mm which aims to select particles with the same diameter because the diameter of the catalyst has an influence on the catalytic activity. It was then diluted to a constant volume by SiC (not active in CO₂ purification from 50 to 500 °C). CO₂ purification was then carried out by catalytic reduction of NO by CO in a fixed-bed flow reactor containing 150 mg Pt/SiO₂ catalyst at ambient pressure. All above experiments were carried out at a GHSV (Gas Hour Space Velocity : the ratio between the volumetric flow rate and the volume of the catalyst) of 2.24 10⁴ h⁻¹.

In a typical catalytic reaction process (Fig. 7 left), the flow of the reactant gases was composed of 20% CO₂, 10% O₂, 0.5% CO, 0.02% NO and He (eluent gas) with a total flow rate of 200 mL/min. The products of CO₂ and N₂ from the catalytic reduction of NO by oxidizing CO were analyzed by an on-line gas chromatography (TranceGC 1300 XXL, Global Analyzer Solutions G.A.S., Inc.), NO was analyzed with a NO analyzer (Xentra 4900C, Servomex Inc.), NO₂ was measured with the same NO analyzer after conversion of NO₂ to NO by a converter BÜNOx (Bühler Technologies Inc.), while N₂O was monitored by the EC-QCL-based Laser sensor (Fig. 7 right).

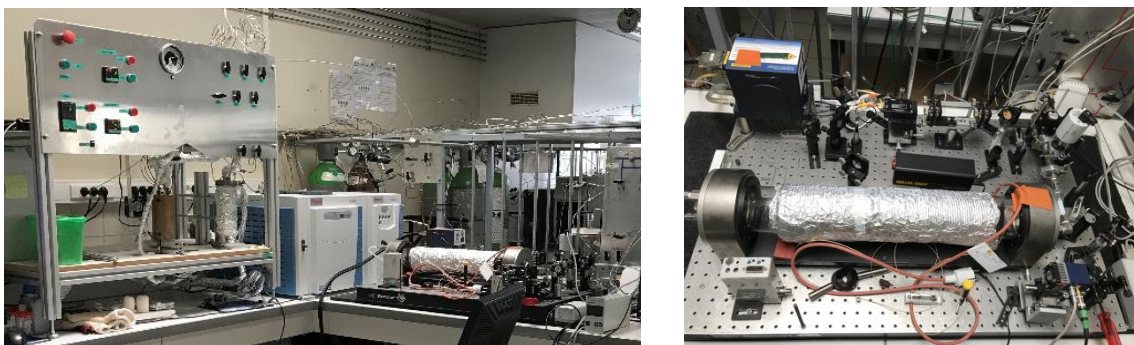


Fig. 7. *left:* Experience of catalytic reduction of NO to purify CO₂ in exhaust gas flow from oxyfuel-combustion, *right:* EC-QCL-based Laser sensor.

3.1 N₂O evolution in catalytic reaction of NO with CO

The catalytic reaction of NO with CO over the pre-treated Pt/SiO₂ catalyst in the temperature range of 50-500 °C was performed, N₂O production was monitored and analyzed by the developed EC-QCL sensor.

A N₂O absorption spectrum recorded during the process of NO reaction with CO over a Pt/SiO₂ catalyst at 190 °C is shown in Fig. 8. It was recorded at a pressure of 120 mbar in the multi-pass cell with 240 spectral averages in 12 s.

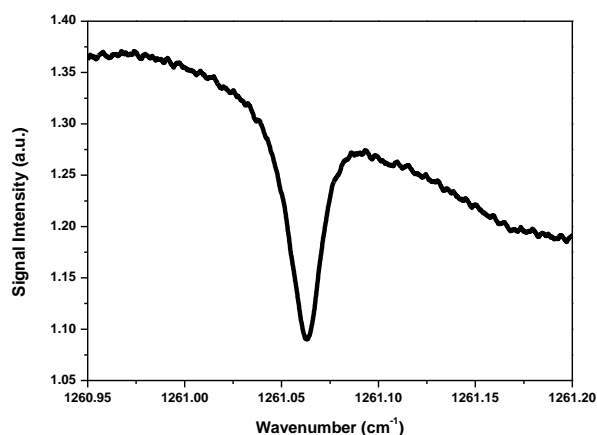


Fig. 8. Absorption spectrum of 6.13 ppmv N₂O during a catalytic reaction of NO with CO over a Pt/SiO₂ catalyst at 190 °C @ 120 mbar.

Fig. 9 shows time series measurement (with a step of 1 °C from 50 to 500 °C) of N₂O concentrations produced during the NO-CO reaction over the Pt/SiO₂ catalyst. A maximum concentration of ~ 6.1 ppmv N₂O was observed at 190 °C.

3.2 Result analyses and conclusion

According to the chemical reaction mechanism shown in Eq. (2), combining the result shown in Fig. 9 with a given initial NO concentration (0.02% or 200 ppmv) in the catalytic reaction process, one can determine the conversion efficiency of NO to N₂O using the concentration ratio of N₂O to NO.

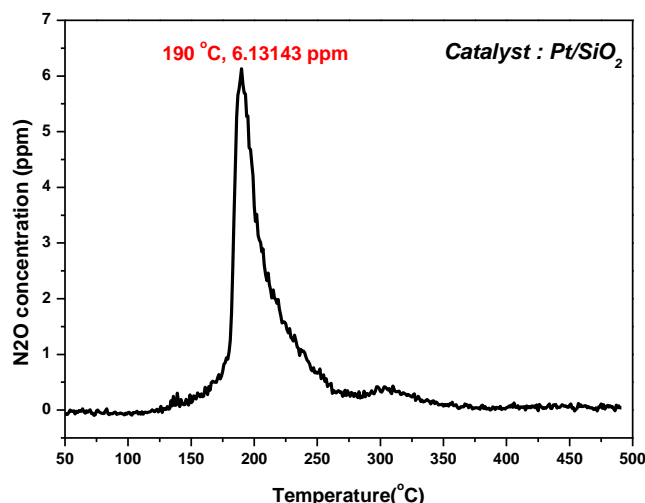


Fig. 9. Concentration of N_2O in a NO-CO reaction over a Pt/SiO_2 catalyst vs. temperature.

Efficiencies of the catalytic conversion using Pt/SiO_2 catalyst are plotted in Fig. 10 in the temperature range of 50-500 °C. The conversion efficiencies of NO to N_2 (red) by reduction, to NO_2 (blue) by oxidation and to N_2O (green) by reduction; as well as the conversion efficiency of CO to CO_2 (black) are shown in the figure. It can be seen that both N_2 (red data) and NO_2 (blue data) are the primary by-products, while N_2O (green data, the data in curve are magnified 10 times) is a secondary product with a very small amount after 100% conversion of CO to CO_2 (black data) at 180 °C. At the temperature of max. N_2O production, the reduction efficiencies of NO to N_2 (red data) and to N_2O (green data) reach about 59% and 6%, respectively, and the oxidation efficiency of NO to NO_2 (blue data) is around 31%, accompanied with 100% oxidation efficiency of CO (black data) to CO_2 .

As shown in Fig. 10, at 250 °C, the reduction efficiency of NO to N_2 (red data) is 63%, nearly 4% to N_2O (green data), and 30% oxidation efficiency of NO to NO_2 (blue data).

As can be seen, NO_2 (blue data) was produced after the full CO- CO_2 conversion (black data) through oxidation of NO by the residual O_2 in the exhaust gas flow, which reached 20% at 160 °C. The maximum favorable reduction efficiency of NO to N_2 (red data) was 63% at 250 °C. The optimal catalytic reaction conditions for zero N_2O production was observed at a temperature higher than 340 °C where 47% of NO is converted to N_2 (red data) and 26% of NO converted to NO_2 (blue data) and still 27% residual NO in the exhaust flow gas. All NO conversion efficiencies at specific temperatures discussed above are summarized in Table 3.

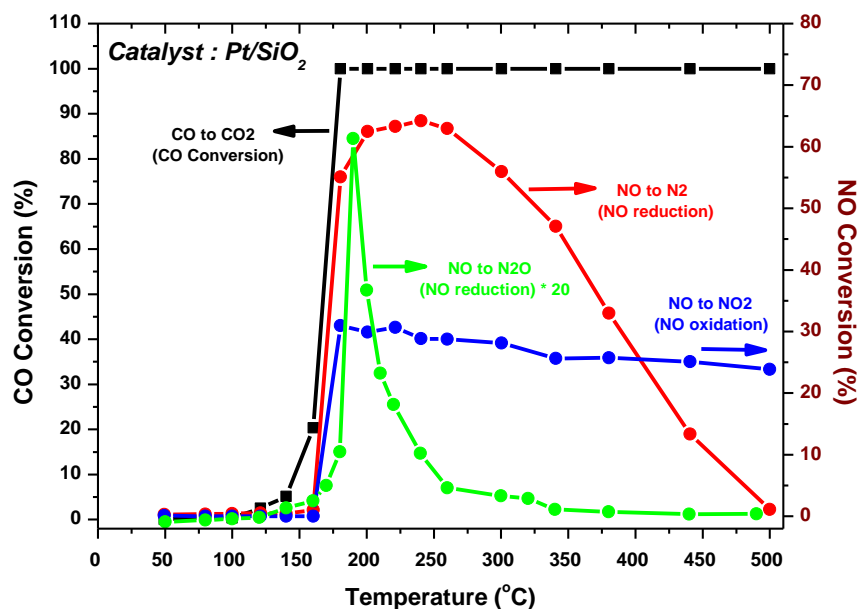


Fig. 10. Conversion efficiency of NO to N₂ (red), NO₂ (blue) and N₂O (green, the values are magnified 20 times); and CO to CO₂ (black) over Pt/SiO₂ vs. temperature.

Table 3. Conversion efficiency of NO to N₂, N₂O and NO₂ vs. temperature.

Temperature (°C)	NO conversion efficiency			
	NO → N ₂	NO → N ₂ O	NO → NO ₂	NO
190	59%	6%	31%	4%
250	63%	4%	30%	3%
340	47%	0%	26%	27%

4 Conclusions

We demonstrated the application of an 8 μm EC-QCL to real-time optical monitoring of N₂O evolution in a catalytic reaction of NO-CO. Productions of N₂O through catalytic reduction of NO by oxidizing CO over a Pt/SiO₂ catalyst were experimentally investigated under different temperatures, which allowed us to study the conversion efficiency of NO to N₂O and to determine the optimal catalytic reaction temperature for zero N₂O production.

Acknowledgements The authors thank the financial supports from the CaPPA project (ANR-10-LABX005) and the CPER-CLIMIBIO program. S. F. thanks the Labex CaPPA program and the “Pôle Métropolitain de la Côte d’Opale” (PMCO) for the PhD fellowship.

References

- [1] Denman KL, Brasseur G, Chidthaisong A, Ciais P, Cox PM, Dickinson RE, Hauglustaine D, Heinze C, Holland E, Jacob D, Lohmann U, Ramachandran S, Silva Dias PL, Wofsy SC, Zhang X, in *Climate Change 2007 : The Physical Science Basis*, (Solomon S, Qin D, Manning M, Chen Z, Marquis M, Averyt KB, Tignor M and Miller

- HL (eds.)). Cambridge Univ. Press, Cambridge, U.K. 2007; 499-588.
- [2] Tahir M, Amin NS, Recycling of carbon dioxide to renewable fuels by photocatalysis : Prospects and challenges, *Renew Sust. Energ. Rev.* 2013; 25: 560-579.
 - [3] Lee HJ, Lee JD, Linga P, Englezos P, Kim YS, Lee MS, Kim YD, Gas hydrate formation process for pre-combustion capture of carbon dioxide, *Energy* 2010; 35: 2729-2733.
 - [4] Adeyemo A, Kumar R, Linga P, Ripmeester J, Englezos P, Capture of carbon dioxide from flue or fuel gas mixtures by clathrate crystallization in a silica gel column, *Int. J. Greenh. Gas Control* 1010; 4: 478-485.
 - [5] Iloeje C, Field R, Ghoniem AF, Modeling and parametric analysis of nitrogen and sulfur oxide removal from oxy-combustion flue gas using a single column absorber, *Fuel* 2015; 160: 178-188.
 - [6] Skalska K, Miller JS, Ledakowicz S, Trends in NO_x abatement : A review, *Sci. Total Environ.* 2010; 408: 3976-3989.
 - [7] Pârvolescu VI, Grange P, Delmon B, Catalytic removal of NO, *Catal. Today* 1998; 46: 233-316.
 - [8] Giuliani N, Beyer J, Augsburger M, Varlet V, Validation of an analytical method for nitrous oxide (N₂O) laughing gas by headspace gas chromatography coupled to mass spectrometry (HS-GC-MS) : Forensic application to a lethal intoxication, *J. Chromatogr. B* 2015; 983: 90-93.
 - [9] Mizanuzzaman M, Dastidar AG, Azam R, Exhaust Gas Analysis of SI Engine and Performance of Catalytic Converter, *Int. J. Eng. Res. Appl.* 2013; 3: 313-320.
 - [10] Price P, Standard definitions of terms relating to mass spectrometry, *J. Am. Soc. Mass Spectrom.* 1991; 2: 336-348.
 - [11] Chen W, Yi H, Wu T, Zhao W, Lengignon C, Wang G, et al., Photonic Sensing of Reactive Atmospheric Species, in *Encyclopedia of Analytical Chemistry*, eds R.A. Meyers, John Wiley : Chichester. DOI: 10.1002/9780470027318.a9432.
 - [12] Rothman LS, Gordon IE, Barbe A, Benner DC, Bernath PF, Birk M, Boudon V, Brown LR, Campargue A, Champion JP, Chance K, Gamache RR, Goldman A, Jacquemart D, Kleiner I, Lacombe N, Lafferty W, Naumenko OV, Nikitin AV, Orphal J, Perevalov VI, Perrin A, Predoi-Cross A, Rinsland CP, Rotger M, Simeckova M, Smith MAH, Sung K, Tashkun SA, Tennyson J, Toth RA, Vandaele AC, Vander Auwera J, The HITRAN 2008 molecular spectroscopic database, *J. Quant. Spec. Rad. Transfer* 2005; 96: 139-204.
 - [13] Cui X, Lengignon C, Wu T, Zhao W, Wysocki G, Fertein E, Coeur C, Cassez A, Crois é L, Chen W, Wang Y, Zhang W, Gao X, Liu W, Zhang Y, Dong F, Photonic Sensing of the Atmosphere by absorption spectroscopy, *J. Quant. Spectrosc. Rad. Transfer* 2012; 113: 1300-1316.
 - [14] Werle P, Tunable diode laser absorption spectroscopy : Recent findings and novel approaches, *Infrared Phys. Technol.* 1996; 37: 59-66.
 - [15] Werle P, Mücke R, Slemr F, The limits of signal averaging in atmospheric trace-gas monitoring by tunable diode-laser absorption spectroscopy (TDLAS), *Appl. Phys. B* 1993; 57: 131-139.

Appendix 6 Invited talk, 41st PIERS, 17-20 June 2019, Rome, Italy

Laser Heterodyne Radiometry for Ground-based Measurement of CH₄ and N₂O in the Atmospheric Column

Fengjiao SHEN (1), Pascal JESECK (2), Yao-Veng TE (2), Tu TAN (3), Xiaoming GAO (3), Eric FERTEIN (1), and Weidong CHEN (1)

(1) Laboratoire de Physicochimie de l'Atmosphère, Université du Littoral Côte d'Opale, Dunkerque, France, (2) Laboratoire d'Etudes du Rayonnement et de la Matière en Astrophysique et Atmosphères, Université Pierre et Marie Curie, Paris, France, (3) Anhui Institute of Optics and Fine Mechanics, Chinese Academy of Sciences, Hefei, China

Measurements of vertical concentration profiles of the key atmospheric trace gases, such as ozone (O₃) [1,2], carbon dioxide (CO₂) [3,4], methane (CH₄) [2,4], nitrous oxide (N₂O) [2] and water vapor (H₂O) [2], is extremely important for our understanding of regional air quality and global climate change trends.

In this context, a portable mid-infrared laser heterodyne radiometer (mid-IR LHR) has been developed [5] in the present work which aims at ground-based remote measurements of trace gases in the atmospheric column.

The solar radiation undergoing absorption by multi-species in the atmosphere was coupled into an optical fiber through a telescope that was installed on a sun tracker following the Sun's movement. An external cavity quantum cascade laser (EC-QCL) tunable from 1223 to 1263 cm⁻¹ was used as local oscillator (LO) to mix the Sun light in a fast photodetector to generate a beat note at radio frequency (RF). Scanning the LO frequency across absorption lines allows one to recover the absorption feature of the target molecular trace gases from the total absorption of the solar radiation in the atmospheric column.

A field test has been performed on the roof of the laboratory in Dunkerque (51.05°N/2.34°E). The preliminary result of heterodyne measurement of tropospheric CH₄ and N₂O in the atmospheric column will be presented and discussed.

Acknowledgments The authors thank the financial supports from the CaPPA project (ANR-10-LABX005) and the CPER CLIMIBIO program. S. F. thanks the program Labex CaPPA and the "Pôle Métropolitain de la Côte d'Opale" (PMCO) for the PhD fellowship support.

References

- [1] R.T. Menzies, and R.K. Seals, Ozone monitoring with an infrared heterodyne radiometer, *Science* **197** (1977) 1275-1277
- [2] D. Weidmann, T. Tsai, N.A. Macleod, and G. Wysocki, Atmospheric observations of multiple molecular species using ultra-high-resolution external cavity quantum cascade laser heterodyne radiometry, *Opt. Lett.* **36** (2011) 1951-1953
- [3] E.L. Wilson, M.L. McLinden, J.H. Miller, Miniaturized laser heterodyne radiometer for measurements of CO₂ in the atmospheric column, *Appl. Phys. B* **114** (2014) 385-393
- [4] A. Rodin, A. Klimchuk, A. Nadezhdinskiy, D. Churbanov, and M. Spiridonov, High resolution heterodyne spectroscopy of the atmospheric methane NIR absorption, *Opt. Express* **22** (2014) 13825-13834
- [5] F. Shen, P. Jeseck, Y. Te, T. Tan, X. Gao, E. Fertein, and W. Chen, Laser heterodyne radiometry for ground-based monitoring of multi-species in the atmospheric column, *Geophys. Res. Abstracts*, Vol. **20**, EGU2018-79 (2018), EGU General Assembly 2018
- [6] F. Shen, P. Jeseck, Y. Te, T. Tan, X. Gao, E. Fertein, and W. Chen, Quantum cascade laser heterodyne radiometry for ground-based measurement of greenhouse gas in the atmospheric column, *Abstracts, Environmental 3, FLAIR* (2018), Field Laser Applications in Industry and Research 2018

Publications

- [1] **Fengjiao Shen**, Joudia Akil, Gaoxuan Wang, Christophe Poupin, Renaud Cousin, Stéphane Siffert, Eric Fertein, Tong-Nguyen Ba, Weidong Chen, "Real-time monitoring of N₂O production in a catalytic reaction process using mid-infrared quantum cascade laser ", Journal of Quantitative Spectroscopy & Radiative Transfer, 2018, **221**, 1-7.
- [2] **Fengjiao SHEN**, Pascal Jeseck, Yao-Veng Te, Tu Tan, Xiaoming Gao, Eric Fertein, Weidong Chen, "Development of a Ground-based Fully Transportable Mid-Infrared External Cascade Quantum Cascade Laser Heterodyne Radiometer (EC-QC-LHR)", in revision.
- [3] Gaoxuan Wang, Dong Chen, **Fengjiao Shen**, Hongming Yi, Rabih Maamary, Patrick Augustin, Marc Fourmentin, Dorothée Dewaele, Fabrice Cazier, Patrice Hubert, Alexandre Deguine, Denis Petitprez, Eric Fertein, Markus W. Sigrist, Weidong Chen, "Monitoring of short-lived climate pollutants by laser absorption spectroscopy", Proc. SPIE, 2017, 10111.
- [4] Gaoxuan Wang, **Fengjiao Shen**, Hongming Yi, Patrice Hubert, Alexandre Deguine, Denis Petitprez, Rabih Maamary, Patrick Augustin, Marc Fourmentin, Eric Fertein, Markus W. Sigrist Tong-Nguyen Ba, Weidong Chen, "Laser absorption spectroscopy applied to monitoring of short-lived climate pollutants (slcps)", Journal of Molecular Spectroscopy, 2018, **348**, 142-151.

Conferences

- [1] **Fengjiao Shen**, Gaoxuan Wang, Hongming Yi, Tao Wu, Rabih Maamary, Patrick Augustin, Marc Fourmentin, Cécile Coeur, Eric Fertein, Weidong Chen, "Photonic Sensing the Atmosphere : Challenges and Opportunities" (*sur invitation*), 14TH Workshop on urban and regional air quality, October 5-6, 2016. Hotel Rey Don Jaime, Valencia, Spain.
- [2] Gaoxuan Wang, Dong Chen, **Fengjiao Shen**, Hongming Yi, Patrice Hubert, Alexandre Deguine, Denis Petitprez, Eric Fertein, Markus W. Sigrist, Weidong Chen, "Monitoring of short-lived climate pollutants by laser absorption spectroscopy" (*invited talk*), SPIE Photonics West, 28 January - 2 February 2017, San Francisco, California, USA.

- [3] **Fengjiao Shen**, Dong Chen, Hongming Yi, Tong Nguyen Ba, Rabih Maamary, Patrick Augustin, Marc Fourmentin, Dorothée Dewaele, Fabrice Cazier, Cécile Coeur, Eric Fertein, Weidong Chen, "Applications of spectroscopic techniques to trace gas sensing (*oral*)", 9th THz days, 12-15 June 2017, Dunkerque, France.
- [4] **Fengjiao Shen**, Pascal Jeseck, Yao-Veng Te, Tu Tan, Xiaoming Gao, Eric Fertein, Weidong Chen, "Laser Heterodyne Radiometry for Ground-based Monitoring of Multi-Species in the Atmospheric Column (*poster*)", European Geosciences Union General Assembly 2018, Vienna, Austria, 8-13 April 2018.
- [5] **Fengjiao Shen**, Joudia Akil, Christophe Poupin, Renaud Cousin, Stéphane Siffert, Eric Fertein, Weidong Chen, "Real-time monitoring of N₂O concentration in an oxyfuel-combustion by quantum cascade laser absorption spectroscopy (*poster*)", JSM-Lyon 2018, 28-30 May 2018.
- [6] **Fengjiao Shen**, Pascal Jeseck, Yao-Veng Te, Tu Tan, Xiaoming Gao, Eric Fertein, Weidong Chen, "Mid-Infrared Laser Heterodyne Radiometry for Ground-based Monitoring of GHGs in the Atmospheric Column", OSA LACSEA, 25-28 June 2018, Orlando, USA.
- [7] **Fengjiao Shen**, Lingshuo Meng, Gaoxuan Wang, Tong Nguyen Ba, Eric Fertein, Cécile Coeur, Weidong Chen, "Techniques avancées en instrumentation spectroscopique pour la métrologie optique des composés atmosphériques" (*invited*), Optique Toulouse 2018, session PAMO, 3-6 Juillet 2018, Toulouse, France.
- [8] **Fengjiao Shen**, Pascal Jeseck, Yao-Veng Te, Tu Tan, Xiaoming Gao, Eric Fertein, Weidong Chen, "QCL-based measurement of the atmospheric CH₄ column by laser heterodyne radiometry" (*oral*), MidIR Spectroscopy Workshop, iGent, Gent, Belgium, 10 July 2018.
- [9] **Fengjiao Shen**, Pascal Jeseck, Yao-Veng Te, Tu Tan, Xiaoming Gao, Eric Fertein, Weidong Chen, "Ground-based monitoring of GHGs in the atmospheric column using mid-infrared laser heterodyne radiometry (LHR)", 40th PIERS, 1-4 August 2018, Toyama, Japan.
- [10] **Fengjiao Shen**, Pascal Jeseck, Yao-Veng Te, Tu Tan, Xiaoming Gao, Eric Fertein, Weidong Chen, "Mid-infrared laser heterodyne radiometry for ground-based monitoring of GHGs in the atmospheric column", OSA Optics and Photonics for Energy & the Environment (E2), 5-8 November 2018, Singapore.

- [11] **Fengjiao Shen**, Pascal Jeseck, Yao-Veng Te, Tu Tan, Xiaoming Gao, Eric Fertein, Weidong Chen, "Laser Heterodyne Radiometry for Ground-based Measurement of CH₄ and N₂O in the Atmospheric Column" (*invited talk*), 41st PIERS, 17-20 June 2019, Rome, Italy.
- [12] Dong Chen, **Fengjiao Shen**, Hongming Yi, Tao Wu, Gaoxuan Wang, Rabih Maamary, Dorothée Dewaele, Fabrice Cazier, Patrick Augustin, Marc Fourmentin, Cécile Coeur-Tourneur, Eric Fertein, Weidong Chen, "Mid-infrared laser based gas sensors for atmospheric applications (*invited talk*)", The 13th International Conference on Mid-IR Optoelectronics : Materials and Devices (MIOMD-XIII), September 18-22, 2016, Beijing, China.
- [13] Gaoxuan Wang, **Fengjiao Shen**, Dong Chen, Hongming Yi, Rabih Maamary, Patrice Hubert, Alexandre Deguine, Denis Petitprez, Eric Fertein, Markus W. Sigrist, Weidong Chen "Laser-based sensing of short-lived climate pollutants" (*invited talk*), 38th PIERS, **22-25 May 2017**, Saint Petersburg, Russia.
- [14] Jingjing Wang, **Fengjiao Shen**, Tu Tan, Zhensong Cao, Xiaoming Gao, Pascal Jeseck, Yao-Veng Te, Eric Fertein, Weidong Chen, "Infrared laser heterodyne radiometers for ground-based measurements of greenhouse gases in the atmospheric column (*poster*)", JSM-Cr éteil, 21-23 May 2019, France.